

University of Alberta

**Void Fraction and Bubble Size Distribution Measurements Underneath
Laboratory Breaking Waves**

by



German Rojas Orozco

A thesis submitted to the Faculty of Graduate Studies and Research in partial fulfillment
of the requirements for the degree of

**Doctor of Philosophy
in
Water Resources Engineering**

Department of Civil and Environmental Engineering

**Edmonton, Alberta
Fall 2008**



Library and
Archives Canada

Bibliothèque et
Archives Canada

Published Heritage
Branch

Direction du
Patrimoine de l'édition

395 Wellington Street
Ottawa ON K1A 0N4
Canada

395, rue Wellington
Ottawa ON K1A 0N4
Canada

Your file *Votre référence*
ISBN: 978-0-494-46411-3
Our file *Notre référence*
ISBN: 978-0-494-46411-3

NOTICE:

The author has granted a non-exclusive license allowing Library and Archives Canada to reproduce, publish, archive, preserve, conserve, communicate to the public by telecommunication or on the Internet, loan, distribute and sell theses worldwide, for commercial or non-commercial purposes, in microform, paper, electronic and/or any other formats.

The author retains copyright ownership and moral rights in this thesis. Neither the thesis nor substantial extracts from it may be printed or otherwise reproduced without the author's permission.

AVIS:

L'auteur a accordé une licence non exclusive permettant à la Bibliothèque et Archives Canada de reproduire, publier, archiver, sauvegarder, conserver, transmettre au public par télécommunication ou par l'Internet, prêter, distribuer et vendre des thèses partout dans le monde, à des fins commerciales ou autres, sur support microforme, papier, électronique et/ou autres formats.

L'auteur conserve la propriété du droit d'auteur et des droits moraux qui protègent cette thèse. Ni la thèse ni des extraits substantiels de celle-ci ne doivent être imprimés ou autrement reproduits sans son autorisation.

In compliance with the Canadian Privacy Act some supporting forms may have been removed from this thesis.

Conformément à la loi canadienne sur la protection de la vie privée, quelques formulaires secondaires ont été enlevés de cette thèse.

While these forms may be included in the document page count, their removal does not represent any loss of content from the thesis.

Bien que ces formulaires aient inclus dans la pagination, il n'y aura aucun contenu manquant.


Canada

ABSTRACT

This thesis describes a series of laboratory experiments that were conducted to study the air entrainment produced underneath mechanical generated deep-water breaking waves.

Two fiber-optic probes were calibrated for making void fraction and bubble size measurements underneath breaking waves. Tests showed that the normalized RMS error in the void fraction measurements was $\sim 10\%$. It was also determined that if a minimum of ~ 15 individual bubble velocities were averaged, the mean bubble velocities were accurate to $\pm 10\%$. The bubble size distribution measured with the probes was compared to the size distribution measured from digital video recordings, and it was found that these two distributions agreed closely with each other.

Three significant events were identified during the breaking process of a plunging wave: the plunging water jet impacting the forward face of the wave; the air cavity collapsing and evolving into a dense bubble cloud; and the splash-up impacting the water surface. Numerical models must be able to accurately predict the timing and nature of these events. There were 13 measurement positions along the plunging wave and the peak void fractions measured inside the bubble cloud varied from 0.024 to 0.97; and the mean void fractions varied from 0.012 to 0.37. For the spilling wave case, there were 4 measurement positions and the mean void fractions at these positions varied from 0.17 to 0.29. Based on ensemble averaged time series of $\langle \alpha \rangle$ it was deduced that, for the spilling wave case, the void fraction contours run parallel to the free surface. The speed of advance of the air cavity and the splash-up cloud beneath the plunging wave were

estimated to be ~ 75 and $\sim 90\%$ of the phase speed, respectively. For the spilling wave, the speed of advance of the bubble cloud was estimated to be $\sim 100\%$ of the phase speed.

ACKNOWLEDGEMENTS

I would like to take this opportunity to thank my supervisor, Professor Mark Loewen who gave me the privilege of working with him. He always believed in me and guided me. He provided me with the technical equipment on time, thus I was able to develop the experiments.

I would also like to express my appreciation to the members of my thesis committee, Dr. Hicks, Dr. Rajaratnam, Dr Kresta, and Dr. Yu for their time and thorough evaluation of my work

Thanks also to Mr. Perry Fedun for his laboratory assistance. He helped me with the set ups of all the experiments. He also helped me in the solution of many experimental problems.

I would like to say a special thank you to my family. My wife Liliana always had a word of love, support and understanding. My kids Juan Sebastian and Daniel Mateo also encouraged me and help me to remember that there was life outside the lab, like swimming lessons, soccer and softball practices. Thanks to you all for being so patient!

Thanks to the people in Colombia. My parents, with their continuous and generous support throughout all my studies, also deserve the credit. To Universidad Javeriana and COLFUTURO, thanks a lot.

This research was funded by the Natural Science and Engineering Research Council of Canada.

TABLE OF CONTENTS

Chapter	1	Introduction	
	1.1	Void Fraction and Bubble Size Distribution beneath Breaking Waves	1
	1.2	Objectives of This Thesis	6
	1.3	Organization of Thesis	6
	1.4	References	7
Chapter	2	Calibration of Fiber-optic Probes for Void Fraction and Bubble Size Distribution Measurements	
	2.1	Introduction	13
	2.2	Void Fraction	16
	2.3	Bubble Velocity Calibration	20
	2.4	Air Entrainment under Breaking Waves	26
	2.5	Conclusions	31
	2.6	References	32
Chapter	3	Measurements of Local Void Fraction under Breaking Waves	
	3.1	Introduction	50
	3.2	Experimental set-up	54
	3.3	Results	63
	3.4	Discussion and Conclusions	68
	3.5	References	73
Chapter	4	Measurements of Bubble size Distributions under Breaking Waves	
	4.1	Introduction	110
	4.2	Experimental Procedures	114
	4.3	Results	118

	4.4	Discussion	122
	4.5	Conclusions	127
	4.6	References	128
Chapter	5	Conclusions and Recommendations	
	5.	Conclusions	162
	5.2	Recommendations for Future Work	165
Appendix	A	Computer programs for void fraction and bubble velocity calibrations	166
Appendix	B	Wave maker programs	193
Appendix	C	Computer programs for the estimation of void fraction and bubble size distribution	198

LIST OF TABLES

Table	Caption	
2.1	Listing of the correlation parameters from the linear regression of rise time, T_R , versus bubble velocity, v_B	49
3.1	Plunging wave measurement positions, number of repeat waves, and clouds. \hat{x} is the dimensionless distance with respect to the breaking point. \hat{y} is the dimensionless depth with respect to the still water depth.	106
3.2	Spilling wave measurement positions, number of repeat waves, and clouds. \hat{x} is the dimensionless distance with respect to the breaking point. \hat{y} is the dimensionless depth with respect to the still water depth.	107
3.3	Plunging wave. \hat{t}_{\max} is the time when the maximum ensemble void fraction, $\langle \alpha \rangle_{\max}$ occurred. $\hat{t}_1 - \hat{t}_2$ is the lag time used to compute the mean void fraction, $\bar{\alpha}$.	108
3.4	Spilling wave. $\hat{t}_1 - \hat{t}_2$ is the lag time used to compute the mean void fraction, $\bar{\alpha}$.	109
4.1	Measurement positions, measurement locations, number of repeat plunging waves, number of identified bubbles and bubble clouds. \hat{x} from Eq. (3.3) and \hat{y} from Eq. (3.2).	159
4.2	Measurement positions, measurement locations, number of	160

repeat spilling waves, number of identified bubbles and bubble

clouds. \hat{x} from Eq. (3.3) and \hat{y} from Eq. (3.2).

4.3	Mean void fraction, plunging wave case.	161
4.4	Mean void fraction, spilling wave case.	161
A.1	Computer programs used in Chapter 2.	166
B.1	Computer programs used in the wave maker	193
C.1	Computer programs used in the estimation of void fraction and bubble size distribution	198

LIST OF FIGURES

Figure	Caption	
1.1	Plunging wave	11
1.2	Spilling wave	12
2.1	Close up of the tip of a fiber-optic probe	36
2.2	Histogram of digital voltage values used for void fraction computation. The data is from probe 1 and corresponds to a mean void fraction of 0.07. \downarrow threshold voltage. Voltages smaller than the threshold voltage occur when the tip of the probe is surrounded by water	37
2.3	Comparison of the average void fraction measured using the differential pressure transducer, $\alpha_{\Delta H}$ and the average void fraction measured using the fiber-optic probes, α_p . The solid line has a 1:1 slope. Probe 1 (open circle) and probe 2 (open square)	38
2.4	Normalized root mean square error in the void fraction expressed as a percent, $\varepsilon[\alpha_p](\%)$, versus the void fraction estimated using the probes, α_p . Probe 1 (open circle) and probe 2 (open square)	39
2.5	(a) A good bubble signature showing the four characteristics points (A–D). (b) A poor bubble signature with a standard deviation that exceeds the threshold (i.e. $>0.244 V$)	40

- 2.6 (a) Schematic of the flow cell apparatus showing the set-up for low bubble velocities. (b) Schematic of the flow cell showing the high speed camera and data acquisition systems 41
- 2.7 (a–c) Sequence of high-speed digital video images showing a bubble crossing the tip of a fiber-optic probe. Water flows downwards and bubbles rising slowly upwards in this configuration. (d) The corresponding bubble signature showing the four characteristics points (A–D). t is time in ms. and V is the voltage in volts. The times corresponding to the three images are denoted by arrows 42
- 2.8 Bubble velocity, v_B (cm/s), versus rise time, T_R (ms) for probe 2 mounted at 0° . The solid line is the regression of the logarithm of the bubble velocity, v_B , versus the logarithm of the rise time, T_R calculated using the least squares method. The 95% confidence limits of the experimental data are denoted by the dash-dot line 43
- 2.9 Plots of the four calibration equations relating the bubble velocity, v_B (cm/s) to the rise time, T_R (ms). Probe 1 at 90° (filled diamond), probe 1 at 0° (asterisk), probe 2 at 90° (open circle), and probe 2 at 0° (open square) 44
- 2.10 A digital video image used to make independent measurements of the bubble size distribution. The symbol, filled circle, marks 45

the location of the tip of the fiber-optic probe

- 2.11 A comparison of bubble size distributions measured using the fiber-optic probes and the photographic technique. ℓ denotes various measurements of the bubble size; C_{90} (*) and C_0 (+) are the cord length measurements from the fiber-optic probes using calibration equations for 90° and 0° , respectively; the major bubble axis size (open square) and the minor axis size (open diamond) measured using the photographic technique. N is the number of bubbles per size bin. (b) A comparison of the cord length distributions, C_{90} (*) and C_0 (+), adjusted by multiplying by $3/2$, and the minor axis size distribution (open diamond) 46
- 2.12 (a–c) A sequence of three digital video images showing the leading edge of the splash-up zone created by a plunging breaking wave as it passes the fiber-optic probes. (d) A time series of the average void fraction, α_p , computed by averaging the fiber-optic probe signals measured for 565 repeated breaking waves. Time, t , in seconds after breaking. The times corresponding to the three images are denoted by arrows 47
- 2.13 The bubble size distribution measured in the splashing zone using the fiber-optic probes. s is the cord length and N is the number of bubbles per bin size. The solid lines are obtained by linear regression; the slopes and the 95% confidence limits of the slopes are also shown. The magnitude of the Hinze scale is 48

denoted with ↓

- 3.1 (a) Jet formation at the crest of a plunging wave, $t = 9.2$ s. (b) 77
Cavity of entrapped air, $t = 9.3$ s. (c) Initial stages of the splash-
up process, $t = 9.4$ s. t equals zero at the start of the paddle
motion.
- 3.2 (a-d) Water jet impact and splash-up generation. (a) $t = 8.53$ s. 78
(b) $t = 8.73$ s. (c) $t = 8.93$ s. (d) 1st cloud had clockwise rotation
and 2nd cloud had counter clockwise rotation, $t = 9.13$ s. White
arrows indicate rotation direction. t equals zero at the start of the
paddle motion.
- 3.3 (a)-(c) Sequence of a spilling wave breaking process. (a) $t =$ 79
 12.17 s. (b) $t = 12.27$ s. (c) $t = 12.37$ s. t equals zero at the start
of the paddle motion.
- 3.4 Detailed schematic of the experimental equipment. 80
- 3.5 Time series of the instantaneous void fraction, $\alpha(i,t)$, measured 81
at position M, repeats (a) 5, (b) 6 and (c) 7. t equals zero at the
start of the paddle motion.
- 3.6 Time series of $\langle \alpha \rangle$ at position C, plunging wave, 60 repeat 82
waves. Position C is located at 0.37 m from the breaking
location. y is the vertical distance from the still water. (a) $y =$
0.085 m. (b) $y = 0.060$ m. (□) $\langle \alpha \rangle_{\max}$. (c) $y = 0.035$ m.
- 3.7 Locations of the probe tip inside the plunging wave. (a) 83
Positions A to E. (b) Positions F to K. The boxed in letters

- identify the surface profile corresponding to each probe position.
- is the location of the tip of the probe.
- 3.8 Locations of the probe tip inside the spilling wave. ○ is the location of the probe tip. 84
- 3.9 Time series of $\langle \alpha \rangle$ position 38, spilling wave, 6362 repeat breaking waves. t equals zero at the start of the paddle motion. 85
- 3.10 A sequence of images displaying the fiber-optic probes crossing the bubble cloud at position A under the plunging breaker. (white*) is the location of the bubble cloud's centroid. (○) is the tip of the fiber-optic probes. (a) $\hat{t} \sim 0.12$, (b) $\hat{t} \sim 0.23$, (c) $\hat{t} \sim 0.35$. (d) Sequence of the tip position related to the bubble centroid. The arrow positions out the braces that were installed to reduce the probe tip movement. 86
- 3.11 (a) Image showing the instant when $\langle \alpha \rangle_{\max}$ occurred at position A under the plunging breaker. The white line is the approximate path of the fiber-optic when crossing the air cavity. (○) is the position of the fiber-optic probe tips. (b) $\langle \alpha \rangle$. (□) indicates $\langle \alpha \rangle_{\max}$. The time interval between open triangles (Δ) is the interval of time used to compute $\bar{\alpha}$. (1) Water. (2) Air cavity. (3) Splash-up. 87
- 3.12 (a) Image showing the instant when $\langle \alpha \rangle_{\max}$ occurred at position B under the plunging breaker. The white line is the 88

approximate path of the fiber-optic. (o) is the position of the fiber-optic probe tips. (b) Time series of $\langle \alpha \rangle$. (\square) indicates $\langle \alpha \rangle_{\max}$. The time interval between the open triangles (Δ) is the time interval used to compute $\bar{\alpha}$. Three time zones are identified as (1) pure water, (2) air cavity and (3) splash-up.

3.13 (a) Image showing the instant when $\langle \alpha \rangle_{\max}$ occurred at 89

position C under the plunging breaker. The white line is the approximate path of the fiber-optic. (o) is the position of the fiber-optic probe tips. (b) Time series of $\langle \alpha \rangle$. (\square) indicates $\langle \alpha \rangle_{\max}$. The time interval between the open triangles (Δ) is the time interval used to compute $\bar{\alpha}$. Three time zones are identified as (1) pure water, (2) air cavity and (3) splash-up.

3.14 Sequence of images showing the collapse of the air cavity under 90

the plunging breaker. (a) $\hat{t} = 0.27$. (b) $\hat{t} = 0.33$. (c) $\hat{t} = 0.38$. The arrow in (b) points to an air filament.

3.15 (a) Image showing the instant when $\langle \alpha \rangle_{\max}$ occurred at 91

position D under the plunging breaker. The white line is the approximate path of the fiber-optic when crossing the 1st bubble plume. (o) is the position of the fiber-optic probe tips. (b) Time series of $\langle \alpha \rangle$. (\square) indicates $\langle \alpha \rangle_{\max}$. The time interval between open triangles (Δ) is the interval of time used to

compute $\bar{\alpha}$.

3.16 (a) Image showing the instant when $\langle \alpha \rangle_{\max}$ occurred at 92

position E under the plunging breaker. The white line is the approximate path of the fiber-optic when crossing the 1st bubble plume. (o) is the position of the fiber-optic probe tips. (b) Time series of $\langle \alpha \rangle$. (\square) indicates $\langle \alpha \rangle_{\max}$. The time interval between open triangles (Δ) is the interval of time used to compute $\bar{\alpha}$.

3.17 (a) Image showing the instant when $\langle \alpha \rangle_{\max}$ occurred at 93

position F under the plunging breaker. The white line is the approximate path of the fiber-optic when crossing the 2nd bubble plume. (o) is the position of the fiber-optic probe tips. (b) Time series of $\langle \alpha \rangle$. (\square) indicates $\langle \alpha \rangle_{\max}$. The time interval between open triangles (Δ) is the interval of time used to compute $\bar{\alpha}$.

3.18 (a) Image showing the instant when $\langle \alpha \rangle_{\max}$ occurred at 94

position G under the plunging breaker. The white line is the approximate path of the fiber-optic when crossing first the 3rd bubble plume and then the 2nd bubble plume. (o) is the position of the fiber-optic probe tips. (b) Time series $\langle \alpha \rangle$. (\square) indicates $\langle \alpha \rangle_{\max}$. The time interval between open triangles (Δ)

is the interval of time used to compute $\bar{\alpha}$.

- 3.19 (a) Image showing the instant when $\langle \alpha \rangle_{\max}$ occurred at position H under the plunging breaker. The white line is the approximate path of the fiber-optic when crossing the 3rd bubble plume. (o) is the position of the fiber-optic probe tips. (b) Time series of $\langle \alpha \rangle$. (\square) indicates $\langle \alpha \rangle_{\max}$. The time interval between open triangles (Δ) is the interval of time used to compute $\bar{\alpha}$. 95
- 3.20 (a) Image showing the instant when $\langle \alpha \rangle_{\max}$ occurred at position I under the plunging breaker. The white line is the approximate path of the fiber-optic when crossing the 3rd bubble plume. (o) is the position of the fiber-optic probe tips. (b) Time series of $\langle \alpha \rangle$. (\square) indicates $\langle \alpha \rangle_{\max}$. The time interval between open triangles (Δ) is the interval of time used to compute $\bar{\alpha}$. 96
- 3.21 (a) Image showing the instant when $\langle \alpha \rangle_{\max}$ occurred at position J under the plunging breaker. The white line is the approximate path of the fiber-optic when crossing the 3rd bubble plume. (o) is the position of the fiber-optic probe tips. The arrow points out a marker. (b) Time series of $\langle \alpha \rangle$. (\square) indicates $\langle \alpha \rangle_{\max}$. The time interval between open triangles (Δ) 97

is the interval of time used to compute $\bar{\alpha}$.

3.22 (a) Image showing the instant when $\langle \alpha \rangle_{\max}$ occurred at 98

position K under the plunging breaker. The white line is the approximate path of the fiber-optic when crossing the 3rd bubble plume. (o) is the position of the fiber-optic probe tips. The arrow points out a marker. (b) Time series of $\langle \alpha \rangle$. (\square) indicates $\langle \alpha \rangle_{\max}$. The time interval between open triangles (Δ)

is the interval of time used to compute $\bar{\alpha}$.

3.23 (a) Image showing the instant when $\langle \alpha \rangle_{\max}$ occurred at 99

position L under the plunging breaker. The white line is the approximate path of the fiber-optic when crossing the 3rd bubble plume. (o) is the position of the fiber-optic probe tips. (b) Time series of $\langle \alpha \rangle$. (\square) indicates $\langle \alpha \rangle_{\max}$. The time interval between open triangles (Δ) is the interval of time used to compute $\bar{\alpha}$.

3.24 (a) Image showing the instant when $\langle \alpha \rangle_{\max}$ occurred at 100

position M under the plunging breaker. The white line is the approximate path of the fiber-optic when crossing the 3rd bubble plume. (o) is the position of the fiber-optic probe tips. (b) Time series of $\langle \alpha \rangle$. (\square) indicates $\langle \alpha \rangle_{\max}$. The time interval between open triangles (Δ) is the interval of time used to

compute $\bar{\alpha}$.

- 3.25 (a) Image at position 21 under the spilling breaker. The white line is the approximate path of the fiber-optic when crossing the small air pocket. (o) is the position of the fiber-optic probe tips. (b) Time series of $\langle \alpha \rangle$. (- · - · -) time interval used to compute the mean void fraction. (\square) indicates frame time, $\hat{t} \sim 0.08$. 101
- 3.26 (a) Image at position 23 under the spilling breaker. The white line is the approximate path of the fiber-optic when crossing the bubble cloud. (o) is the position of the fiber-optic probe tips. (b) Time series of $\langle \alpha \rangle$. (- · - · -) time interval used to compute the mean void fraction. (\square) indicates frame time, $\hat{t} \sim 0.34$. 102
- 3.27 (a) Image at position 38 under the spilling breaker. The white line is the approximate path of the fiber-optic when crossing the small air pocket. (o) is the position of the fiber-optic probe tips. (b) Time series of $\langle \alpha \rangle$. (- · - · -) time interval used to compute the mean void fraction. (\square) indicates frame time, $\hat{t} \sim 0.65$. 103
- 3.28 Time series of $\langle \alpha \rangle$ at position 50 under the spilling breaker. (- · - · -) time interval used to compute the mean void fraction. 104
- 3.29 Void fraction fields. (a) Plunging wave (b) Spilling wave 105
- 4.1 (a) A good bubble signature showing the four characteristic points (t_A - t_D) (b) A poor bubble signature. 133

- 4.2 $\langle \alpha \rangle$ and bubble frequency of arrival to the tip of the probe, 134
 F_a . (a-b) Position A, interval of time (\square). (c-d) Position B. (e-f)
Position C. First interval of time: between markers (\square). Second
interval of time: between markers (O).
- 4.3 Comparison between the 0° and the 90° size distributions. N is 135
the number of bubbles per wave per μm increment and s is the
cord length. The cord length bins were centered at 1.0, 1.6, 2.2,
2.8, 3.7, 4.9, 6.6, 8.4, 10.5, 13.5, 16.5, and 19.5 mm. (a) Position
D, plunging wave. (b) Position 50, spilling wave.
- 4.4 (a) Image showing the instant when $\langle \alpha \rangle_{\max}$ occurred at 136
position A under the plunging breaker. The white line is the
approximate path of the fiber-optic when crossing the air cavity.
(o) is the position of the fiber-optic probe tips. (b) Bubble size
distribution. N is the number of bubbles per wave per μm
increment and s is the cord length. The cord length bins were
centered at 1.0, 1.6, 2.2, 2.8, 3.7, 4.9, 6.6, 8.4, 10.5, 13.5, 16.5,
and 19.5 mm. (o-) measured size distribution. (—) is the linear
regression. The numbers are the mean slope \pm 95% confidence
band limits on the slope.
- 4.5 (a) Image showing the instant when $\langle \alpha \rangle_{\max}$ occurred at 137
position B under the plunging breaker. The white line is the
approximate path of the fiber-optic when crossing the air cavity.

(o) is the position of the fiber-optic probe tips. (b) Bubble size distribution. N is the number of bubbles per wave per μm increment and s is the cord length. The cord length bins were centered at 1.0, 1.6, 2.2, 2.8, 3.7, 4.9, 6.6, 8.4, 10.5, 13.5, 16.5, and 19.5, 30, and 45 mm . (o-) measured size distribution. (—) is the linear regression. The numbers are the mean slope \pm 95% confidence band limits on the slope.

- 4.6 (a) Image showing the instant when $\langle \alpha \rangle_{\max}$ occurred at position C, before the collapsing of the air cavity, under the plunging breaker. The white line is the approximate path of the fiber-optic. (o) is the position of the fiber-optic probe tips. (b) Bubble size distribution. N is the number of bubbles per wave per μm increment and s is the cord length. The cord length bins were centered at 1.0, 1.6, 2.2, 2.8, 3.7, 4.9, 6.6, 8.4, 10.5, 13.5, 16.5, 19.5, 30, and 45 mm . (o-) measured size distribution. (—) is the linear regression. The numbers are the mean slope \pm 95% confidence band limits on the slope. 138

- 4.7 Bubble size distribution for position C under the plunging breaker, after the collapsing of the air cavity. N is the number of bubbles per wave per μm increment and s is the cord length. The cord length bins were centered at 1.0, 1.6, 2.2, 2.8, 3.7, 4.9, 6.6, 8.4, 10.5, 13.5, 16.5, 19.5, 30, and 45 mm . (o-) measured size 139

distribution. (—) is the linear regression. The numbers are the mean slope \pm 95% confidence band limits on the slope. (a) Before the fragmentation of the air cavity. (b) After the fragmentation of the air cavity.

- 4.8 (a) Image showing the instant when $\langle \alpha \rangle_{\max}$ occurred at position D under the plunging breaker. The white line is the approximate path of the fiber-optic when crossing the 1st bubble plume. (o) is the position of the fiber-optic probe tips. (b) Bubble size distribution. N is the number of bubbles per wave per μm increment and s is the cord length. The cord length bins were centered at 1.0, 1.6, 2.2, 2.8, 3.7, 4.9, 6.6, 8.4, 10.5, 13.5, 16.5, and 19.5 mm. (o-) measured size distribution. (—) is the linear regression. The numbers are the mean slope \pm 95% confidence band limits on the slope. 140

- 4.9 (a) Image showing the instant when $\langle \alpha \rangle_{\max}$ occurred at position E under the plunging breaker. The white line is the approximate path of the fiber-optic when crossing the 1st bubble plume. (o) is the position of the fiber-optic probe tips. (b) Bubble size distribution. N is the number of bubbles per wave per μm increment and s is the cord length. The cord length bins were centered at 1.0, 1.6, 2.2, 2.8, 3.7, 4.9, 6.6, 8.4, 10.5, 13.5, 16.5, and 19.5 mm. (o-) measured size distribution. (—) is the 141

linear regression. The numbers are the mean slope \pm 95% confidence band limits on the slope.

- 4.10 (a) Image showing the instant when $\langle \alpha \rangle_{\max}$ occurred at position F under the plunging breaker. The white line is the approximate path of the fiber-optic when crossing the 1st bubble plume. (o) is the position of the fiber-optic probe tips. (b) Bubble size distribution. N is the number of bubbles per wave per μm increment and s is the cord length. The cord length bins were centered at 1.0, 1.6, 2.2, 2.8, 3.7, 4.9, 6.6, 8.4, 10.5, 13.5, 16.5, and 19.5 mm. (o-) measured size distribution. (—) is the linear regression. The numbers are the mean slope \pm 95% confidence band limits on the slope. 142
- 4.11 (a) Image showing the instant when $\langle \alpha \rangle_{\max}$ occurred at position G under the plunging breaker. The white line is the approximate path of the fiber-optic when crossing first the 3rd bubble plume and then the 2nd bubble plume. (o) is the position of the fiber-optic probe tips. (b) Bubble size distribution. N is the number of bubbles per wave per μm increment and s is the cord length. The cord length bins were centered at 0.9, 1.3, 1.7, 2.1, 2.5, 2.9, 3.5, 4.3, 5.15, 6.3, and 47.5 mm. (o-) measured size distribution. (—) is the linear regression. The numbers are the mean slope \pm 95% confidence band limits on the slope. 143

- 4.12 Bubble size distribution for position G under the plunging breaker, 3rd bubble cloud. N is the number of bubbles per wave per μm increment and s is the cord length. The cord length bins were centered at 1.0, 1.6, 2.2, 2.8, 3.7, 4.9, 6.6, 8.4, 10.5, 13.5, 16.5, and 19.5 mm . (o-) measured size distribution. (—) is the linear regression. The numbers are the mean slope \pm 95% confidence band limits on the slope. 144
- 4.13 (a) Image showing the instant when $\langle \alpha \rangle_{\max}$ occurred at position H under the plunging breaker. The white line is the approximate path of the fiber-optic when crossing the 3rd bubble plume. (o) is the position of the fiber-optic probe tips. (b) Bubble size distribution. N is the number of bubbles per wave per μm increment and s is the cord length. The cord length bins were centered at 1.0, 1.6, 2.2, 2.8, 3.7, 4.9, 6.6, 8.4, 10.5, 13.5, 16.5, and 19.5 mm . (o-) measured size distribution. (—) is the linear regression. The numbers are the mean slope \pm 95% confidence band limits on the slope. 145
- 4.14 (a) Image showing the instant when $\langle \alpha \rangle_{\max}$ occurred at position I under the plunging breaker. The white line is the approximate path of the fiber-optic when crossing the 3rd bubble plume. (o) is the position of the fiber-optic probe tips. (b) Bubble size distribution. N is the number of bubbles per wave 146

per μm increment and s is the cord length. The cord length bins were centered at 1.0, 1.6, 2.2, 2.8, 3.7, 4.9, 6.6, 8.4, 10.5, 13.5, 16.5, and 19.5 mm . (o-) measured size distribution. (—) is the linear regression. The numbers are the mean slope \pm 95% confidence band limits on the slope.

4.15 (a) Image showing the instant when $\langle \alpha \rangle_{\max}$ occurred at 147

position J under the plunging breaker. The white line is the approximate path of the fiber-optic when crossing the 3rd bubble plume. (o) is the position of the fiber-optic probe tips. The arrow points out a marker. (b) Bubble size distribution. N is the number of bubbles per wave per μm increment and s is the cord length. The cord length bins were centered at 1.0, 1.6, 2.2, 2.8, 3.7, 4.9, 6.6, 8.4, 10.5, 13.5, 16.5, and 19.5 mm . (o-) measured size distribution. (—) is the linear regression. The numbers are the mean slope \pm 95% confidence band limits on the slope.

4.16 (a) Image showing the instant when $\langle \alpha \rangle_{\max}$ occurred at 148

position K under the plunging breaker. The white line is the approximate path of the fiber-optic when crossing the 3rd bubble plume. (o) is the position of the fiber-optic probe tips. The arrow points out a marker. (b) Bubble size distribution. N is the number of bubbles per wave per μm increment and s is the cord length. The cord length bins were centered at 1.0, 1.6, 2.2, 2.8, 3.7, 4.9,

6.6, 8.4, 10.5, 13.5, 16.5, and 19.5 *mm*. (o-) measured size distribution. (—) is the linear regression. The numbers are the mean slope \pm 95% confidence band limits on the slope.

4.17 (a) Image showing the instant when $\langle \alpha \rangle_{\max}$ occurred at 149

position L under the plunging breaker. The white line is the approximate path of the fiber-optic when crossing the 3rd bubble plume. (o) is the position of the fiber-optic probe tips. (b) Bubble size distribution. N is the number of bubbles per wave per μm increment and s is the cord length. The cord length bins were centered at 0.8, 1.0, 1.2, 1.4, 1.6, 1.8, 2.0, 2.2, 2.4, 2.6, 2.8, 3.0, 3.3, 3.7, 4.1, 4.5, 4.9, 5.4, 6.0, 6.6, 7.2, 7.8, 8.4, 9.0, 9.6, 10.5, 11.5, 12.5, 13.5, 14.5, and 16.5 *mm*. (o-) measured size distribution. (—) is the linear regression. The numbers are the mean slope \pm 95% confidence band limits on the slope.

4.18 (a) Image showing the instant when $\langle \alpha \rangle_{\max}$ occurred at 150

position M under the plunging breaker. The white line is the approximate path of the fiber-optic when crossing the 3rd bubble plume. (o) is the position of the fiber-optic probe tips. (b) Bubble size distribution. N is the number of bubbles per wave per μm increment and s is the cord length. The cord length bins were centered at 0.8, 1.0, 1.2, 1.4, 1.6, 1.8, 2.0, 2.2, 2.4, 2.6, 2.8, 3.0, 3.3, 3.7, 4.1, 4.5, 4.9, 5.4, 6.0, 6.6, 7.2, 7.8, 8.4, 9.0, 9.6,

10.5, 11.5, 12.5, 13.5, 14.5, and 16.5 *mm*. (o-) measured size distribution. (—) is the linear regression. The numbers are the mean slope \pm 95% confidence band limits on the slope.

- 4.19 (a) Image at position 21 under the spilling breaker. The white line is the approximate path of the fiber-optic when crossing the small air pocket. (o) is the position of the fiber-optic probe tips. (b) Bubble size distribution. N is the number of bubbles per wave per μm increment and s is the cord length. The cord length bins were centered at 1.0, 1.6, 2.2, 2.8, 3.7, 4.9, 6.6, 8.4, 10.5, 13.5, 16.5, and 19.5 *mm*. (o-) measured size distribution. (—) is the linear regression. The numbers are the mean slope \pm 95% confidence band limits on the slope. 151
- 4.20 (a) Image at position 23 under the spilling breaker. The white line is the approximate path of the fiber-optic when crossing the bubble cloud. (o) is the position of the fiber-optic probe tips. (b) Bubble size distribution. N is the number of bubbles per wave per μm increment and s is the cord length. The cord length bins were centered at 1.0, 1.6, 2.2, 2.8, 3.7, 4.9, 6.6, 8.4, 10.5, 13.5, 16.5, and 19.5 *mm*. (o-) measured size distribution. (—) is the linear regression. The numbers are the mean slope \pm 95% confidence band limits on the slope. 152
- 4.21 (a) Image at position 38 under the spilling breaker. The white 153

line is the approximate path of the fiber-optic when crossing the small air pocket. (o) is the position of the fiber-optic probe tips. (b) Bubble size distribution. N is the number of bubbles per wave per μm increment and s is the cord length. The cord length bins were centered at 1.0, 1.6, 2.2, 2.8, 3.7, 4.9, 6.6, 8.4, 10.5, 13.5, 16.5, and 19.5 mm. (o-) measured size distribution. (—) is the linear regression. The numbers are the mean slope \pm 95% confidence band limits on the slope.

- 4.22 Bubble size distribution for position 50 under the spilling breaker. N is the number of bubbles per wave per μm increment and s is the cord length. The cord length bins were centered at 1.0, 1.6, 2.2, 2.8, 3.7, 4.9, 6.6, 8.4, 10.5, 13.5, 16.5, and 19.5 mm. (o-) measured size distribution. (—) is the linear regression. The numbers are the mean slope \pm 95% confidence band limits on the slope. 154
- 4.23 Evidence of air filaments generated as the air cavity rotates under the plunging breaker. Also, there is evidence of the fragmentation into bubbles of the air filaments, $\hat{t} \sim 0.29$. This image was taken with the camera located below the air-cavity and looking downstream. 155
- 4.24 Average bubble size distribution, 2nd cloud (positions F and G), plunging wave. (o-) measured size distribution. (—) is the linear 156

regression. The numbers are the mean slope \pm 95% confidence band limits on the slope.

- 4.25 Average bubble size distribution for the plunging wave, 157
positions A to K. (o-) measured size distribution. (—) is the
linear regression. The numbers are the mean slope \pm 95%
confidence band limits on the slope.
- 4.26 Average bubble size distribution for the spilling wave, positions 158
23, 38 and 50. (o-) measured size distribution. (—) is the linear
regression. The numbers are the mean slope \pm 95% confidence
band limits on the slope.

LIST OF SYMBOLS

a_H	=	Hinze scale;
ak	=	Slope of a wave packet component;
b	=	Constant to compute bubble velocity;
$b[\alpha_P]$	=	Bias error of the void fraction measurements;
C	=	Constant to compute bubble size distribution;
f_C	=	Wave packet center frequency;
m	=	Constant to compute bubble velocity;
N	=	Number of bubbles per μm increment;
$N(j)$	=	Number of bubbles per μm increment, in bin j ;
$N_i(j)$	=	Instantaneous number of bubbles beneath the i^{th} wave, in bin j ;
N_B	=	Total number of bubbles in void fraction estimation;
N_R	=	Number of repeated waves at measuring positions underneath breaking waves;
$RMSE$	=	Total mean square error on the void fraction measurements;
r	=	Bubble radius;
s	=	Bubble cord length;
s_C	=	Critical bubble cord length;
t	=	Time referenced to the initiation of the wave paddle motion;
\hat{t}	=	Dimensionless time;
$t_{A,B,C,D}$	=	Characteristic points of the bubble signature;
T	=	Wave period of the centre frequency;
$(T_g)_i$	=	Gas residence time of the i^{th} bubble;
t_b	=	Breaking time;
T_R	=	Bubble rise time;
T_s	=	Total sampling time for void fraction estimation;

v_B	=	Bubble velocity;
$VAR[\alpha_P]$	=	Variance of the void fraction measurements;
v_B	=	Bubble velocity;
We_C	=	Critical Webber number;
x	=	Horizontal distance measured from the mean position of the wave paddle;
\hat{x}	=	Dimensionless horizontal distance;
x_b	=	Horizontal distance measured from the mean position of the wave paddle to the location where the falling water jet collides with the undisturbed water on the forward face of the wave (plunging wave case) or the location where a small water jet was detected at the wave crest (spilling wave);
y	=	Vertical distance measured from the tank bottom;
\hat{y}	=	Dimensionless vertical distance;
y_0	=	Still water depth;
α	=	True value of the void fraction;
$\bar{\alpha}$	=	Time averaged void fraction underneath breaking waves;
$\langle \alpha \rangle$	=	Ensemble void fraction underneath breaking waves;
$\langle \alpha \rangle_{\max}$	=	Peak ensemble void fraction underneath breaking waves;
$\alpha(i, t)$	=	Instantaneous local void fraction underneath breaking waves;
α_P	=	Void fraction measured by a fiber-optic probe;
$\alpha_{\Delta H}$	=	Void fraction measured by the differential pressure transducer;
β	=	Slope of the bubble size distribution;
Δf	=	Wave packet frequency band width;
ϵ	=	rate of dissipation of turbulent kinetic energy;
$\varepsilon[\alpha_P](\%)$	=	Normalized root mean square error on the void fraction

		measurements, expressed as percent;
ε_{NE}	=	Normalized standard error on $N(j)$;
φ	=	Angle at which the flow crosses the tip of the fiber-optic probes;
γ	=	Surface tension;
λ	=	Wave length of the center frequency;
ℓ	=	Denotes various measurements of the bubble size: bubble cord, minor bubble axis, or mayor bubble axis;
$\sigma[\alpha_p]$	=	Random error on the void fraction measurements;
σ_{N_j}	=	Standard deviation of the instantaneous $N_i(j)$ measurements;
ρ	=	Water density;

Chapter 1: Introduction

1.1 Void Fraction and Bubble Size Distribution beneath Breaking Waves

This thesis describes an experimental investigation of the air entrainment process beneath deep-water breaking waves. These waves have a depth to wave length ratio greater than $\sim 1/2$ and may break as a result of constructive interference, wave-wave, wave-current, and wind-wave interactions (Melville, 1996). Waves propagating into shallow water steepen and break because of the influence of the bottom and are referred to as shoaling waves (Mori et al, 2007).

The breaking process may or may not entrain air. Microscale breaking waves are short wind waves (i.e. less than 1 m wavelength) in which surface tension prevents air entrainment (Banner and Peregrine, 1993). Loewen and Siddiqui (2006) argued that a threshold scheme based on the variance of the vorticity accurately detects microscale breaking waves. This detection is important because the gas and heat transfer across the air-water interface are enhanced by the near surface turbulence generated beneath microscale breaking waves (Siddiqui et al. 2004; Zappa et al. 2004). As the wave length increases, gravitational effects dominate over surface tension effects; and the breaking process produces air entrainment (Lamarre and Melville, 1991). At the sea surface, the entrained air generates whitecaps which are visible at scales in the range from approximately 1m to 100m (Melville, 1996).

In deep water, the breakers are generally described as plunging or spilling breaking waves. The first stage of a plunging breaking wave is the formation of a water jet at the wave crest. Thereafter, the falling water jet collides with the undisturbed water on the forward face of the wave and two processes occur simultaneously: the creation of

a cavity of entrapped air beneath the water jet, and the water splash-up (Bonmarin, 1989), **Fig 1.1**. This air cavity is unstable and collapses, evolving into the first bubble cloud. Simultaneously, the initial jet impact creates the second cloud. The impact of the drops produced by the splash-up process creates a third cloud. In a spilling wave, the breaking process may be started by the appearance of a rough surface, or by the appearance of a small jet at the wave crest (Duncan, 2001). After this initial stage, a small region of turbulence forms at the crest of the wave and this region grows as water spills down the face of the wave (Duncan et al, 1994), **Fig 1.2**.

Bubbles entrained by dense bubble plumes enhance the different processes occurring at the air-sea interface, e.g. gas transfer (Farmer et al, 1993; Liss et al, 1997), and aerosol formation (Blanchard and Woodcock, 1957; Monahan, 1986). Therefore, entrained bubbles affect the prediction of bubble mediated oxygen transfer across the air-sea interface which is important in biological oceanography (Jochum and Murtugudde, 2006). Also, the entrained bubbles influence the transfer rates of CO₂ between the atmosphere and the ocean and accurate estimates of these rates are crucial for predicting global warming (Leifer et al. 2006b). Moreover, the air entrainment process consumes up to 50% of the initial wave energy (Rapp and Melville, 1990; Lamarre and Melville, 1991). Breaking waves have also been blamed for damaging coastal structures. In this regard, Bullock, et al, (2001) reported that the maximum impact pressures are influenced by the amount of air entrained by breaking waves at the impact point. In addition, as entrained bubbles rise back to the surface, they transport bacteria and organic material (Blanchard and Sysdek, 1970; Duncan, 2001).

Breaking waves generate a complex two phase flow, in which the entrained bubble sizes range between tens of micro meters to centimeters (Monahan, 1986; Haines and Johnson, 1995). Large bubbles (transient bubbles) quickly rise back to the surface, leaving a degassed plume composed of a diffuse cloud of microbubbles (background bubbles) which have small rise velocities and are easily advected by currents (Loewen, et al, 1996). These two types of bubble clouds had been previously defined as alpha (dense) and beta (diffuse) plumes by Monahan (1986). The presence of large bubbles in the dense alpha plumes being the most important difference between the two types of bubble clouds (Leifer and Leeuw, 2006a, b).

The role of large bubbles in air-sea gas exchange is poorly understood (Meville, 1996). Studies modelling the air-sea gas transfer have indicated that large bubbles have a significant impact on bubble-mediated gas transfer process (Keeling, 1993; Wolf, 1993). Upstill-Goddard (2006) pointed out that existing models of bubble mediated gas transfer have not been properly validated because of a lack of measurements of bubble properties measurements such as bubble size distributions, air volume concentrations and depth distributions.

Progress in quantifying the effect of bubble entrainment will be achieved by making accurate measurements of the void fraction (defined as the ratio of the volume of air to the total volume of the air-water mixture), bubble velocity and bubble size distributions beneath breaking waves (Melville, 1996; Blenkinsopp and Chaplin, 2007a; Deane and Stokes 2002). These measurements can be performed in the field as well as in the laboratory. Equipment deployment in the open ocean field is difficult; furthermore, many measuring techniques require averaging over periods of time which are

significantly longer than the wave periods (Loewen et al, 1996). Moreover, breaking waves are temporally and spatially intermittent, making field measurements especially challenging (Lamarre and Melville, 1991). As a consequence, laboratory measurements have proven to be a particularly valuable tool for studying breaking waves (Melville, 1996). In the laboratory controlled repeatable experiments can provide measurements that can be easily ensemble averaged.

Bubble size distributions and void fraction measurements may be affected by water chemistry (Leifer et al, 2007). Chanson et al. (2006) performed measurements beneath the bubble clouds generated by vertical circular plunging jets in freshwater and saltwater and found that a greater number of small bubbles occurred in seawater compared to freshwater and that there was less air entrainment in seawater. However, it has been pointed out that the flow and entrainment process created by a circular plunging jet may be quite different from those created by breaking wave packets (Blenkinsopp and Chaplin, 2007b).

There have been several studies comparing the bubble size distribution beneath breaking waves in freshwater and saltwater. Cartmill and Su (1993) studied large breaking waves (wave heights equal to 1.2 m) using mechanically generated plunging waves to simulate the air entrainment process. They observed that the shape of the large-transient bubble size distribution (bubbles larger than $r \sim 1.0 \text{ mm}$) was the same in freshwater and saltwater. However, they observed that a greater number of small bubbles ($0.034 < r < 1.2 \text{ mm}$) per unit volume occurred in saltwater than in freshwater. Haines and Johnson (1995) studied bubble clouds using a tipping bucket suspended 70 cm above the surface of the main tank and observed large differences in saltwater and freshwater.

Using a photographic technique, they detected bubbles in the range $0.050 < r < 1.2 \text{ mm}$. They found that there were more small bubbles in saltwater (bubbles smaller than $r \sim 1.0 \text{ mm}$), and that there were more large bubbles in freshwater (bubbles larger than $r \sim 1.0 \text{ mm}$). Loewen, et al. (1996) using a video technique, to study air entrained underneath gently spilling mechanically-generated laboratory waves, found that the size distributions were the same in freshwater and saltwater, for bubbles in the range $1.0 < r < 4.0 \text{ mm}$. Recently, Blenkinsopp and Chaplin (2007b) also observed that the differences between air entrainment beneath laboratory-scale plunging breaking waves in fresh and seawater were insignificant.

Laboratory-scale effects have been studied by Mori (2007) for shoaling breaking waves. Using a dual tip resistivity probe, they measured bubble size distributions, for bubble cord lengths larger than $s \sim 0.1 \text{ mm}$, and found that they were independent from the experimental scale. Deane and Stokes (1999, 2002) used a video technique to measure the size distributions beneath breaking waves in a laboratory flume (filled with seawater) and in the open ocean. In both cases, they found a change in the size distribution slope at $r \sim 1.0 \text{ mm}$. Based on Deane and Stokes (1999, 2002), Blenkinsopp and Chaplin (2007b) argued that the bubble size distribution of large bubbles will be similar at all scales because the same bubble creation mechanisms operate in the laboratory and in the field. Therefore, it is expected that laboratory studies of large-transient bubbles conducted in freshwater, will be applicable not only to the open ocean but also to freshwater waves under similar breaking conditions (Leifer et al, 2007).

Measurements of void fraction concentrations should have sufficient temporal and spatial resolution in order to be used in the verification or calibration of numerical

simulations of the air entrainment process. Furthermore, measurements of the bubble size distribution at different positions along plunging and spilling waves have yet to be performed. Additionally, a better understanding of the connection between the void fraction and bubble size distribution is still needed for engineering applications and mathematical modelling (Mori, 2007).

In this study, we report on the evolution of the void fraction and bubble size distribution of large-transient bubbles beneath deep-water plunging and spilling breaking waves. These properties were studied in the laboratory using controlled deep-water breaking which was possible because the dispersive properties of ocean waves can be reproduced at laboratory scale (Rapp and Meville, 1990; Loewen and Melville, 1991). The ensemble void fraction and the bubble size distribution were obtained by averaging thousands of repeated breaking waves at different positions along the breaking waves.

1.2 Objectives of This Thesis

The objective of this thesis is to study air entrainment beneath mechanical-generated deep-water breaking waves. The specific goals of the present study are to:

- (a) Determine the temporal and spatial evolution of the mean void fraction beneath breaking waves;
- (b) Measure the size distribution of the bubbles generated underneath breaking waves, and analyze its evolution in time and space.

1.3 Organization of Thesis

Chapter 1 presents a general introduction on the relevance of air entrainment beneath breaking waves. Chapter 2 describes the experiments that were conducted to assess the accuracy of two single tip fiber-optic probes that were used to study air

entrainment beneath breaking waves. Chapter 2 has been already published (Rojas and Loewen, 2007). Chapter 3 describes the laboratory experiments that were conducted to measure the local instantaneous void fraction produced by large bubbles entrained beneath breaking waves. Chapter 4 presents the measurements of the bubble size distributions measurements at different positions along a plunging and a spilling wave. Chapter 5 summarizes the conclusions of the entire study and provides recommendations for future studies in this field.

1.4 References

Banner, M.L. and Peregrine, D. H. (1993). Wave breaking in deep water *Ann. Rev. Fluid Mech.* 25 373–97.

Blanchard, D.C. and Syzdek L.D. (1970). Mechanism for the water-to-air transfer and concentration of bacteria. *Science*, 170, 626-628.

Blanchard, D.C. and Woodcock. (1957). Bubble formation and modification in the sea and its meteorological significance. *Tellus*, 9, 145-158.

Blenkinsopp, C. E. and Chaplin, J. R. (2007a). Void fraction measurements in breaking waves. *Proc. R. Soc. A* 453, 3151-3170.

Blenkinsopp, C. E. and Chaplin, J. R. (2007b). Validity of small-scale physical models involving breaking waves. In *Proc. 22nd Int. Workshop on Water Waves and Floating Bodies*, Plitvice, Croatia.

Bonmarin, P. (1989). Geometric properties of deep-water breaking waves. *J. Fluid Mech.* 209, 405 -433.

- Bullock, G.N., Crawford, A.R., Hewson, P.J., Walkden, M.J.A., and Bird P.A.D. (2001). The influence of air and scale on wave impact pressures. *Coastal Engineering* 42 (4): 291-312.
- Cartmill, J.W. and Su, M.Y. (1993). Bubble size distribution under saltwater and freshwater breaking waves. *Dyn. Atmos. Oceans* 20, 25–31.
- Chanson, H., Aoki, S. and Hoque, A. (2006). Bubble entrainment and dispersion in plunging jet flows: freshwater vs. seawater. *J. Coast. Res.* 22, 664–677.
- Deane, G.B. and Stokes, M.D. (1999). Air entrainment processes and bubble size distributions in the surf zone. *J. Phys. Oceanogr.* 29, 1393–1403.
- Deane, G. B. and Stokes, D. (2002). Scale dependence of Bubble Creation Mechanisms in Breaking Waves. *Nature*, 418: 839-844.
- Duncan, J. H. (2001). Spilling breakers. *Annu. Rev. Fluid Mech.* 33, 519–547.
- Duncan, J. H., Qiao, H., Behres, H. & Kimmel, J. (1994). The formation of a spilling breaker. *Phys. Fluids* 6 (8), 2558–2560.
- Farmer, D.M., McNeil, C.L., and Johnson, B.D. (1993) Evidence for the importance of bubbles in increasing air-sea gas flux. *Nature* 361: 620-623.
- Haines, P.A. and Johnson, B.D. (1995). Injected bubble population in seawater and freshwater measured by a photographic method. *J. Geophys. Res.*, 100, 7057-7068.
- Jochum, M and Murtugudde R (Eds). (2006) *Physical oceanography: developments since 1950*. Springer, New York.
- Keeling, R.F. (1993). On the role of large bubbles in air-sea gas exchange and supersaturation in the ocean. *J. Mar. Res.*, 51, 237-271.

- Lamarre, E. and Melville, W. K. (1991). Air entrainment and dissipation in breaking waves. *Nature*, 351, 469–472.
- Leifer, I. and de Leeuw, G., (2006a). Bubbles generated from wind-steepened breaking waves: Part 1. Bubble from bubble plumes. *J. Geophys. Res.* 111, C06020.
- Leifer, I., and de Leeuw, G. (2006b). Bubbles generated from wind-steepened breaking waves: Part 2. Bubble plumes, bubbles, and wave characteristics. *J. Geophys. Res.* 111, C06021.
- Leifer, I., Caulliez, G., and De Leew, G. (2007). Characteristics of bubble plumes, bubble-plume bubbles, and waves from wind-steepened wave-breaking. *Journal of Marine Systems* 66, 61–70.
- Liss, P.S. et al. (1997). Physical processes in the microlayer and the air-sea exchange of trace gases.
- Loewen, M.R. and Melville, W.K. (1991). Microwave backscatter and acoustic radiation from breaking waves. *Journal of Fluid Mechanics* 224: 601-623.
- Loewen, M.R., O’Dor, M.A., and Skafel, M.G. (1996). Bubbles entrained by mechanically generated breaking waves. *J. Geophys. Res.* 101: 20,759-20,769.
- Loewen, M. R. and Siddiqui, M.H.K. (2006). Detecting microscale breaking waves. *Meas. Sci. Technol.* 17, 771–780.
- Melville, W.K. (1996). The role of surface-wave breaking in air–sea interaction *Ann. Rev. Fluid Mech.* 28 279–321.
- Monahan, E.C. (1986). The ocean as a source for atmospheric particles, in *The Role of Air-Sea Exchange in Geochemical Cycling*, edited by P. Baut-Menard, pp. 129-163, Springer, New York.

- Mori, N., Suzuki, T., and Kakuno, S. (2007). Experimental study of air bubbles and turbulence characteristics in the surf zone. *J. Geophys. Res.* 112 (C5): Art. No. C05014.
- Rapp, R.J. and Melville, W.K. (1990). Laboratory measurements of deep-water breaking waves. *Phil. Trans. R. Soc. Lond, A* 331, 735-800.
- Rojas, G, and Loewen, M.R. (2007) Fiber-optic probe measurements of void fraction and bubble size distribution beneath breaking waves. *Exp Fluids*. 43: 895-906.
- Siddiqui, M.H.K., Loewen, M.R., Asher, W.E. & Jessup, A.T. (2004). Coherent structures beneath wind waves and their influence on air–water gas transfer. *J. Geophys. Res.* 109, C3, C03024.
- Upstill-Goddard, R.C. (2006). Air-sea gas exchange in the coastal zone. *Estuarine, Coastal and Shelf Science*, 70: 388-404.
- Woolf, D.K. (1993). Bubbles and the air-sea transfer velocity of gases. *Atmos.-Ocean*, vol. 31, no. 4, pp. 517–540.
- Zappa, C.J., Asher, W.E., Jessup, A.T., Klinke, J. and Long, S.R. (2004). Microbreaking and the enhancement of air–water gas transfer velocities. *J. Geophys. Res.* 109, C8, C08S16.

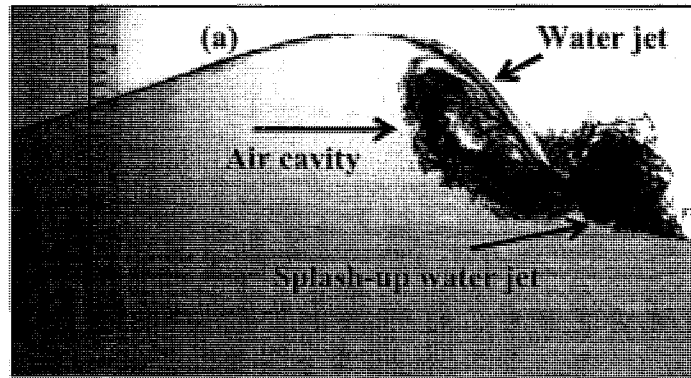


Fig. 1.1 Plunging wave

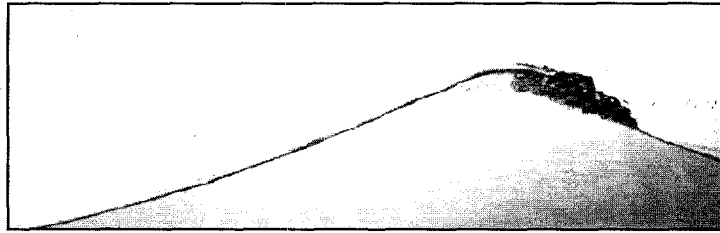


Fig. 1.2 Spilling wave

Chapter 2: Calibration of Fiber-Optic Probes for Void Fraction and Bubble Size Distribution Measurements

2.1 Introduction

There have been a number of previous studies of the bubble plume characteristics beneath breaking waves; however, few of them report on the accuracy of the applied technique. For example, Lamarre and Melville (1991) used a conductivity probe to measure the void fraction, in bubble plumes generated by breaking waves. They estimated that the percentage error in the void fraction measurements was no greater than 10%. Deane and Stokes (2002) performed laboratory (using sea water) measurements of the bubble size distribution inside breaking waves. Using high speed video images of the breaking wave process, they manually identified and sized bubbles and found that the bubble density (number of bubbles per m^3 per μm radius increment) was proportional to the bubble radius to the power of $-3/2$ for small bubbles (radii less than 1.0 mm) and to the power of $-10/3$ for larger bubbles. Loewen et al. (1996) used a photographic technique to make measurements of the size distributions of large bubbles entrained by mechanically generated spilling breaking waves, in freshwater and saltwater for large bubbles ($0.8 - 5.0\text{ mm}$ radius). They found that the uncertainty (i.e. standard deviation/mean value) in measured bubble size distributions increased from $\sim 50\%$ to $\sim 70\%$ when the bubble radius increased from 0.4 to 5.0 mm .

A variety of techniques for measuring bubble velocities and void fractions have been tested at laboratory scale. Chang et al. (2003) developed a technique based on the coherent mixing of the scattered signal with the Fresnel signal reflected from the tip of an optical fiber. They found that the root-mean-square (RMS) error in the void fraction measurements was 0.0019 for void fractions up to 0.15 ; and that the probe was able to

measure bubble velocities up to 85 *cm/s* with an accuracy of 3%. Kiambi et al. (2003) evaluated the accuracy of a double optical probe technique for making local two-phase flow measurements for bubbles of sizes 2.15 *mm* and 4.5 *mm*. By comparing this technique with an imaging one, they concluded that the optical probes underestimated the void fraction by ~ 14% (for 2.15 *mm* bubbles) and ~ 6% (for 4.5 *mm* bubbles). They also reported errors less than 5% for bubble velocities up to 38 *cm/s*. Luther et al. (2004) developed an algorithm to estimate the aspect ratio, and velocity of bubbles from the signals obtained using a four-point fiber-optic probe. A comparison between the algorithm's predictions and measurements from images showed that this technique predicted the geometry of bubbles with an accuracy of ~ 20% for bubbles with equivalent diameters of 2–4 *mm*.

Cartellier (1990, 1992) characterized the performance of single fiber-optic probes for measuring void fraction. He concluded that this type of probe was better suited for the quantification of large bubbles rather than finely dispersed bubbles. Also, he concluded that bubble velocities could be inferred from the analog voltage signal produced when bubbles cross the probe tip. The advantage of using this type of single-tip fiber-optic probe, over a dual tip one, is that the problem of spacing between the double-tip probe is eliminated (Chang et al. 2004). Serdula and Loewen (1998) conducted a series of experiments in order to evaluate the feasibility of using single-tip fiber-optic probes for measuring void fraction and bubble properties beneath breaking ocean waves. They found that these probes could be used to make measurements of void fraction, bubble velocity and bubble sizes. The probes were calibrated for bubble velocities up to 100 *cm/s* and the relative errors in void fraction measurements were found to be ~ -43% to

+50% when the void fraction varied from 0.0007 to 0.0044. Elkamash et al. (2005) investigated the use of the same single-tip fiber-optic probes for measuring void fraction, bubble sizes, and bubble velocities in the highly aerated unidirectional flow generated over a stepped chute. The accuracy of the measurements was assessed by comparing the discharge measured using a magnetic flow meter with the integrated discharge computed from the time averaged void fraction and bubble velocity measurements. Using the calibration coefficients determined by Serdula and Loewen (1998) for computing bubble velocities, they found that these two discharges agreed to within 0.6% and concluded that single-tip fiber-optic probes can provide accurate measurements of average bubble velocities and void fraction in unidirectional high velocity flows.

In this Chapter we report on four experiments that were conducted to assess the accuracy of the same single-tip fiber-optic probes used previously by Serdula and Loewen (1998) and Elkamash et al. (2005). If these probes are to be used to study air entrainment beneath plunging breaking waves their performance at higher void fractions and larger velocities must be assessed. Therefore, in the first series of experiments the accuracy of void fraction measurements in the range 0.02 to 0.21 was investigated. In the second series the probes were calibrated to make bubble velocity measurements in the range 10 to 300 *cm/s*. In the third series of experiments the bubble size distributions measured under breaking waves using the fiber-optic probes were compared to the size distribution obtained from images. In the fourth series void fraction and bubble size distributions under a plunging breaking wave were measured using the fiber-optic probes.

2.2 Void Fraction

The fiber-optic probe system consisted of two fiber-optic probes (Model F32-10-1 Photonetics, Inc.), and a signal conditioning module (Optoflow 2210). An image of the tip of one of the fiber-optic probes is shown in Fig. 2.1. Each probe is constructed with two optical fibers, one fiber for transmitting light and another for receiving it. The tip of each probe is a 1-*mm* diameter conical sapphire. If the probe tip is surrounded by liquid there is very little light reflected back, but if it pierces a gas bubble the light is almost totally reflected because the refractive index of the medium has changed. The reflected light is transmitted back to the signal conditioning module via the second optical fiber.

The accuracy of the void fraction measurements made using the fiber-optic probes was assessed by conducting controlled experiments in a cylindrical bubble tank. The bubble tank was a 92 *cm* high acrylic cylindrical tank with an internal diameter of 29 *cm*. In order to distribute air bubbles across the tank, an acrylic diffuser plate, with 225 one-*mm*-diameter holes, was installed in the bottom of the tank. Air was supplied to the tank at a maximum pressure of 480 *Pa* through an inlet beneath the diffuser plate. Streams of air bubbles were produced as the air flowed through the holes in the diffuser plate, creating a uniform air-water mixture in the tank. A regulator was used to control the air flow rate and this allowed the void fraction in the tank to be varied systematically.

The fiber-optic probes measure the local void fraction in a small volume surrounding the probe tip (Serdula and Loewen, 1998, and Elkamash, et al., 2005). The void fraction measured by the fiber-optic probe, α_p is given by,

$$\alpha_p = \frac{1}{T_s} \sum_{i=1}^{N_B} (T_g)_i \quad (2.1)$$

where T_g is the gas residence time of the i th bubble (i.e. the time the bubble takes to cross the probe tip), N_B is the total number of bubbles for which the gas residence time was measured, and T_s is the total sampling time. Note that equation (2.1) provides the fraction of time the probe tip is surrounded by air. It is necessary to define a threshold voltage, below which, the probe is considered to be in water and above which, it is considered to be in air. This threshold is set by plotting histograms of the digital probe signals. The histogram always had two peaks corresponding to the signal levels in air and water, and the threshold voltage was selected so that it fell between these two peaks. A histogram corresponding to a void fraction of 0.07 is plotted in Fig 2.2.

Independent measurements of the void fraction were also made using a differential pressure transducer. In this case, the void fraction is given by,

$$\alpha_{\Delta H} = \frac{H_A - H_B}{h} \quad (2.2)$$

where $(H_A - H_B)$ is the differential pressure head measured between points A and B; and h is the vertical distance between A and B. The fiber-optic probes were installed at a depth midway between points A and B. Three preliminary runs, with different void fractions, were conducted in order to determine the minimum sampling duration, T , which is the time required to obtain a stable measurement of the mean local void fraction. A sufficiently long sampling duration ensures that fluctuations introduced by the two-phase flow are reduced so that the distribution of the void fraction between A and B can be assumed to be steady and uniform (Lamarre and Melville, 1992). It was found that a sampling duration of 90 s was sufficient for this purpose. Chang et al. (2003) used a similar procedure to assess the accuracy of their fiber-optic probe reflectometer and concluded that $T_s \sim 52$ s was sufficient. The threshold voltage was varied from -1.0 to

+2.0 V in 0.5 V increments and the values that produced best results were 0.0 V for probe 1 and 1.5 for probe 2. At these threshold voltages the differences between the void fractions measured with the probes and the pressure transducer were minimized.

At the start of a particular experimental run, the differential pressure transducer was calibrated. Next, the flow rate of air and hence the void fraction was set by adjusting the regulator. Finally, the analog voltage signals produced by the fiber-optic probes and the differential pressure transducer were sampled at a rate of 20 kHz per channel for 450 s (five runs at 90 s each). This sampling procedure was repeated 5 times at each of 20 void fractions. The experiments were carried out over three days and the void fraction was varied each day systematically from 0.02 to 0.21 using the regulator. The upper limit of 0.21 was governed by the capacity of the air supply line in the laboratory.

The mean value of the void fraction (α_p and $\alpha_{\Delta H}$ for the fiber-optic probes and pressure transducer, respectively) was computed over the total sampling duration of 450 s . The errors in the void fraction measurements can be classified as either bias (systematic) or random errors. The mean value may or may not equal the true value of the void fraction, α (Bendat and Piersol, 2000). If it does not, the estimate α_p is said to be biased. The bias error, which is denoted as $b[\alpha_p]$, is defined as, the difference between the mean and the true values. The true value of the void fraction, α , was assumed to be the mean value measured using the differential pressure transducer, $\alpha_{\Delta H}$.

The total root mean square error (RMSE) is defined as,

$$RMSE = \sqrt{VAR[\alpha_p] + (b[\alpha_p])^2} \quad (2.3)$$

where $VAR[\alpha_p]$ is the variance of the estimate. The normalized RMS (root mean square) error expressed as a percent, is defined as,

$$\varepsilon[\alpha_p](\%) = \frac{RMSE}{\alpha} * 100 \quad (3.4)$$

In Fig. 2.3 the mean void fractions measured using the fiber-optic probes are compared to the values measured simultaneously using the differential pressure transducer. The mean and maximum bias errors in the void fraction were estimated to be 0.0043 and 0.0342, respectively.

The random error is defined as the standard deviation (*i.e.* $\sqrt{VAR[\alpha_p]}$) of the 5 repeat runs, $\sigma[\alpha_p]$. The mean and maximum values of the random error were estimated to be 0.0039 and 0.0068, respectively. The average value of the coefficient of variation was 0.037, which indicates that the random errors are relatively small. The normalized RMS error, $\varepsilon[\alpha_p]$ was computed using equation (2.4) and is plotted as a function of void fraction in Fig. 2.4. The normalized RMS error is ~42% for $\alpha < 0.02$ but decreases rapidly as α increases and the average the normalized total RMS error is 9% for $0.02 < \alpha_p < 0.21$. Note that the normalized total RMS error for both probes increased by less than 2% when the threshold voltage was varied between 0 and 2 V. Therefore, errors in mean void fraction measurements are insensitive to the value of the threshold value.

Cartellier and Achard (1991) performed a survey of the literature and found that various types of probes (e.g. fiber optic, conductivity probes, etc.) used to measure void fraction had relative errors that varied from -56 to +11%. Cartellier (2001) reported that the typical magnitude of errors in void fraction measurements using optical probes, if there was a preferred flow direction, were between 0 and -6% for a liquid superficial velocity between 0.2 and 1.0 m/s; bubble sizes > 1.5 mm; and void fractions less than 0.25. However, if there is no preferred flow direction, as was the case in the bubble tank,

the errors were 0% to -16%. Chanson and Manasseh (2003) studied air entrainment produced by a circular plunging jet and measured the void fraction using a single-tip conductivity probe. They estimated that the errors in the void fraction measurements were $\sim 3\%$ for void fractions greater than 0.05 and $\sim 0.5\%$ for void fractions smaller than 0.05. These comparisons demonstrate that the performance of the fiber-optic probes tested in this study was comparable to previous studies.

2.3 Bubble Velocity Calibration

In Fig. 2.5a a typical signal produced when a bubble crosses the tip of a fiber optic probe is plotted. A voltage signal of approximately -2.5 V is produced when the tip is surrounded by liquid, and a +7.5 V signal when the tip is surrounded by a gas bubble. The time the tip takes to fully penetrate the bubble is called the rise time, T_R (time from C to D in Fig 2.5a). Cartellier (1990) stated that T_R will be a function of the bubble velocity (v_B), the angle of the probe axis with respect to the bubble interface (φ), the liquid and gas (e.g. air and water), and the individual probe characteristics. Therefore, for a particular probe used to detect air bubbles in water, the rise time will be a function of v_B and φ .

After time B, the bubble leaves the tip and the voltage returns to the lower value. The total time the tip is inside the bubble is identified as T_g (points A to B in Fig. 2.5a), and the voltage produced by a crossing bubble is referred to as the bubble signature. Cartellier (1990) defined a good bubble signature as a voltage pulse that has a short rise time (i.e. large slope between points A to D; small standard deviation of the voltage signal between points D to B; and a voltage average between points D to B greater than a certain value. In this study the limits for slope, standard deviation and average threshold

value were 2.44 V/ms , 0.244 and 1.95 V , respectively. A poor bubble signature with a large standard deviation (i.e. $> 0.244 V$) is plotted in Fig. 2.5b.

The bubble cord length, s , is given by,

$$s = v_B * T_g \quad (2.5)$$

where v_B is the bubble velocity and, T_g is the gas residence time. The cord length is a measure of the size of the crossing bubble. If the bubbles are assumed to be spherical, it can be shown that the average correction factor by which a measured cord length must be multiplied by to get an estimate of bubble diameter is 3/2 (Saber et al., 1995). If the bubbles are assumed to be oblate ellipsoids, then the measured cord length multiplied by 1.5 gives an estimate of the average bubble minor axis. In this study we only present bubble cord length distributions and did not examine the issue of bubble shape. The fiber-optic probes do not provide any information about bubble shape. The user must make an assumption about bubble shape or obtain information on bubble shape using another technique such as digital video. Serdula and Loewen (1998) found that for bubble velocities, in the range 5 to 100 cm/s , the bubble rise time was related to bubble velocity by the following equation,

$$v_B = 10^b T_R^m \quad (2.6)$$

where, v_B is the bubble velocity (cm/s), T_R (ms) is the rise time, and b and m are constants computed using a least squares regression. In this study experiments were conducted to calibrate the probes at higher velocities. (i.e. in the range 10 to 300 cm/s) because in many flows bubble velocities higher than 100 cm/s are encountered.

The calibration experiments were performed in a small Plexiglas flow cell 40 cm in length with an inner cross-section of $2.5 \times 2.5 cm$. The flow cell had ports on the sides

for injecting air and inserting the fiber-optic probes. The probes were aligned perpendicular (90°) and parallel (0°) to the flow, while compressed air was injected through a stainless steel tube, installed in the air injection port as shown in Fig. 2.6a. High speed digital video recordings of bubbles crossing the tip of each probe were used to obtain accurate independent measurements of bubble velocities. A schematic of the complete setup is shown in Fig 2.6b. A Motion-Scope High Speed Digital Imaging System, PCI 1000 (Redlake Imaging, San Diego, CA) that included a high speed video camera, digital frame grabber (onboard memory), and interface software was used to gather 8 bit monochrome digital images with resolution of 210×240 pixels. The digital video camera was equipped with a 7.5 mm zoom lens with a $2\times$ extender ring and was mounted on a tripod and focused on the tip of the probe to give a field of view of 42 mm. The flow cell was backlit by placing a 500W light bulb ~ 20 cm behind the flow cell. A sheet of sanded Plexiglas was used to diffuse the light and to provide uniform illumination in the digital video images.

The frame rate of the high speed video system was set to 125, 250, or 500 frames per second, depending on the mean flow velocity. The probes' analog voltage signals were sampled using a data acquisition system that included a PCI-6035E NI (National Instruments) board (input range ± 10 V), and LABVIEW software, installed in a Pentium II personal computer. A digital oscilloscope (Tektronix TDS210 Digitalizing Real Time Oscilloscope) was used to visually monitor the probe signals throughout the experiments. The data acquisition board sampling rate was set at 100 kHz. The camera system and the data acquisition board were synchronized using an external trigger to start both systems simultaneously. Individual bubbles were visually identified in the video images as they

crossed the tip of a probe (Fig. 2.7a-c), and the synchronization allowed each bubble to be matched to its corresponding bubble signature in the probe signal (Fig. 2.7d).

Fiber-optic probes were installed one at a time in the flow cell at orientations of 90 and 0°. With the flow cell full of tap water a single background image was acquired. Next the flow rate of water through the flow cell was set and then the air supply was turned on and bubbles were injected into the flow so that they crossed the probe tip. The external trigger was used to start the data acquisition and the high speed video system and data was gathered for 4.096, 8.192, or 16.384 *s* at frame rates of 500, 250, or 125 frames per seconds, respectively. The digital video images acquired by the high speed camera were stored on a computer hard disk. This process was typically repeated nine times at a given flow rate in order to have a sufficient number of bubbles crossing the probe tip. Thereafter, the water flow rate was increased or decreased to vary the bubble velocity and a new set of measurements were taken. This procedure was repeated for both probes at both 90 and 0°.

A MATLAB (Mathworks, Natick, MA) program was used to process the digitized probe signals and the digital video images. The first step in the algorithm was the identification of bubbles that produced good signatures. Based on the initial time of the bubble signature, point C in Fig 2.7d, the frame containing the bubble that produced the signal (crossed the tip of the probe) was displayed on the computer screen. The conditions for a bubble to be included in the calibration data set were that it could be clearly identified as causing the bubble signature. The image analysis algorithm included correction for non-uniform illumination by subtracting the background image; conversion of the bubble intensity image to a binary image using a threshold; erosions and dilatations

in order to eliminate very small bubbles; and bubble detection or segmentation. Once a bubble was detected, its contour and center of mass were computed and stored. The bubble's contour was used to identify the leading edge of the bubble.

Serdula and Loewen (1998) used the displacement of the leading edge of a bubble to compute its velocity. However in these experiments, we found that when the displacement of the bubble centroid was used, this reduced the scatter of the data. The calibration data for probe 2 at 0° in freshwater is plotted in Fig. 2.8, and the values of m and b (Eq. 2.6) are tabulated in Table 2.1 for both probes at 0° and 90° . Also listed in Table 2.1 are the number of data points (i.e. crossing bubbles) used in each calibration, the correlation coefficient for each linear regression and the 95% confidence limits of the slope. The highest correlation coefficients of 0.83 and 0.88 were obtained for probe 2 at 90° and 0° , respectively. The calibration equations for the two probes at 90° are statistically different at the 5% level; however they are not different at the 5% level when they were oriented at 0° .

The four calibration equations are compared in Fig. 2.9. Although the calibration equations for probes mounted at 90° are statistically different at the 5% level, the slopes of the regression lines are very similar but the curves are slightly offset. The equations for probes 1 and 2 mounted at 0° are not different at the 5% level. Note that the calibration equations for individual probes at 0° and 90° are different at the 5% level.

The calibration coefficients obtained by Serdula and Loewen (1998) are shown in brackets in Table 2.1. By comparing the two sets of calibration constants, it can be seen that the most significant change was in the slope of the equations at 90° ; the 95% confidence bands on m are now much smaller; the number of bubbles used in each

calibration was increased by a factor of ~ 5 . The correlation coefficients for the equations at 0° are 0.86 and 0.88. The correlation coefficients for the equations at 90° are 0.68 and 0.83 compared to 0.91 and 0.83 in Serdula and Loewen (1998). The difference between the two sets of calibration constants (b and m) are likely due to the fact that the most recent calibrations were carried out over a much larger range of bubble velocities. If only bubble velocities up to ~ 100 cm/s are used in the regression analysis, the slopes of the resulting regression equations are not different at the 5% significant level from Serdula and Loewen's (1998).

The scatter of the data in Fig. 2.8 indicates that there is considerable uncertainty in measurements of individual bubble velocities. However, with sufficient averaging this uncertainty can be reduced to acceptable levels and accurate measurements of mean bubble velocities are possible. This is exactly the same principle of operation employed by instruments such as the acoustic Doppler velocimeter (ADV). The noise in instantaneous measurements of velocity is too high for practical use and therefore the ADV samples a minimum of 10 instantaneous velocity measurements and then computes an average velocity (<http://www.sontek.com/princop/adv/advpo.htm>). Statistical analysis of the calibration data showed that mean bubble velocities accurate to $\pm 10\%$ can be obtained by averaging ~ 15 instantaneous bubble velocity measurements. This analysis is based on probe 1 at 90° which had the minimum correlation coefficient (Table 2.1), therefore it is a conservative estimate. Elkamash et al. (2005) found that the probes were able to measure mean bubble velocities with accuracies of $<1\%$ in the aerated flow on a stepped chute and this is consistent with our analysis.

2.4 Air Entrainment under Breaking Waves

The ability of the probes to measure void fraction and bubble size distribution under breaking waves was investigated in two sets of experiments. In the first, the bubble size distribution measured using the fiber-optic probes was compared to one obtained from digital video images. In the second, the properties of the air entrained under breaking waves were studied using the fiber-optic probes. Experiments were conducted in a wave channel located in the Hydraulics Laboratory, Department of Civil and Environmental Engineering, University of Alberta. The glass-walled channel is a horizontal flume, 36.6 *m* long, 0.94 *m* wide and 1.04 *m* deep filled with fresh water to a depth of 0.60 *m*. At one end of the channel there is an electro-mechanical actuator that drives a piston type wave paddle and at the other end a sloping beach prevents wave reflections. Breaking waves were generated by focusing a dispersive wave packet (Loewen and Melville, 1991). The wave packets are synthesized from 32 sinusoidal components with constant slope $ak=0.01$ where a is the component amplitude and k is the component wave number. The wave components were equally spaced over a frequency band width, $\Delta f/f_c = 0.73$, centered at a frequency, $f_c = 0.88$ Hz. The slope of the wave packet was set to 0.50 and this produced a very repeatable plunging breaking wave and this permitted measurements to be ensemble averaged over repeated runs.

The two fibre-optic probes were mounted beside each other separated by 2 *cm* on the center line of the channel. Accurate positioning of the probes was achieved using a BSLIDE computer controlled x-z traverse accurate within $\pm 1.8 \mu\text{m}/\text{m}$ and a VXM stepping motor controller (Velmex, Inc., Bloomfield N.Y.). The probes were mounted such that the tips were parallel to the still water level. The interval between successive

breaking waves was set at 2 minutes to allow the water surface oscillations to decay to negligible amplitudes.

In the first series of experiments a PULNIX TM 1040 camera (30 frames/s 1008 × 1008 pixels) digital video camera was used to image entrained bubbles. The channel wall was backlit by placing a 500W light bulb ~20 cm behind it. A piece of Mylar was used to diffuse the light and to provide uniform illumination in the digital video images. The two fiber-optic probes were set at a depth of 8 cm below the still water level at the downstream edge of the main bubble cloud produced by the breaking wave. The camera was positioned such that the tips of the fiber optic probes were located in the center of the 10x10 cm field of view image as shown in Fig. 2.10. This measuring location was chosen because the bubble cloud is dispersed here, and as a result individual bubbles could easily be identified in the images.

Digital videos were taken of the bubbles entrained by 10 identical plunging breakers. A total of 165 digital images were analyzed using a MATLAB program. The program displayed each image on the computer screen and the major and minor axes of individual bubbles were measured using the PC pointing device. A size distribution comprised of 2064 bubbles was measured in this manner. The two fiber-optic probes were used to measure the bubble size distribution at the same location. It was necessary to repeat the breaking wave many times in order to detect enough bubbles for a bubble cord length distribution. The wave was repeated 3000 times and a total of 591 bubbles were detected by the two probes. The cord distributions measured using the probes with the calibration equations for $\varphi = 0$ and 90° , are compared to the distributions of the

minor and major bubble axes obtained from the images in Fig. 2.11a. The bubble cord distributions have the form

$$N = C * r^{-\beta} \quad (2.7)$$

where N is the number of bubbles, C and β are constants; and r is the bubble size (cord length from the fiber-optic probe measurements or axis from the image measurements). This type of equation has been observed in previous studies and the value of β was found to vary from $2.0 < \beta < 4.0$ (Baldy and Bourguel 1987; Baldy 1988; and Loewen, et al. 1996). The bubble size distributions in Fig. 2.11a are all similar in shape and have slopes in the range $3.1 < \beta < 4.7$. The video recordings indicated that the bubble trajectories were quite chaotic at this location and bubbles appeared to cross the probe tips at random angles between 0 and 90°. This is likely the reason why the 0 and 90° cord length distributions are so similar in Fig. 2.11a. The size distributions of the minor and major axes are shifted up relative to the cord length distributions because they contain approximately four times as many bubbles. In addition, the fact that the bubble cord length is smaller than both the minor and major axes is the reason that the cord length distributions are shifted to the left of the minor and major axes distributions in Fig. 2.11a.

To allow direct comparison of the probe data with the image data the cord length distributions were shifted upwards to match the amplitude of the image data. As discussed previously the average ratio between the minor axis of an oblate spheroid shaped bubble and the cord length is 1.5 when the cord length is measured parallel to the minor axis. Therefore, the cord length distributions were adjusted by multiplying the measured cord lengths by 1.5. This shifts the cord length distributions to the right and produces size distributions that are very similar to the minor axis distribution, as seen in

Fig. 2.11b. This comparison confirms that the cord length distributions measured by the fiber-optic probes beneath breaking waves are accurate.

In the last series of experiments, the void fraction and bubble size distribution inside the bubble cloud produced under a plunging breaking wave were measured in the splash-up zone. This term was used by Bonmarin (1989, see his Fig. 19) to describe the splashing that occurs after the impact of the falling water jet on the forward face of the wave. The probes were set at a depth of 1.5 *cm* below the still water level and the plunging breaking wave was repeated 565 times in order to obtain a sufficient number of good bubble signatures. The leading edge of the splash-up zone is seen approaching the probes in Fig 2.12a, b, and c the probe tips are inside the resulting bubble cloud. A time series of the ensemble averaged void fraction was computed by calculating the fraction of time the probes were in air at a given time after breaking. The ensemble averaged void fraction is plotted in Fig. 2.12d. The mean void fraction at this location was 0.02 and the maximum value was 0.10. This time series is consistent with the measurements of Lamarre and Melville (1992, see their Fig 3b) who measured maximum void fractions up to 0.20 in the splash-up zone beneath plunging breakers.

Video recordings showed that the bubbles were crossing the probe tips at an angle of approximately 20° at this location. Therefore, the bubble cord length distribution computed using the calibration coefficients for $\varphi = 0^\circ$ should be the most accurate. In Fig. 2.13 this cord length distribution is plotted. A significant feature of this size distribution is the change in slope that occurs at a cord length of $s = 2.0$ *mm*. For $s < 2.0$ *mm* the slope is 1.5 (i.e. $\beta = 1.5$) and for $s > 2.6$ *mm* the slope is 3.0. This size distribution is consistent with the measurements of Deane and Stokes (2002) who

measured bubble size distributions inside breaking waves in the laboratory (using sea water) and in the open ocean. They concluded that for bubble radii larger than approximately 1 mm, turbulent fragmentation produced bubble size distributions with a slope of $\beta = 10/3$ and for radii less than 1 mm, jet and drop impact on the wave face produced size distributions with slopes of $\beta = 3/2$. They hypothesized that the length scale separating these processes was the scale where turbulent bubble fragmentation ceases, the Hinze scale. The fact that the slopes of the size distribution plotted in Fig. 2.13 (1.5 ± 0.22 and 3.0 ± 0.44) are not statistically different from the values observed by Deane and Stokes' (2002) provides additional evidence that single-tip fiber-optic probes can be used to obtain accurate measurements of bubble size distributions beneath breaking waves.

The change in slope in Fig. 2.13 occurs at a cord length of 2.0 mm which corresponds to an equivalent bubble radius of approximately 1.5 mm. Therefore, the Hinze scale beneath these freshwater breakers was approximately 1.5 mm or 50% larger than the value Deane and Stokes (2002) found beneath seawater breakers. The effect of electrolytes in seawater (Leasard and Zieminski 1971) or the fact that the wave packet properties were different in the two experiments could explain this difference.

This series of experiments demonstrated that video recordings of the bubble entrainment process beneath the breaking waves were complementary to the probe measurements for two reasons. First, when the angle at which the bubbles cross the probes, φ , could be determined from the video recordings this improved the accuracy of the estimated cord length distributions. Secondly, information regarding the shape of the

bubbles could be obtained from the recordings and this assisted in the conversion of cord lengths to equivalent bubble radii.

2.5 Conclusions

In this Chapter we have reported on experiments to determine the accuracy of two fiber-optic probes for making measurements of void fraction and bubble size distributions beneath breaking waves. Tests in a vertical bubble column showed that the normalized RMS error in void fraction was approximately 10% in the range, $0.02 < \alpha < 0.21$. The relationship between rise time, T_R , and bubble velocity, v_B , was investigated in a unidirectional flow cell. Similar to previous studies v_B and T_R were found to be related by a power law equation. It was found that in order to obtain mean bubble velocities accurate to $\pm 10\%$ a minimum of ~ 15 individual bubble velocities must be averaged. The fiber-optic probes were deployed beneath plunging breaking waves in a laboratory wave channel. The slope and shape of the cord length size distribution measured with the probes was found to agree well with the bubble size distribution measured from digital video recordings. The probes were then positioned in the splash-up zone of a plunging breaker and data was gathered for 565 repeated waves. The resulting cord length distribution had a shape and slope that was in agreement with the measurements of Deane and Stokes (2002).

Deploying these probes in the ocean would present several challenges. First, the orientation of the probes with respect to the dominant wave direction should be controlled. If the probes are pointing in the same direction as the wind, breaking waves will entrain air bubbles and then advect them past the probe tips at angles close to 180° with respect to the probe axis. In this situation very few bubbles will tend to cross the

probe tips. This problem could be addressed by mounting the probes on a buoy that turns into the wind. A second challenge is the fact that, the probe tips may be susceptible to fouling when deployed in the ocean. If this occurs the probe tips may need to be cleaned at regular intervals. Lastly, the probes can only sense bubbles with diameters greater than ~ 1 mm and large numbers of smaller bubbles are entrained beneath breaking ocean waves. Therefore, if measurements of smaller bubble sizes are required another measurement technique will need to be used.

In conclusion, the results presented in this study have demonstrated that single tipped fiber-optic probes are able to provide accurate measurements of void fraction and large bubble sizes beneath breaking waves. This is a significant result because we are not aware of any other measurement techniques that can provide accurate simultaneous measurements of void fraction and bubble sizes in the dense bubble clouds entrained by breaking waves.

2.6 References

- Baldy, S. (1988). Bubbles in the close vicinity of breaking waves. *J. Geophys. Res.* 93: 8239-8249.
- Baldy, S. and Bourguel, M. (1987). Bubbles between the wave trough and wave crest levels. *J. Geophys. Res.* 92: 2919-2929.
- Bendat, J. and Piersol, A.G. (2000). *Random Data*. New York: Wiley Inter-Science
- Bonmarin, P. (1989) Geometric properties of deep-water breaking waves. *Journal of Fluid Mechanics*. 209: 405-433.

- Bullock, G.N., Crawford, A.R., Hewson, P.J., Walkden, M.J.A., and Bird P.A.D. (2001). The influence of air and scale on wave impact pressures. *Coastal Engineering* 42 (4): 291-312.
- Cartellier, A. (1990). Optical Probes for local void fraction measurements: Characterization of performance. *Rev. Sci. Instrum.* 61 (2): 874-886.
- Cartellier, A. and Achard, J.L. (1991). Local phase detection probes in fluid/fluid two-phase flows. *Rev. Sci. Instrum.* 62 (2): 279-303.
- Cartellier, A. (1992). Simultaneous void fraction measurement, bubble velocity, and size estimate using a single optical probe in gas-liquid two phase flows. *Review of scientific instruments* 63 (11): 5442-5453.
- Cartellier, A. (2001). Optical probes for multiphase flow characterization: Some recent improvements. *Chemical Engineering & Technology* 24 (5): 535-538.
- Chang, K.A. et al. (2003). Fiber optic reflectometer for velocity and fraction ratio measurements in multiphase flows. *Review of Scientific instruments* 74 (7): 3559-3565
- Chang, K.A. et al. (2004). Reply to Fiber optic reflectometer for velocity and fraction ratio measurements in multiphase flows. *Review of Scientific instruments* 75 (1): 286.
- Chanson, H. (1996). *Air bubble entrainment in free surface turbulent shear flows*. San Diego: Academic Press.
- Chanson, H. and Manasseh, R. (2003). Air entrainment processes in a circular plunging jet: Void-fraction and acoustic measurements. *Journal of Fluids Engineering-Transaction of the ASME* 125 (5): 910-921.
- Chanson, H. (2005). Air-water and momentum exchanges in unsteady surging waters: An experimental study. *Experimental Thermal and Fluid Science* 30 (1): 37-47.

- Deane, G. B. and Stokes, D. (2002). Scale dependence of bubble creation mechanisms in breaking waves. *Nature* 418: 839-844.
- Elkamash, M.K., Loewen, M.R., and Rajaratnam, N. (2005). Measurements of void fraction and bubble properties on a stepped chute using a fiber-optic probe. *Canadian Journal of Civil Engineering* 32: 636-643.
- Farmer, D.M., McNeil, C.L., and Johnson, B.D. (1993) Evidence for the importance of bubbles in increasing air-sea gas flux. *Nature* 361: 620-623.
- Kiambi, S.L., Duquenne, A.M., Dupont, J. B., Colin, C., Risso, F., and Delmas, H. (2003) Measurements of bubble characteristics: Comparison between double optical probe and imaging. *The Canadian Journal of Chemical Engineering*, 81 (3-4): 764-770
- Lamarre, E. and Melville, W.K. (1991). Air entrainment and dissipation in breaking waves. *Nature* 351: 469-472
- Lamarre, E. and Melville, W.K. (1992). Instrumentation for the Measurement of Void-Fraction in Breaking Waves: Laboratory and Field Results. *IEEE Journal of Oceanic Engineering* 17 (2): 204-215.
- Leasard, R.R. and Zieminski, S.A. (1971). Bubble coalescence and gas transfer in aqueous electrolytic solutions. *Ind. Eng. Chem. Fundam.* (10): 260-269.
- Loewen, M.R. and Melville, W.K. (1991). Microwave backscatter and acoustic radiation from breaking waves. *Journal of Fluid Mechanics* 224: 601-623.
- Loewen, M. R., O'Dor, M. A., and Skafel, M. G. (1996). Bubbles Entrained by Mechanically Generated Breaking Waves. *J. Geophys. Res.* 101: 20,759-20,769.
- Luther, S., Rensen, J., and Guet, S. (2004). Bubble aspect ratio and velocity measurement using a four-point fiber-optical probe. *Experiments in Fluids* 36 326–333.

Rojas, G. and Loewen, M.R. (2005). Experiments investigating the accuracy of fiber-optic probes for measuring void fraction. 17th CSCE Conference. Edmonton, AB.

Saberi, S. Shakourzadeh, K., Bastoul, D. and Militzer, J. (1995) Bubble size and velocity measurements in gas liquid systems: application of fiber-optic technique to pilot plant scale. *The Canadian Journal of Chemical Engineering*. 73: 253-257.

Serdula, C. and Loewen, M.R. (1998). Experiments investigating the use of fiber-optic probes for measuring bubble-size distributions. *IEEE J. Oceanic Eng.* 23: 385-399.

Wallace, D.W.R. and Wirick, C.D. (1992). Large air-sea gas fluxes associated with breaking waves. *Nature* 356: 694-696.

Wood, I.R. (Editor). (1991). *Air entrainment in free-surface flows*. Rotterdam: IAHR.

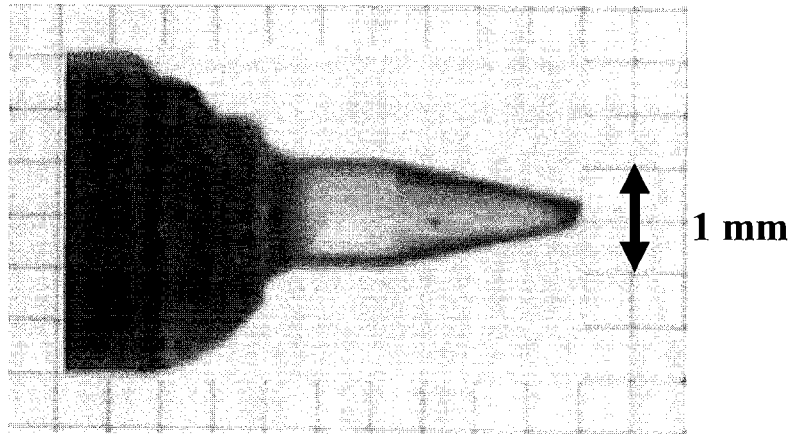


Fig. 2.1 Close up of the tip of a fiber-optic probe

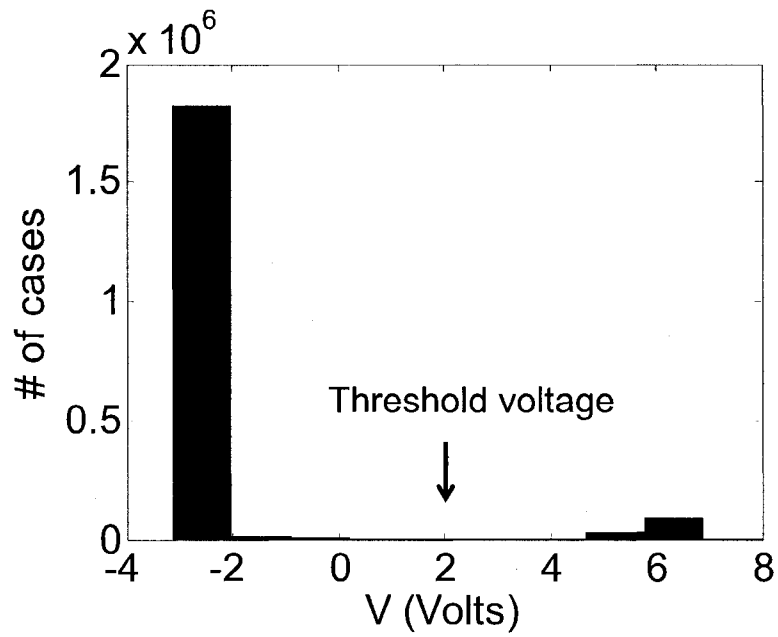


Fig. 2.2 Histogram of digital voltage values used for void fraction computation. The data is from probe 1 and corresponds to a mean void fraction of 0.07. ↓ threshold voltage. Voltages smaller than the threshold voltage occur when the tip of the probe is surrounded by water.

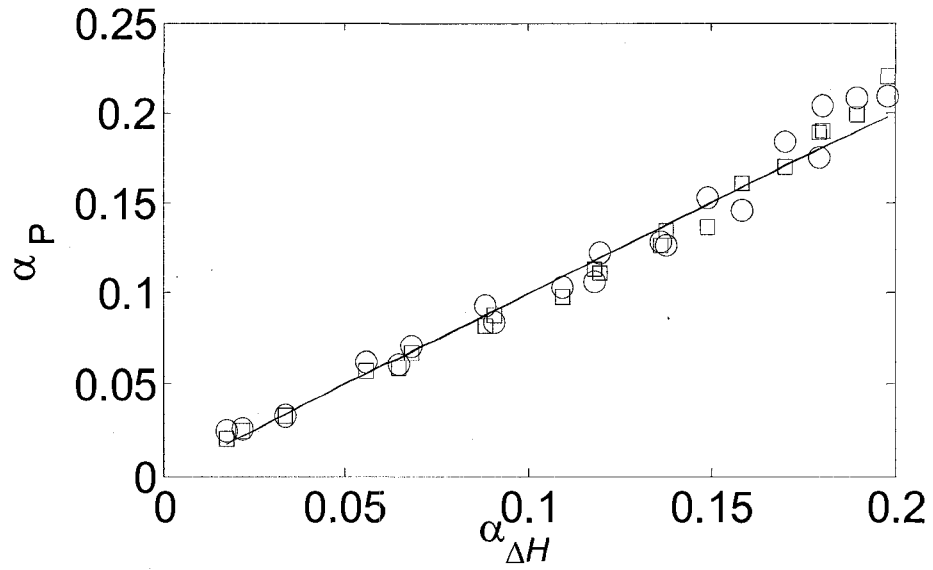


Fig. 2.3 Comparison of the average void fraction measured using the differential pressure transducer, $\alpha_{\Delta H}$ and the average void fraction measured using the fiber-optic probes, α_P . The solid line has a 1:1 slope. Probe 1 (open circle) and probe 2 (open square).

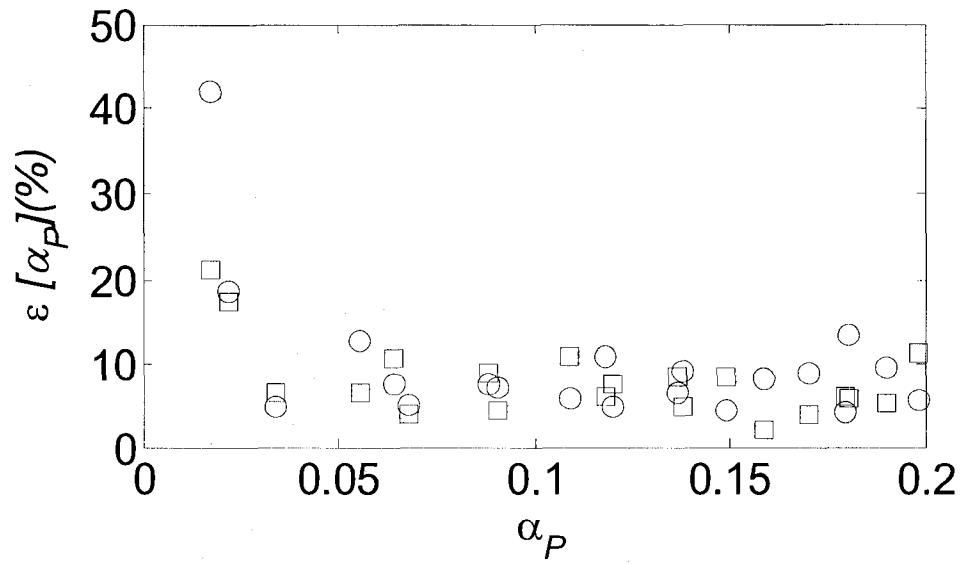


Fig. 2.4 Normalized root mean square error in the void fraction expressed as a percent, $\varepsilon[\alpha_P](\%)$, versus the void fraction estimated using the probes, α_P . Probe 1 (open circle) and probe 2 (open square).

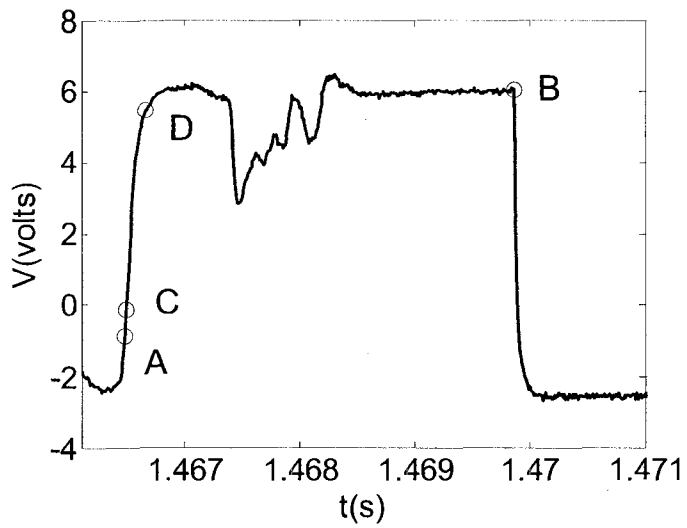
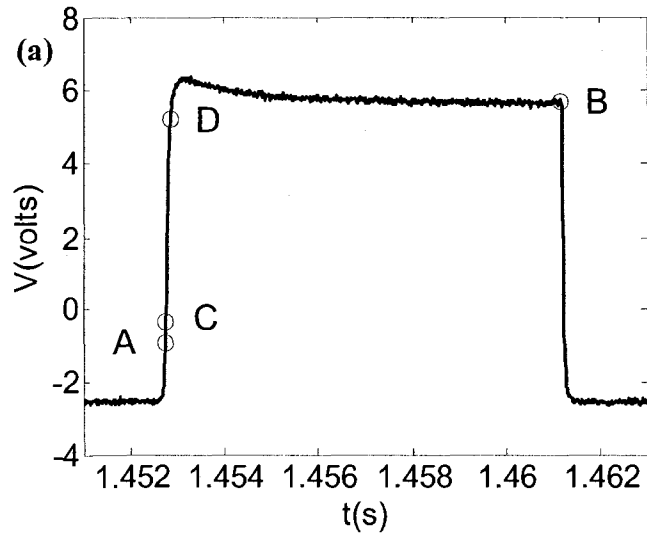


Fig. 2.5 (a) A good bubble signature showing the four characteristics points (A–D). (b) A poor bubble signature with a standard deviation that exceeds the threshold (i.e. $>0.244 V$).

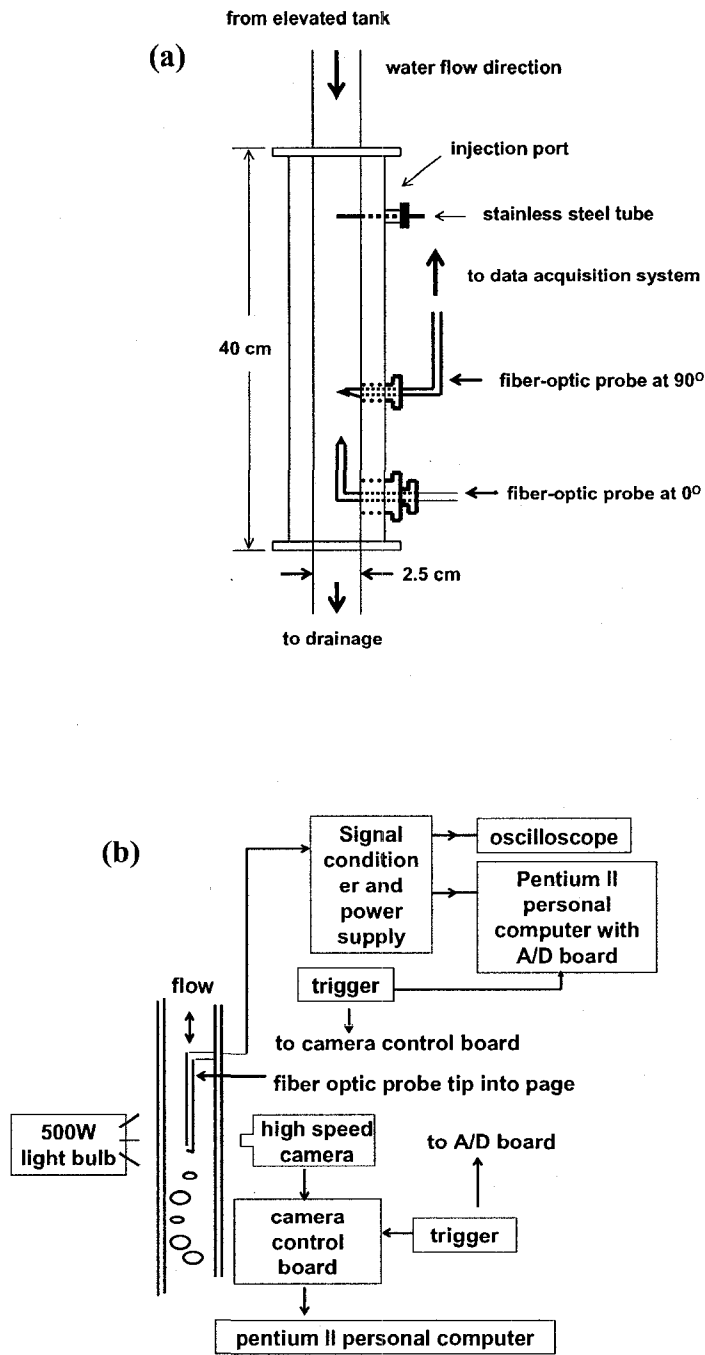


Fig. 2.6 (a) Schematic of the flow cell apparatus showing the set-up for low bubble velocities. (b) Schematic of the flow cell showing the high speed camera and data acquisition systems.

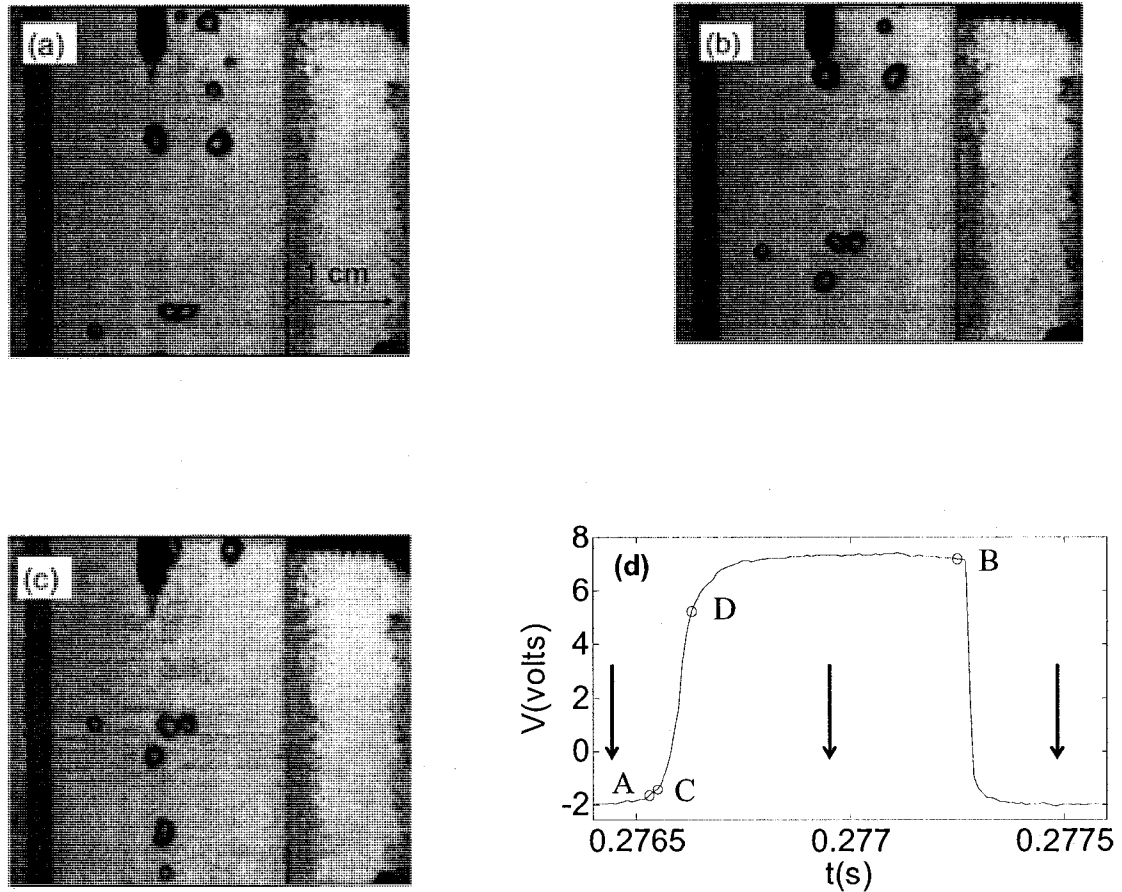


Fig. 2.7 (a–c) Sequence of high-speed digital video images showing a bubble crossing the tip of a fiber-optic probe. Water flows downwards and bubbles rising slowly upwards in this configuration. (d) The corresponding bubble signature showing the four characteristics points (A–D). t is time in ms . and V is the voltage in volts. The times corresponding to the three images are denoted by arrows.

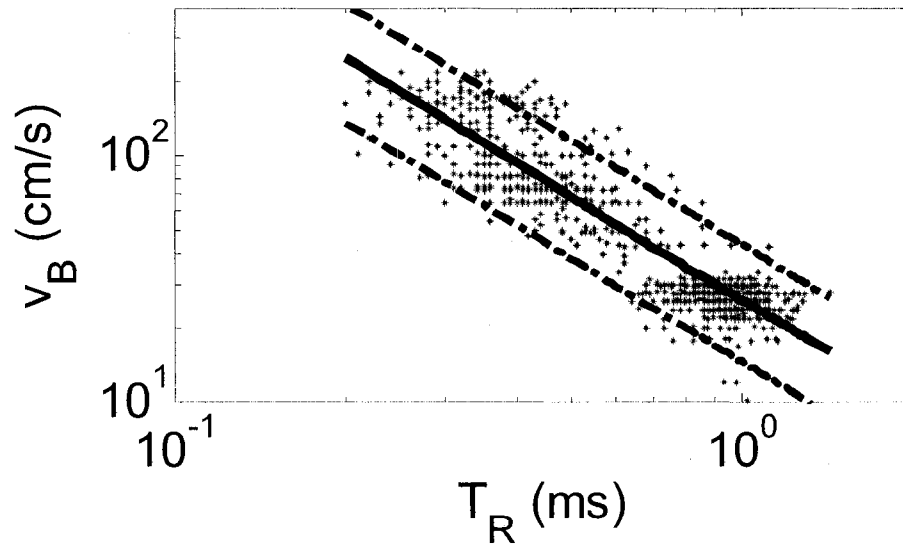


Fig. 2.8 Bubble velocity, v_B (cm/s), versus rise time, T_R (ms) for probe 2 mounted at 0° . The solid line is the regression of the logarithm of the bubble velocity, v_B versus the logarithm of the rise time, T_R calculated using the least squares method. The 95% confidence limits of the experimental data are denoted by the dash-dot line.

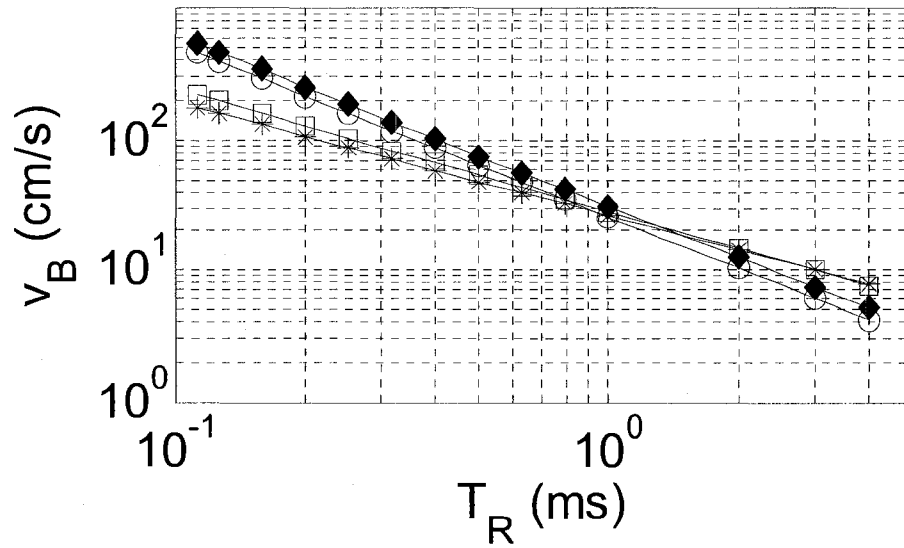


Fig. 2.9 Plots of the four calibration equations relating the bubble velocity, v_B (cm/s) to the rise time, T_R (ms). Probe 1 at 90° (filled diamond), probe 1 at 0° (asterisk), probe 2 at 90° (open circle), and probe 2 at 0° (open square).

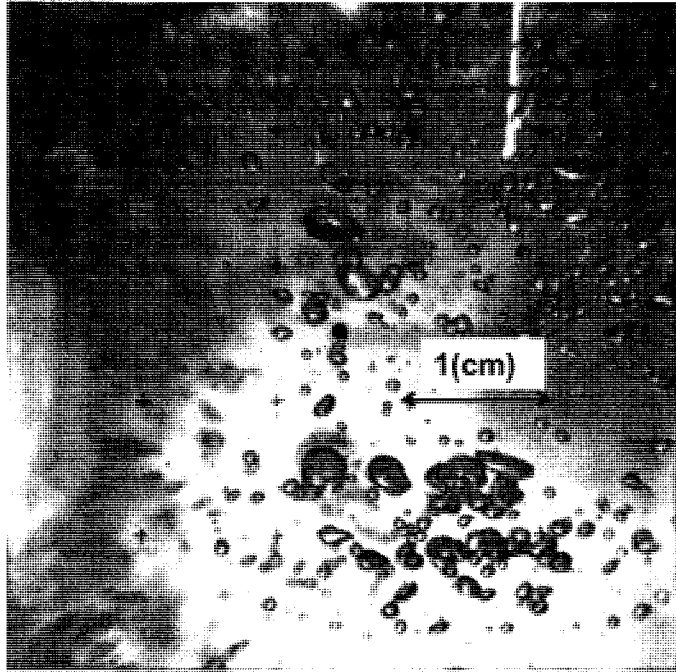


Fig. 2.10 A digital video image used to make independent measurements of the bubble size distribution. The symbol, filled circle, marks the location of the tip of the fiber-optic probe.

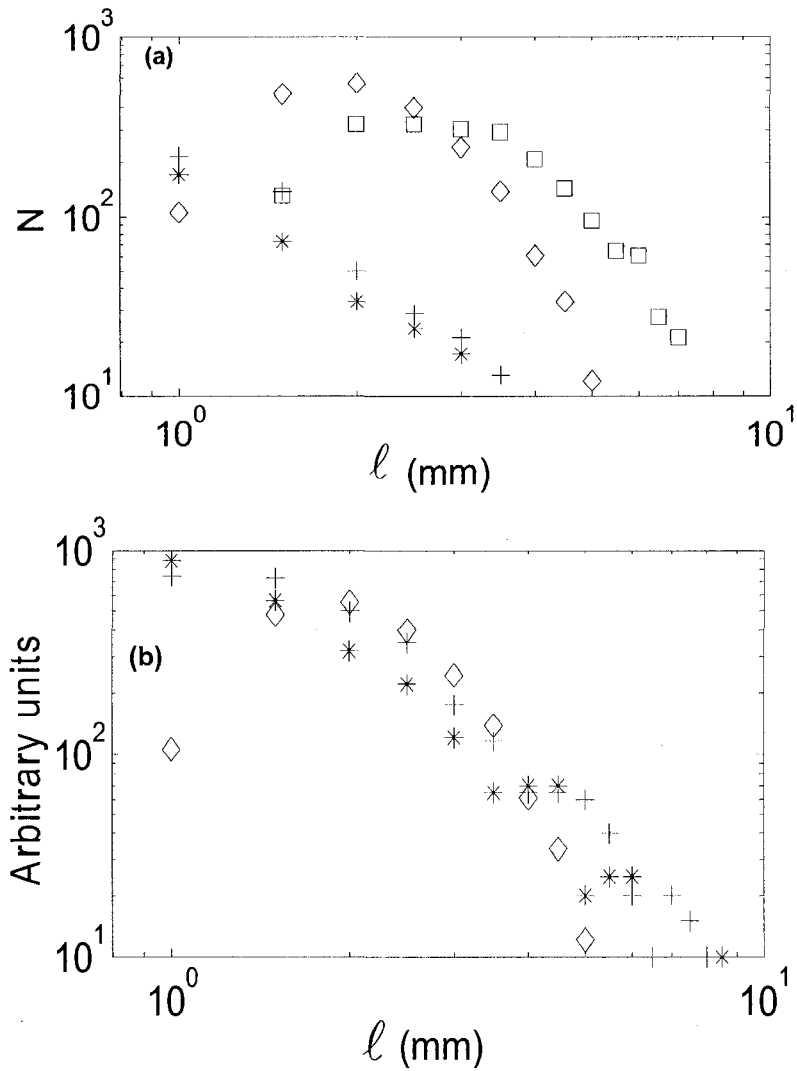


Fig. 2.11 (a) A comparison of bubble size distributions measured using the fiber-optic probes and the photographic technique. l denotes various measurements of the bubble size; C_{90} ($*$) and C_0 ($+$) are the cord length measurements from the fiber-optic probes using calibration equations for 90° and 0° , respectively; the major bubble axis size (open square) and the minor axis size (open diamond) measured using the photographic technique. N is the number of bubbles per size bin. (b) A comparison of the cord length distributions, C_{90} ($*$) and C_0 ($+$), adjusted by multiplying by $3/2$, and the minor axis size distribution (open diamond).

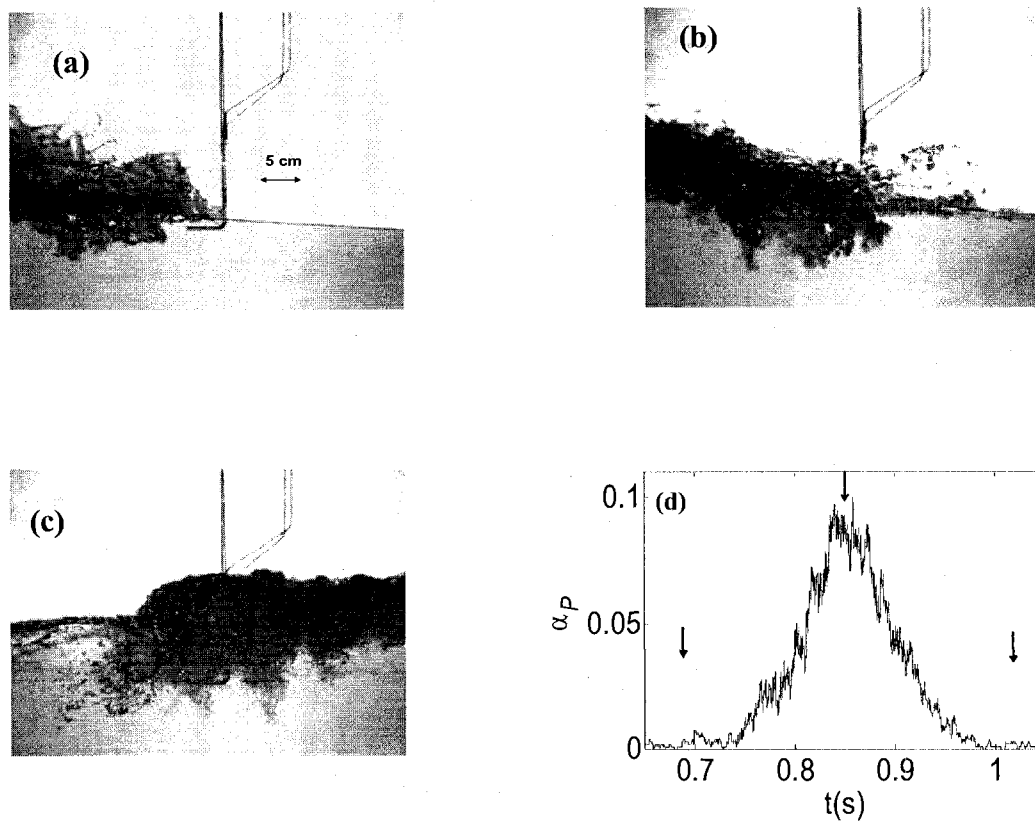


Fig. 2.12 (a–c) A sequence of three digital video images showing the leading edge of the splash-up zone created by a plunging breaking wave as it passes the fiber-optic probes. (d) A time series of the average void fraction, α_p , computed by averaging the fiber-optic probe signals measured for 565 repeated breaking waves. Time, t , in seconds after breaking. The times corresponding to the three images are denoted by arrows.

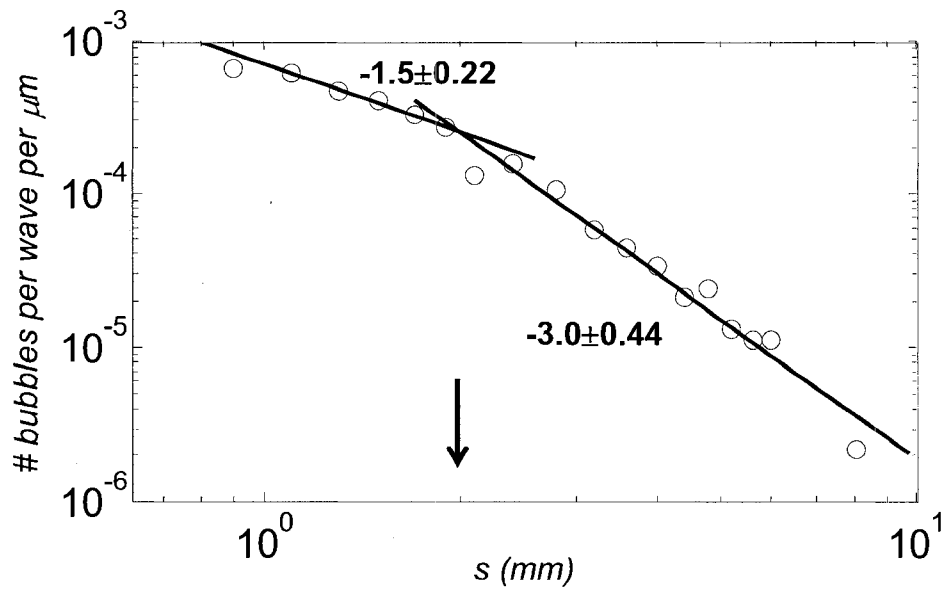


Fig. 2.13 The bubble size distribution measured in the splashing zone using the fiber-optic probes. s is the cord length. The solid lines are obtained by linear regression; the slopes and the 95% confidence limits of the slopes are also shown. The magnitude of the Hinze scale is denoted with \downarrow

Table 2.1 Listing of the correlation parameters from the linear regression of rise time, T_R , versus bubble velocity, v_B *

Probe ID	Angle	Slope m	Intercept b	Corr. Coeff.	95% confidence bands on m	Number of bubbles used in correlation
1	90°	-1.30	1.49	0.68	0.042	1655
		(-0.76)	(1.64)	(0.91)	(0.109)	(219)
1	0°	-0.87	1.42	0.86	0.024	831
2	90°	-1.32	1.41	0.83	0.034	1216
		(-0.89)	(1.69)	(0.83)	(0.207)	(151)
2	0°	-0.94	1.45	0.88	0.021	1317

* The probe angle equals 90° when the axis of the probe is perpendicular to the flow and 0° when the axis of the probe is parallel to the flow. The coefficients in brackets () are from Serdula and Loewen (1998).

Chapter 3: Measurements of Local Void Fraction under Breaking Waves

3.1. Introduction

Breaking waves produce a complex two-phase flow in which bubbles are entrained beneath the air-sea interface. These bubbles enhance the rate of air-sea gas exchange (Farmer et al. 1993); affecting the cycling and global budget of trace gases (Wallace and Wirick, 1992). The amount of gas transferred is related to the void fraction (the ratio of gas volume to total volume) and is enhanced by the large bubbles created in the first second after a wave breaking (Leifer and Leew, 2006; and Deane and Stokes, 1999). Any bubble mediated gas transfer across the air-sea interface varies both spatially and temporally (Frew, et al., 2007). Consequently, detailed void fraction measurements will contribute to a better understanding of this gas transfer process.

Melville (1996) pointed out that the bubble plumes generated beneath high energetic breaking waves should be considered as a continuum, instead of a collection of discrete bubbles, described by its geometry and void fraction field. Also, he argued that controlled laboratory studies have been useful in gaining a better understanding of the kinematics and dynamics of the breaking process. Jansen (1986) used a video technique to visualize the flow in the upper part of shallow-water laboratory breaking waves. He qualitatively described the locations of high concentrations of entrained bubbles inside the bubble plume generated underneath breaking waves. Lamarre and Melville (1992) developed an impedance probe to measure the void fraction in the transient bubble plumes generated beneath two dimensional (2-D) laboratory breaking waves. They used a piston-type wave-maker to generate a dispersive wave packet and reported contour maps

of the void fraction field. They also performed measurements in the open ocean and reported void fractions as large as 0.24.

In a series of laboratory experiments, Lamarre and Melville (1991) performed measurements beneath mechanically generated plunging breakers and concluded that the moments of the void fraction field (volume of entrained air, mean plume void fraction, and the potential energy of the bubble cloud) scaled with the pre-breaking wave variables and evolved as simple functions of time. Moreover, they measured local void fractions in the range from approximately 0.1 to 1.0 and observed that the void fraction decreased rapidly as the large bubbles rose back to the surface. In a third series of laboratory experiments, Lamarre and Melville (1994), used a vertical array of six void fraction probes, to measure the evolution of the void fraction field generated beneath three dimensional (3-D) breaking waves. They studied laboratory scale waves for three different wave packet amplitudes, and concluded that the 3-D void fraction moments also evolved as simple functions of time and that the decay rates were similar to the 2-D experiments for times after breaking, up to half of the wave period. Lamarre and Melville (1991, 1994) also reported that up to 40% of the total pre-breaking wave energy is expended in entraining the bubble cloud generated underneath breaking waves.

Recently, Blenkinsopp and Chaplin (2007) used two optical fibres to estimate the time varying void fraction field beneath 2-D breaking waves. They proposed that time series measurements should be normalized by the time it takes for a representative bubble (2.5mm in their case) to rise a distance equal to the breaking wave height. They argued that this would be a new and better time scale than the wave period that was used in previous studies (e.g. Lamarre and Melville, 1991), because there would not be a strong

physical influence of the wave properties on the bubble plume, once it was generated. They produced contour plots of the void fraction field and, similar to Lamarre and Melville (1991) also found that the void fraction moments evolved as simple functions of time.

Kalvoda et al. (2003) used a wind wave tank for the generation of spilling breaking waves and estimated the void fraction from a bubble size distribution. They reported a void fraction ~ 0.004 which was produced by clouds of bubbles with diameters in the range 1.0 to 10 mm. These measurements were performed employing a photographic technique. Leifer and Leeuw (2006) used a video system to measure void fractions between 0.002 and 0.023 beneath breaking wind waves which were paddle-amplified. Loewen et al. (1996) used a photographic technique to make measurements of the size distributions of large bubbles entrained by mechanically generated gently spilling breaking waves, in freshwater and saltwater. The total volume of entrained air was computed from the bubble size distribution and they reported average void fractions between 0.0013 and 0.0026. Furthermore, they did not find significant differences between the bubble size distribution in fresh and salt water similar to the results reported by Wu (2000). Chanson, et al. (2006) studied the air entrainment generated by vertical circular plunging jets in freshwater and saltwater using a conductivity probe. They reported a greater number of small bubbles in seawater compared to freshwater but less air entrainment in seawater.

Cox and Shin (2003) used an impedance void fraction meter in a controlled laboratory setting to measure the void fraction in the surf zone beneath spilling and plunging breaking waves. They measured ensemble-averaged void fractions in the range

0.15 to 0.20; and in some cases, the void fractions were higher beneath spilling waves than beneath plunging waves. Hoque and Aoki (2005) also performed a study of the void fraction underneath laboratory breaking waves in the surf zone. Using a conductivity probe and tap water, their results indicated that the horizontal and vertical distributions of the void fraction agreed with an analytical solution of the diffusion equation. Mori et al. (2007) generated wave packets using a wave maker and, studied scale effects in the air entrainment process of breaking waves in the surf zone. They measured void fractions of ~ 0.15 beneath spilling and plunging waves.

Kimmoun and Branger (2007) used particle image velocimetry (PIV) images and velocity measurements to estimate the void fraction at different points in a bubble cloud generated underneath laboratory surf-zone breaking waves. They used two methods to estimate the void fraction. The first one was the zero-flux method in which the vertically integrated void fraction was estimated using conservation of mass in the horizontal direction. The second method was a light extinction technique (Shamoun, et. al, 1999) in which the void fraction was estimated from the ratio of incident to transmitted light intensity when a light beam traverses a bubble cloud. Based on light-intensity images, they reported void fractions that agreed with the semi-analytical formulation proposed by Hoque and Aoki (2005).

Lubin et al. (2006) simulated 3-D plunging breaking waves in shallow water and used these numerical simulations to describe the different processes occurring during the breaking, including the occurrence of air entrainment and highlighted its major role in the energy dissipation process. They also pointed out that this model could be improved if there were more information related to the rate of air entrained as a function of time.

Previous measurements of void fraction concentrations may not have sufficient temporal and spatial resolution to be used to verify or to calibrate numerical simulations. Therefore, state of the art numerical simulations of the two phase flows generated beneath plunging waves, like the one performed by Lubin, et al. (2006), and future models developed for deep water breakings, similar to the one reported by Kimmoun and Branger (2007) for the surf zone, will require detailed void fraction measurements for their calibration and improvement.

In this paper, we report on laboratory experiments that were conducted to measure the local instantaneous void fraction, $\langle \alpha \rangle$ (or ensemble void fraction) produced by large bubbles entrained beneath deep-water breaking waves. The measurements provide high resolution time series of the void fraction at various locations along a plunging and spilling breaker. Preliminary results from these experiments were presented in Rojas and Loewen (2007b).

3.2 Experimental set-up

Instrumentation

Experiments were conducted in a wave channel located in the Hydraulics Laboratory, Department of Civil and Environmental Engineering, University of Alberta. The Lexan-walled channel is a horizontal flume, 36.6 m long, 0.94 m wide and 1.04 m deep filled with fresh water to a depth of 0.60 m. At one end of the channel there is an electro-mechanical actuator that drives a piston type wave paddle, and at the other end a sloping beach prevents wave reflections. The generation of the wave packets followed the procedure described by Loewen and Melville (1991) in which the breaking waves were generated by focusing a dispersive wave packet. The wave packets are synthesized from

32 sinusoidal components with constant slope ($a*k$), where a , is the component amplitude and k , is the component wave number. The wave components were equally spaced over a frequency band width, $\Delta f = 0.64$ Hz, centered at a frequency, $f_c = 0.88$ Hz. The slope of the plunging wave packet was equal to 0.50, and for the spilling wave, the slope was equal to 0.38.

Measurements of the void fraction inside the dense bubble clouds were performed using a fiber-optic probe system. This system included two fiber-optic probes, a signal conditioning module, and a data acquisition computer. The two fiber-optic probes provide void fraction measurements which had normalized total RMS (Root-Mean-Square) errors that are less than 10% in the range 0.02 to 0.21, Rojas and Loewen, 2007a). These probes take advantage of the difference in the refractive index between the liquid and the bubble gas. A low voltage signal (-2.5 V) is produced when the tip of a probe is surrounded by water; and a high voltage signal (+7.5 V) is produced when the tip of the probe is surrounded by air. In addition to the void fraction measurements, the fiber-optic probes can also measure bubble size distributions, simultaneously (Rojas and Loewen, 2007a). Detailed measurements of the bubble size distribution will be presented in Chapter 4.

In order to relate the void fractions to the physical process which occurs when a wave breaks, a digital imaging system was used. This system included a PULNIX TM 1040, progressive scanning high-resolution monochrome CCD camera (8-bit, 30 Hz frame rate, 1008 x 1008 pixels size, Pulnix, Sunnyvale, California), a Roadrunner frame grabber (Bitflow Inc., MA), and interface software (VideoSavant 4, IO Industries Inc., ON). The digital video camera was equipped with a 25 mm zoom lens with a 2X

extender. Accurate positioning of the fiber-optic probes was accomplished using a BISLIDE computer controlled x-z traverse accurate to within $\pm 1.8 \mu\text{m}/\text{m}$ (Velmex, Inc., Bloomfield N.Y.).

Experimental Procedures

A plunging and a spilling breaking wave were studied in these experiments. The entire breaking process of the plunging wave is shown in a continuous sequence of the images in Fig. 3.1 and 3.2. The jet formation at the crest of the wave is shown in Fig. 3.1 and the water jet impact, splash-up process and the generation bubble clouds in Fig. 3.2. It should be noted that the bubble cloud entrained by this plunging breaker was too long to be imaged in a single panel of the wave tank. Each panel is 1.20 m in length with a vertical steel support at each end. As a result, in order to obtain unobstructed views of the entire bubble cloud, the breaking location was shifted upstream by ~ 20 cm for the video recordings presented in Fig. 3.2.

The first stage of a plunging breaking wave is the formation of a water jet at the wave crest, Fig. 3.1a. The front face of the wave becomes almost vertical and the vertical scale in Fig. 3.1a indicates a wave height of ~ 0.20 m. When the falling water jet collides with the undisturbed water on the forward face of the wave, a cavity of entrapped air is formed (Fig. 3.1b) (Bonmarin, 1989) and thereafter water splashes up (Fig. 3.1c, 3.2a and 3.2b). This splashing water or splash-up process reaches heights that were comparable to the wave height, Fig. 3.2b. In addition, the major and minor axes of the air cavity were measured in another closer image (not shown), and it was estimated that the total volume of air injected is of the order of $\sim 0.011 \text{ m}^2$ per m wide. This air cavity is unstable and collapses, evolving into a dense bubble cloud that rotates clockwise imaged in Fig. 3.2c

and labelled 1st cloud in Fig. 3.2d. Simultaneously, the initial jet impact creates a second cloud that rotates counter-clockwise and is labelled 2nd cloud in Fig. 3.2d. Deane and Stokes (2002) also observed a primary and a secondary cloud beneath a plunging breaking wave. The impact of the drops produced by the splash-up process creates a third cloud, labelled 3rd cloud in Fig. 3.2d. Note that the occurrence of the 2nd cloud was not reported by Lamarre and Melville (1991) or by Blenkinsopp and Chaplin (2007).

The spilling wave was generated using the same wave packet used in the plunging wave case but with a lower slope of 0.38. Fig. 3.3 displays a sequence of images showing the evolution of the spilling breaking wave. In a spilling wave, the breaking process may be started by the appearance of a rough surface, or by the appearance of a small jet at the wave crest (Duncan, 2001). In Fig. 3.3a it is not clear which one of these two processes occurred. However, it is apparent in Fig. 3.3b and 3.3c that after an initial stage, a small region of turbulence forms at the crest of the wave and that this region grows as water spills down the face of the wave as described by Duncan, et al. (1994).

The two fibre-optic probes were mounted beside each other separated by 2 cm, on the center line of the channel, and in such a way that the tips of the probes were parallel to the still water level. The wave maker was controlled by a PC which was equipped with a multifunction DAQ AT-MIO 16XE-50 (National Instruments) data acquisition card. A MATLAB (Mathworks, Natick, MA) program was used to generate and then send a digital wave packet signal to a digital to analog converter which then transmitted an analog voltage signal to the wave maker (Fig. 3.4). This same MATLAB program also digitally sampled the signal from the wave paddle's position transducer, to verify the repeatability of the wave paddle movement. Furthermore, this program was also used to

synchronize the wave-maker system with the fiber-optic probe data by sending a trigger signal to the fiber-optic probe data acquisition computer which was equipped with a DAQ PCI-6035E (National Instruments) data acquisition card. This PC used a MATLAB (Mathworks, Natick, MA) program to sample the data for 20 seconds at a rate of 100 KHz per channel. After each breaking event, the wave maker system paused for a period of 2 minutes to allow the water surface oscillations to decay to negligible amplitudes. The wave-maker PC was also programmed to move the probes to a new location after a prescribed number of repeat runs.

At each measurement position, the digital video images provided contextual information needed to: describe the complicated two phase flow created by the breaking wave; determine the time the probes were inside a bubble cloud; determine if the probes were subjected to splashing before sampling the actual bubble cloud; and to measure the approximate volume of entrained air in the plunging wave case. To produce these videos, the wave channel wall was backlit by placing multiple 500W light bulbs ~10 cm behind it. A piece of Mylar taped to the back channel wall was used to diffuse the light and to provide uniform illumination in the digital video images (Rojas and Loewen, 2007a).

Data Analysis

Computing estimates of the void fraction from the raw probe signals requires the selection of a voltage level (i.e. threshold voltage) which defines if the tip of the probe is surrounded by water (voltage lower than the threshold) or if it is surrounded by air (voltage higher than the threshold) (Rojas and Loewen, 2007a). Once this threshold is selected, each digital voltage measurement was assigned a void fraction value of zero if it was less than the threshold voltage; otherwise it was assigned a value of one. Note that

zero signifies that the probe tip is in water and one that it is in air. Fig. 3.5 displays three time series of the instantaneous void fraction, $\alpha(i,t)$, for $i = 5, 6,$ and 7 (i.e. the 5th, 6th, and 7th repeated runs) at position M. For $t < 9.75$ s, $\alpha(i,t)$ is equal to one since the probes were in the air and then, $\alpha(i,t)$ goes to zero as the probes passed through the forward face of the wave and entered the water. The probes then passed through the bubble cloud and whenever the probe tips intersected a bubble, a voltage pulse was produced. Finally the probes left the water at $t \sim 10.4$ s and $\alpha(i,t)$ returns to a value of one. The ensemble void fraction at a given position can be computed by averaging over N_R repeated runs as follows,

$$\langle \alpha \rangle = \frac{\sum_{i=1}^{N_R} \alpha(i,t)}{N_R} \quad (3.1)$$

where $\langle \alpha \rangle$ is the ensemble void fraction at time t , $\alpha(i,t)$ is the instantaneous local void fraction (i.e. zero or one) for run i at time t , and N_R is the number of repeated waves. At each location the upper and lower vertical limits of the bubble cloud were determined by analysing the digital video images. Thereafter the ensemble void fractions, based on 60 repeat runs, were measured at a minimum of four vertical locations inside the bubble cloud. An example of three vertical measurements of $\langle \alpha \rangle$, at position C, is plotted in Fig. 3.6. At position C, the peak or maximum ensemble void fraction, $\langle \alpha \rangle_{\max}$, was located 0.06 m above the still water levels shown in Fig. 3.6b. The probes were also located above the still water level and initially $\langle \alpha \rangle$ was equal to 1.0. The fiber-optic probes first passed through the front face of the wave at $t \sim 9.65$ s. Thereafter, the ensemble void fraction increases up to $\langle \alpha \rangle_{\max} \sim 0.89$ at $t \sim 9.70$ s. Then, the probes

passed out of the air cavity and $\langle \alpha \rangle$ decreased to ~ 0 as the probes encountered pure water at $t \sim 9.85$ s. Finally, at $t \sim 9.9$ s, the probes exit the water and $\langle \alpha \rangle$ returns to a value of 1.0.

Non-dimensionalizing the variables helps to generalize the results from specific experiments. Therefore, the horizontal and vertical locations, as well as time were made dimensionless as follows,

$$\hat{y} = \frac{(y - y_0)}{\lambda} \quad (3.2)$$

$$\hat{x} = \frac{(x - x_b)}{\lambda} \quad (3.3)$$

$$\hat{t} = \frac{(t - t_b)}{T} \quad (3.4)$$

where x is the horizontal distance measured from the mean position of the wave paddle, y is the vertical position referenced to the tank bottom and increasing upwards, t is the time referenced to the initiation of wave paddle motion, y_0 is the still water depth; λ is the wave length of the center frequency; t_b is the breaking time obtained from the video analysis; T is the wave period of the centre frequency ($= 1/f_c$); and x_b is the point where the falling jet impacts the wave face in the case of the plunging wave and it is the place where the instability at the wave crest is first detected (from video analysis), for the spilling wave case. This dimensionless set of variables means that $\hat{x} = 0$, at $x = x_b$, $\hat{y} = 0$, at $y = y_0$, and $\hat{t} = 0$, at $t = t_b$. The positions of the measurements as well as the number or repeated runs are listed in Table 3.1 and 3.2. Detailed measurements were made at 13 horizontal positions for the plunging wave (labelled positions A-M). The relative

locations of the probe tips along the plunging wave are displayed in Fig. 3.7. The water surface profiles were extracted from the images showing the instant when $\langle \alpha \rangle_{\max}$ occurred at each position. The length of each water surface profile corresponded to the width of the camera field of view. Note that the splash-up profile was ignored for positions A-E and G in Fig. 3.7a&b. In addition, for positions H-K, the water surface profiles corresponded to the upper edge of the bubble cloud, Fig. 3.7b. In Fig. 3.7a the movement of the wave is downwards while in Fig. 3.7b the wave is moving downwards at position F and upwards at positions G-K.

There were 4 measurement positions for the spilling wave (labelled positions 21, 23, 38, and 50). The relative locations of these measuring positions are displayed in Fig. 3.8. The images taken at position 50 could not be processed because they were out of focus. Note that the size of the bubble cloud increases as the spilling process developed. The vertical positions for the spilling wave were selected based on the highest number of detected bubbles. This criterion was applied because no local maximum in $\langle \alpha \rangle$ were observed beneath the spilling wave, e.g. Fig. 3.9. At position 38 the probes were located above the still water level and therefore $\langle \alpha \rangle$ was initially 1.0. The probes then passed through the forward face of the wave and $\langle \alpha \rangle$ decreased to a minimum value as the probes passed through the bubble cloud. Then $\langle \alpha \rangle$ returned to 1.0 as the probes passed out of the water through the rear wave face.

The lowest number of repeat waves generated to compute $\langle \alpha \rangle$ was 1130 at position M. Based on positions F and G, it was estimated that the average value of the standard error of the mean $\langle \alpha \rangle$ values was ~ 0.005 when 1130 repeat breaking waves were used. This error was considered to be acceptable because this was the largest value

of the standard error of the mean since the number of repeated breaking waves was higher at all other positions.

The estimation of the mean void fraction, $\bar{\alpha}$, was performed by averaging $\langle \alpha \rangle$ in the time interval displayed in Table 3.3 and Table 3.4, for the plunging and spilling waves, respectively. For the plunging wave, these time limits were selected as the instant when the first and second local minima were detected. For the spilling wave, this time interval corresponded to the time when $\langle \alpha \rangle$ was ≤ 0.5 , as explained later.

The interpretation of the time series of $\langle \alpha \rangle$ required the identification of the approximate path the probe tips traversed through the bubble cloud as the breaking wave passed over them. To determine the approximate path it was necessary to track different reference points in the bubble cloud and then, determine their positions with respect to the tip of the fiber-optic probes, in sequential images. For example, at position A this path was estimated by determine the displacement of the centroid of the air cavity, relative to the probe tip position. A MATLAB program was used to process the digital images and to compute the air cavity contour and the location of its centroid. Initially, the position of the probes is lower with respect to the bubble centroid, Fig. 3.10a. Then, as the probes passed through the splash-up zone, the tips were located approximately at the same elevation as the cavity centroid, see Fig. 3.10b. After the probes have passed through the cavity of air and reached pure water, the tips were now slightly above the centroid, see Fig. 3.10c. In Fig. 3.10d an image showing the relative position of the probe tips, determined by analyzing 6 sequential images, is presented. The complete approximate path is overlain on the plot of the image corresponding to the time when $\langle \alpha \rangle_{\max}$ was measured in Fig. 3.11a, at position A. This path was obtained by fitting a cubic

polynomial to the 6 points shown in Fig. 3.10d. A similar procedure was followed for positions B and C. For positions D – M (plunging wave) and for the spilling wave, different reference points were used, e.g. the displacements of part of the bubble cloud (because it was not possible to image the entire bubble cloud at once) or a particular large bubble that appeared in sequential images was tracked.

The time series of $\langle \alpha \rangle$ also provided information related to the time when the probes entered the water. A value of $\langle \alpha \rangle \sim 0.5$ will approximately identify the free surface (Blenkinsopp and Chaplin, 2007). This criterion is particularly useful in the interpretation of the measurements performed beneath the spilling wave.

3.3 Results

The probes intersected the air cavity prior to its collapse at positions A, B, and C. The image in Fig. 3.11a shows the plunging wave at the instant when $\langle \alpha \rangle_{\max} \sim 0.96$, at $\hat{t} = 0.18$, with the probes at position A, Fig. 3.11b. Initially, $\langle \alpha \rangle$ was equal to 1.0 because the probes were located above the still water level. As the wave approached, the fiber-optic probes first passed through the splash-up flow at $\hat{t} \sim 0.10$ and they passed through the front face of the wave at $\hat{t} \sim 0.15$. At position A the probes passed through the centroid of the air cavity. Thereafter, the probes passed out of the air cavity and $\langle \alpha \rangle$ decreased to ~ 0 as the probes encountered pure water. Finally, at $\hat{t} \sim 0.45$, the probes exit the water and $\langle \alpha \rangle$ returned to a value of 1.0. The time averaged void fraction was $\bar{\alpha} = 0.33$, Table 3.3. Fig. 3.12a shows the image when $\langle \alpha \rangle_{\max}$ was detected at position B. The approximate probe path indicates that at this position the probes also

passed through the splash-up flow which reached a minimum of $\langle \alpha \rangle = 0.25$ at $\hat{t} = 0.21$. The probes then passed through the air cavity and the maximum and time averaged void fractions were $\langle \alpha \rangle_{\max} = 0.95$ (at $\hat{t} = 0.25$) and $\bar{\alpha} = 0.37$, respectively, Table 3.3. The probes passed out of the cavity into pure water ($\langle \alpha \rangle = 0.0$) and finally entered the air again just behind the wave crest as shown in Fig. 3.12b.

The air cavity was also studied at position C where the approximate path of the fiber-optic probes passed through the air cavity above its center, Fig. 3.13a. In Fig. 3.13b, it can be seen that $\langle \alpha \rangle_{\max} = 0.89$, at $\hat{t} = 0.32$, and $\bar{\alpha} = 0.29$ for the time interval $0.27 < \hat{t} < 0.35$. Note that the measurements performed close to the bubble cloud centroid indicated $\langle \alpha \rangle_{\max} = 0.50$. Fig. 3.14 displays a sequence of images taken with the camera located below the air-cavity and looking downstream. It is evident in Fig. 3.14a that the air cavity started to collapse from the tank's wall towards the center line of the tank at $\hat{t} = 0.27$. In Fig. 3.14b, taken at $\hat{t} = 0.33$, filaments of air similar to those described by Deane and Stokes (2002) were observed around the periphery of the air cavity. These filaments were distributed randomly across the air cavity and had lengths of the order of several centimetres. In Fig. 3.14c the air cavity has collapsed across the entire channel in the time interval $0.33 < \hat{t} < 0.38$.

The upper portion of the 1st cloud, generated as a consequence of the fragmentation of the air cavity, was sampled at position D. Fig. 3.15a corresponds to position D where the probes entered the water and then traversed the bubble cloud where $\langle \alpha \rangle_{\max} = 0.18$, at $\hat{t} = 0.47$, and $\bar{\alpha} = 0.11$, Fig. 3.15b. It was also observed that the 1st

and 2nd bubble clouds were connected at this time. However, analysis of the video images determined that at $\hat{t} \sim 0.7$ these two clouds separated from each other.

The 2nd cloud was sampled at position E. Fig. 3.16a could not be extended to the right because the vertical tank support blocked the view of that part of the bubble cloud. At this position, the time series of $\langle \alpha \rangle$ indicated that $\langle \alpha \rangle_{\max} = 0.17$, at $\hat{t} = 0.55$, and $\bar{\alpha} = 0.10$, Fig. 3.16b. The probes are also seen traversing the 2nd cloud which rotates counter-clockwise at position F, Fig. 3.17a. The corresponding time series of $\langle \alpha \rangle$, Fig. 3.17b, indicated that before the probes encountered the 2nd bubble cloud at $\hat{t} \sim 0.58$, they had been in pure water since the time of breaking, i.e. $\langle \alpha \rangle = 0$. As the fiber-optic probes crossed the bubble, the ensemble void fraction increased until it reached $\langle \alpha \rangle_{\max} = 0.024$, at $\hat{t} = 0.74$ and $\bar{\alpha} = 0.012$.

The 3rd cloud produced by the splash-up was sampled at positions G to K. The probes are also seen traversing the 3rd cloud at position G (G** in Table 3.3), Fig. 3.18a. This image was taken at $\hat{t} \sim 0.32$ when $\langle \alpha \rangle_{\max} = 0.061$. The probes traversed this bubble cloud in the time interval $0.30 < \hat{t} < 0.37$ and $\bar{\alpha} = 0.037$, Fig. 3.18b. At this position, the probes also traversed the 2nd cloud (G* in Table 3.3) in the time interval $0.61 < \hat{t} < 0.74$, and the time averaged void fraction was $\bar{\alpha} = 0.01$. The digital images in Fig. 3.19a, 3.20a, 3.21a, and 3.22a corresponded to the instant when $\langle \alpha \rangle_{\max}$ was measured to be 0.43, 0.42, 0.60 and 0.37 at $\hat{t} = 0.51, 0.57, 0.61, \text{ and } 0.68$, for positions H to K, respectively. For these positions, it was observed that the tips of the fiber-optic

probes were located approximately at mid-depth of the bubble cloud which had a total depth of ~ 10 cm (or $\hat{y} \sim 0.051$). Due to the small field of view, the approximate path the fiber-optic probes inside these bubble clouds approximated a straight line. The time series of $\langle \alpha \rangle$ are plotted in Fig. 3.19b, 3.20b, 3.21b, and 3.22b for positions H to K, respectively. These time series have a similar pattern. Initially $\langle \alpha \rangle = 1.0$ because the probes were in air. Then $\langle \alpha \rangle$ decreased and reaches a first local minimum and then $\langle \alpha \rangle$ increases to a local maximum. After that, $\langle \alpha \rangle$ decreases to a second local minimum. Finally, as the probes leave the water, $\langle \alpha \rangle \sim 1.0$. The estimated time averaged void fractions were $\bar{\alpha} = 0.18, 0.16, 0.26,$ and 0.13 , for positions H to K, respectively.

The variation of $\langle \alpha \rangle$ as a function of depth was examined at positions K, L, and M which were located in the 3rd cloud at $\hat{y} \sim 0.02, 0.01,$ and -0.01 , respectively. The approximate path that the fiber-optic probes followed inside the cloud is displayed in Fig. 3.23a and 3.24a, for positions L and M, respectively. Moving down from position K to position L, $\langle \alpha \rangle_{\max}$, was reduced to 33% of its original value, from 0.37 to 0.12 (Fig. 3.23b, 3.24b and Table 3.3). Moving from position L to M, $\langle \alpha \rangle_{\max}$ was reduced to $\sim 75\%$ of its original value, from 0.12 to 0.089 and $\bar{\alpha}$ was reduced by half, from 0.043 to 0.021.

The speed of advance of the air cavity was estimated based on the time elapsed between the ensemble peak void fraction measured at positions A and C. It was determined that the speed at which the air cavity was advected downstream was ~ 1.22 m/s. The centre frequency component of the wave packet has a phase speed of 1.70 m/s,

which means that the speed of advance of the air cavity was $\sim 75\%$ of the phase speed. Similarly, the speed of advance of the 3rd cloud was computed based on positions J and K and it was found to be 1.52 m/s or 90% of the phase speed.

Spilling wave

The analysis of the images of the spilling breaking wave confirmed that near the breaking position, the bubble cloud was very compact and as time progressed, its size increased as it elongated. Also, it was determined that the maximum depth of penetration was $\sim 5 \text{ cm}$ (or $\hat{y} \sim 0.026$). Furthermore, this analysis determined that the start of breaking occurred $\sim 12.3 \text{ s}$ after the initiation of the wave paddle motion. The images in Fig. 3.25a, 3.26a, and 3.27a correspond to $\hat{t} \sim 0.08, 0.34$ and 0.65 at positions 21, 23 and 38, respectively. The image at position 50 could not be processed because it was out of focus. The corresponding time series of $\langle \alpha \rangle$ for the spilling wave are shown in Fig. 3.25b, 3.26b, 3.27b and 3.28 for positions 21, 23, 38, and 50, respectively. For all positions, the probes were mounted above the still water level and therefore, $\langle \alpha \rangle$ initially was equal to 1.0 (the probes were in air), and as the probe passed through the bubble cloud, $\langle \alpha \rangle$ decreased (the probes encounter an air-water mixture), and then increased as the probes re-entered the air on the back side of the wave. Note that there might be a cluster of bubbles which produced a highly localized $\langle \alpha \rangle$, e.g. at $\hat{t} \sim 0.08$, Fig. 3.25b. Estimates of $\bar{\alpha}$ were based on the interval time where $\langle \alpha \rangle \leq 0.5$. $\bar{\alpha} = 0.17, 0.29, 0.20$, and 0.26 for positions 21, 23, 38 and 50, respectively. Finally, by measuring the time elapsed between the lowest ensemble void fractions measured at positions 21 and 50, it was

possible to estimate that the speed at which the bubble plume was advected downstream was ~ 1.73 m/s, or $\sim 100\%$ of the phase speed.

3.4 Discussion and Conclusions

Experiments to measure the air entrainment, produced under mechanically generated deep-water breaking waves, were conducted to study the ensemble average of the void fraction, $\langle \alpha \rangle$, at different positions beneath plunging and spilling waves. Two fiber-optic probes were used to capture the rapid variations of the void fraction. The time series of $\langle \alpha \rangle$ have similar patterns which can be summarized as follows. For the plunging wave case, initially $\langle \alpha \rangle = 1.0$ because the probes were located above the still water level. The probes then passed through the forward face of the wave and $\langle \alpha \rangle$ decreased and reached a first local minimum. The probes then traversed the bubble cloud where $\langle \alpha \rangle$ increased to a local maximum. The probes then passed out of the bubble cloud and $\langle \alpha \rangle$ decreased to a second local minimum and finally, $\langle \alpha \rangle$ returned to a value of 1.0 when the probes re-entered the air on the back side of the wave.

The fact that the time series of $\langle \alpha \rangle$ did not instantaneously change from one to zero or from zero to one when the probes entered pure water or pure air, respectively, was an indication that the wave was not exactly repeatable, despite the careful control in the wave packet generation and the two minute interval between repeat waves, to allow the water surface oscillation to decay to negligible amplitudes. Based on the measurements at position A, the repeatability of the breaking wave process was examined by measuring the interval of time it took for $\langle \alpha \rangle$ to change from 0.0 (probes immersed in water) to 1.0 (probes are set on air) just behind the wave crest. It was determined that the time at

which the probes entered the air varied by ± 50 ms. Therefore, the repeatability of the breaking wave was assumed to be ± 50 ms.

The shape of the time series of $\langle \alpha \rangle$ indicates that the instantaneous void fraction field inside the air cavity and the three clouds generated underneath the plunging wave could be sketched as depicted in Fig. 3.29a. The wave profile and the bubble cloud shape are similar to the ones displayed in Fig. 3.12a. In this idealization, the approximate probe path starts when the probes are set on air, i.e. $\langle \alpha \rangle = 1.0$. Then, as the probes enter the bubbles cloud the ensemble void fraction decreases to $\langle \alpha \rangle = 0.1$, the first local minimum. Thereafter, as the probes pass through the cloud, a local maximum of $\langle \alpha \rangle_{\max} = 0.9$ is reached. After that, the ensemble void fraction decreases to a second local minimum, in this case $\langle \alpha \rangle \sim 0.10$. Finally, $\langle \alpha \rangle \sim 1.0$ as the probes enter the air. This type of void fraction field has been previously reported by Lamarre and Melville (2001) and Blenkinsopp and Chaplin (2007).

Numerical simulations of breaking waves should accurately predict occurrence of significant events that occur during the breaking process. The first significant event in the breaking of a plunging wave is the instant when the plunging water jet impacts the undisturbed water on the forward face of the wave. Right after this event, the highest value of the ensemble void fraction, $\langle \alpha \rangle_{\max} \sim 0.97$, was measured at position A, which is similar to previous reported measurements by Lamarre and Melville (1991) and Blenkinsopp and Chaplin (2007). The second significant event is the collapse of the air cavity which was observed to occur sometime between $0.33 < \hat{t} < 0.38$. Therefore, numerical simulations should accurately predict both the timing of the jet impact and the collapse of the air cavity.

After the collapsing of the air cavity, $\langle \alpha \rangle_{\max} = 0.18$ at position D where the probes were located near the upper edge of the 1st cloud, and therefore it was decided to perform an additional set of experiments, based on 300 repeated waves, at the centre of the cloud defined as position Z at $\hat{x} = 0.22$ and $\hat{y} = 0.0052$ (see Fig. 3.15a). The measurements indicated that at this position $\langle \alpha \rangle_{\max} = 0.18$ at $\hat{t} = 0.42$. Therefore, $\langle \alpha \rangle_{\max}$ was reduced by a factor of ~ 5 between the air cavity (position C) and the 1st cloud (positions Z and D). The mean void fraction was reduced by a factor of ~ 2.6 between positions C and D. This reduction in the mean void fraction was also observed by Lamarre and Melville (1991) who reported that the mean void fraction evolution can be well represented by a power law equation of the form $\bar{\alpha} \sim (\hat{t})^{-2.3}$. Using \hat{t}_{\max} at positions C and D, this equation predicts a reduction in the mean void fraction of ~ 2.4 .

The 1st and 2nd cloud had a similar $\langle \alpha \rangle_{\max}$ (positions D and E) which would indicate that the total amount of air entrained by the two processes, the collapsing of the air cavity and jet and drop impact, are comparable at the initial stages of the formation of the 2nd cloud. The value of $\langle \alpha \rangle_{\max}$ in the 2nd cloud, also decreased rapidly in a very short period of time; it was reduced by a factor of ~ 7 in $\Delta \hat{t} = 0.19$, between points E and F. This reduction may be a consequence of the small depth of the 2nd cloud since large bubbles will rise back to the surface quicker.

The collision of the splash-up water jet with the undisturbed water on the forward face of the wave, created the 3rd cloud. An initial $\langle \alpha \rangle_{\max} = 0.061$ was measured at position G where some water-jet drops impacted the water (this is the third significant

event, $\hat{t} = 0.32$). As the center line of the jet collided with the forward face of the wave, $\langle \alpha \rangle_{\max}$ increased up to 0.60 at position J (this is the fourth significant event, $\hat{t} = 0.61$).

The time series of $\langle \alpha \rangle$ have similar patterns for the spilling wave case. Initially $\langle \alpha \rangle = 1.0$ and as the probe passed through the bubble cloud, $\langle \alpha \rangle$ decreased to a local minimum, and then increased to 1.0 as the probes re-entered the air on the back side of the wave. This pattern suggests that the instantaneous void fraction field underneath spilling waves could be sketched as depicted in Fig. 3.29b. The wave profile and the bubble cloud shape are similar to the ones displayed in Fig. 3.25a. In this idealization, the approximate probe path starts when the probes are located in air, i.e. $\langle \alpha \rangle = 1.0$. The probes then cross the air-water interface defined as $\langle \alpha \rangle = 0.5$. The probes immediately encounter the bubble cloud; thereafter, the probes traverse the air-water mixture and the ensemble void fraction decreases to a minimum, in this case $\langle \alpha \rangle \sim 0.30$. Finally, $\langle \alpha \rangle \sim 1.0$ as the probes re-enter the air.

A comparison with the measurements obtained by Leifer and Leew (2006) indicated that our values of $\bar{\alpha}$ were higher by one to two orders of magnitude. Note that they blew wind over paddle generated waves that had a wavelength of 1.3 m, a frequency of 1.2 Hz, and wave heights of ~ 12 cm. These were smaller waves than the one used in these experiments; therefore, lower void fractions would be expected. The experiments of Loewen et al. (1996) were conducted with very gentle spilling breaking waves and they reported void fractions that were lower than our $\bar{\alpha}$ values by two orders of magnitude. Note that if the slope of the wave packet is increased slightly to 0.40 a plunging breaker occurs indicating that the spilling wave generated at a slope of 0.38 breaks energetically.

Therefore, it is likely that a larger amount of air will be entrained beneath this energetic spilling wave compared to the waves used by Leifer and Leew (2006) and Loewen et al. (1996). Therefore, similar void fraction measurements would be obtained if we had used a smaller wave slope. Other reason for these differences may be the fact that their void fraction measure techniques were different from the one used in our experiments.

The average value of $\bar{\alpha}$ for the plunging wave (average for positions A-K), was ~ 0.15 . This value is similar to the values observed in the laboratory by Cox and Shin, 2003, in the surf zone. Their peak ensemble-averaged void fractions were in the range 0.15-0.20. The average value of $\bar{\alpha}$ measured beneath the spilling wave was ~ 0.23 which was similar to the measurements performed by Mori et al. (2007) who reported void fractions, beneath spilling and plunging waves (breaking at the surf zone), that were of the same order of magnitude as those measured here, ~ 0.15 . Note that the average value of $\bar{\alpha}$ measured beneath the spilling wave was higher than the average measured at the plunging wave, similar to the measurements of Cox and Shin (2003).

The speed of advance of the air cavity and the 3rd cloud were ~ 75 and $\sim 90\%$ of the phase speed, respectively. These results are comparable to the measurements performed by Rapp and Melville (1990) beneath mechanical generated wave packets. They used dye to visualize the region of the flow directly affected by breaking and found that the length of the dye cloud increased at a speed of 70-80% of the linear wave phase speed. Thereafter, Melville et al. (2002) also used wave packets and performed digital particle image velocimetry measurements, reporting that the speed of advanced of the breaking region that was $\sim 80\%$ of the phase speed. For the spilling wave, we measured a

speed of advance of the bubble cloud that was 100% of the phase speed; to our knowledge, there has not been any previous measurement of this speed.

These detailed void fraction measurements will help in gaining a better understanding of the air-sea gas transfer process, especially under spilling breaking waves. In addition, these measurements can be used to calibrate and improve numerical models of the two phase flow generated beneath plunging and spilling breaking waves.

3.5. References

Blenkinsopp, C. E. and Chaplin, J. R. (2007a) Void fraction measurements in breaking waves. *Proc. R. Soc. A* 453, 3151-3170.

Bonmarin, P. (1989). Geometric properties of deep-water breaking waves. *J. Fluid Mech.* 209, 405 -433.

Chanson, H., Aoki, S. and Maruyama, M. (2002). Unsteady air bubble entrainment and detrainment at a plunging breaker dominant time scales and similarity of water level variations. *Coastal Engng* 46, 139–157.

Chanson, H., Aoki, S. and Hoque, A. (2006). Bubble entrainment and dispersion in plunging jet flows: freshwater vs. seawater. *J. Coast. Res.* 22, 664–677.

Cox, D. T. & Shin, S. (2003). Laboratory measurements of void fraction and turbulence in the bore region of surf zone waves. *J. Engng. Mech.* 129, 1197–1205.

Deane, G.B., and Stokes, M.D. (1999). Air entrainment processes and bubble size distributions in the surf zone. *J. Phys. Oceanogr.* 29, 1393–1403.

Deane, G. B. and Stokes, D. (2002). Scale dependence of Bubble Creation Mechanisms in Breaking Waves. *Nature*, 418: 839-844.

Duncan, J. H. (2001). Spilling breakers. *Annu. Rev. Fluid Mech.* 33, 519–547.

- Duncan, J. H., Qiao, H., Behres, H. & Kimmel, J. (1994). The formation of a spilling breaker. *Phys. Fluids* 6 (8), 2558–2560.
- Farmer, D.M., McNeil, C.L., and Johnson, B.D. (1993) Evidence for the importance of bubbles in increasing air-sea gas flux. *Nature* 361: 620-623.
- Frew, N. M., Glover, D.M., Bock, E.J, and McCue, S. J. (2007). A new approach to estimation of global air-sea gas transfer velocity fields using dual-frequency altimeter backscatter. *J. Geophys. Res.* 112, C11, C11003.
- Hoque, A. and Aoki, S. (2005). Distributions of void fraction under breaking waves in the surf zone. *Ocean Eng.* 32, 1829–1840.
- Jansen, P. C. (1986). Laboratory observation of the kinematics in the aerated region of breaking waves. *Coastal Engng* 9, 453–477.
- Kalvoda, P.M., Xu, L. and Wu, J. (2003). Macrobubble clouds produced by breaking wind waves: A laboratory study. *J. Geophys. Res.* 108, C6, 3207.
- Kimmoun, O. and Branger, H. (2007). A particle image velocimetry investigation on laboratory surf-zone breaking waves over a sloping beach. *J. Fluid Mech.* 588, 353-397.
- Lamarre, E. and W. K. Melville. (1991). Air entrainment and dissipation in breaking waves. *Nature*, 351, 469–472.
- Lamarre, E. and Melville, W. K. (1992). Instrumentation for the measurement of void-fraction in breaking waves: Laboratory and field results. *IEEE J. Ocean. Eng.*, 17, 204–215.
- Lamarre, E. and Melville, W. K. (1994). Void fraction measurements and sound-speed fields in bubble plumes generated by breaking waves. *J. Acoust. Soc. Am.*, 95(3), 1317 – 1328.

- Leifer, I., de Leeuw, G., 2006. Bubbles generated from wind-steepened breaking waves: Part 1. Bubble from bubble plumes. *J. Geophys. Res.* 111, C06020.
- Loewen M.R. and Melville WK (1991) Microwave backscatter and acoustic radiation from breaking waves. *J. of Fluid Mech.* 224: 601-623.
- Loewen, M. R., O'Dor, M. A., and Skafel, M. G. (1996). Bubbles Entrained by Mechanically Generated Breaking Waves. *J. Geophys. Res.* 101: 20,759-20,769.
- Lubin, P., Vincent, S., Abadie, S., and Caltagirone, J.P. (2006) Three-dimensional large eddy simulation of air entrainment under plunging breaking waves. *Coastal Engng* 53, 631–655.
- Melville W K 1996 The role of surface-wave breaking in air–sea interaction *Ann. Rev. Fluid Mech.* 28 279–321.
- Melville, W.K., Veron, F., and White, C.J. (2002) The velocity field under breaking waves: Coherent structures and turbulence. *J. Fluid Mech.* 454: 203-233.
- Mori N., Suzuki T., and Kakuno S. (2007) Experimental study of air bubbles and turbulence characteristics in the surf zone. *J. Geophys. Res.* 112 (C5): Art. No. C05014.
- Rapp, R.J. and Melville, W.K. (1990) Laboratory measurements of deep-water breaking waves. *Phil. Trans. R. Soc. Lond, A* 331, 735-800.
- Rojas, G, and Loewen, M.R. (2007a) Fiber-optic probe measurements of void fraction and bubble size distribution beneath breaking waves. *Exp Fluids.* 43: 895-906.
- Rojas G. Loewen MR (2007b). Air entrainment by breaking waves. CSCE 2007 Annual General Meeting and Conference. Yellow Knife , Northwest Territories.
- Shamoun, B., El Beshbeeshy, M. and Bonazza, R. (1999) Light extinction technique for void fraction measurements in bubbly flow. *Exps. Fluids* 26, 16–26.

Wallace, D.W.R., and Wirick, C.D. (1992) Large air-sea gas fluxes associated with breaking waves. *Nature* 356: 694-696.

Wu, J. (2000). Bubbles produced by breaking waves in fresh and salt waters: notes and correspondance. *J. Phys. Oceanogr.* 30, 1809–1813.

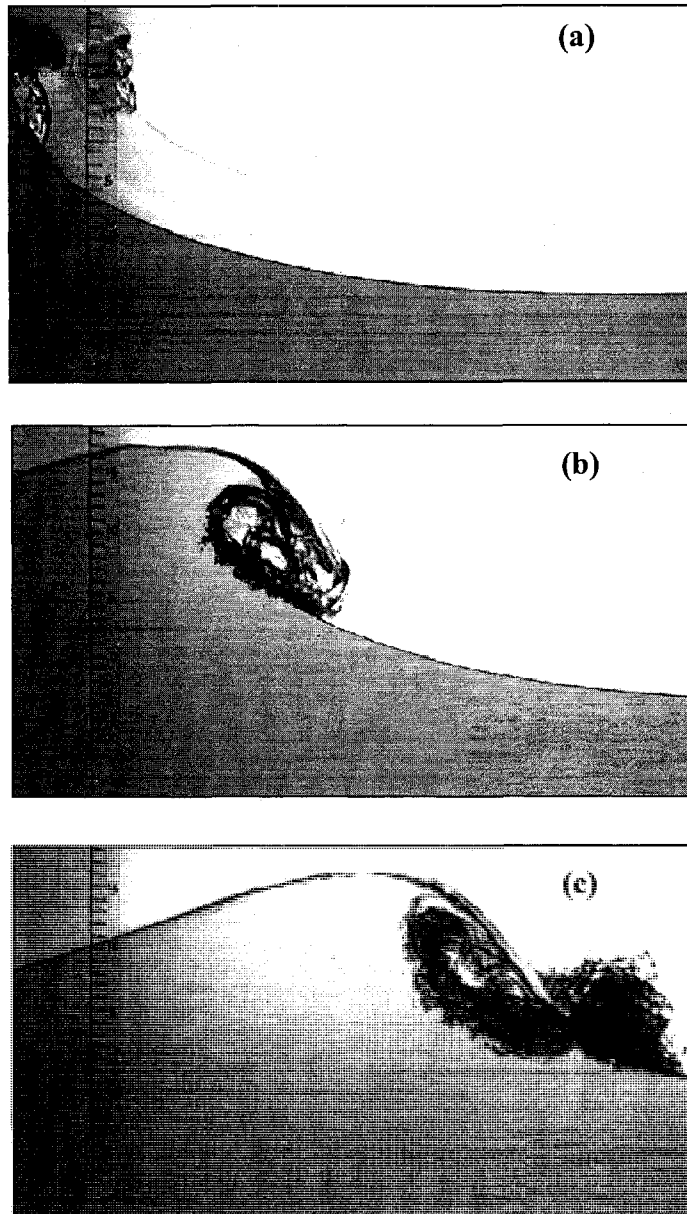


Fig. 3.1 (a) Jet formation at the crest of a plunging wave, $t = 9.2$ s. (b) Cavity of entrapped air, $t = 9.3$ s. (c) Initial stages of the splash-up process, $t = 9.4$ s. t equals zero at the start of the paddle motion.

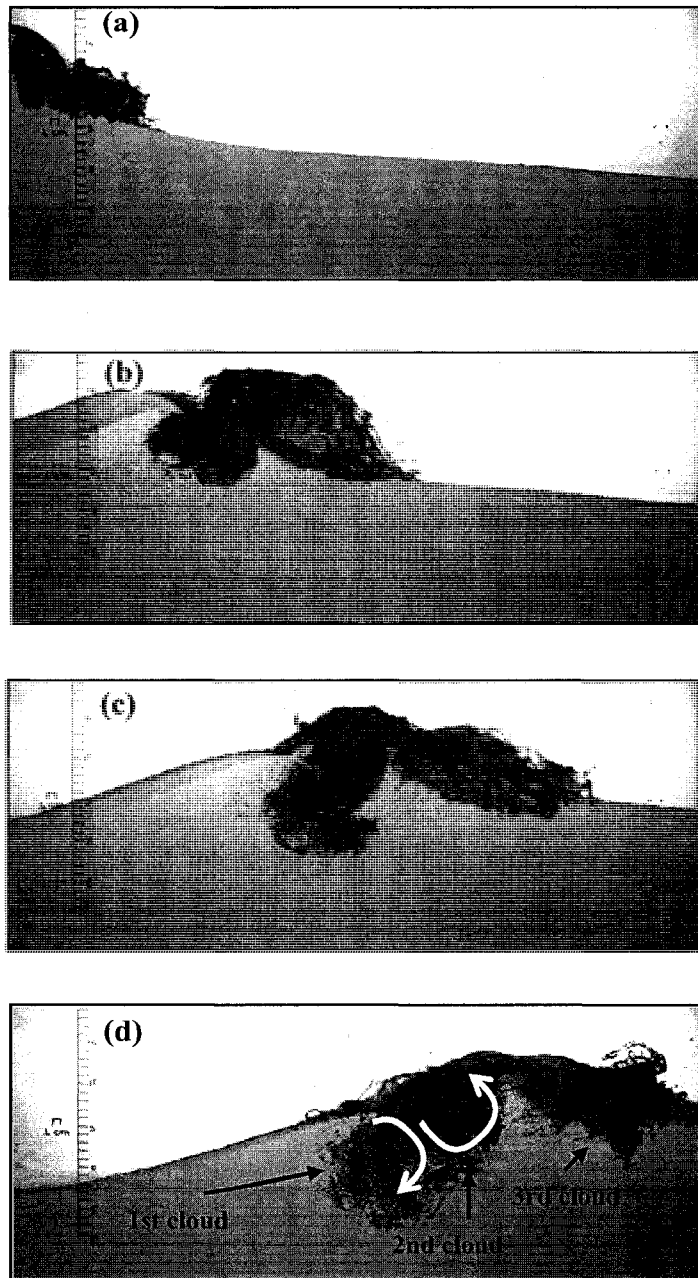


Fig. 3.2 (a-d) Water jet impact and splash-up generation. (a) $t = 8.53 \text{ s}$. (b) $t = 8.73 \text{ s}$. (c) $t = 8.93 \text{ s}$. (d) 1st cloud had clockwise rotation and 2nd cloud had counter clockwise rotation, $t = 9.13 \text{ s}$. White arrows indicate rotation direction. t equals zero at the start of the paddle motion.

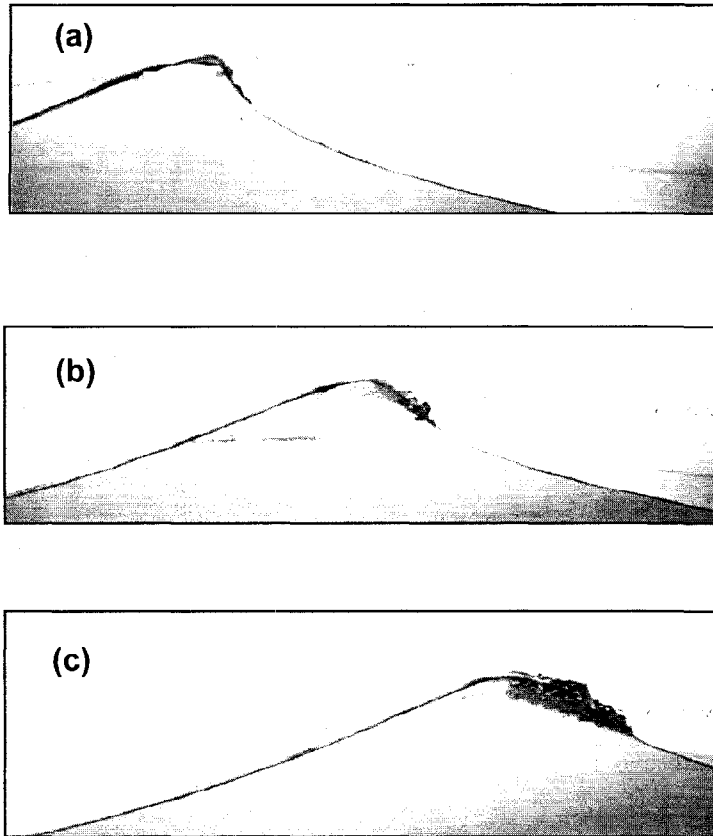


Fig. 3.3 (a)-(c) Sequence of a spilling wave breaking process. (a) $t = 12.17$ s. (b) $t = 12.27$ s. (c) $t = 12.37$ s. t equals zero at the start of the paddle motion.

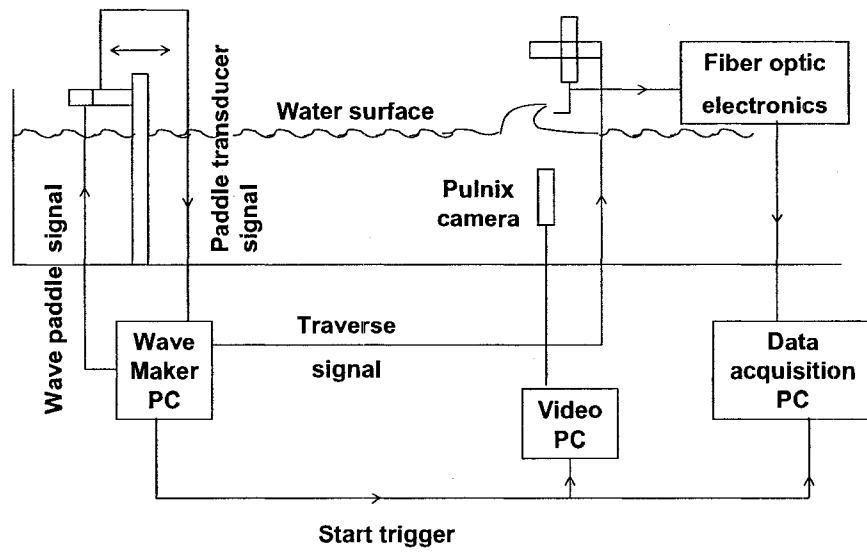


Fig. 3.4 Detailed schematic of the experimental equipment.

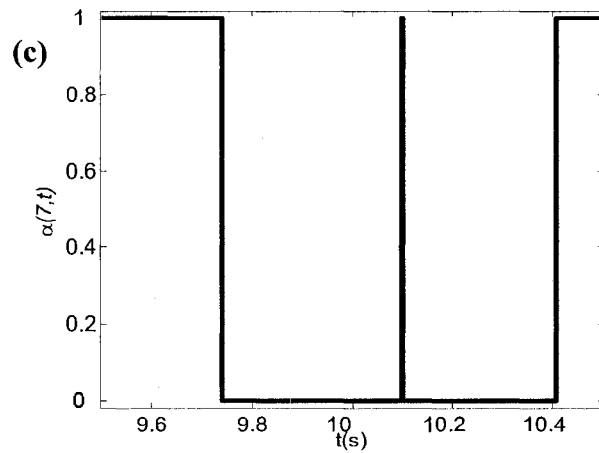
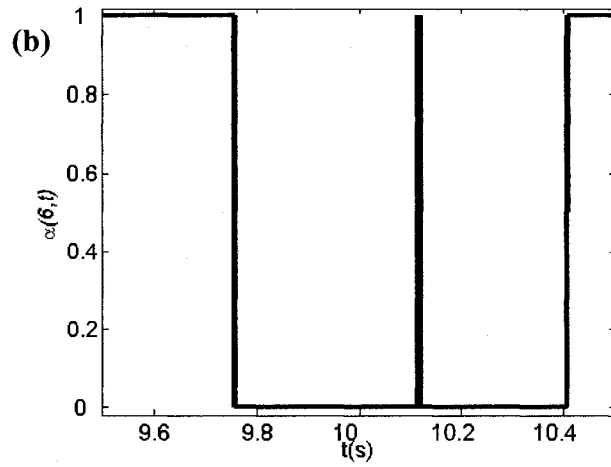
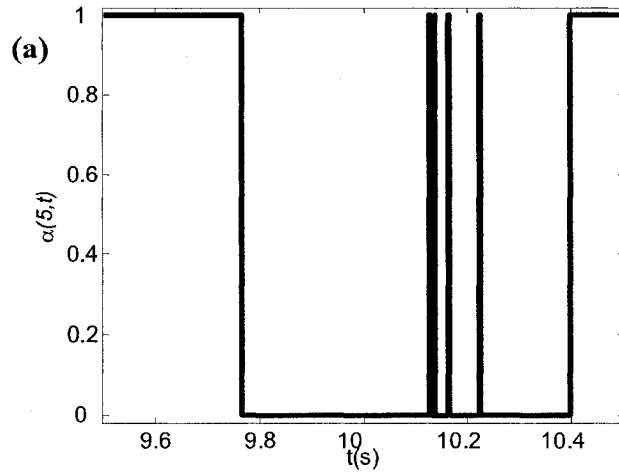


Fig. 3.5 Time series of the instantaneous void fraction, $\alpha(i,t)$, measured at position M, repeats (a) 5, (b) 6 and (c) 7. t equals zero at the start of the paddle motion.

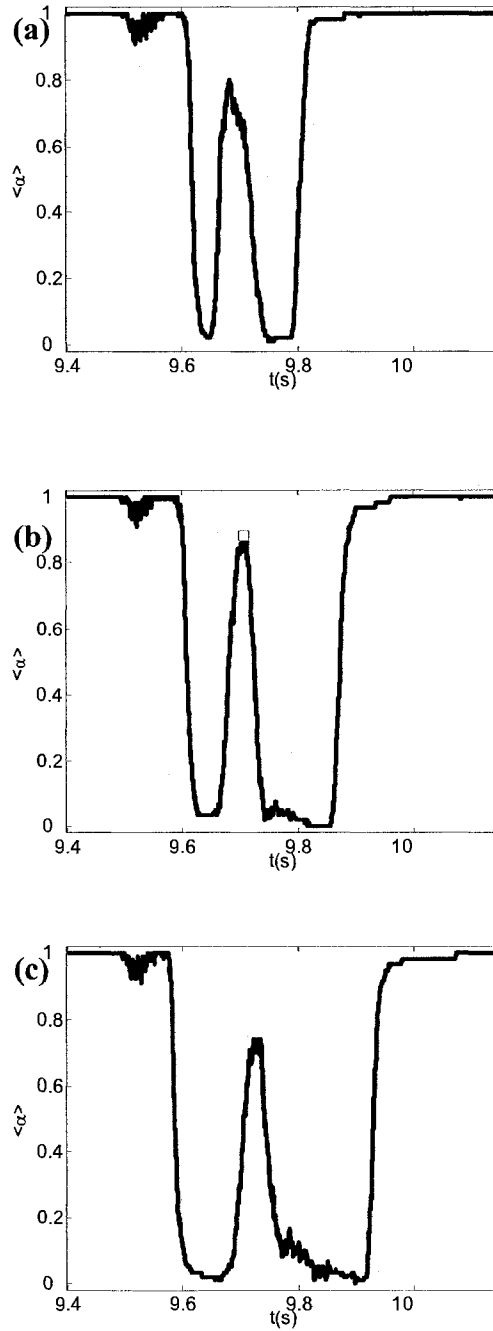


Fig. 3.6 Time series of $\langle \alpha \rangle$ at position C, plunging wave, 60 repeat waves. Position C is located at 0.37 m from the breaking location. y is the vertical distance from the still water. (a) $y = 0.085$ m. (b) $y = 0.060$ m. (\square) $\langle \alpha \rangle_{\max}$. (c) $y = 0.035$ m.

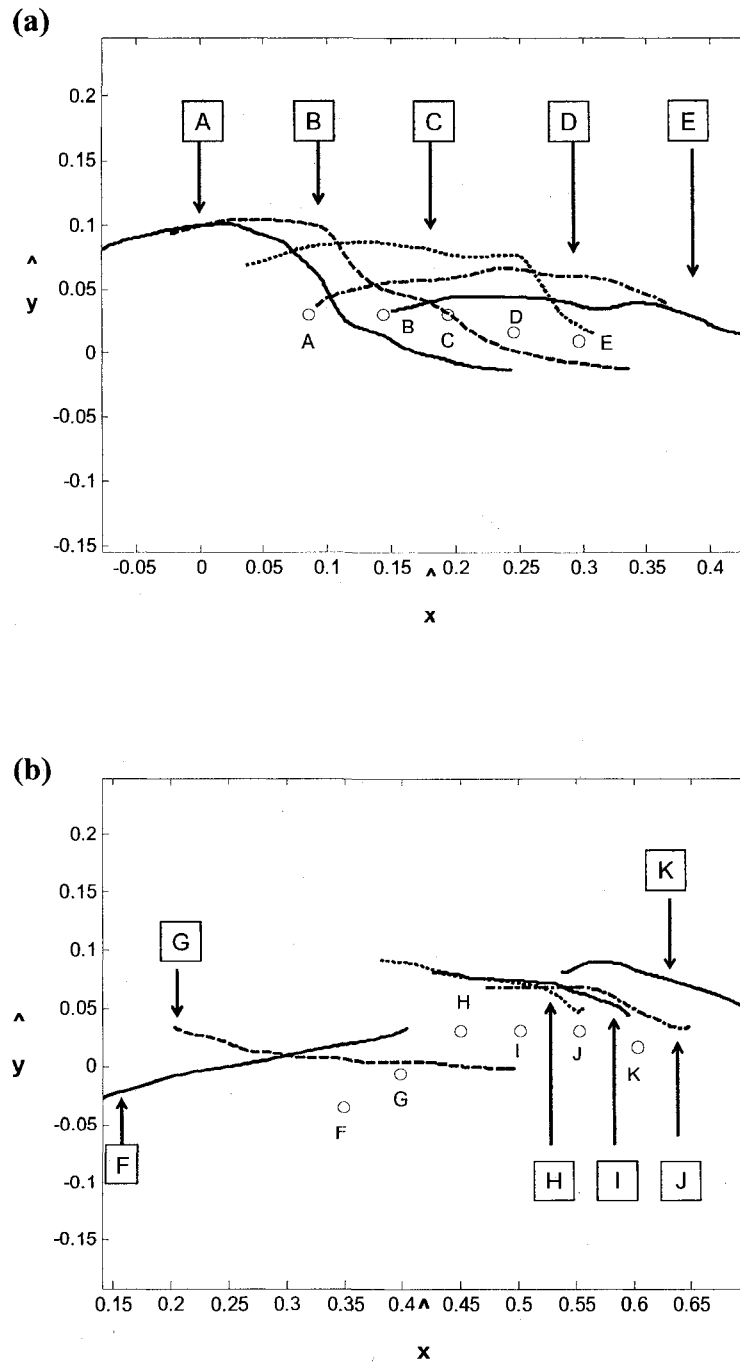


Fig. 3.7 Locations of the probe tip inside the plunging wave. (a) Positions A to E. (b) Positions F to K. The boxed in letters identify the surface profile corresponding to each probe position. \circ is the location of the tip of the probe.

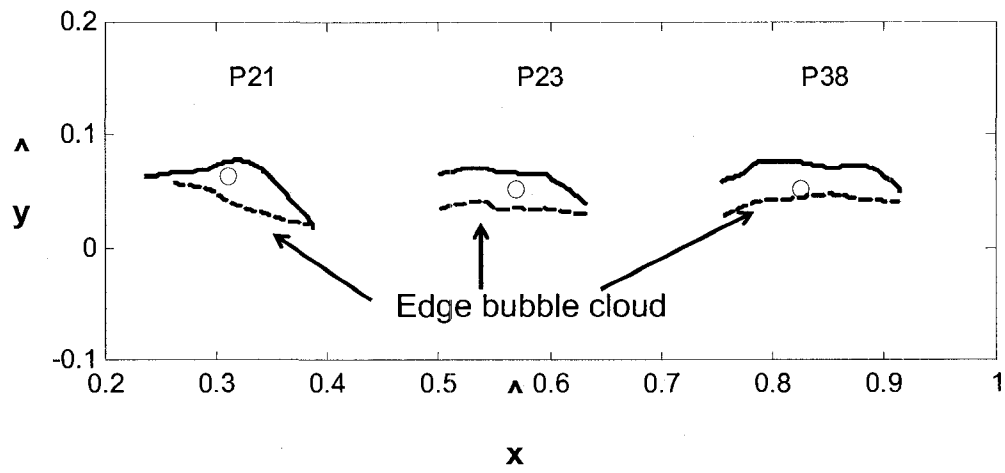


Fig. 3.8 Locations of the probe tip inside the spilling wave. \circ is the location of the probe tip.

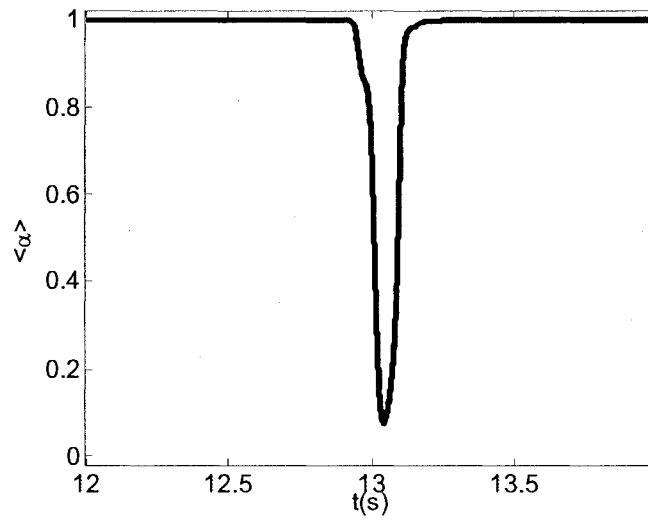


Fig. 3.9 Time series of $\langle \alpha \rangle$ position 38, spilling wave, 6362 repeat breaking waves. t equals zero at the start of the paddle motion.

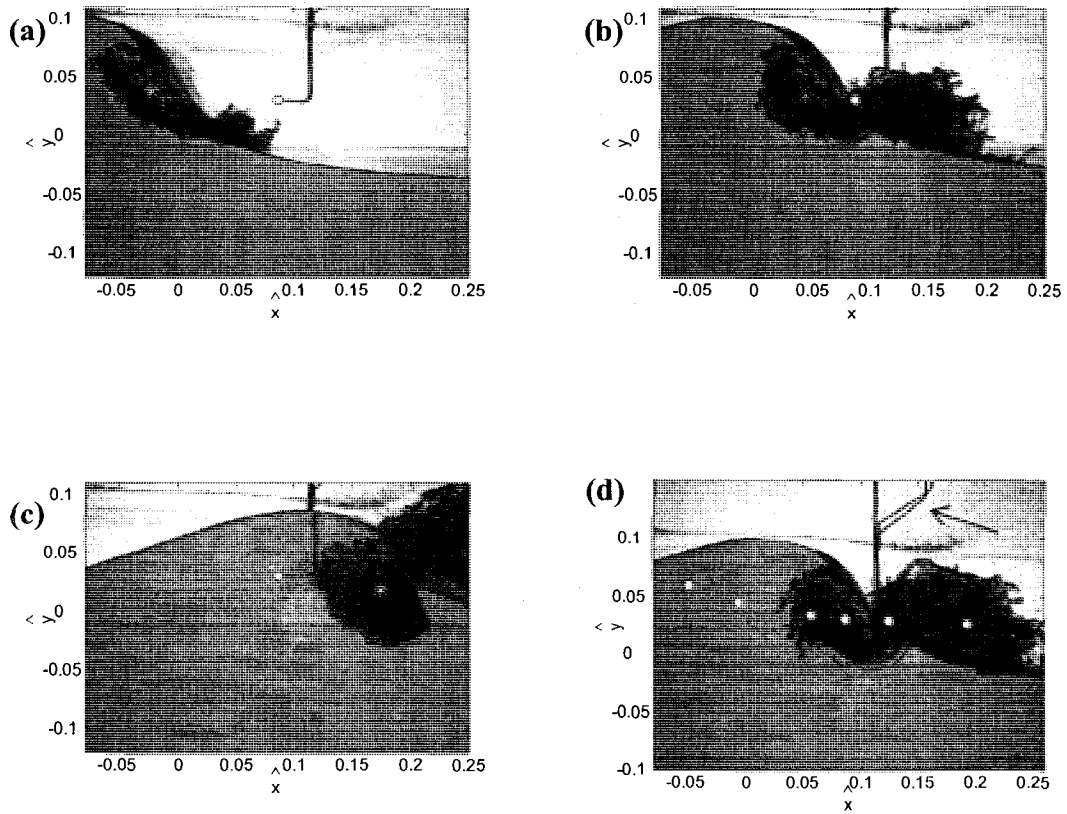


Fig. 3.10 A sequence of images displaying the fiber-optic probes crossing the bubble cloud at position A under the plunging breaker. (white*) is the location of the bubble cloud's centroid. (o) is the tip of the fiber-optic probes. (a) $\hat{t} \sim 0.12$, (b) $\hat{t} \sim 0.23$, (c) $\hat{t} \sim 0.35$. (d) Sequence of the tip position related to the bubble centroid. The arrow positions out the braces that were installed to reduce the probe tip movement.

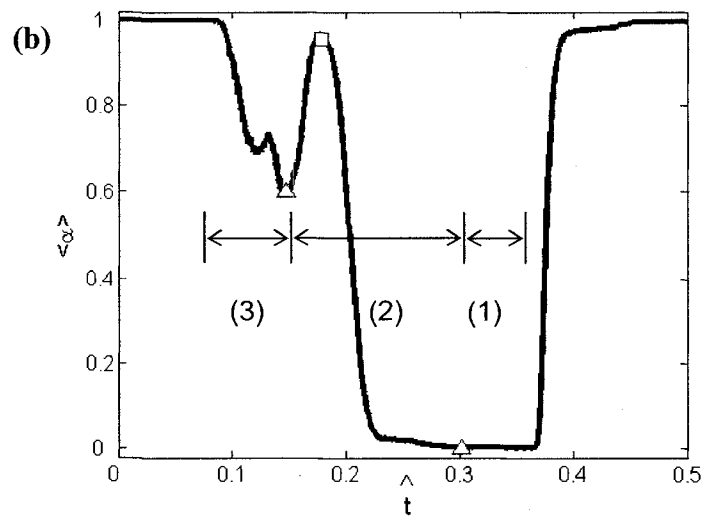
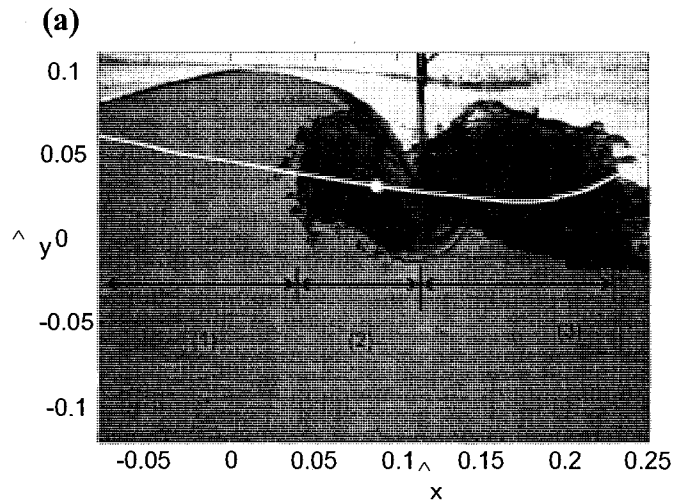


Fig. 3.11 (a) Image showing the instant when $\langle \alpha \rangle_{\max}$ occurred at position A under the plunging breaker. The white line is the approximate path of the fiber-optic when crossing the air cavity. (o) is the position of the fiber-optic probe tips. (b) $\langle \alpha \rangle$. (□) indicates $\langle \alpha \rangle_{\max}$. The time interval between open triangles (Δ) is the interval of time used to compute $\bar{\alpha}$. (1) Water. (2) Air cavity. (3) Splash-up.

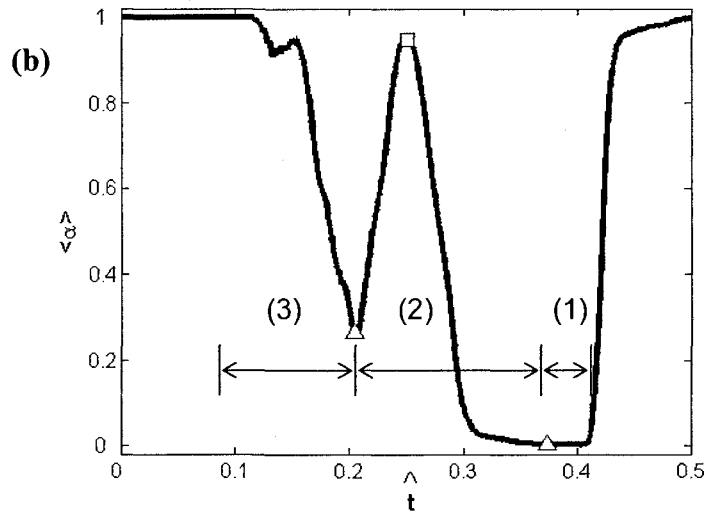
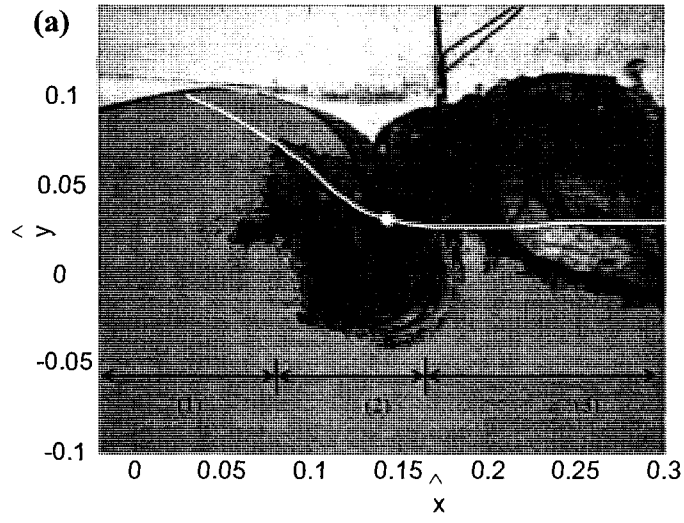


Fig. 3.12 (a) Image showing the instant when $\langle \alpha \rangle_{\max}$ occurred at position B under the plunging breaker. The white line is the approximate path of the fiber-optic. (o) is the position of the fiber-optic probe tips. (b) Time series of $\langle \alpha \rangle$. (\square) indicates $\langle \alpha \rangle_{\max}$. The time interval between the open triangles (Δ) is the time interval used to compute $\bar{\alpha}$. Three time zones are identified as (1) pure water, (2) air cavity and (3) splash-up.

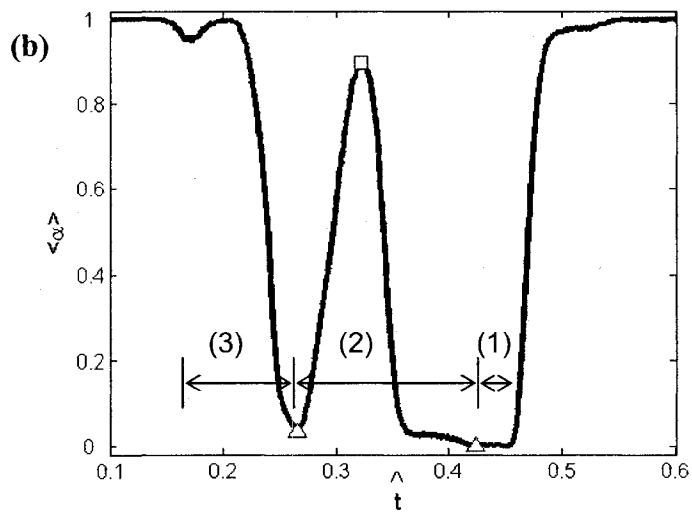
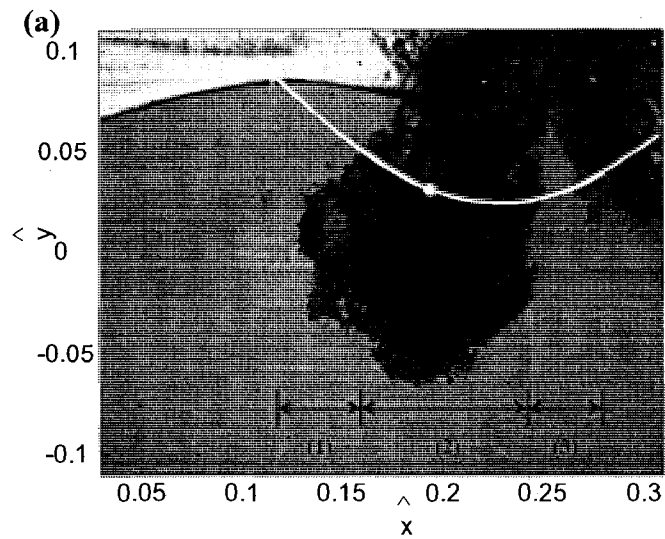


Fig. 3.13 (a) Image showing the instant when $\langle \alpha \rangle_{\max}$ occurred at position C under the plunging breaker. The white line is the approximate path of the fiber-optic. (o) is the position of the fiber-optic probe tips. (b) Time series of $\langle \alpha \rangle_0$. (□) indicates $\langle \alpha \rangle_{\max}$. The time interval between the open triangles (Δ) is the time interval used to compute $\bar{\alpha}$. Three time zones are identified as (1) pure water, (2) air cavity and (3) splash-up.

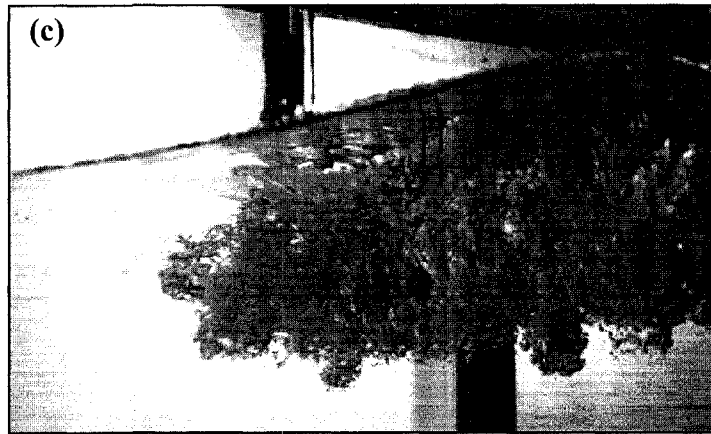
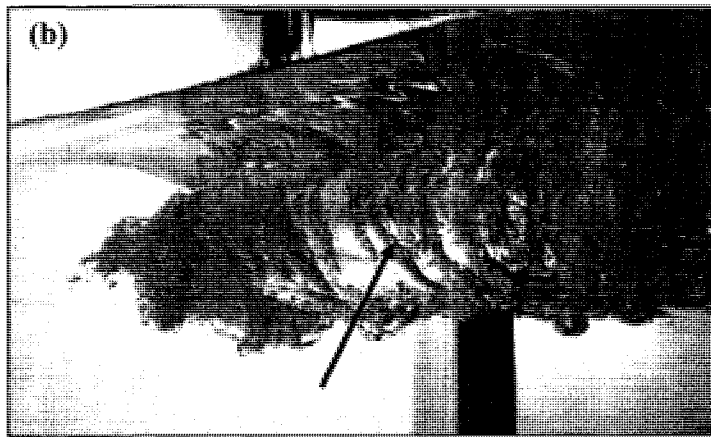
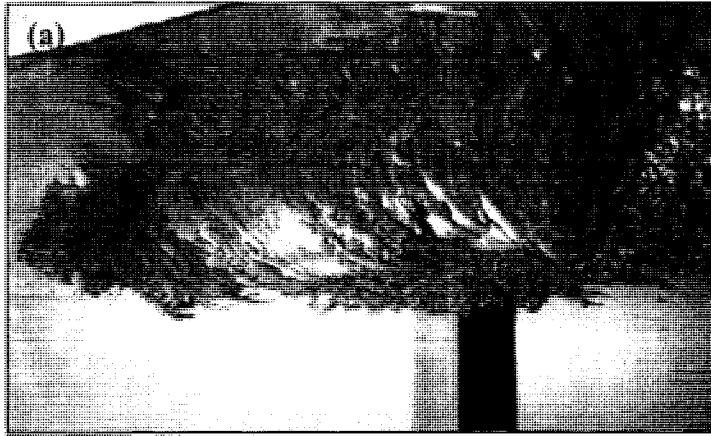


Fig. 3.14 Sequence of images showing the collapse of the air cavity under the plunging breaker. (a) $\hat{t} = 0.27$. (b) $\hat{t} = 0.33$. (c) $\hat{t} = 0.38$. The arrow in (b) points to an air filament.

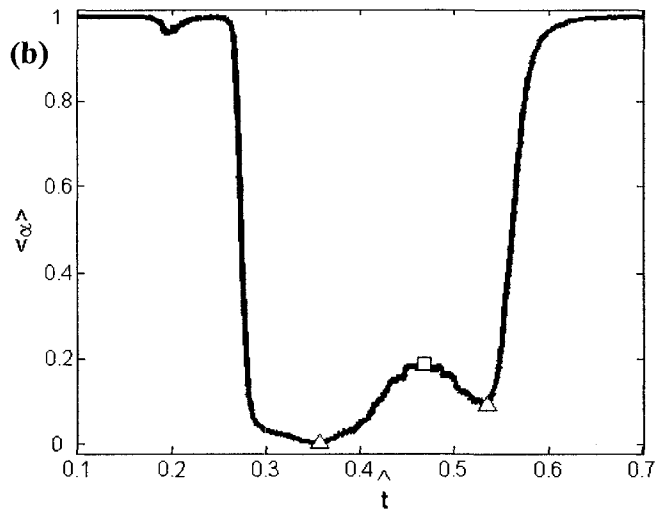
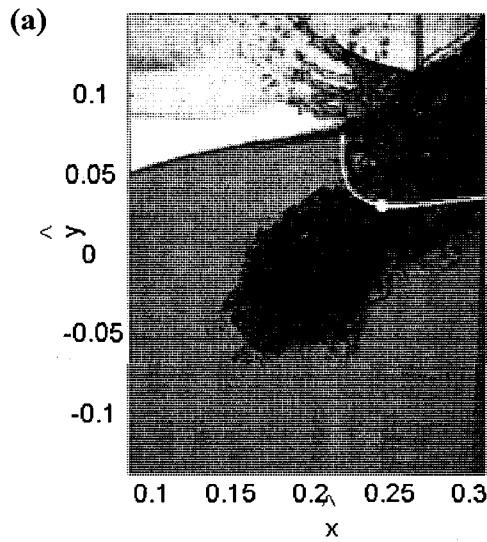


Fig. 3.15 (a) Image showing the instant when $\langle \alpha \rangle_{\max}$ occurred at position D under the plunging breaker. The white line is the approximate path of the fiber-optic when crossing the 1st bubble plume. (o) is the position of the fiber-optic probe tips. (b) Time series of $\langle \alpha \rangle$. (\square) indicates $\langle \alpha \rangle_{\max}$. The time interval between open triangles (Δ) is the interval of time used to compute $\bar{\alpha}$.

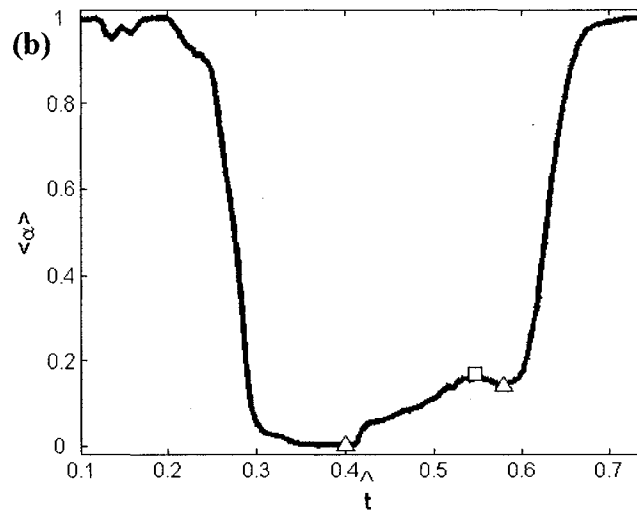
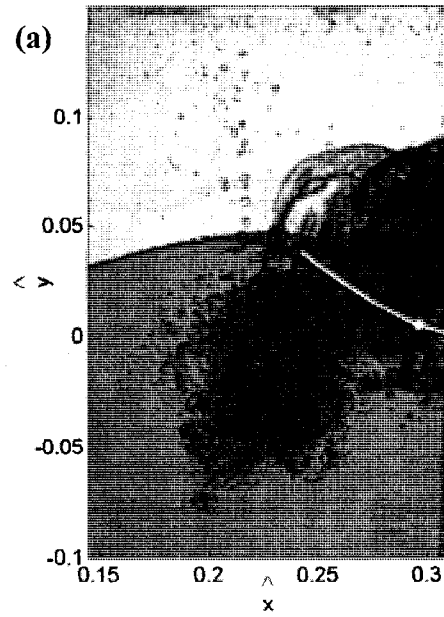


Fig. 3.16 (a) Image showing the instant when $\langle \alpha \rangle_{\max}$ occurred at position E under the plunging breaker. The white line is the approximate path of the fiber-optic when crossing the 1st bubble plume. (o) is the position of the fiber-optic probe tips. (b) Time series of $\langle \alpha \rangle$. (\square) indicates $\langle \alpha \rangle_{\max}$. The time interval between open triangles (Δ) is the interval of time used to compute $\bar{\alpha}$.

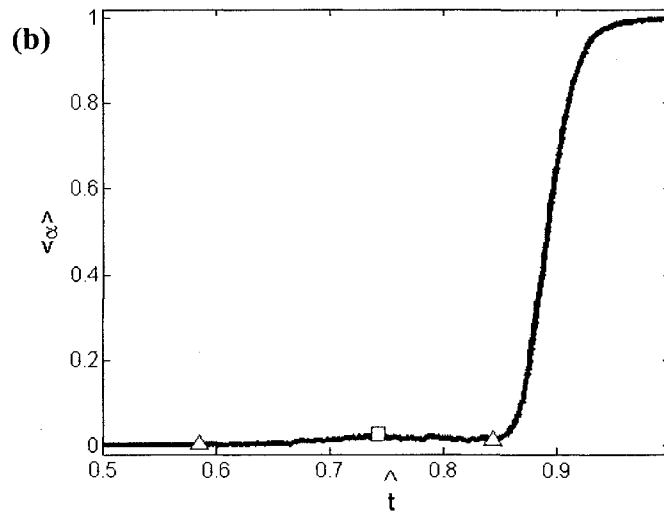
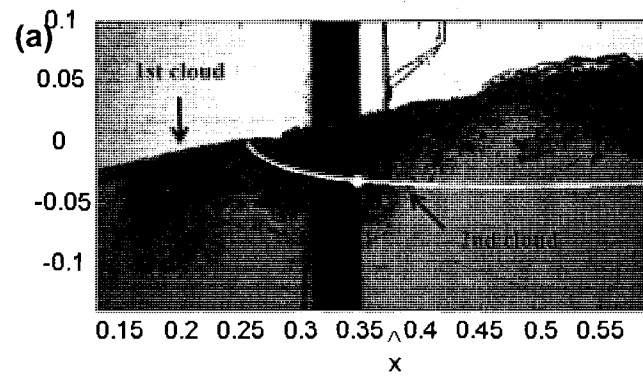


Fig. 3.17 (a) Image showing the instant when $\langle \alpha \rangle_{\max}$ occurred at position F under the plunging breaker. The white line is the approximate path of the fiber-optic when crossing the 2nd bubble plume. (o) is the position of the fiber-optic probe tips. (b) Time series of $\langle \alpha \rangle$. (\square) indicates $\langle \alpha \rangle_{\max}$. The time interval between open triangles (Δ) is the interval of time used to compute $\bar{\alpha}$.

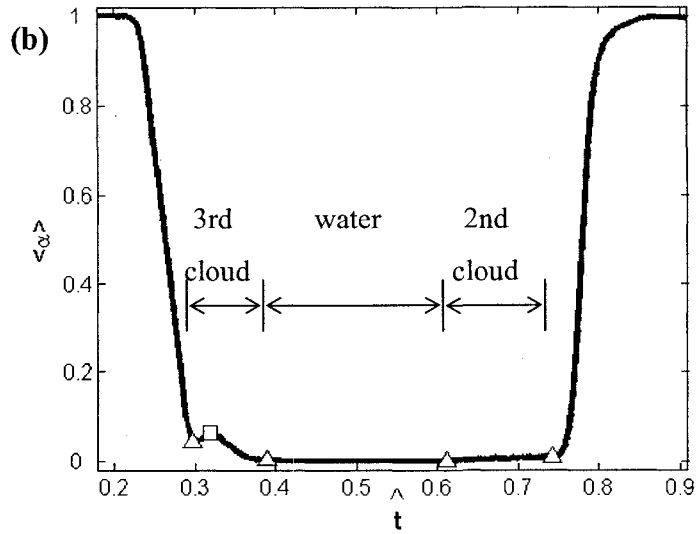
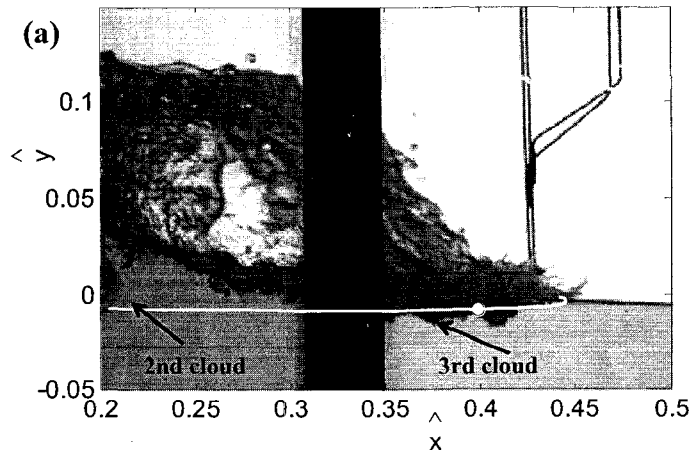


Fig. 3.18 (a) Image showing the instant when $\langle \alpha \rangle_{\max}$ occurred at position G under the plunging breaker. The white line is the approximate path of the fiber-optic when crossing first the 3rd bubble plume and then the 2nd bubble plume. (o) is the position of the fiber-optic probe tips. (b) Time series $\langle \alpha \rangle$. (\square) indicates $\langle \alpha \rangle_{\max}$. The time interval between open triangles (Δ) is the interval of time used to compute $\bar{\alpha}$.

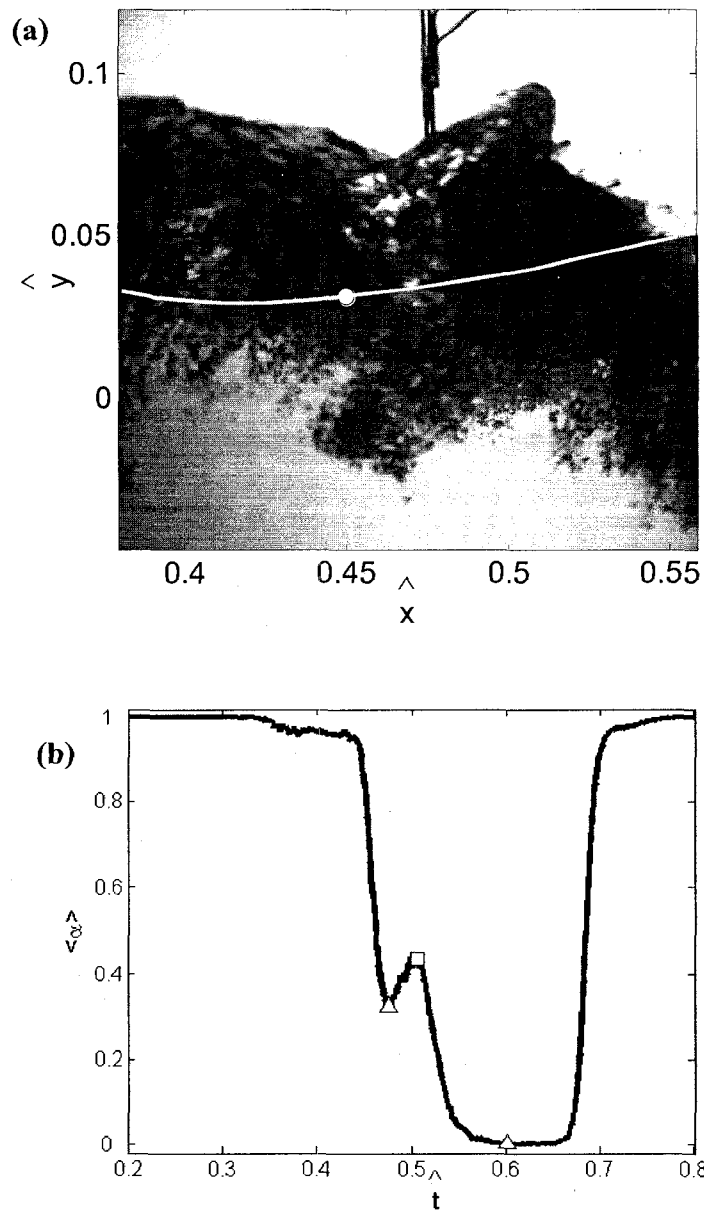


Fig. 3.19 (a) Image showing the instant when $\langle \alpha \rangle_{\max}$ occurred at position H under the plunging breaker. The white line is the approximate path of the fiber-optic when crossing the 3rd bubble plume. (o) is the position of the fiber-optic probe tips. (b) Time series of $\langle \alpha \rangle$. (\square) indicates $\langle \alpha \rangle_{\max}$. The time interval between open triangles (Δ) is the interval of time used to compute $\bar{\alpha}$.

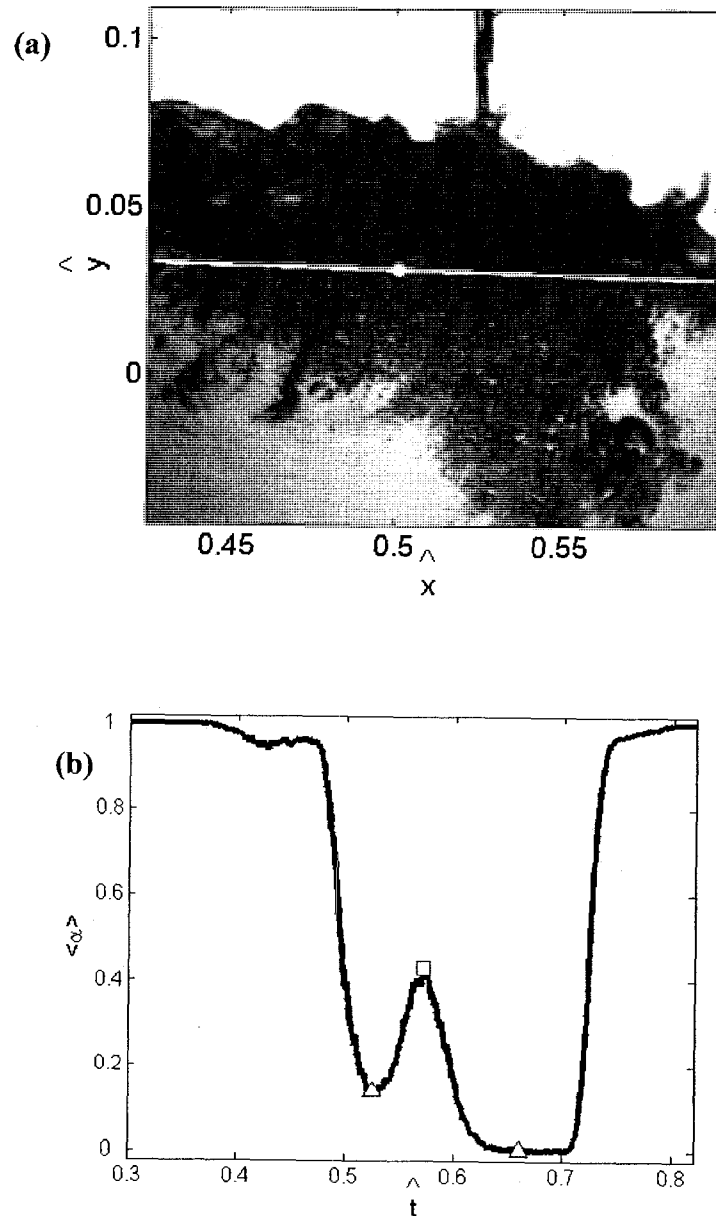


Fig. 3.20 (a) Image showing the instant when $\langle \alpha \rangle_{\max}$ occurred at position I under the plunging breaker. The white line is the approximate path of the fiber-optic when crossing the 3rd bubble plume. (o) is the position of the fiber-optic probe tips. (b) Time series of $\langle \alpha \rangle$. (\square) indicates $\langle \alpha \rangle_{\max}$. The time interval between open triangles (Δ) is the interval of time used to compute $\bar{\alpha}$.

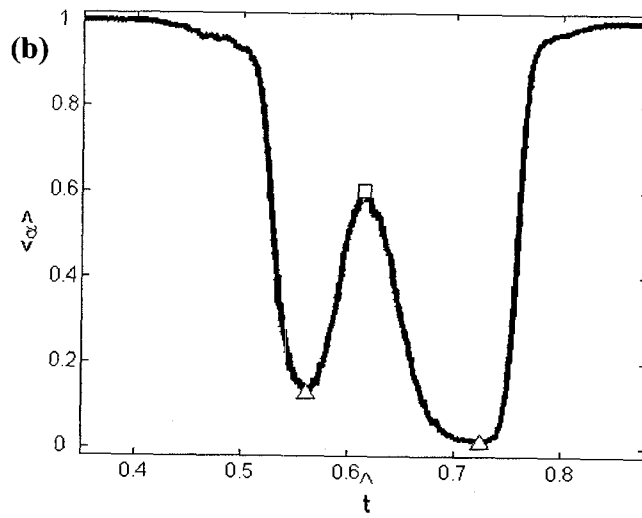
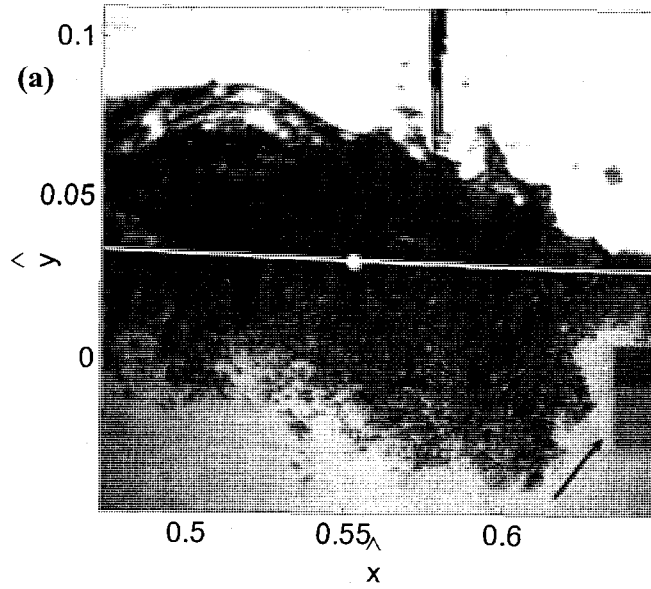


Fig. 3.21 (a) Image showing the instant when $\langle \alpha \rangle_{\max}$ occurred at position J under the plunging breaker. The white line is the approximate path of the fiber-optic when crossing the 3rd bubble plume. (o) is the position of the fiber-optic probe tips. The arrow points out a marker. (b) Time series of $\langle \alpha \rangle$. (\square) indicates $\langle \alpha \rangle_{\max}$. The time interval between open triangles (Δ) is the interval of time used to compute $\bar{\alpha}$.

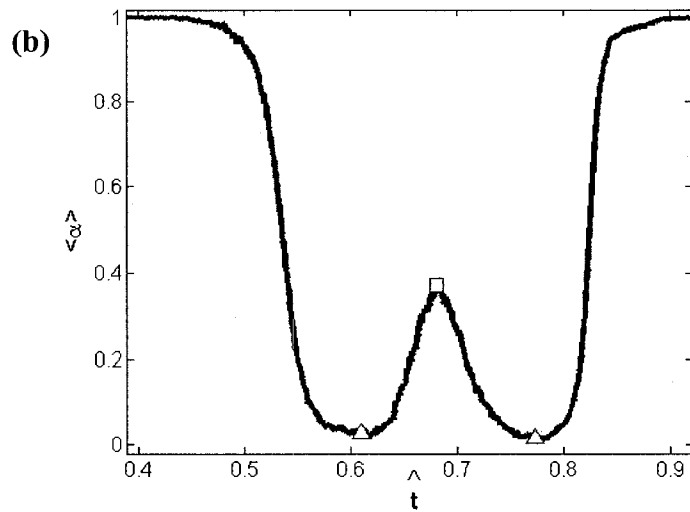
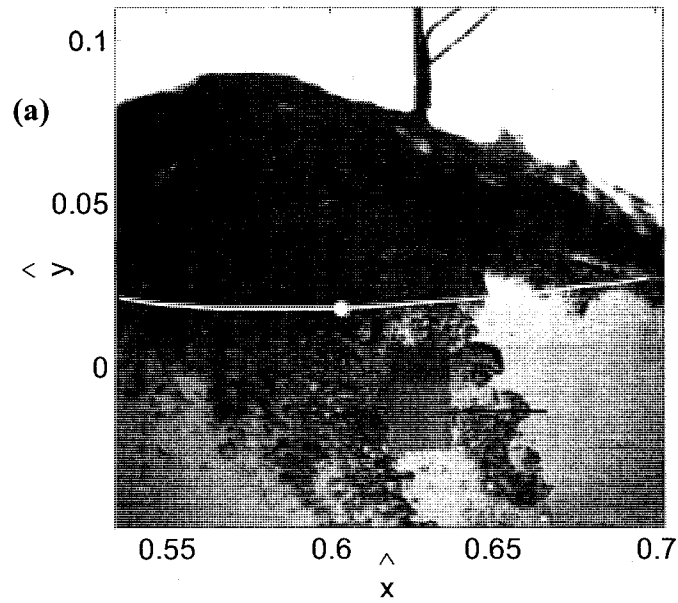


Fig. 3.22 (a) Image showing the instant when $\langle \alpha \rangle_{\max}$ occurred at position K under the plunging breaker. The white line is the approximate path of the fiber-optic when crossing the 3rd bubble plume. (o) is the position of the fiber-optic probe tips. The arrow points out a marker. (b) Time series of $\langle \alpha \rangle$. (\square) indicates $\langle \alpha \rangle_{\max}$. The time interval between open triangles (Δ) is the interval of time used to compute $\bar{\alpha}$.

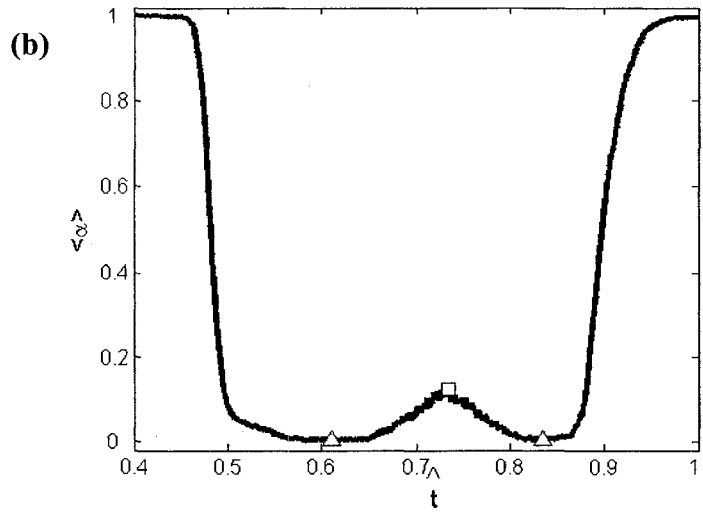
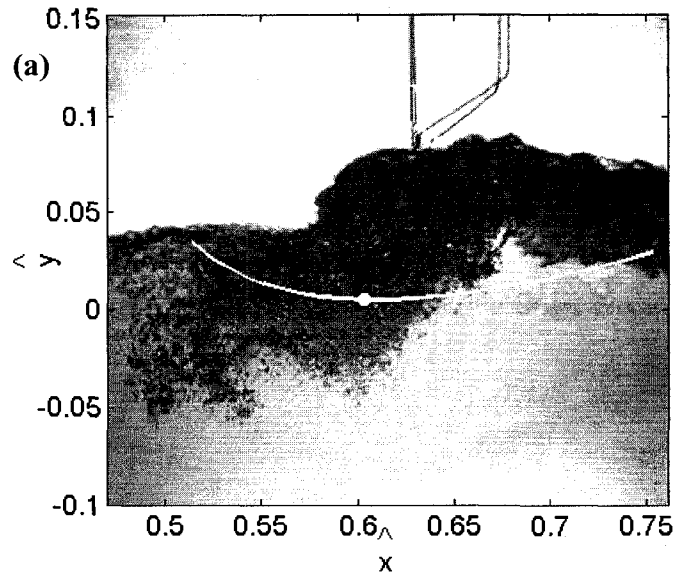


Fig. 3.23 (a) Image showing the instant when $\langle \alpha \rangle_{\max}$ occurred at position L under the plunging breaker. The white line is the approximate path of the fiber-optic when crossing the 3rd bubble plume. (o) is the position of the fiber-optic probe tips. (b) Time series of $\langle \alpha \rangle$. (\square) indicates $\langle \alpha \rangle_{\max}$. The time interval between open triangles (Δ) is the interval of time used to compute $\bar{\alpha}$.

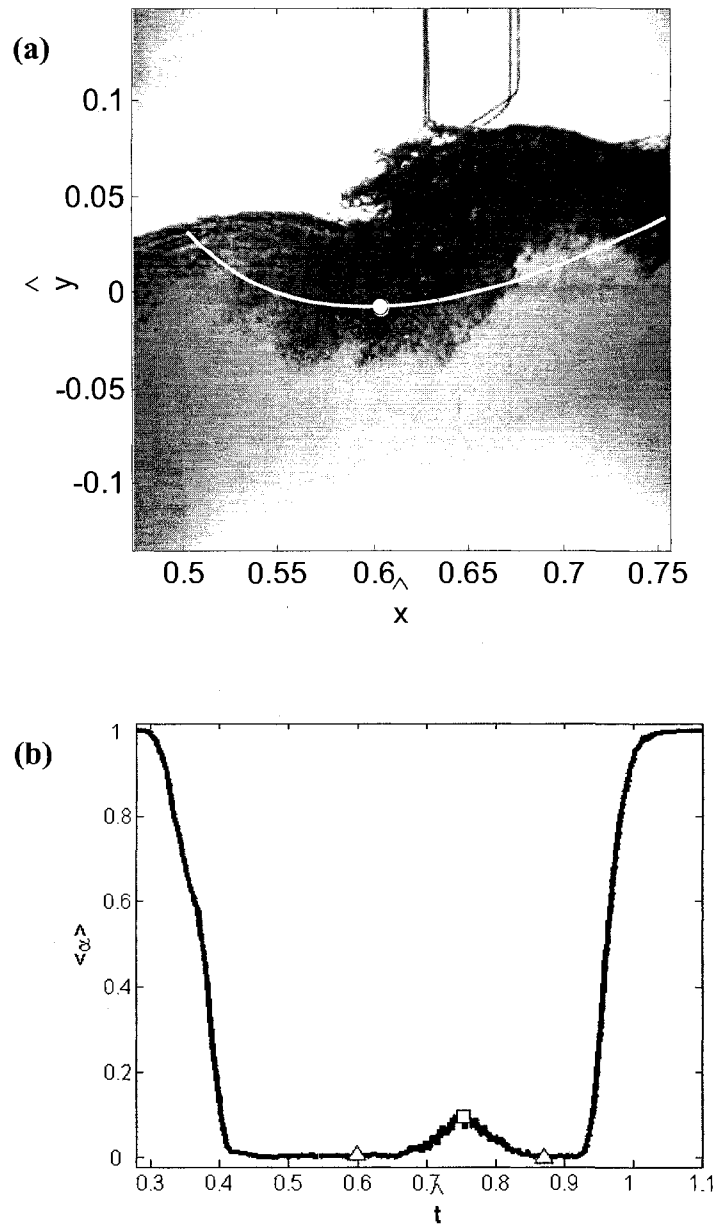


Fig. 3.24 (a) Image showing the instant when $\langle \alpha \rangle_{\max}$ occurred at position M under the plunging breaker. The white line is the approximate path of the fiber-optic when crossing the 3rd bubble plume. (o) is the position of the fiber-optic probe tips. (b) Time series of $\langle \alpha \rangle$. (\square) indicates $\langle \alpha \rangle_{\max}$. The time interval between open triangles (Δ) is the interval of time used to compute $\bar{\alpha}$.

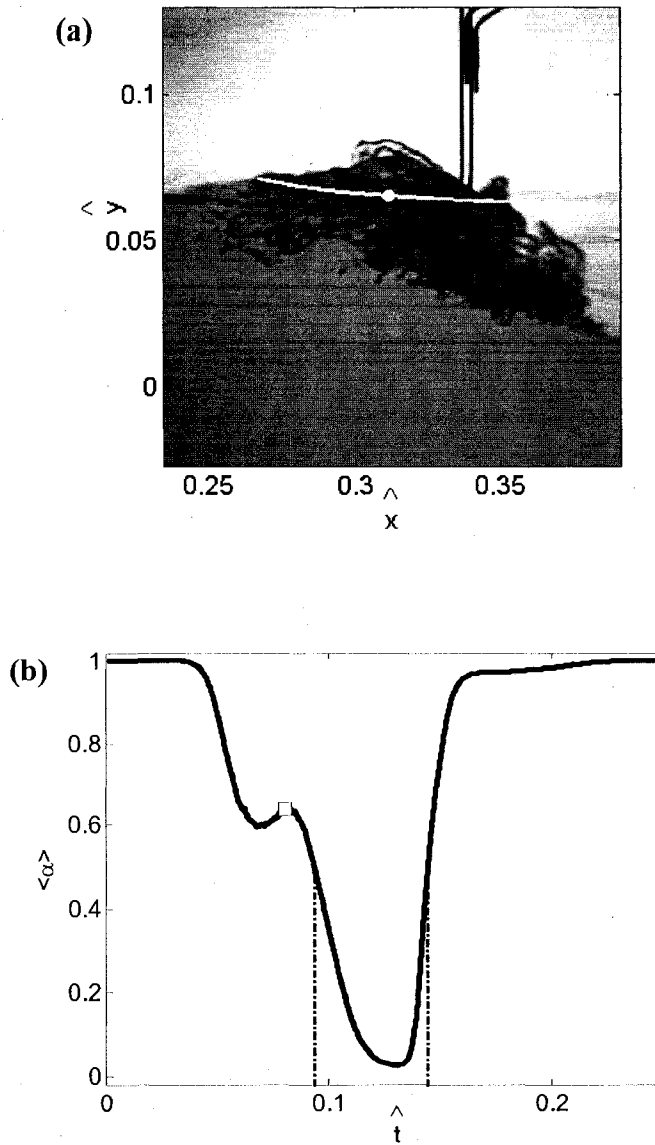


Fig. 3.25. (a) Image at position 21 under the spilling breaker. The white line is the approximate path of the fiber-optic when crossing the small air pocket. (o) is the position of the fiber-optic probe tips. (b) Time series of $\langle \alpha \rangle$. (- - - -) time interval used to compute the mean void fraction. (□) indicates frame time, $\hat{t} \sim 0.08$.

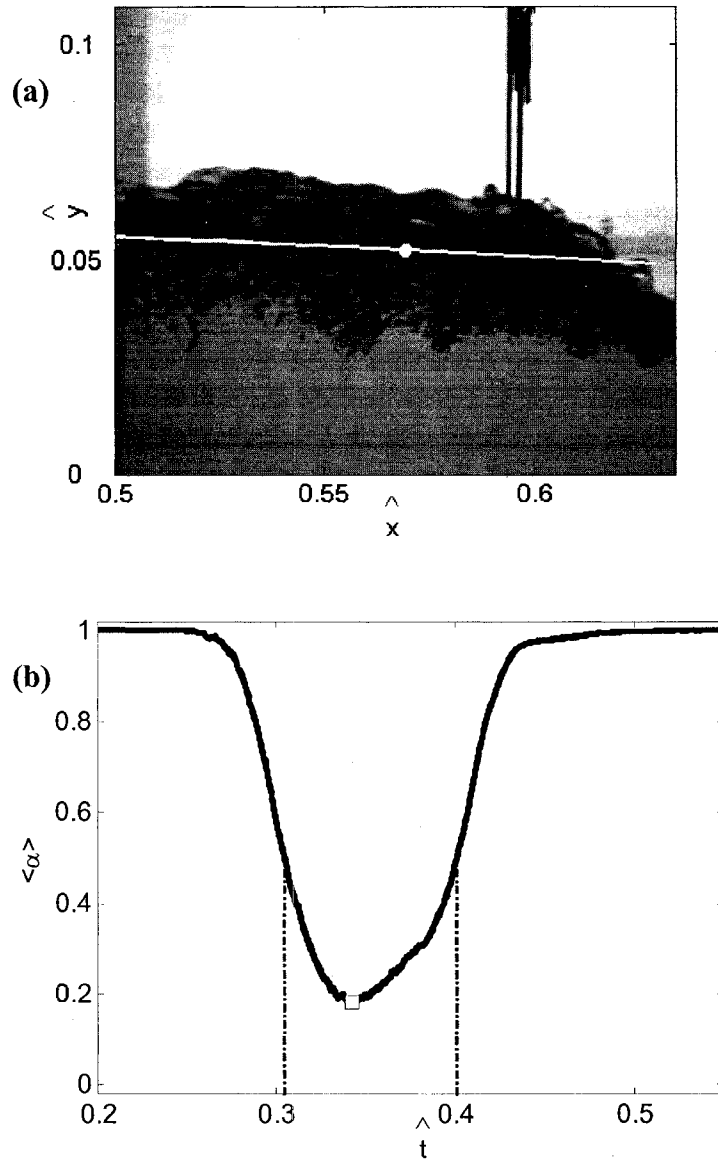


Fig. 3.26. (a) Image at position 23 under the spilling breaker. The white line is the approximate path of the fiber-optic when crossing the bubble cloud. (o) is the position of the fiber-optic probe tips. (b) Time series of $\langle \alpha \rangle$. (- - -) time interval used to compute the mean void fraction. (□) indicates frame time, $t \sim 0.34$.

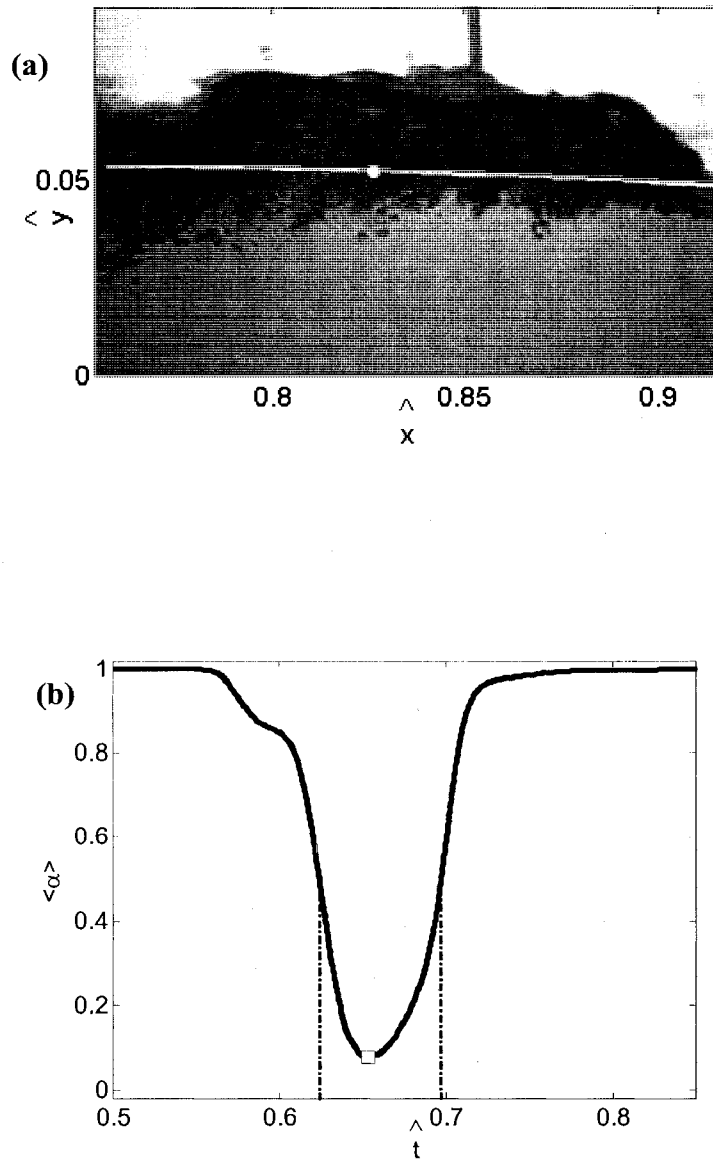


Fig. 3.27. (a) Image at position 38 under the spilling breaker. The white line is the approximate path of the fiber-optic when crossing the small air pocket. (o) is the position of the fiber-optic probe tips. (b) Time series of $\langle \alpha \rangle$. (- · - · -) time interval used to compute the mean void fraction. (\square) indicates frame time, $t \sim 0.65$.

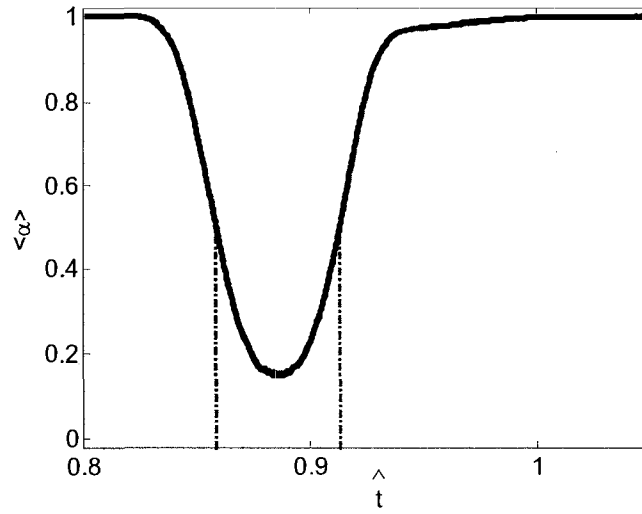


Fig. 3.28. Time series of $\langle \alpha \rangle$ at position 50 under the spilling breaker. (- · - · -) time interval used to compute the mean void fraction.

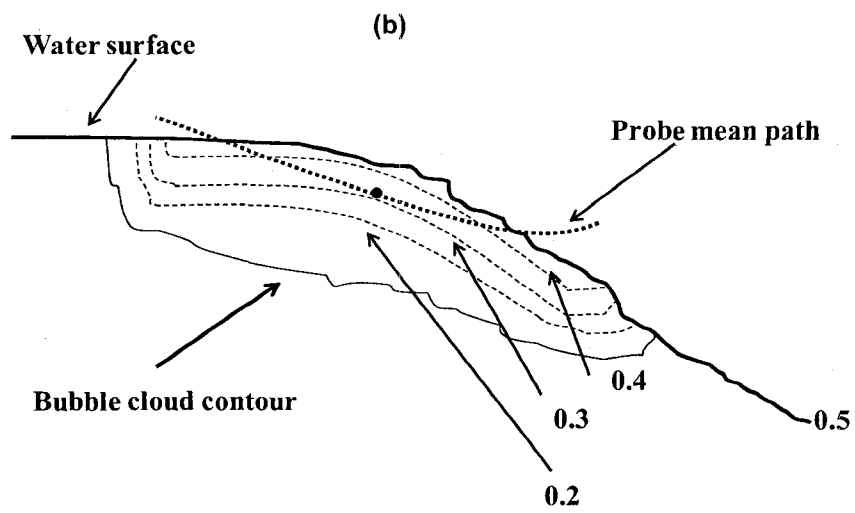
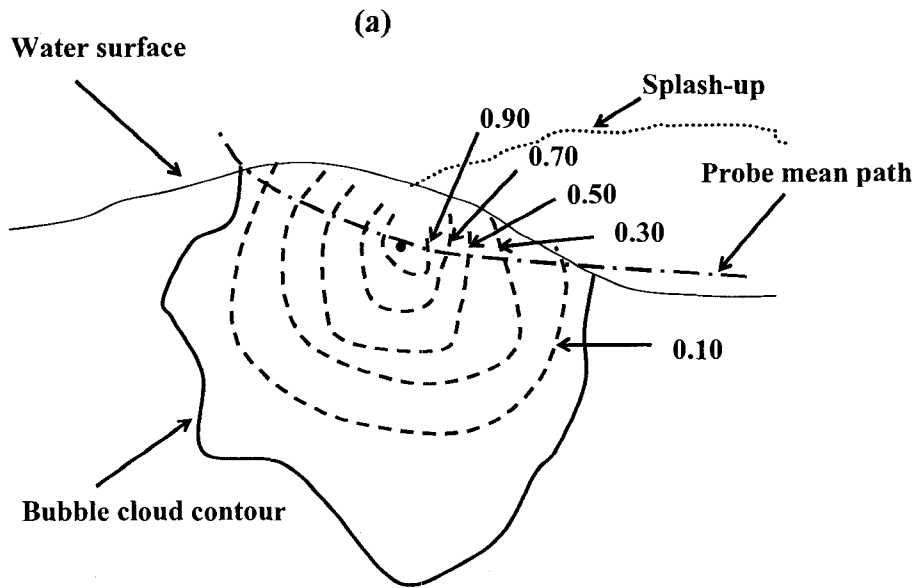


Fig. 3.29. Void fraction fields. (a) Plunging wave (b) Spilling wave

Table 3.1: Plunging wave measurement positions, number of repeat waves, and clouds.

\hat{x} is the dimensionless distance with respect to the breaking point. \hat{y} is the dimensionless depth with respect to the still water depth.

Position	\hat{x}	\hat{y}	# repeat waves ⁺	
A	0.04	0.03	2322	Air cavity
B	0.09	0.03	2132	Air cavity
C	0.14	0.03	3018	Air cavity
D	0.19	0.02	1722	1st cloud
E	0.25	0.01	3720	2nd cloud
F	0.30	-0.03	4920	2nd cloud
G	0.35	-0.01	4920	2nd cloud
H	0.40	0.03	2120	3rd cloud
I	0.45	0.03	2120	3rd cloud
J	0.50	0.03	2180	3rd cloud
K	0.56	0.02	2180	3rd cloud
L	0.56	0.01	2002	3rd cloud
M	0.56	-0.01	1130	3rd cloud

(+) This number is twice the number of repeated waves because two fiber-optic probes were used simultaneously

Table 3.2: Spilling wave wave measurement positions, number of repeat waves, and clouds. \hat{x} is the dimensionless distance with respect to the breaking point. \hat{y} is the dimensionless depth with respect to the still water depth.

Position	\hat{x}	\hat{y}	# repeat waves ⁺
21	0.31	0.07	12266
23	0.57	0.05	3096
38	0.83	0.05	11822
50	1.08	0.05	18952

(+) This number is twice the number of repeated waves because two fiber-optic probes were used simultaneously

Table 3.3: Plunging wave. \hat{t}_{\max} is the time when the maximum ensemble void fraction, $\langle \alpha \rangle_{\max}$ occurred. $\hat{t}_1 - \hat{t}_2$ is the lag time used to compute the mean void fraction, $\bar{\alpha}$.

Position	\hat{t}_{\max}	$\langle \alpha \rangle_{\max}$	$\hat{t}_1 - \hat{t}_2$	$\bar{\alpha}$	
A	0.18	0.96	0.15-0.29	0.33	Air cavity
B	0.25	0.95	0.21-0.35	0.37	Air cavity
C	0.32	0.89	0.27-0.35	0.29	Air cavity
D	0.47	0.18	0.36-0.53	0.11	1st cloud
E	0.55	0.17	0.40-0.58	0.10	2nd cloud
F	0.74	0.024	0.58-0.84	0.012	2nd cloud
G*	---	---	0.61-0.74	0.010	2nd cloud
G**	0.32	0.061	0.30-0.37	0.037	3rd cloud
H	0.51	0.43	0.47-0.60	0.18	3rd cloud
I	0.57	0.42	0.52-0.67	0.16	3rd cloud
J	0.61	0.60	0.56-0.73	0.26	3rd cloud
K	0.68	0.37	0.61-0.78	0.13	3rd cloud
L	0.73	0.12	0.61-0.84	0.043	3rd cloud
M	0.75	0.089	0.47-0.91	0.021	3rd cloud

Table 3.4: Spilling wave. $\hat{t}_1 - \hat{t}_2$ is the lag time used to compute the mean void fraction, $\bar{\alpha}$.

Position	$\hat{t}_1 - \hat{t}_2$	$\bar{\alpha}$
21	0.09-0.14	0.17
23	0.31-0.40	0.29
38	0.62-0.69	0.20
50	0.86-0.91	0.26

Chapter 4: Bubble Size Distribution Measurements under Breaking Waves

4.1 Introduction

At the air-sea interface different physical, chemical, and biological processes take place, including compound volatilization, air-sea gas transfer, and marine aerosol formation. These processes are influenced by the dense clouds of bubbles entrained by deep-water breaking waves (Liss et al., 1997; Farmer et al., 1993; Wallace and Wirrick, 1992; Blanchard and Woodcock, 1957). This is a complex two phase flow, in which the entrained bubble sizes range between tens of micro meters to centimetres (Monahan, 1986; Haines and Johnson, 1995). Large bubbles (transient bubbles) quickly rise back to the surface, leaving a degassed plume composed of a diffuse cloud of microbubbles (background bubbles) which have small rise velocities and are easily advected by currents, (Loewen, et al., 1996). The most important characteristic of these bubble clouds is the bubble size distribution (Deane and Stokes, 2002).

Previous measurements have indicated that the bubble size distribution can be described using a power law equation given by,

$$N = C * s^{-\beta} \quad (4.1)$$

where N is the number of bubbles, C is a constant; β is the slope of the size distribution, and s is the bubble cord length (Bezzabotnov et al., 1991). Leifer et al. (2006b) reviewed 15 reported oceanic and laboratory background bubble measurements. Even though the size distributions showed enormous variability, they suggested that the size distributions showed a power law dependency with slopes in the range $1.8 < \beta < 5$. The sources of variability for the measurements performed in the open ocean were attributed to

differences in water temperature and chemistry, wave development, measuring technique, and location and timing of the measurements. However the eldest bubble size distribution measurements, performed in the open ocean, showed smaller variability in the slope and β was in the range 4.0 to 4.7 (Blanchard and Woodcock, 1957; Kolovayev, 1976; Johnson and Cooke, 1979).

There are only few studies in which the size distributions of the large-transient bubbles generated underneath oceanic breaking waves have been measured. Bezzabotnov, et al. (1991) used a photographic technique and measured the size distributions generated by whitecaps formed as a result of breaking oceanic wind waves. For the transient bubbles larger than 0.4 mm, they reported that the slope β varied from 1 – 1.5. Bowyer (2001) measured the large-transient bubble population near the surface (10 to 20 cm depth) by attaching a video camera to a surface following float. For bubbles created beneath open sea and freshwater breaking waves, he reported slopes in the range $1 < \beta < 2$, for large-transient bubbles having sizes, $r > 0.5$ mm. Deane and Stokes (1999, 2002) used a video technique to measure the size distributions beneath breaking waves in a laboratory flume (filled with seawater) and in the open ocean. In both cases, they found a change in the size distribution slope at $r \sim 1.0$ mm. and two slopes, 1.5 and 10/3 for bubbles smaller and larger than this critical radius. The critical radius is defined as the bubble radius where the slope of the size distribution changes significantly. For the laboratory waves, they defined the initial large-transient bubble size distribution as the distribution measured within the first 1.0 s after the breaking had occurred. During this interval of time, large-transient bubbles are entrained and fragmented inside the breaking wave crest of a plunging wave. In the laboratory they also observed size distributions

having critical radii $\sim 1.0 \text{ mm}$, and slopes of $\beta \sim 1.5$. They argued that bubbles smaller than the critical radii were stabilized by surface tension. In addition they proposed that bubbles larger than this critical size were subject to fragmentation by turbulent flow; producing a size distribution with a slope of $\beta \sim 10/3$. Therefore, they identified the critical size as the Hinze scale which is given by,

$$a_H = 2^{-8/5} \varepsilon^{-2/5} (\gamma We_c / \rho)^{3/5} \quad (4.2)$$

where a_H is the Hinze scale, ε is the rate of dissipation of turbulent kinetic energy, γ is the surface tension, We_c is the critical Weber number, and ρ is the water density.

Cipriano and Blanchard (1981) simulated the air entrainment mechanism by plunging waves using a continuous seawater waterfall. They used a photographic technique and measured a slope, $\beta \sim 1.5$ for large-transient bubbles as large as 10 mm . Similarly, Bowyer (1992) analyzed the bubbles generated when a volume of 500 cc of salt water was dropped 1.07 m into a water-filled basin. Using a video technique, he found a slope, $\beta \sim 1.5$ for large-transient rising bubbles in the radius range $0.3\text{--}1.6 \text{ mm}$, produced by the splash-up process. Haines and Johnson (1995) simulated a plunging breaker using a tipping bucket. They reported $\beta \sim 2.7$ for fresh water bubbles, larger than $s \sim 2.6 \text{ mm}$.

Baldy and Bourguel (1987) and Baldy (1988), using a laser technique to measure bubble size distributions in freshwater (underneath laboratory wind waves), reported that β varied from 2 to 4. Hwang, et al. (1990) used an optical technique to measure the size distribution of the bubbles entrained underneath laboratory wind waves in freshwater. They observed a slope, $\beta \sim 2.0$ for measurements performed close to the free surface. Leifer and de Leeuw (2006a) and Leifer et al. (2007) studied bubble plumes entrained

beneath mechanically generated breaking waves stressed by wind using an imaging technique. For large-transient bubbles created in freshwater, they reported bubble size distributions that had a change in slope at a radius, $r \sim 1.7$ to 2.0 mm. For bubbles in the range $r \sim 1.0$ to 1.8 mm, they reported a slope, $\beta \sim 0.9$; and for bubbles larger than $r \sim 2.2$ mm, they reported a slope, $\beta \sim 2.8$.

Loewen, et al. (1996) using a video technique, measured large-transient bubble size distributions entrained underneath gently mechanically generated spilling laboratory waves and found $\beta \sim 3.7$ which was approximately the same in freshwater and saltwater. Kalvoda, et al. (2003) performed a series of experiments in freshwater on bubble clouds produced by laboratory-breaking wind-waves. Using a video technique, they measured a slope, $\beta \sim 2.0$ for large-transient bubble in the size range $0.5 < r < 2.5$ mm and $\beta \sim 3.7$ for larger bubbles.

Baldy (1993) theorized that β should have a value of 2 in the close vicinity of breaking waves, for large-transient bubbles as large as 3.0 mm in diameter, based on the assumption that the rate of large bubble generation is only function of the turbulent dissipation rate, and bubble formation energy. Garret et al. (2000) theorized that the fragmentation of larger bubbles into smaller ones was a consequence of turbulent shear flow and concluded that $\beta \sim 10/3$. In their study, the rate of bubble generation was a function of the turbulent dissipation rate, and the average rate of supply of air to a given volume. Recently, Han and Yan (2007) proposed a bubble size spectrum model based on the turbulent kinetic energy spectral density instead of the turbulent kinetic energy dissipation rate, and obtained a slope, $\beta \sim 2.0$.

A better understanding of the connection between the void fraction and bubble size distribution is still needed for engineering applications and mathematical modelling (Mori, 2007). Moreover, numerical models of the air entrainment process underneath breaking waves still require measurements of local bubble size distributions of transient bubbles (Leifer et al., 2006a). For these reasons, the purpose of this study was to investigate the characteristics and evolution of the size distribution of large-transient bubbles beneath plunging and spilling breaking waves; and to relate these distributions with the mean void fraction measurements for bubbles created within the first wave period following breaking. We performed measurements at different positions along plunging and spilling waves and we were able to quantify several changes in the size distribution of bubbles. Preliminary results from these experiments have been presented by Rojas and Loewen (2007b).

4.2 Experimental procedures

Bubble size distribution and void fraction measurements were taken simultaneously and a complete description of the experimental set up and procedures was presented in Chapter 3. In summary, laboratory plunging and spilling waves were generated using a dispersive wave packet. Two fiber-optic probes were used to measure the void fraction and the bubble sizes inside the transient bubble clouds generated beneath breaking waves. Detailed measurements were made at 13 and 4 positions along the plunging and spilling waves, respectively. This was accomplished by repeating the breaking wave thousands of times (Table 4.1 and Table 4.2).

The full description on how the fiber-optic probes were used to estimate bubble cord length was presented in Chapter 2. In summary, when a bubble crosses the tip of a

fiber-optic probe, a voltage pulse is produced, Fig. 4.1. This voltage pulse has four characteristic points, labelled t_A , t_B , t_C , and t_D . If the average voltage, between point t_A and t_B (this interval of time is called the bubble residence time, T_g), is higher than a threshold voltage; if the slope of the voltage signal, between points t_C and t_D (this interval of time is called the rise time, T_R), is higher than a threshold slope; and if the standard deviation of the voltage signal, between point t_D and t_B , is lower than a threshold voltage, this voltage pulse is defined as a good bubble signature, Fig. 4.1a; otherwise is defined as a bad bubble signature, Fig. 4.1b. Using a good bubble signature, the bubble velocity can be estimated (Cartellier, 1992; Sedula and Loewen, 1998; Elkamash et. al., 2005; Rojas and Loewen, 2007), using the following equation,

$$v_B = 10^b T_R^m \quad (4.3)$$

where, v_B is the bubble velocity (cm/s), T_R is the rise time (ms); and b and m are constants. Once the bubble velocity is known, the bubble cord length, s , can be estimated,

$$s = V \cdot T_g \quad (4.4)$$

where s is the cord length (cm); V is the bubble velocity (cm/s); and T_g is the bubble residence time (ms).

Data Analysis

The minimum bubble size that the fiber-optic probes were able to measure is $s \sim 0.7 \text{ mm}$ (minimum size used in the estimation of the bubble size distribution), and the total number of detected bubbles, listed as # of bubbles in Table 4.1 and 4.2, only includes bubbles in the size $0.7 < s < 20 \text{ mm}$. The cord length, s , is a measure of the size of the crossing bubble and if these bubbles are assumed to be spherical, the bubble equivalent diameter is on average $1.5 s$. (Saberri et al., 1995). However, if the bubbles are

assumed to be oblate ellipsoids, then the measured cord length multiplied by 1.5 gives an estimate of the average bubble minor axis. As discussed in Chapter 2, in this study we did not examine the issue of bubble shape because the fiber-optic probes do not provide any information about bubble shape. This information could be obtained using another technique such as digital video.

Bubbles that were detected within the interval of time used to compute the mean void fraction (Chapter 3) were included in the bubble size distribution analysis. This procedure was adopted to ensure that only mixtures comprised of bubbles entrained in water and not mixtures comprised of water droplets in air were analyzed. At positions A, B, and C the procedure for selecting the time interval was modified slightly. At these measurement positions the fiber-optic probes cut through the air cavity, and at these times it was difficult to distinguish if the bubbles were being detected or if water drops inside the air cavity were being detected. Note that the fiber-optic probe voltage signals are essentially the same when bubbles cross the tip or when the tip traverses the void space between two water drops. Therefore, for measurements at positions A, B, and C, only bubbles that were detected when the ensemble void fraction, $\langle \alpha \rangle$, was less than 0.50 were included in the size distributions. Fig. 4.2a-b displays the ensemble void fraction ($\langle \alpha \rangle$) and the frequency of bubble arrival at the probe's tip (F_a) at position A, respectively. At this position, the detected bubbles were located in the downstream side of the air cavity, i.e. after the peak $\langle \alpha \rangle$ was detected. Fig. 4.2 c-f displays plots of the same data for positions B and C. At these two positions, a higher number of bubbles were detected on the upstream side of the air cavity (before the peak $\langle \alpha \rangle$ was detected) than on the downstream side (after the peak $\langle \alpha \rangle$ was detected).

After each breaking wave (i^{th} wave), the instantaneous bubble size histogram was computed using bins centered at, e.g. $j = 1.0, 1.6, 2.2, 2.8, 3.7, 4.9, 6.6, 8.4, 10.5, 13.5, 16.5,$ and 19.5 mm . The bin sizes become progressively larger with bubble size to account for the fact that there are a much fewer larger bubbles. The number of bubbles detected in each bin was then divided by the corresponding bin size (in μm). These histograms were defined as $N_i(j)$, the number of bubbles per μm cord length increment in size bin j , detected beneath the i^{th} wave. The breaking wave was repeated N_R times and the average bubble bin size distribution was computed giving $N(j)$, the average number of bubbles detected per μm cord length per wave.

At each measurement position, the 0 and 90° size distributions were computed. Fig. 4.3a-b displays the size distribution measured at position D (1st cloud, plunging wave) and at position 50 (spilling wave), respectively. In each case, it was clear that the two size distributions were similar for bubbles smaller than $s \sim 10 \text{ mm}$. The flow produced underneath breaking waves is not unidirectional; and the angle at which the probes crossed the bubble cloud may be different from 0 or 90° . As discussed in Chapter 2, the analysis of the images indicated that the maximum angle at which the fiber-optic probes crossed the bubble cloud was $\varphi \sim \pm 30^\circ$ with respect to the horizontal, except for position D where the approximate probe path indicated that the probes crossed the rear edge of the cloud at an angle $\sim 90^\circ$ with respect to the fiber-optic probe axis, Fig. 3.13a. However, at position D, the 0 and 90° size distributions were not statistically different, Fig. 4.3a. Therefore, because on average φ was closer to 0° than to 90° , all of the subsequent bubble size analysis uses bubble cord length distributions measured at 0° .

The accuracy of the size distribution measurements was estimated by first computing each $N(j)$'s standard deviation, σ_{Nj} . The normalized standard error on $N(j)$, ε_{NE} , was then computed as,

$$\varepsilon_{NE} = \frac{\sigma_{Nj}}{N(j) * N_R^{0.5}} \quad (4.5)$$

where N_R is the number of repeated breaking waves. By averaging these errors at each position, it was determined that ε_{NE} were $\sim \pm 0.30$, ± 0.18 , and ± 0.10 , for the air cavity, the 1st and 2nd clouds, and the 3rd cloud, respectively. For the spilling wave case, ε_{NE} was $\sim \pm 0.01$. These errors are comparable to errors reported in previous experiments (Deane and Stokes, 2002; Loewen et al., 1996).

At each location, the measured size distribution data was fitted to equation 4.1 using least-square linear regression analysis. If a critical size (i.e., a change in slope) was visible in a given size distribution, two regression lines which intersected at this critical size, were fitted to the data. Following this the critical size was varied by ± 1 mm and two new regressions lines were fitted to the data. The critical size that produced the lowest uncertainty in the slope (in terms of the 95% confidence level) was selected as the final value for s_c . However, if the two slopes were not statistically independent at the 95% confidence level, then the size distribution was represented by a single regression line for bubbles in the range $0.7 < s < 10$ mm.

4.3 Results

The air entrained by the air cavity was studied at positions A, B, and C shown in Fig. 4.4a, 4.5a and 4.6a. Fig. 4.4b displays the size distribution at position A where only 39 bubbles were detected. The linear regression analysis indicated a slope $\beta \sim 0.89$. Fig.

4.5b displays the size distribution at position B where 553 bubbles were detected. Initially, the linear regression was performed for bubbles in the size range $1.0 < s < 7.0$ mm. However, this slope was not statistically different from the slope obtained when bubbles in the size range $1.0 < s < 20.0$ mm were used in the linear regression analysis. Using this size range, it was measured a slope $\beta \sim 0.38$ which is not statistically different from zero. Fig. 4.6b displays the size distribution at position C (C* in Table 4.1) where 925 bubbles were detected. At this location, the size distribution was independent from the bubble size, i.e. $\beta \sim 0.00$.

Fig. 4.7 displays the size distribution of the 1st cloud, sampled at position C (C** in Table 4.1), for the time interval $0.35 < \hat{t} < 0.42$. The initial time, $\hat{t} = 0.35$, was determined from the video analysis which indicated that the air cavity had collapsed by this time (Fig. 3.14). There were 170 detected bubbles at this location, and the linear regression analysis indicated $\beta \sim 1.24$, for bubbles as large as $s \sim 20$ mm. The 1st cloud was studied at position D (Fig. 4.8a) where 2876 bubbles were detected. The size distribution had a critical size at $s_c \sim 7.0$ mm, Fig 4.8b. For bubbles smaller than s_c the slope was $\beta \sim 0.91$ and for bubbles larger than s_c the slope was $\beta \sim 2.36$. These two slopes are statistically different at the 95% confidence level.

The 2nd cloud was sampled at positions E, F, and G shown in Fig. 4.9a, 4.10a, and 4.11a. Fig. 4.9b displays the size distribution measured at position E. There were 2847 detected bubbles and s_c occurred at ~ 6.5 mm, similar to the results at position D in the 1st cloud. The slopes were $\beta \sim 1.08$ and ~ 2.73 , for bubbles smaller and larger than s_c , respectively. These two slopes were not statistically different. Fig. 4.10b displays

the size distribution measured at position F. There were 1097 detected bubbles and the size distribution had a s_c of ~ 3.0 mm. The slopes were $\beta \sim 1.14$ and ~ 3.77 , for bubbles smaller and larger than s_c , respectively. Fig. 4.11b displays the size distribution measured at position G (G*) in Table 4.1). Note that at position G, digital video recordings showed that the probes first traversed the 3rd cloud and then the 2nd cloud. There were 343 detected bubbles and the size distribution indicated that a critical size occurred at $s_c \sim 2.8$ mm, and the slopes for bubbles smaller and larger than this critical size were $\beta \sim 0.93$ and ~ 4.91 , respectively.

The 3rd cloud was sampled at positions G to K shown in Fig. 4.12a, 4.13a, 4.14a, 4.15a and 4.16a. Fig. 4.12b displays the size distribution measured at position G (G** in Table 4.1). Based on video analysis it was determined that this cloud arrived at the tip of the probes at $\hat{t} \sim 0.30$. There were 681 detected bubbles and the slope of the size distribution was $\beta \sim 1.42$. Fig. 4.13b displays the size distribution measured at position H. There were 6195 detected bubbles and the size distribution indicated that a critical size occurred at $s_c \sim 10$ mm. The slopes for bubbles smaller and larger than s_c were $\beta \sim 1.38$ and ~ 3.35 , respectively. Fig. 4.14b displays the size distribution measured at position I. There were 6847 detected bubbles and the size distribution indicated that a critical size occurred at $s_c \sim 10$ mm. The slopes for bubbles smaller and larger than s_c were $\beta \sim 1.49$ and ~ 3.56 , respectively. Fig. 4.15b displays the size distribution measured at position J. There were 7583 detected bubbles and the size distribution indicated that a critical size occurred at $s_c \sim 10$ mm; also, the slopes for bubbles smaller and larger than s_c were $\beta \sim 1.27$ and ~ 2.43 , respectively. Fig. 4.16b displays the size distribution measured at

position K. There were 6536 detected bubbles and the size distribution indicated that a critical size occurred at $s_c \sim 10 \text{ mm}$. The slopes for bubbles smaller and larger than s_c were $\beta \sim 1.51$ and ~ 3.21 , respectively.

The variations of the bubble size distribution as a function of depth were studied at positions K, L, and M (Fig. 4.16a, 4.17a and 4.18a) which were located in the splashing zone, also known as the 3rd cloud. Fig. 4.17b displays the size distribution measured at position L. There were 4155 detected bubbles and the measurements indicated that $s_c \sim 2.2 \text{ mm}$. The slopes for bubbles smaller and larger than s_c were $\beta \sim 1.31$ and ~ 2.73 , respectively. Fig. 4.18b displays the size distribution measured at position M. There were 1866 detected bubbles and the measurements indicated that $s_c \sim 2.2 \text{ mm}$. The slopes for bubbles smaller and larger than s_c were $\beta \sim 1.36$ and ~ 3.44 , respectively. Note that at positions L and M, the size distribution slopes for bubbles smaller than s_c , were not statistical different.

The spilling wave was sampled at positions 21, 23, 38, and 50. Images of the probes crossing the bubble cloud are displayed in Fig. 4.19a, 4.20a and 4.21a for positions 21, 23, and 38, respectively. Fig. 4.19b displays the size distribution measured at position 21 where 641 bubbles were detected. The size distribution had a $s_c \sim 8.0 \text{ mm}$ and the slopes were $\beta \sim 0.51$ and ~ 5.46 for bubbles smaller and larger than s_c , respectively. These two slopes were not statistically different. Fig. 4.20b displays the size distribution measured at position 23 where 5288 bubbles were detected. The size distribution had a $s_c \sim 2.5 \text{ mm}$ and the slopes were $\beta \sim 0.95$ and ~ 1.85 for bubbles smaller and larger than s_c , respectively. Fig. 4.21b displays the size distribution

measured at position 38 where 3760 bubbles were detected. The size distribution had a $s_c \sim 2.8 \text{ mm}$ and the slopes were $\beta \sim 0.34$ and ~ 1.93 for bubbles smaller and larger than s_c , respectively. Fig. 4.22 displays the size distribution measured at position 50 where 7872 bubbles were detected. The size distribution had a $s_c \sim 3.0 \text{ mm}$ and the slopes were $\beta \sim 0.39$ and ~ 1.57 for bubbles smaller and larger than s_c , respectively. At positions 38 and 50 the slope of the size distribution increased at for $s > 10 \text{ mm}$ and therefore, only data for $s < 10 \text{ mm}$ was used when fitting the regression lines.

4.4 Discussion

Bubble size distributions in the air cavity were sampled at positions A, B, and C. Bubbles at position A were detected at the back side of the cavity of air, Fig. 4.2b. The vast majority of bubbles at positions B and C were detected at the front side of the air cavity, Fig. 4.2d and 4.2f, respectively. The average slope of the size distribution at the air cavity air (i.e. average of positions A, B, and C) was $\beta \sim 0.25 \pm 0.31$ (plot not shown), which means that N was independent of s . Note that the size distributions measured at positions B and C likely contain some data that resulted from the detection of air “filaments” rather than bubbles. These air filaments were first identified by Deane and Stokes (2002) and a video image of them beneath the plunging wave is displayed in Fig. 4.23.

Following the collapsing of the air cavity, two bubble clouds were created. The bubble size distribution at position D was created by the collapse of the air cavity, and the size distribution measured at position E was created by the jet and drop impact, simultaneously. Measurements at position D (corresponding to the 1st cloud at the time

interval $0.36 < \hat{t} < 0.53$) and at position E (corresponding to the 2nd cloud at the time interval $0.40 < \hat{t} < 0.58$) had similar β , s_c , and sampling time interval. This would indicate that the bubble size distribution is independent from the bubble creation mechanisms. In both cases, the slopes are not statistically different from the slopes measured by Bowyer (2001) in the oceanic sea and freshwater measurements.

Fig. 4.24 displays the averaged size distribution measured at positions F and G (G* in Table 4.1). At these two positions in the 2nd cloud, they had similar size distribution shape, similar s_c , and similar sampling time interval. The average size distribution has a $s_c \sim 2.5 \text{ mm}$ and slopes of $\beta = 1.01 \pm 0.47$ and 3.43 ± 0.47 for bubbles smaller and larger than s_c , respectively. These two slopes were not statistically different from the slopes reported by Deane and Stokes (2002), $\beta = 1.5$ and $10/3$ for bubbles smaller and larger than a critical radius $\sim 1.0 \text{ mm}$. A s_c value of 2.5 mm converts to a radius of $r \sim 1.9 \text{ mm}$, assuming that the bubble shape is spherical.

The measurements of the bubble size distributions in the splash-up zone, positions H to K were similar and the size distribution of the 3rd cloud can be well represented by a single regression line, having an average slope $\beta \sim 1.41 \pm 0.10$ (plot not shown), for bubbles smaller than $s \sim 10 \text{ mm}$. This slope is similar to those observed by Cipriano and Blanchard (1981) and Bowyer (1992) who simulated the air entrainment mechanism using a continuous waterfall or by dropping a known volume of water into a water-filled basin, respectively. They both reported slopes $\beta \sim 1.5$.

The variation of the bubble size distribution as a function of depth was examined at positions K, L, and M in the 3rd cloud at $\hat{y} \sim 0.02, 0.01, \text{ and } -0.01$, respectively. At

position K, the size distribution slope for bubbles smaller than $s \sim 10 \text{ mm}$, was $\beta \sim 1.51$, Fig. 4.16b. The size distribution changed as the measurements were performed deeper in the water, to a distribution that had a critical size at $s_c \sim 2.2 \text{ mm}$; and two distinct slopes. At positions L and M (Fig. 4.17b and 4.18b), the size distribution slopes for bubbles smaller than s_c were not statistically different and equal to ~ 1.3 . Therefore, as the measurements were performed deeper into the water, the bubble concentration of larger bubbles decreased rapidly with depth, in agreement with Baldy (1993). Finally, the measured slopes at position M were very similar to the measurements reported by Deane and Stokes (2002). They reported a bubble critical size at $r \sim 1.0 \text{ mm}$ while our measurements indicated a critical size at $r \sim 1.9 \text{ mm}$, assuming that the bubble shape is spherical.

Fig. 4.25 displays the average size distribution measured beneath the plunging wave. This distribution was obtained by averaging the size distributions at positions A-K. This wave had an average void fraction ~ 0.15 and the average size distribution, based on 45713 detected bubbles that were up to $\hat{t} \sim 0.90$ old, was well represented by a single line with $\beta \sim 1.50$. This slope was similar to the slopes reported by Mori, et al. (2007) who used a dual tip resistivity probe; and found that the bubble size distribution had a slope $1.5 < \beta < 1.7$, for shoaling breaking waves which had maximum void fraction values of ~ 0.22 . This would indicate that similar air entrainment processes occur in deep and shallow water breaking waves, if the void fractions are similar. Note also that the measuring techniques (fiber-optic and resistivity probes) produced point measurements in both studies.

At position E, the slope for bubbles larger than $s_c \sim 6.5 \text{ mm}$ was $\beta = 2.73 \pm 0.73$ which is not statistically different from $\beta = 10/3$ reported by Deane and Stokes (2002). A critical size $s_c \sim 6.5 \text{ mm}$ corresponds to $r \sim 4.9 \text{ mm}$, assuming that the bubble shape is spherical. Deane and Stokes (2002) reported a bubble size distribution having two slopes and a critical size ($r \sim 1.0 \text{ mm}$) which they identified as the Hinze scale, as mentioned previously, equation (4.2). Using $We_c = 4.7$, $\gamma/\rho = 7.3 \times 10^{-5} \text{ m}^3 \text{ s}^{-2}$ and assuming $a_H = 1.0 \text{ mm}$ Deane and Stokes (2002) estimated that $\epsilon = 12 \text{ W kg}^{-1}$ (Deane and Stokes 2002). Garrett et al. (2000) estimated that $\epsilon \sim 20 \text{ W kg}^{-1}$ which is consistent with Deane and Stokes (2002). If we assume that $a_H = 4.9 \text{ mm}$, equation (4.2) gives $\epsilon \sim 0.2 \text{ W kg}^{-1}$ which is considerably lower than the estimates by Garret et al. (2000) and Deane and Stokes (2002). Therefore, it is unlikely that the observed critical size, $s_c \sim 6.5 \text{ mm}$, corresponds to the Hinze scale.

At positions F, G (2nd cloud) and M, a critical size of $s_c \sim 2.5 \text{ mm}$ was observed. If the bubbles are assumed to have spherical shape, this corresponds to $r \sim 1.90 \text{ mm}$. Also, the slopes at these positions, for bubbles larger than the critical size, were not statistically different from $\beta = 10/3$ reported by Deane and Stokes (2002). This critical size would imply an energy dissipation rate of $\sim 3.7 \text{ W kg}^{-1}$ which is comparable to 12 W kg^{-1} , proposed by Deane and Stokes (2002). This combined with the fact that at these three positions the two slopes of the bubble size distributions were approximately 1.5 and 10/3 support Deane and Stokes' (2002) hypothesis.

At positions F, G (2nd cloud) and M the void fraction is small, 0.01 to 0.021, indicating that at these positions the probes were traversing parts of the bubble cloud that

were quite diffuse. Inside the denser portions of the bubble clouds, where the void fraction is higher, processes such as bubble coalescence and the buoyant rise of bubbles may influence the size distribution and cause the slopes to differ from 1.5 and 10/3. In particular, at position M video recordings showed that the fiber-optic probes were located very close to the lower edge of the 3rd bubble cloud. It appears that at this position bubbles were created by two mechanisms, that is, turbulent fragmentation and jet and drop impact as proposed by Deane and Stokes (2002) and that the size distribution is not affected by other processes. Similar arguments would apply at positions F and G (2nd cloud).

The shape of the size distributions and the critical sizes, at the different positions along the spilling wave, were similar, except for position 21. Fig. 4.26 displays the average size distribution measured beneath the spilling wave, obtained by averaging the measurements at positions 23, 38, and 50. This average size distribution was based on 16920 detected bubbles that were up to $\hat{t} \sim 0.90$ old. This size distribution has $s_c \sim 2.7$ mm and the slopes were $\beta = 0.90 \pm 0.04$ and 1.75 ± 0.22 for bubbles smaller and larger than s_c , respectively. These slopes are similar to slopes reported by Bowyer (2001) who conducted measurements in ocean and freshwater very close to the free surface. However, our measurements are different from previous experiments performed at laboratory scale (Loewen, et al. 1996; Kaldova et al., 2003). The average slope, for bubbles larger than s_c , was ~ 2 times smaller than the slope reported by Loewen, et al. (1996). They used an averaged in time and space photographic technique and reported a time and space averaged size distribution with slopes $\beta \sim 3.7$, for a very gently spilling mechanically-generated wave. This difference may be due to the fact that the fiber-optic

probes make point measurements and the video measurements by Loewen et al. (1996) spatially average the data.

The critical sizes at position F,G,L, and M (plunging wave); and the average critical size for the spilling wave are comparable with the critical bubble sizes measured by Leifer and de Leeuw (2006a) and Leifer et al. (2007) who reported $r \sim 1.7$ to 2.0 mm for their dense plume case. Note that they used wind waves which were paddle amplified in order to increase breaking wave activity.

4.5 Conclusions

The bubble clouds underneath breaking waves were studied using two fiber-optic probes. The main conclusions are:

1. For the plunging wave case, the average bubble size distribution measured near the air cavity indicated was independent of s .
2. For the plunging wave case, the bubble size distribution at position D (created by the collapse of the air cavity) and the size distribution at position E (created by the jet and drop impact, were very similar). This suggests that these bubble size distributions are independent from the bubble creation mechanism(s).
3. The air entrainment process in the splashing zone of the plunging wave is similar to the air entrainment process generated by splashing water, i.e. $\beta \sim 1.5$ (Cipriano and Blanchard, 1981; Bowyer, 1992).
4. Only the measurements performed at low void fraction (positions F and G), and deeper in the water in the splashing zone (position M) supported the conclusions of Deane and Stokes (2002).

5. By comparing the average bubble size distribution beneath plunging wave ($\beta \sim 1.5$) with the results of Mori, et al. (2007), it was concluded that similar air entrainment processes occur in deep and shallow water breaking waves.
6. An average slope of 1.5 has also been observed in ocean and freshwater experiments, when the measurements are performed very close to the free surface (Hwang et al., 1990; Bowyer, 2001).
7. The spilling wave bubble size distribution can be well represented by $s_c \sim 2.7 \text{ mm}$ and two slopes: ~ 0.90 and ~ 1.75 for bubbles smaller and larger than s_c . Similarly slopes has been previously observed if the measurements are performed very close to the free surface (Hwang et al., 1990; Bowyer, 2001).
8. The slopes of the size distribution beneath the spilling wave, for most of the bubble size range, were different from the previous experiments (Loewen, 1996; Kalvoda, 2003).
9. The critical sizes beneath the plunging and the spilling waves are comparable to those reported previously (Leifer and de Leeuw, 2006a; Leifer et al., 2007).

4.6 References

- Baldy, S. and Bourguel, M. (1987). Bubbles between the wave trough and wave crest levels. *J. Geophys. Res.* 92: 2919-2929.
- Baldy, S. (1988). Bubbles in the close vicinity of breaking waves. *J. Geophys. Res.* 93: 8239-8249.
- Baldy, S. (1993). A generation-dispersion model of ambient and transient bubbles in the close vicinity of breaking waves. *J. Geophys. Res.*, 98: 18277-18293.

- Bezzabotnov, V.S., Degterev, A. Kh., and Ereemeev, V.N. (1991). Determination of the gas exchange rate in whitecaps using measurements of the bubble concentration. *Svo. J. Phys. Oceanogr.*, Vol 2, No 3, pp 221-225.
- Blanchard, D.C. and Woodcock, A.H. (1957). Bubble formation and modification in the sea and its meteorological significance. *Tellus*, 9, 145-158.
- Bowyer, P.A. (1992). The rise of bubbles in a glass tube and the spectrum of bubbles produced by a splash. *Journal of Marine Research*, 50, 521–543.
- Bowyer, P.A. (2001). Video measurements of near-surface bubble spectra. *J. Geophys. Res.*, vol. 106, no C7, pp. 14179-14190.
- Cartellier, A. (1992). Simultaneous void fraction measurement, bubble velocity, and size estimate using a single optical probe in gas-liquid two phase flows. *Review of scientific instruments* 63 (11): 5442-5453.
- Cipriano, R.J. and Blanchard, D.C. (1981). Bubble and aerosol spectra produced by a laboratory breaking wave. *J. Geophys. Res.*, vol. 86, no C9, pp. 8085-8092.
- Deane, G.B. and Stokes, M.D. (1999). Air entrainment processes and bubble size distributions in the surf zone. *J. Phys. Oceanogr.* 29, 1393–1403.
- Deane, G. B. and Stokes, D. (2002). Scale dependence of Bubble Creation Mechanisms in Breaking Waves. *Nature*, 418: 839-844.
- Elkamash, M.K., Loewen, M.R., and Rajaratnam, N. (2005). Measurements of void fraction and bubble properties on a stepped chute using a fiber-optic probe. *Canadian Journal of Civil Engineering* 32: 636-643.
- Farmer, D.M., McNeil, C.L., and Johnson, B.D. (1993). Evidence for the importance of bubbles in increasing air-sea gas flux. *Nature* 361: 620-623.

- Garrett, C., Li, M., and Farmer, D. (2002). The connection between the bubble size spectra and energy dissipation rates in the upper ocean. *J. Phys. Oceanogr.* 30, 2163-2171.
- Haines, P.A. and Johnson, B.D. (1995). Injected bubble population in seawater and freshwater measured by a photographic method. *J. Geophys. Res.*, 100, 7057-7068.
- Han, L. and Yuan, Y.L. (2007). Bubbles size distribution in surface wave breaking entering process. *Science in China Series D-Earth Sciences.* 50(11): 1754-1760.
- Hwang, P.A., Hsu, Y.H.L., and Wu, J. (1990). Air bubbles produced by breaking wind waves: a laboratory study. *J. Phys. Oceanogr.* 20: 19-28.
- Johnson, B.D., and Cooke, R.C. (1979). Bubble populations and spectra in coastal waters: A photographic approach, *J. Geophys. Res.*, 84(C7), 3761– 3766.
- Kalvoda, P.M., Xu, L. and Wu, J. (2003). Macrobubble clouds produced by breaking wind waves: A laboratory study. *J. Geophys. Res.* 108, C6, 3207.
- Kolovayev, P.A. (1976). Investigation of the concentration and statistical size distribution of wind-produced bubbles in the near-surface ocean layer. *Oceanology, Engl. Trans.*, 15, 659–661.
- Lamarre, E. and Melville, W. K. (1991). Air Entrainment and Dissipation in Breaking Waves. *Nature*, 351: 469-472.
- Leifer, I. and de Leeuw, G., (2006a). Bubbles generated from wind-steepened breaking waves: Part 1. Bubble from bubble plumes. *J. Geophys. Res.* 111, C06020.
- Leifer, I., and de Leeuw, G. (2006b). Bubbles generated from wind-steepened breaking waves: Part 2. Bubble plumes, bubbles, and wave characteristics. *J. Geophys. Res.* 111, C06021.

- Leifer, I., Caulliez, G., and de Leew, G. (2007). Characteristics of bubble plumes, bubble-plume bubbles, and waves from wind-steepened wave-breaking. *J. of Marine Systems* 66, 61–70.
- Liss, P.S. et al. (1997). Physical processes in the microlayer and the air-sea exchange of trace gases.
- Loewen, M.R. and Melville, W.K. (1991). Microwave backscatter and acoustic radiation from breaking waves. *J. of Fluid Mech.* 224: 601-623.
- Loewen, M. R., O'Dor, M. A., and Skafel, M. G. (1996). Bubbles Entrained by Mechanically Generated Breaking Waves. *J. Geophys. Res.* 101: 20,759-20,769.
- Monahan, E.C. (1986). The ocean as a source for atmospheric particles, in *The Role of Air-Sea Exchange in Geochemical Cycling*, edited by P. Baut-Menard, pp. 129-163, Springer, New York.
- Mori, N., Suzuki, T., and Kakuno, S. (2007). Experimental study of air bubbles and turbulence characteristics in the surf zone. *J. Geophys. Res.* 112 (C5): Art. No. C05014.
- Rojas, G, and Loewen, M.R. (2007a). Fiber-optic probe measurements of void fraction and bubble size distribution beneath breaking waves. *Exp Fluids.* 43: 895-906.
- Rojas, G., and Loewen, M.R. (2007b). Air entrainment by breaking waves. CSCE 2007 Annual General Meeting and Conference. Yellow Knife, Northwest Territories.
- Saberi, S. Shakourzadeh, K., Bastoul, D. and Militzer, J. (1995) Bubble size and velocity measurements in gas liquid systems: application of fiber-optic technique to pilot plant scale. *The Canadian Journal of Chemical Engineering.* 73: 253-257.
- Sam, A., Gomez C.O., and Finch, J.A. (1996). Axial velocity profiles of single bubbles in water/frother solutions. *Int. Miner. Process* 47: 177-196.

Serdula, C. and Loewen, M.R. (1998). Experiments investigating the use of fiber-optic probes for measuring bubble-size distributions. *IEEE J. Oceanic Eng.* 23: 385-399.

Wallace, D.W.R., and Wirick, C.D. (1992). Large air-sea gas fluxes associated with breaking waves. *Nature* 356: 694-696.

Wu, J. (2000). Bubbles produced by breaking waves in fresh and salt waters: notes and correspondence. *J. Phys. Oceanogr.* 30, 1809–1813.

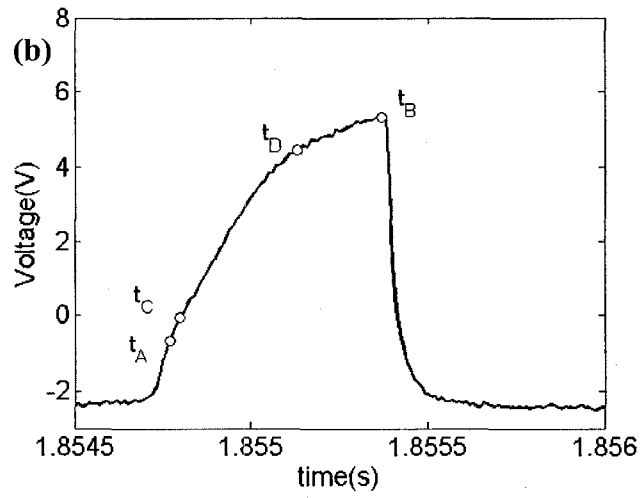
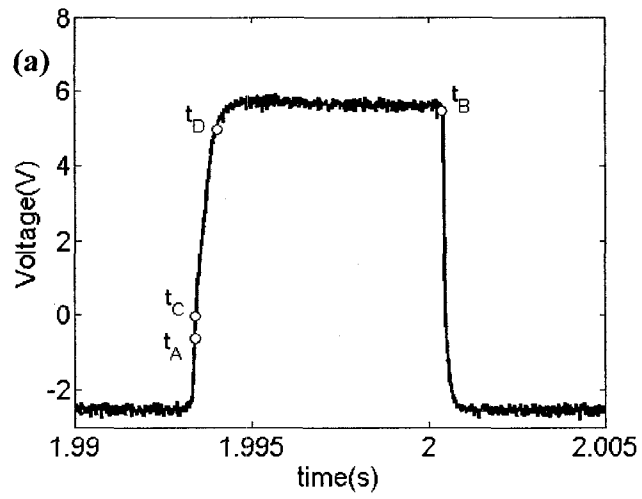


Fig. 4.1 (a) A good bubble signature showing the four characteristic points (t_A - t_D) (b) A poor bubble signature.

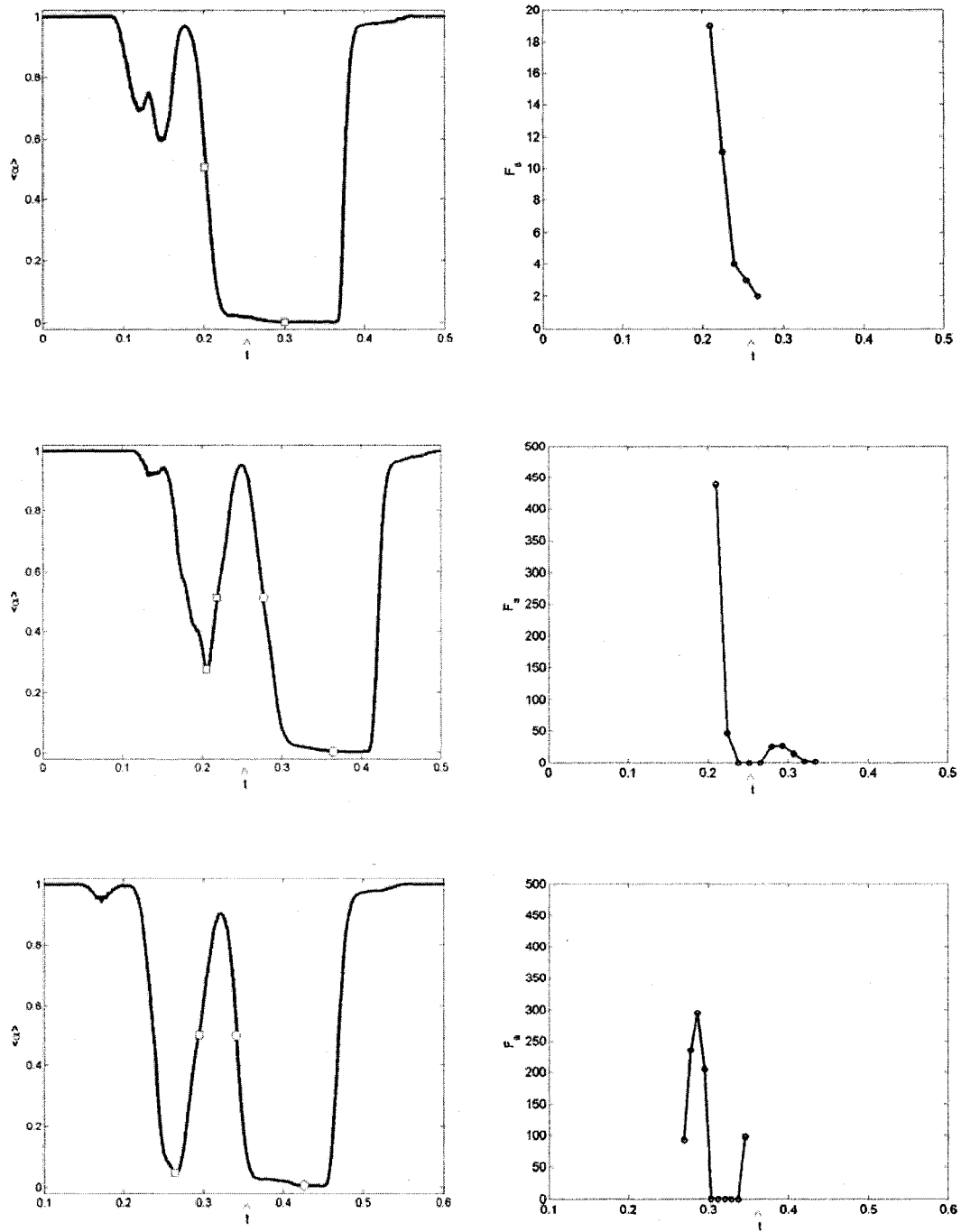


Fig. 4.2 $\langle \alpha \rangle$ and bubble frequency of arrival to the tip of the probe, F_a . (a-b) Position A, interval of time (\square). (c-d) Position B. (e-f) Position C. First interval of time: between markers (\square). Second interval of time: between markers (\circ).

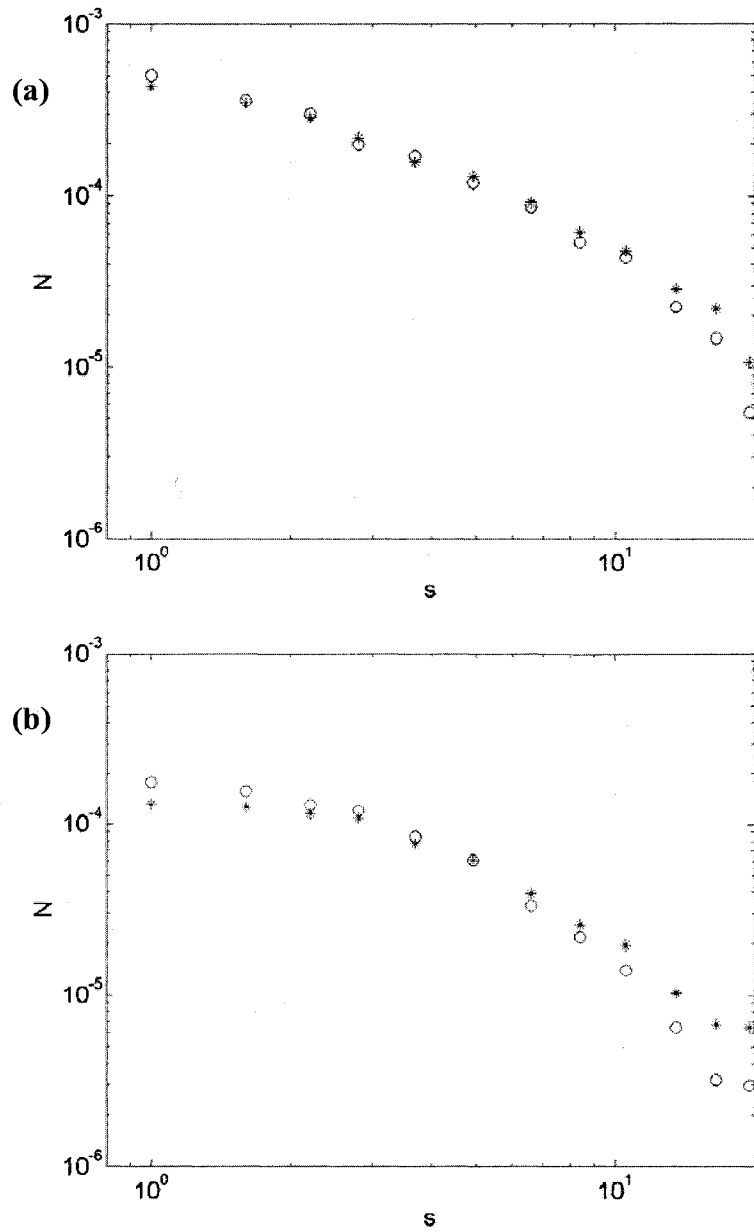


Fig. 4.3 Comparison between the 0° and the 90° size distributions. N is the number of bubbles per wave per μm increment and s is the cord length. The cord length bins were centered at 1.0, 1.6, 2.2, 2.8, 3.7, 4.9, 6.6, 8.4, 10.5, 13.5, 16.5, and 19.5 mm. (a) Position D, plunging wave. (b) Position 50, spilling wave.

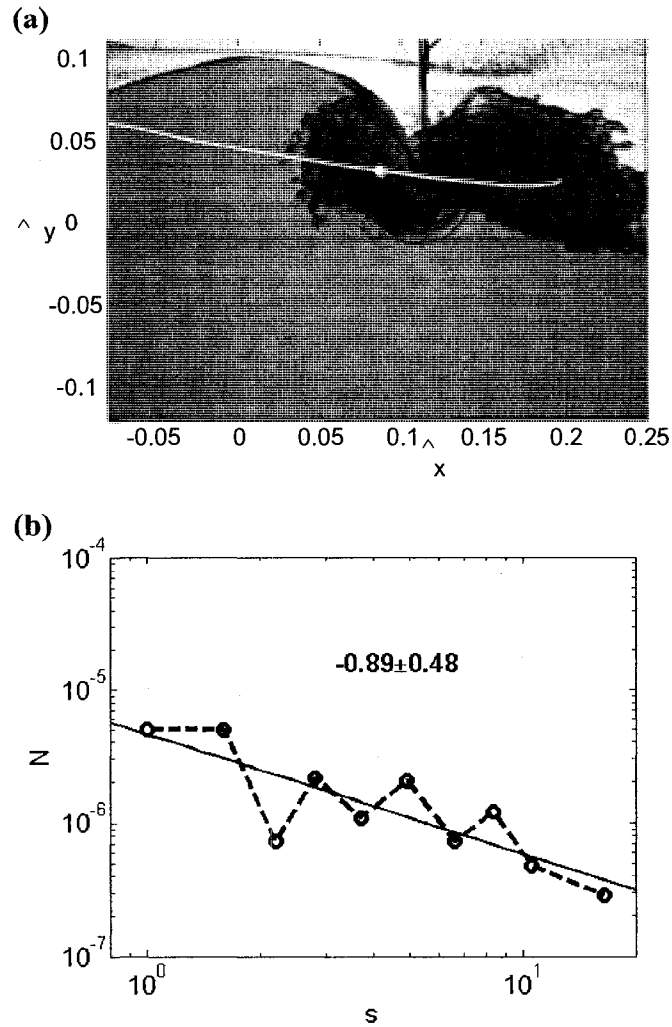


Fig. 4.4 (a) Image showing the instant when $\langle \alpha \rangle_{\max}$ occurred at position A under the plunging breaker. The white line is the approximate path of the fiber-optic when crossing the air cavity. (o) is the position of the fiber-optic probe tips. (b) Bubble size distribution. N is the number of bubbles per wave per μm increment and s is the cord length. The cord length bins were centered at 1.0, 1.6, 2.2, 2.8, 3.7, 4.9, 6.6, 8.4, 10.5, 13.5, 16.5, and 19.5 mm . (o-) measured size distribution. (—) is the linear regression. The numbers are the mean slope \pm 95% confidence band limits on the slope.

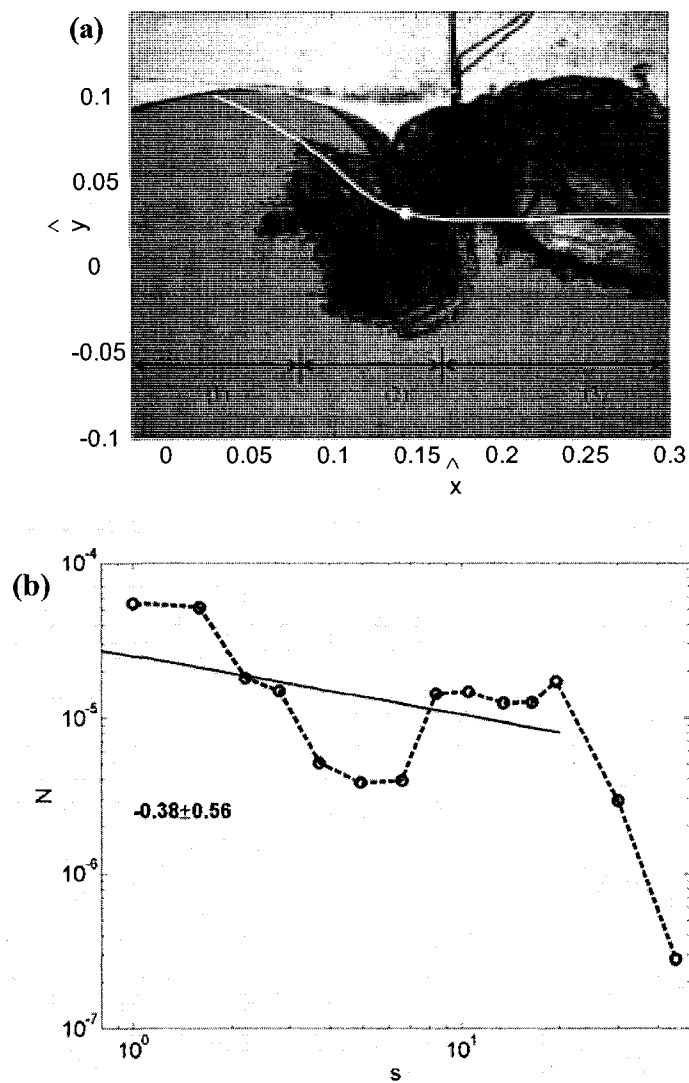


Fig. 4.5 (a) Image showing the instant when $\langle \alpha \rangle_{\max}$ occurred at position B under the plunging breaker. The white line is the approximate path of the fiber-optic when crossing the air cavity. (o) is the position of the fiber-optic probe tips. (b) Bubble size distribution. N is the number of bubbles per wave per μm increment and s is the cord length. The cord length bins were centered at 1.0, 1.6, 2.2, 2.8, 3.7, 4.9, 6.6, 8.4, 10.5, 13.5, 16.5, and 19.5, 30, and 45 mm. (o-) measured size distribution. (—) is the linear regression. The numbers are the mean slope \pm 95% confidence band limits on the slope.

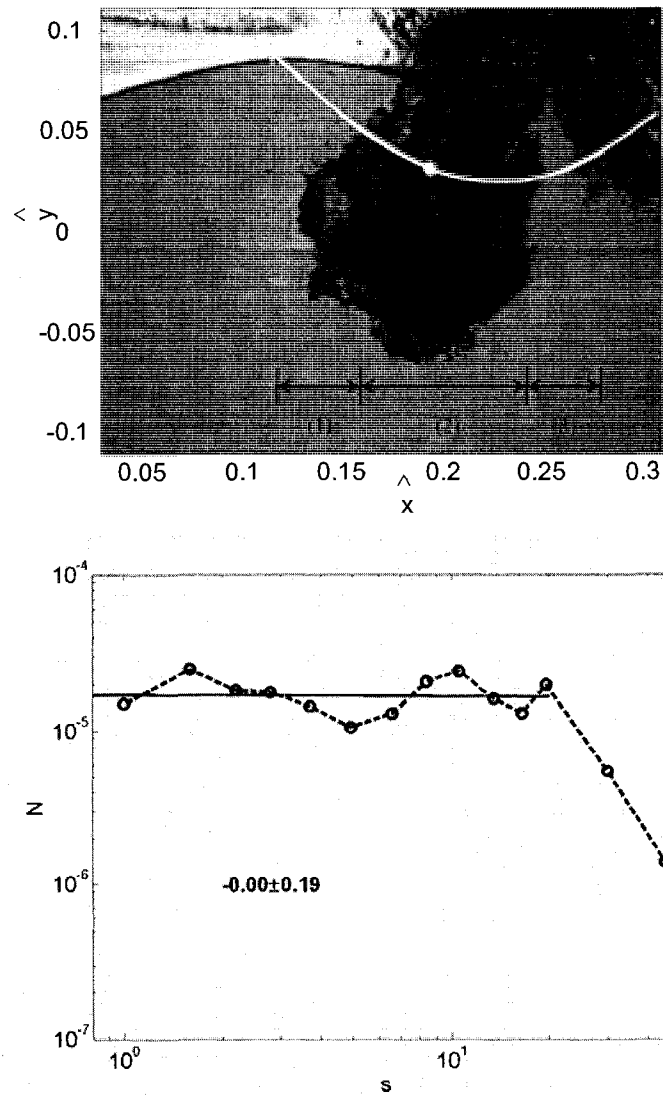


Fig. 4.6 (a) Image showing the instant when $\langle \alpha \rangle_{\max}$ occurred at position C, before the collapsing of the air cavity, under the plunging breaker. The white line is the approximate path of the fiber-optic. (o) is the position of the fiber-optic probe tips. (b) Bubble size distribution. N is the number of bubbles per wave per μm increment and s is the cord length. The cord length bins were centered at 1.0, 1.6, 2.2, 2.8, 3.7, 4.9, 6.6, 8.4, 10.5, 13.5, 16.5, 19.5, 30, and 45 mm . (o-) measured size distribution. (—) is the linear regression. The numbers are the mean slope \pm 95% confidence band limits on the slope.

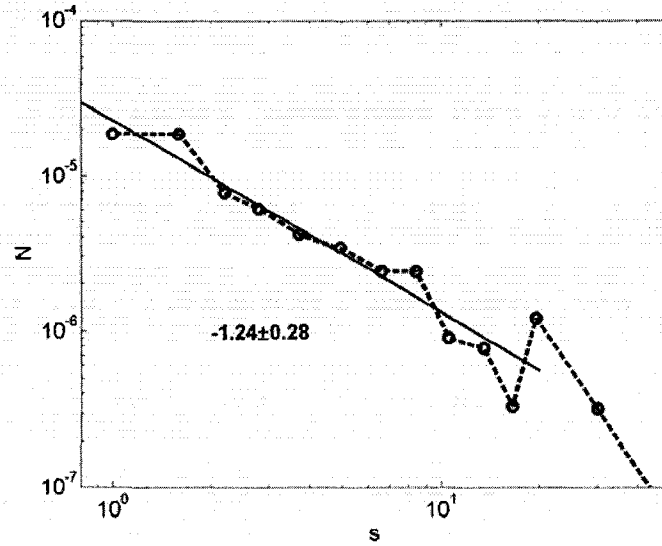


Fig. 4.7 Bubble size distribution for position C under the plunging breaker, after the collapsing of the air cavity. N is the number of bubbles per wave per μm increment and s is the cord length. The cord length bins were centered at 1.0, 1.6, 2.2, 2.8, 3.7, 4.9, 6.6, 8.4, 10.5, 13.5, 16.5, 19.5, 30, and 45 mm. (o-) measured size distribution. (—) is the linear regression. The numbers are the mean slope \pm 95% confidence band limits on the slope. (a) Before the fragmentation of the air cavity. (b) After the fragmentation of the air cavity.

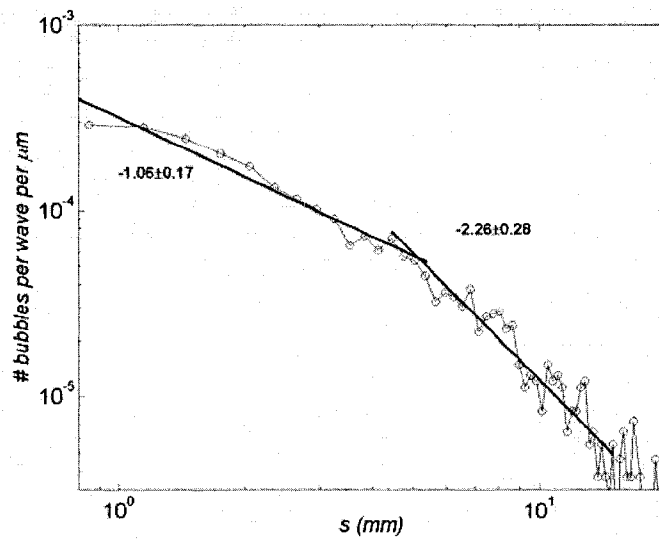
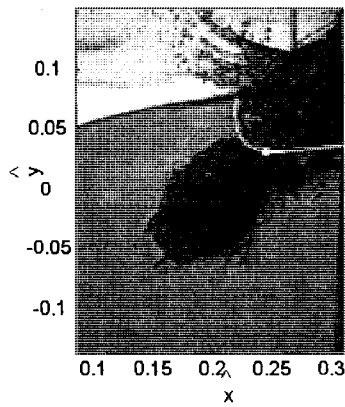


Fig. 4.8 (a) Image showing the instant when $\langle \alpha \rangle_{\max}$ occurred at position D under the plunging breaker. The white line is the approximate path of the fiber-optic when crossing the 1st bubble plume. (o) is the position of the fiber-optic probe tips. (b) Bubble size distribution. N is the number of bubbles per wave per μm increment and s is the cord length. The cord length bins were centered at 1.0, 1.6, 2.2, 2.8, 3.7, 4.9, 6.6, 8.4, 10.5, 13.5, 16.5, and 19.5 mm. (o-) measured size distribution. (—) is the linear regression. The numbers are the mean slope \pm 95% confidence band limits on the slope.

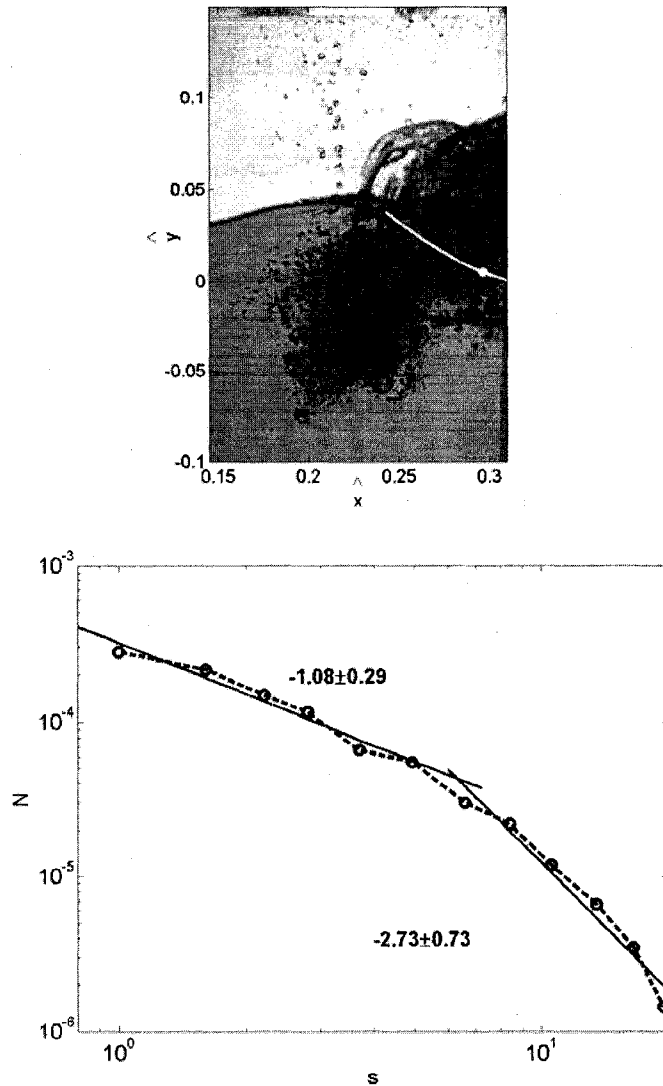


Fig. 4.9 (a) Image showing the instant when $\langle \alpha \rangle_{\max}$ occurred at position E under the plunging breaker. The white line is the approximate path of the fiber-optic when crossing the 1st bubble plume. (o) is the position of the fiber-optic probe tips. (b) Bubble size distribution. N is the number of bubbles per wave per μm increment and s is the cord length. The cord length bins were centered at 1.0, 1.6, 2.2, 2.8, 3.7, 4.9, 6.6, 8.4, 10.5, 13.5, 16.5, and 19.5 mm. (o-) measured size distribution. (—) is the linear regression. The numbers are the mean slope \pm 95% confidence band limits on the slope.

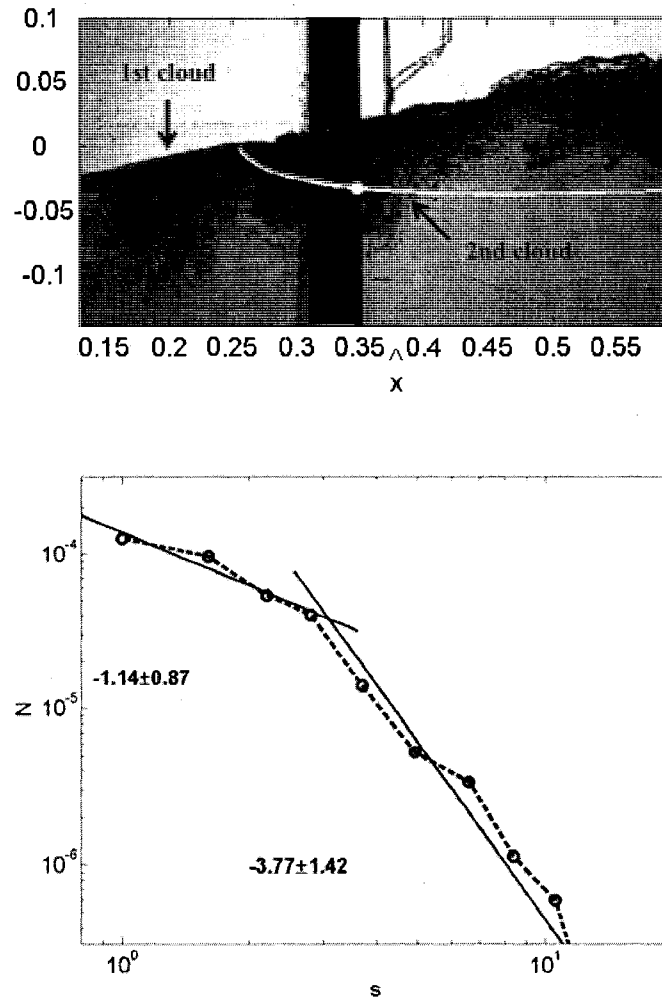


Fig. 4.10 (a) Image showing the instant when $\langle \alpha \rangle_{\max}$ occurred at position F under the plunging breaker. The white line is the approximate path of the fiber-optic when crossing the 1st bubble plume. (o) is the position of the fiber-optic probe tips. (b) Bubble size distribution. N is the number of bubbles per wave per μm increment and s is the cord length. The cord length bins were centered at 1.0, 1.6, 2.2, 2.8, 3.7, 4.9, 6.6, 8.4, 10.5, 13.5, 16.5, and 19.5 mm. (o-) measured size distribution. (—) is the linear regression. The numbers are the mean slope \pm 95% confidence band limits on the slope.

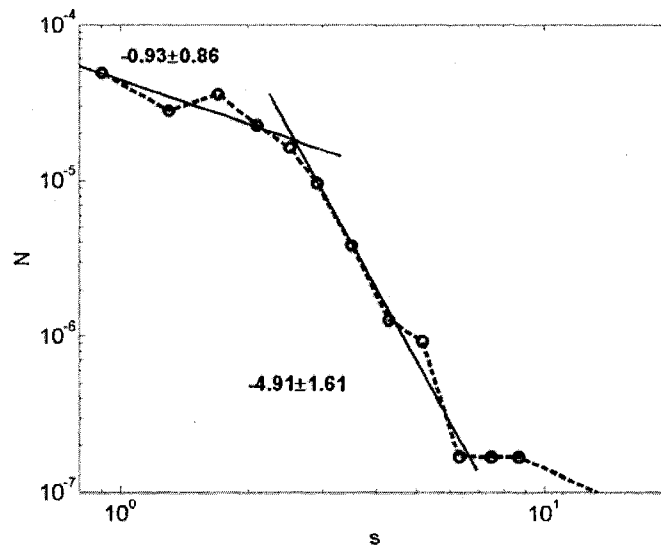
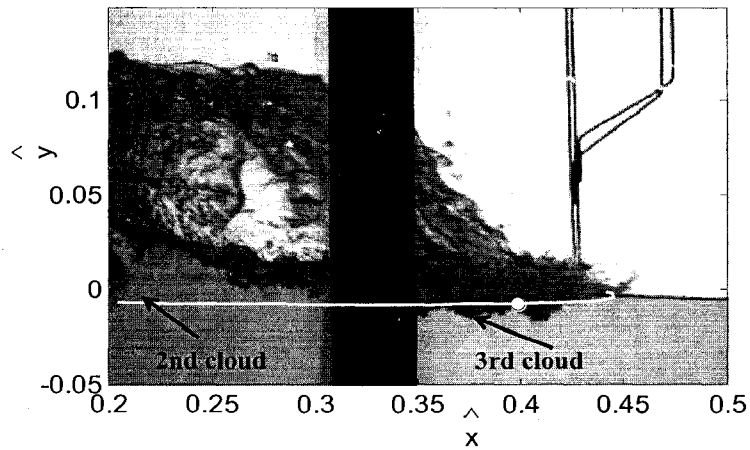


Fig. 4.11 (a) Image showing the instant when $\langle \alpha \rangle_{\max}$ occurred at position G under the plunging breaker. The white line is the approximate path of the fiber-optic when crossing first the 3rd bubble plume and then the 2nd bubble plume. (o) is the position of the fiber-optic probe tips. (b) Bubble size distribution. N is the number of bubbles per wave per μm increment and s is the cord length. The cord length bins were centered at 0.9, 1.3, 1.7, 2.1, 2.5, 2.9, 3.5, 4.3, 5.15, 6.3, and 47.5 mm. (o-) measured size distribution. (—) is the linear regression. The numbers are the mean slope \pm 95% confidence band limits on the slope.

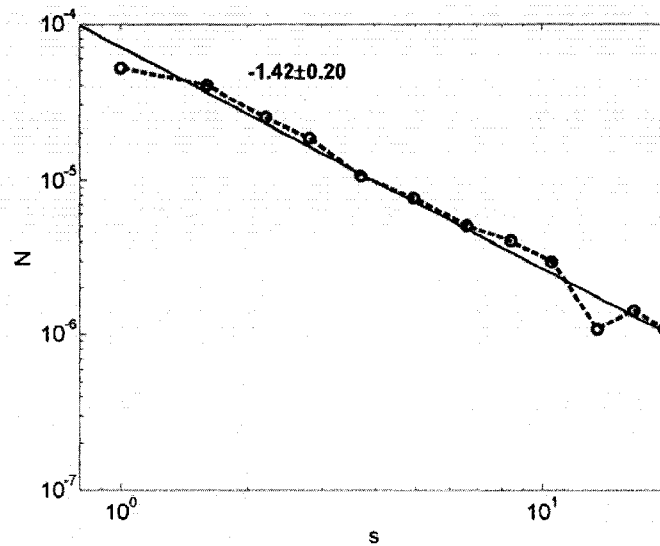


Fig. 4.12 Bubble size distribution for position G under the plunging breaker, 3rd bubble cloud. N is the number of bubbles per wave per μm increment and s is the cord length. The cord length bins were centered at 1.0, 1.6, 2.2, 2.8, 3.7, 4.9, 6.6, 8.4, 10.5, 13.5, 16.5, and 19.5 mm. (o-) measured size distribution. (—) is the linear regression. The numbers are the mean slope \pm 95% confidence band limits on the slope.

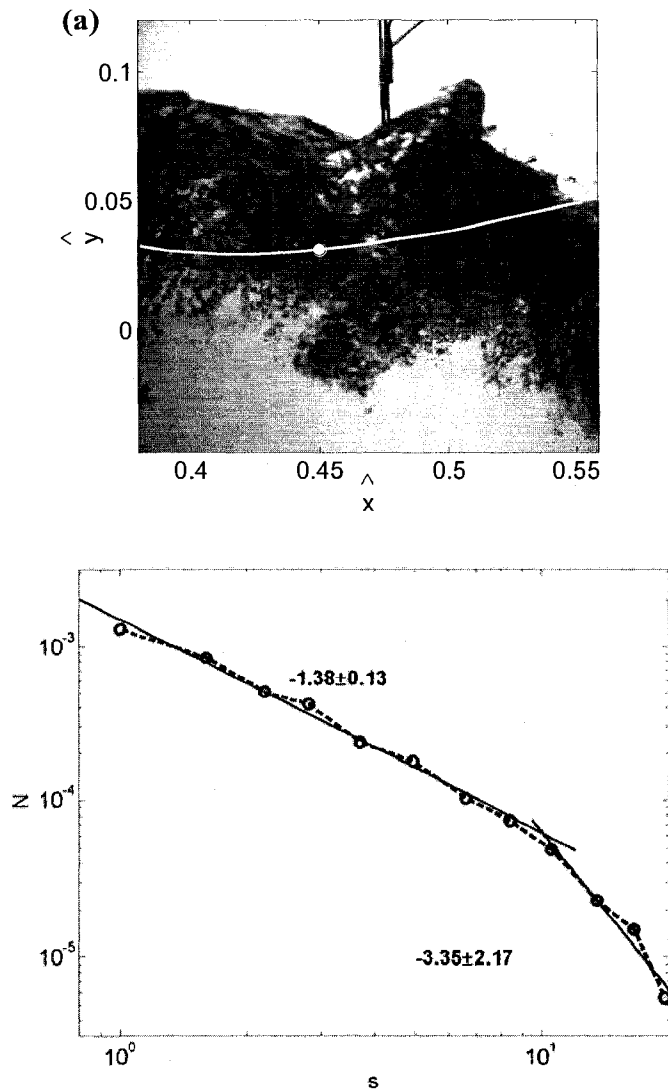


Fig. 4.13 (a) Image showing the instant when $\langle \alpha \rangle_{\max}$ occurred at position H under the plunging breaker. The white line is the approximate path of the fiber-optic when crossing the 3rd bubble plume. (o) is the position of the fiber-optic probe tips. (b) Bubble size distribution. N is the number of bubbles per wave per μm increment and s is the cord length. The cord length bins were centered at 1.0, 1.6, 2.2, 2.8, 3.7, 4.9, 6.6, 8.4, 10.5, 13.5, 16.5, and 19.5 mm. (o-) measured size distribution. (—) is the linear regression. The numbers are the mean slope \pm 95% confidence band limits on the slope.

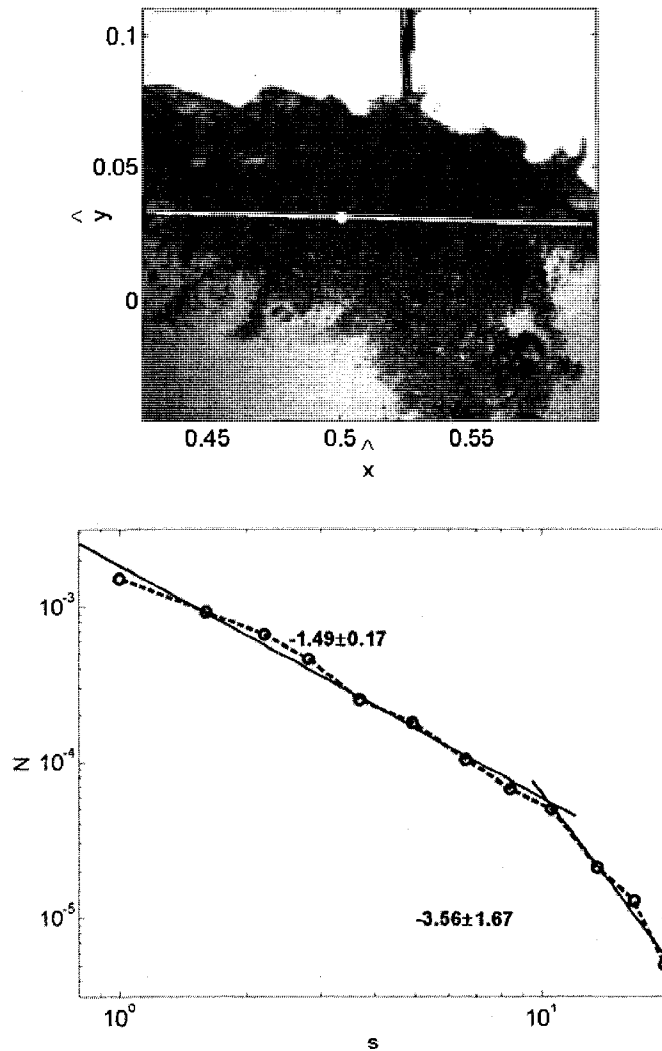


Fig. 4.14 (a) Image showing the instant when $\langle \alpha \rangle_{\max}$ occurred at position I under the plunging breaker. The white line is the approximate path of the fiber-optic when crossing the 3rd bubble plume. (o) is the position of the fiber-optic probe tips. (b) Bubble size distribution. N is the number of bubbles per wave per μm increment and s is the cord length. The cord length bins were centered at 1.0, 1.6, 2.2, 2.8, 3.7, 4.9, 6.6, 8.4, 10.5, 13.5, 16.5, and 19.5 mm. (o-) measured size distribution. (—) is the linear regression. The numbers are the mean slope \pm 95% confidence band limits on the slope.

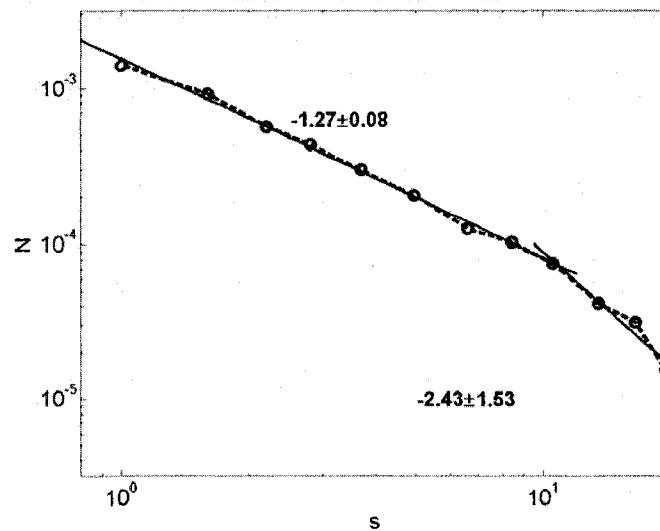
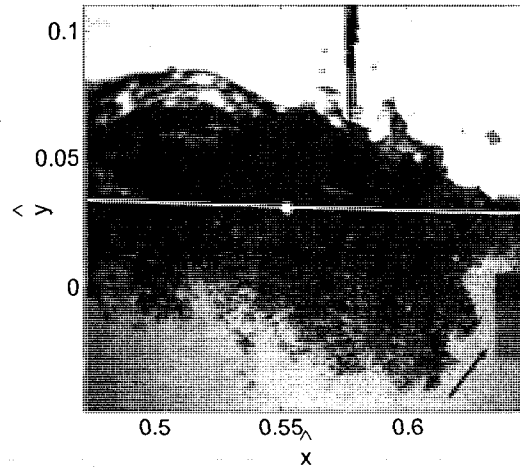


Fig. 4.15 (a) Image showing the instant when $\langle \alpha \rangle_{\max}$ occurred at position J under the plunging breaker. The white line is the approximate path of the fiber-optic when crossing the 3rd bubble plume. (o) is the position of the fiber-optic probe tips. The arrow points out a marker. (b) Bubble size distribution. N is the number of bubbles per wave per μm increment and s is the cord length. The cord length bins were centered at 1.0, 1.6, 2.2, 2.8, 3.7, 4.9, 6.6, 8.4, 10.5, 13.5, 16.5, and 19.5 mm. (o-) measured size distribution. (—) is the linear regression. The numbers are the mean slope \pm 95% confidence band limits on the slope.

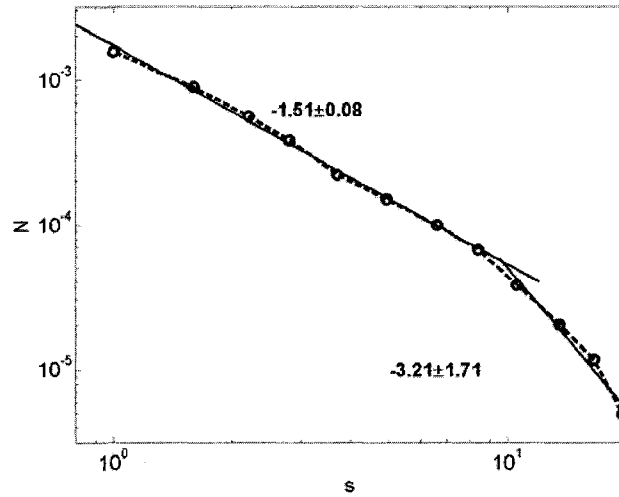
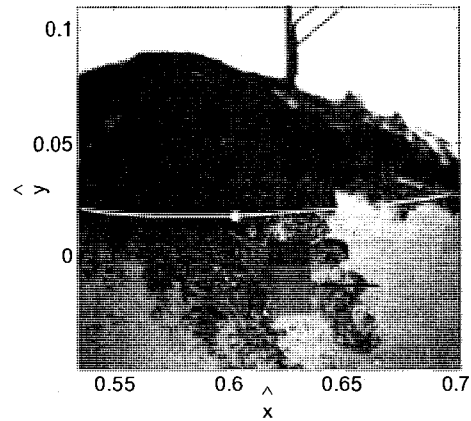


Fig. 4.16 (a) Image showing the instant when $\langle \alpha \rangle_{\max}$ occurred at position K under the plunging breaker. The white line is the approximate path of the fiber-optic when crossing the 3rd bubble plume. (o) is the position of the fiber-optic probe tips. The arrow points out a marker. (b) Bubble size distribution. N is the number of bubbles per wave per μm increment and s is the cord length. The cord length bins were centered at 1.0, 1.6, 2.2, 2.8, 3.7, 4.9, 6.6, 8.4, 10.5, 13.5, 16.5, and 19.5 mm. (o-) measured size distribution. (—) is the linear regression. The numbers are the mean slope \pm 95% confidence band limits on the slope.

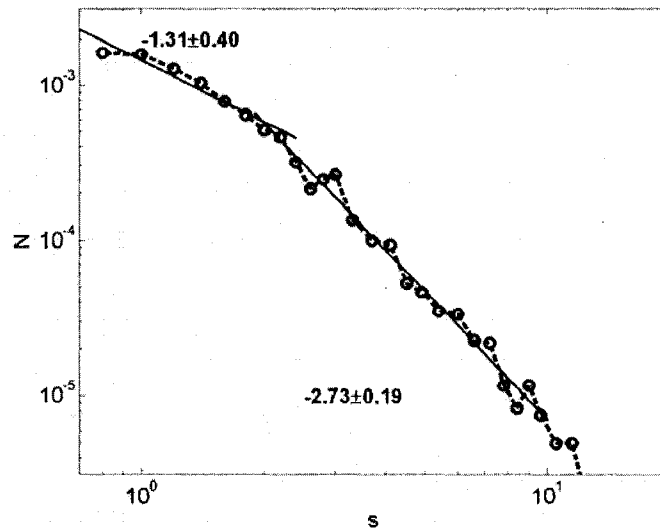
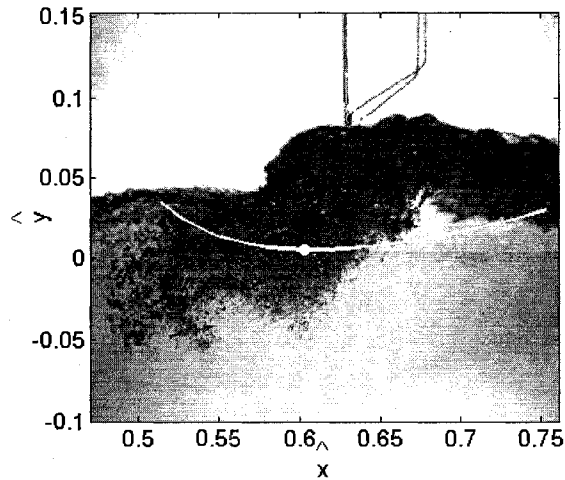


Fig. 4.17 (a) Image showing the instant when $\langle \alpha \rangle_{\max}$ occurred at position L under the plunging breaker. The white line is the approximate path of the fiber-optic when crossing the 3rd bubble plume. (o) is the position of the fiber-optic probe tips. (b) Bubble size distribution. N is the number of bubbles per wave per μm increment and s is the cord length. The cord length bins were centered at 0.8, 1.0, 1.2, 1.4, 1.6, 1.8, 2.0, 2.2, 2.4, 2.6, 2.8, 3.0, 3.3, 3.7, 4.1, 4.5, 4.9, 5.4, 6.0, 6.6, 7.2, 7.8, 8.4, 9.0, 9.6, 10.5, 11.5, 12.5, 13.5, 14.5, and 16.5 mm. (o-) measured size distribution. (—) is the linear regression. The numbers are the mean slope \pm 95% confidence band limits on the slope.

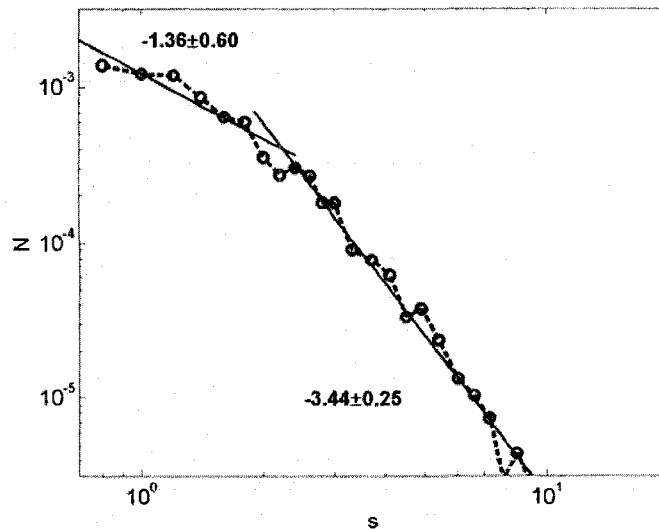
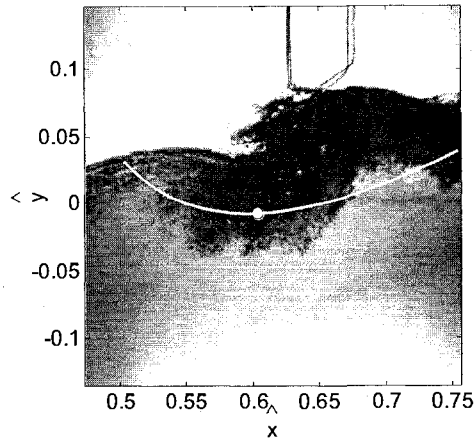


Fig. 4.18 (a) Image showing the instant when $\langle \alpha \rangle_{\max}$ occurred at position M under the plunging breaker. The white line is the approximate path of the fiber-optic when crossing the 3rd bubble plume. (o) is the position of the fiber-optic probe tips. (b) Bubble size distribution. N is the number of bubbles per wave per μm increment and s is the cord length. The cord length bins were centered at 0.8, 1.0, 1.2, 1.4, 1.6, 1.8, 2.0, 2.2, 2.4, 2.6, 2.8, 3.0, 3.3, 3.7, 4.1, 4.5, 4.9, 5.4, 6.0, 6.6, 7.2, 7.8, 8.4, 9.0, 9.6, 10.5, 11.5, 12.5, 13.5, 14.5, and 16.5 mm. (o-) measured size distribution. (—) is the linear regression. The numbers are the mean slope \pm 95% confidence band limits on the slope.

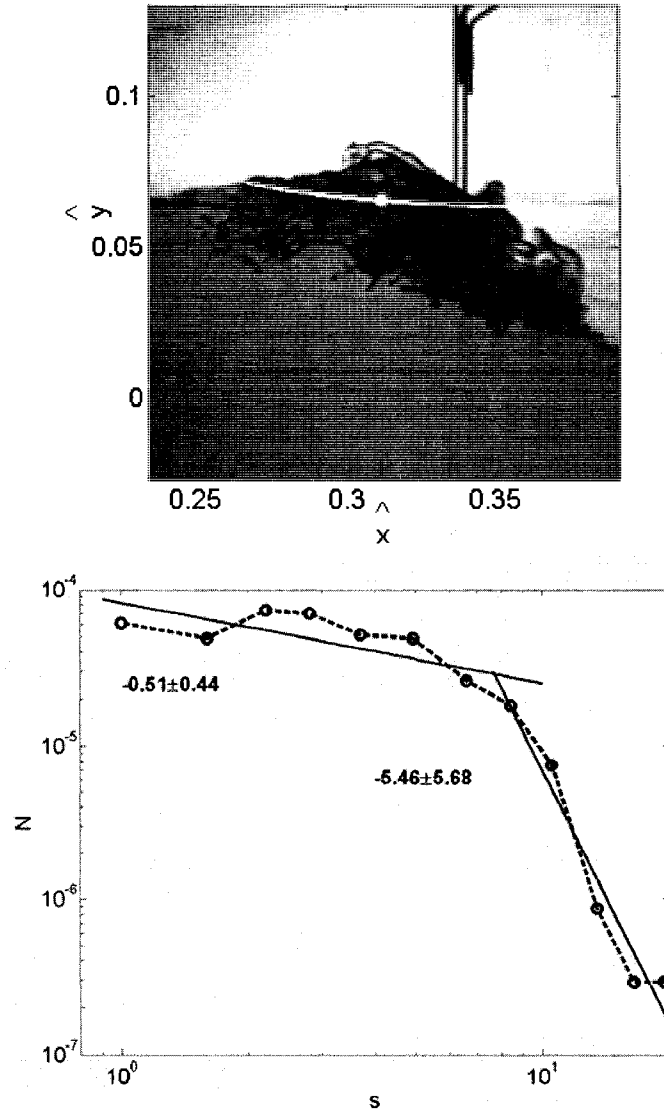


Fig. 4.19 (a) Image at position 21 under the spilling breaker. The white line is the approximate path of the fiber-optic when crossing the small air pocket. (o) is the position of the fiber-optic probe tips. (b) Bubble size distribution. N is the number of bubbles per wave per μm increment and s is the cord length. The cord length bins were centered at 1.0, 1.6, 2.2, 2.8, 3.7, 4.9, 6.6, 8.4, 10.5, 13.5, 16.5, and 19.5 mm. (o-) measured size distribution. (—) is the linear regression. The numbers are the mean slope \pm 95% confidence band limits on the slope.

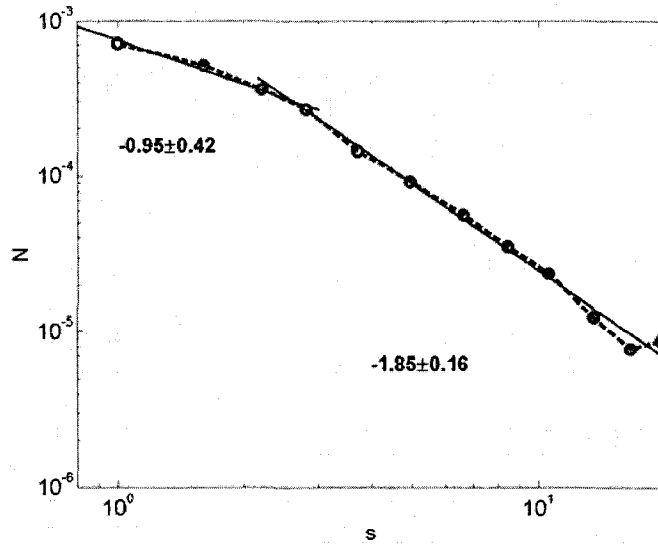
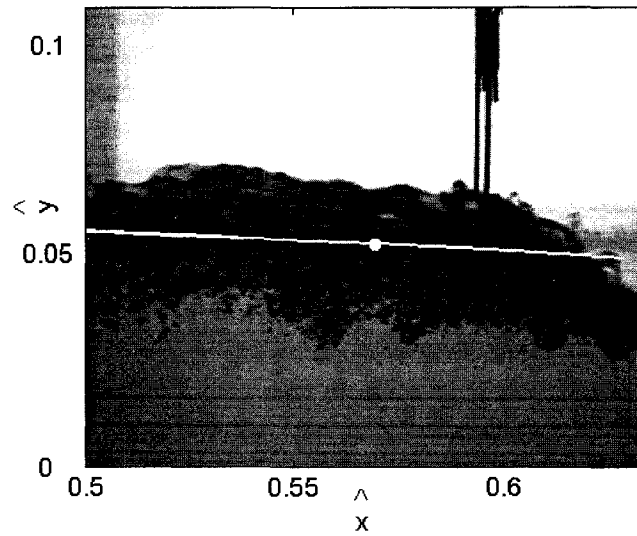


Fig. 4.20 (a) Image at position 23 under the spilling breaker. The white line is the approximate path of the fiber-optic when crossing the bubble cloud. (o) is the position of the fiber-optic probe tips. (b) Bubble size distribution. N is the number of bubbles per wave per μm increment and s is the cord length. The cord length bins were centered at 1.0, 1.6, 2.2, 2.8, 3.7, 4.9, 6.6, 8.4, 10.5, 13.5, 16.5, and 19.5 mm. (o-) measured size distribution. (—) is the linear regression. The numbers are the mean slope \pm 95% confidence band limits on the slope.

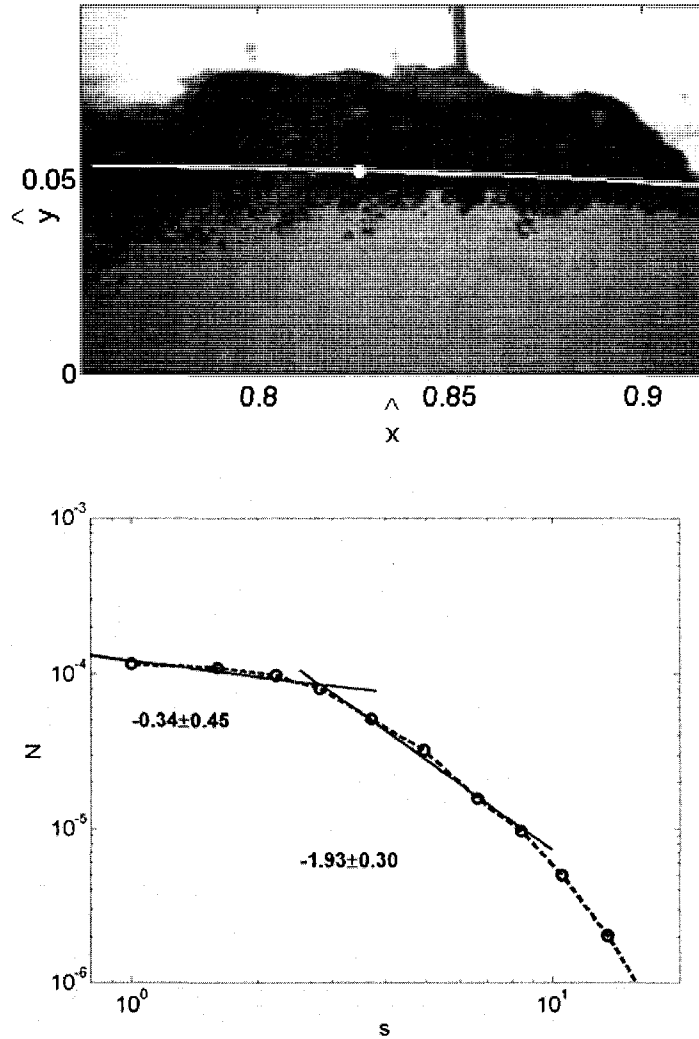


Fig. 4.21 (a) Image at position 38 under the spilling breaker. The white line is the approximate path of the fiber-optic when crossing the small air pocket. (o) is the position of the fiber-optic probe tips. (b) Bubble size distribution. N is the number of bubbles per wave per μm increment and s is the cord length. The cord length bins were centered at 1.0, 1.6, 2.2, 2.8, 3.7, 4.9, 6.6, 8.4, 10.5, 13.5, 16.5, and 19.5 mm. (o-) measured size distribution. (—) is the linear regression. The numbers are the mean slope \pm 95% confidence band limits on the slope.

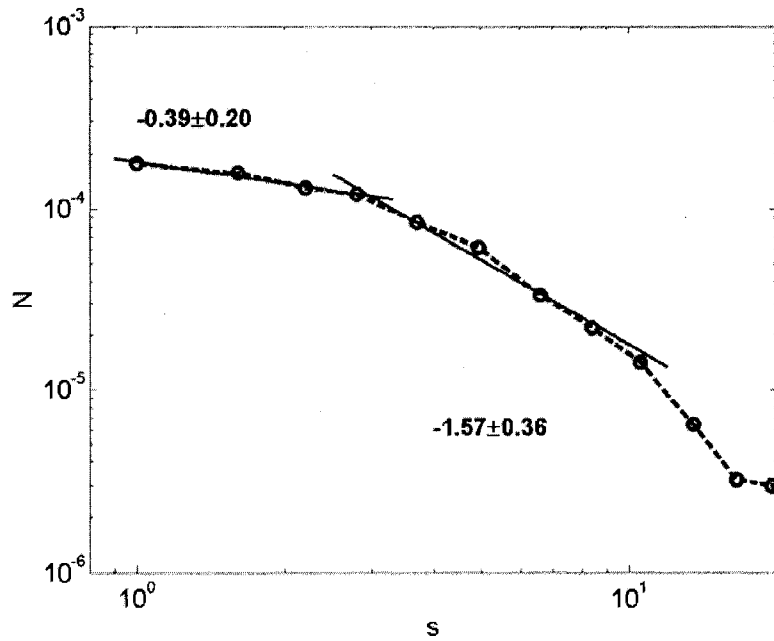


Fig. 4.22 Bubble size distribution for position 50 under the spilling breaker. N is the number of bubbles per wave per μm increment and s is the cord length. The cord length bins were centered at 1.0, 1.6, 2.2, 2.8, 3.7, 4.9, 6.6, 8.4, 10.5, 13.5, 16.5, and 19.5 mm. (o-) measured size distribution. (—) is the linear regression. The numbers are the mean slope \pm 95% confidence band limits on the slope.

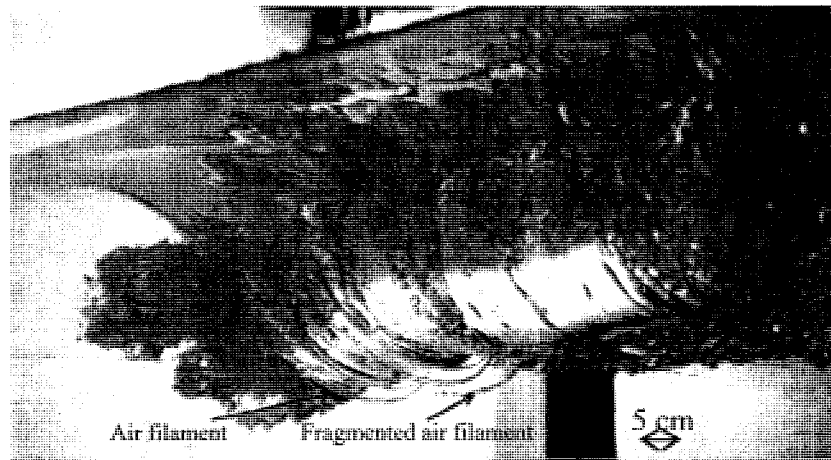


Fig. 4.23 Evidence of air filaments generated as the air cavity rotates under the plunging breaker. Also, there is evidence of the fragmentation into bubbles of the air filaments, $t \sim 0.29$. This image was taken with the camera located below the air-cavity and looking downstream.

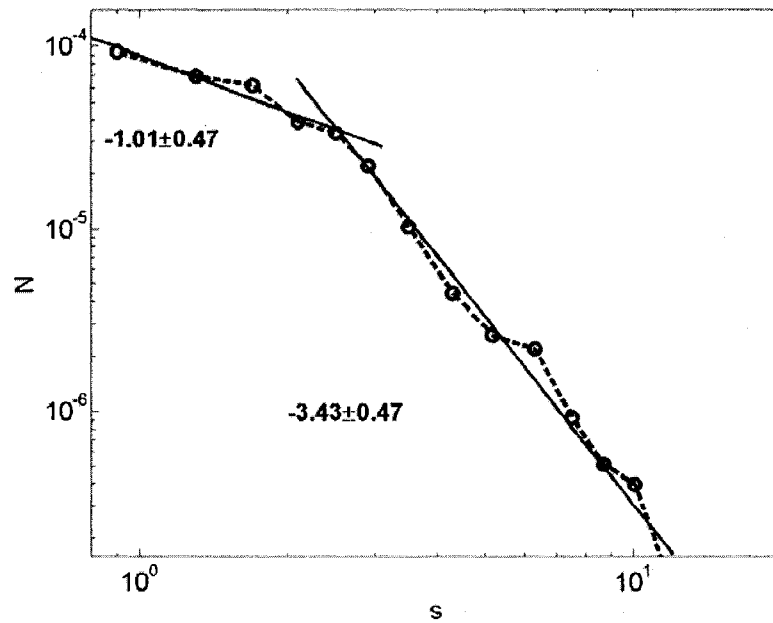


Fig. 4.24 Average bubble size distribution, 2nd cloud (positions F and G), plunging wave. (o-) measured size distribution. (—) is the linear regression. The numbers are the mean slope \pm 95% confidence band limits on the slope.

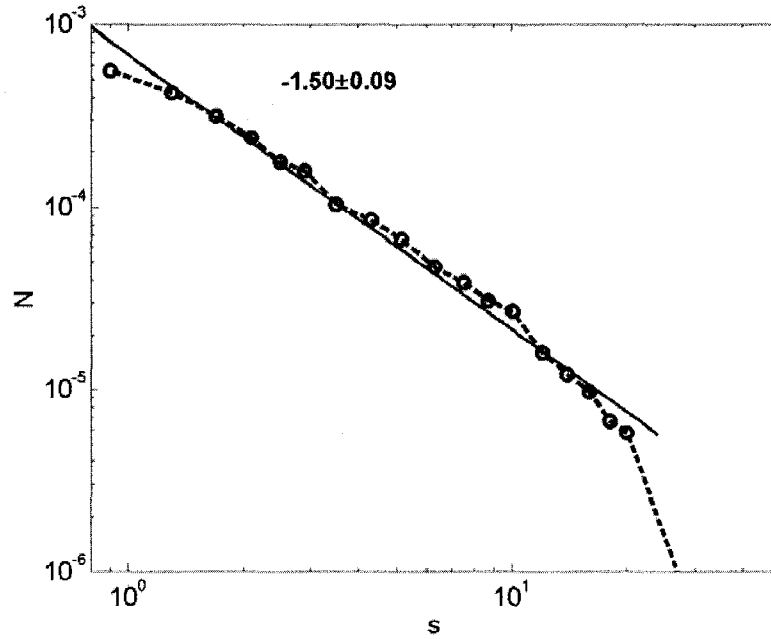


Fig. 4.25 Average bubble size distribution for the plunging wave, positions A to K. (o-) measured size distribution. (—) is the linear regression. The numbers are the mean slope \pm 95% confidence band limits on the slope.

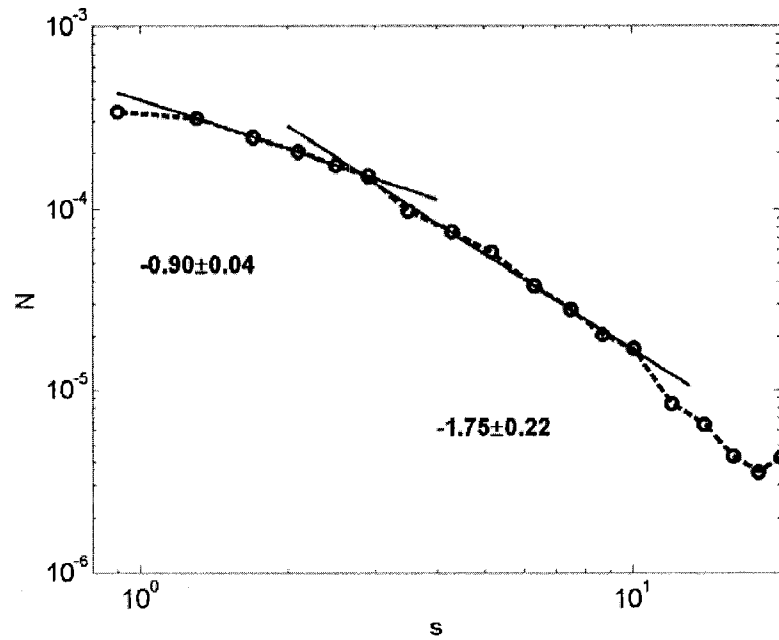


Fig. 4.26 Average bubble size distribution for the spilling wave, positions 23, 38 and 50. (o-) measured size distribution. (—) is the linear regression. The numbers are the mean slope \pm 95% confidence band limits on the slope.

Table 4.1: Measurement positions, measurement locations, number of repeat plunging waves, number of identified bubbles and bubble clouds. \hat{x} from Eq. (3.3) and \hat{y} from Eq. (3.2)

Position	\hat{x}	\hat{y}	# repeat waves ⁺	Time interval	# of bubbles	
A	0.04	0.03	2322	0.15-0.29	39	Air cavity
B	0.09	0.03	2132	0.21-0.23 and 0.26-0.35	553	Air cavity
C*	0.14	0.03	3018	0.27-0.30 and 0.33-0.35	925	Air cavity
C**	0.14	0.03	3018	0.35-0.42	170	1st cloud
D	0.19	0.02	1722	0.36-0.53	2876	1st cloud
E	0.25	0.01	3720	0.40-0.58	2847	2nd cloud
F	0.30	-0.03	4920	0.58-0.84	1097	2nd cloud
G*	0.35	-0.01	4920	0.61-0.74	681	2nd cloud
G**	0.35	-0.01	4920	0.30-0.37	343	3rd cloud
H	0.40	0.03	2120	0.47-0.60	6195	3rd cloud
I	0.45	0.03	2120	0.52-0.67	6847	3rd cloud
J	0.50	0.03	2180	0.56-0.73	7583	3rd cloud
K	0.56	0.02	2180	0.61-0.78	6536	3rd cloud
L	0.56	0.01	2002	0.61-0.84	4155	3rd cloud
M	0.56	-0.01	1130	0.47-0.91	1866	3rd cloud

(+) This number is twice the number of repeated waves because two fiber-optic probes were used simultaneously

Table 4.2: Measurement positions, measurement locations, number of repeat spilling waves, number of identified bubbles and bubble clouds. \hat{x} from Eq. (3.3) and \hat{y} from Eq. (3.2)

Position	\hat{x}	\hat{y}	# repeat waves ⁺	Time interval	# of bubbles
21	0.31	0.22	12266	0.09-0.14	641
23	0.56	0.23	3096	0.31-0.40	5288
38	0.82	0.23	11822	0.62-0.69	3760
50	1.07	0.23	18952	0.86-0.91	7872

(+) This number is twice the number of repeated waves because two fiber-optic probes were used simultaneously

Table 4.3: Mean void fraction, plunging wave case

Position	$\bar{\alpha}$
A	0.33
B	0.37
C	0.29
D	0.11
E	0.10
F	0.012
G*	0.037
G**	0.010
H	0.18
I	0.16
J	0.26
K	0.13
L	0.043
M	0.021

(*) 3rd cloud (**) 2nd cloud

Table 4.4: Mean void fraction, spilling wave case

Position	$\bar{\alpha}$
21	0.17
23	0.29
38	0.20
50	0.26

Chapter 5: Conclusions and Recommendations

5.1 Conclusions

The results of an experimental investigation of the air entrainment beneath deep-water breaking waves are presented in this thesis. Detailed measurements, performed at laboratory scale, of the ensemble void fractions and bubble size distributions are presented in order to elucidate the impact of large bubbles on air-sea gas transfer processes. Breaking waves introduce bubbles into the surface layer of the ocean. These bubbles enhance the gas transfer rate and aerosol formation. In shallow waters, entrained bubbles rise back to the surface transporting bacteria and organic material.

In Chapter 2, the calibration of two fiber-optic probes for making measurements of void fraction and bubble size measurements underneath breaking waves was described. Tests in a vertical bubble column showed that the normalized RMS error in the void fraction measurements was $\sim 10\%$. It was also found that the probes can provide mean bubble velocities accurate to $\pm 10\%$ when a minimum of ~ 15 individual bubble velocities are averaged. The fiber-optic probes were deployed beneath a plunging breaking wave in a laboratory wave channel. The slope and shape of the bubble cord length size distribution measured with the probes was found to agree closely with the size distribution measured from digital video recordings. These probes perform point measurements and have the advantage of being able to measure void fraction and bubble size distribution, simultaneously. Furthermore, the fiber-optic probe measurements have proven to be particularly useful for sampling high void fraction bubble clouds, very close to the free surface where measurements using other techniques, such as video recordings, are extremely challenging.

In Chapter 3, the void fraction measurements are presented. These measurements were performed at sufficient temporal and spatial resolution to allow comparison with future model predictions. Three significant events were identified during the breaking process of a plunging wave. The first stage of a plunging breaking wave is the formation of a water jet at the wave crest. This water jet then collides with the undisturbed water on the forward face of the wave forming a cavity of entrapped air. The first significant event occurs when the plunging water jet impacts the forward face of the wave. The second event occurs when the air cavity becomes unstable and collapses, evolving into a dense bubble cloud that rotates clockwise. The initial jet impact also creates a second cloud that rotates counter-clockwise. The third significant event occurs when the flow produced by the splash-up process impacts the water surface and creates a third cloud. Numerical models must be able to accurately predict the timing and nature of these events.

The time series of the ensemble void fractions, $\langle \alpha \rangle$, measured along the plunging wave had a similar pattern. Initially $\langle \alpha \rangle = 1.0$ because the probes were located above the still water level. Then, $\langle \alpha \rangle$ decreased and reached a first local minimum, as the probes passed through the forward face of the wave. Thereafter, $\langle \alpha \rangle$ increased to a local maximum once the probes traversed the bubble cloud. Next, $\langle \alpha \rangle$ decreased to a second local minimum as the probes passed out of the bubble cloud and finally, $\langle \alpha \rangle$ returned to a value of 1.0 when the probes re-entered the air on the back side of the wave. There were 13 measurement positions along the plunging wave and the peak void fractions measured inside the bubble cloud varied from 0.024 to 0.97; and the mean void fractions varied from 0.012 to 0.37. For the spilling wave case the time series of $\langle \alpha \rangle$ also displayed a consistent pattern. Initially, the probes were located

in air and $\langle \alpha \rangle = 1.0$, as the probe passed through the free surface $\langle \alpha \rangle$ decreased rapidly, then as the probes traversed the bubble cloud, $\langle \alpha \rangle$ decreased to a local minimum, and finally $\langle \alpha \rangle$ increased to 1.0 as the probes re-entered the air on the back side of the wave. Based on these time series of $\langle \alpha \rangle$ it was deduced that, for the spilling wave case, the void fraction contours run parallel to the free surface. There were 4 measurement positions along the spilling wave and the mean void fractions at these positions varied from 0.17 to 0.29. The speed of advance of the air cavity and the third cloud beneath the plunging wave were estimated to be ~ 75 and $\sim 90\%$ of the phase speed, respectively. For the spilling wave, the speed of advance of the bubble cloud was estimated to be $\sim 100\%$ of the phase speed. A comparison to previous measurements of the average void fraction beneath shoaling waves lead to the conclusion that similar air entrainment processes occur in beneath breaking waves in deep and shallow water when the void fraction is greater than ~ 0.05 .

In Chapter 4, the bubble size distribution measurements were presented. For the plunging wave case, the size distributions measured at the air cavity were found to be independent of the bubble size. Deane and Stokes (2002) proposed that two bubble creation mechanisms, air cavity fragmentation and jet and drop impact, govern the shape of the bubble size distribution. Measurements performed at locations where the void fraction was less than ~ 0.05 or very close to the lower edge of a the bubble cloud appear to support this theory. However, bubble size distributions measured inside the dense bubble cloud, that is, at locations where $\langle \alpha \rangle$ was greater than ~ 0.05 did not have slopes consistent with Deane and Stokes (2002) theory. Measurements taken at the location of the water jet impact suggested that the bubble size distributions were

independent from the bubble creation mechanism. In the splashing zone (i.e. the 3rd cloud) the results indicated that the bubble creation mechanism was the same as that observed previously beneath other types of splashing flows. The average size distribution measured underneath the plunging wave in this study was found to be have a similar slope to previous measurements of the size distribution made very close to the free surface in the ocean and freshwater. Furthermore, this average slope ($\beta \sim 1.5$) has also been observed previously in beneath shoaling waves in the laboratory. The average size distributions measured underneath the spilling wave are significantly different from some of the previous laboratory measurements. The most likely explanation for this discrepancy is differences in the measurement techniques used in the various studies. However, the average slope of the bubble size distribution measured beneath the spilling wave, for bubbles larger than $s \sim 2.7 \text{ mm}$, was similar to previously reported slopes in both the ocean and freshwater provided these other measurements were made very close to the free surface.

5.2 Recommendations for Future Work

In order to enhance our knowledge of the air entrainment process beneath breaking waves, the following studies are recommended. Efforts to improve numerical simulation of the air entrainment underneath breaking wave should be undertaken, and model predictions should be compared to the data provided in this experimental investigation. Also, it would be extremely valuable if the fiber-optic probes were deployed in the ocean and measurements of the void fraction and bubble size distribution were performed close to the free-surface, inside the dense bubble clouds.

Appendix A: Computer programs for void faction and bubble velocity calibrations

This appendix contains the computer programs used in Chapter 2. All programs were written in MATLAB V 7.0. Table A.1 gives an overview of the programs treated in the appendix.

Table A.1 Computer programs used in Chapter 2

Program name	Description
dataqvoidA.m	Acquires data from the bubble tank for void fraction calibration
readvoid.m	Reports the void fraction measured from the fiber-optic probes as well as the void fraction from the differential pesure transducer
voids	Subroutine to compute void fraction
goodimageK500_3.m	Main program for bubble velocity calibration. Acquires data from the flow cell and process the video images
fbub6_2.m	Subroutine to identify bubble signature points
ffastidAK.m	Displays images to determine if the bubble that produced a specific signal can be observed in 4 images
fsignature2.m	Subroutine that displays bubble signauure
ffastid100K.m	Computes bubble geometry: Area, centroid, Major Axis, Minor Axis. Image #1
ffastid2K.m	Converts the images to gray scale
ffastid31K.m	Displays a image and performs correction for non uniform illumination, conversion to a binaty image, erosions and dilatations.
opthr.m	This function finds the optimal threshold corresponding to a intensity image
velocities.m	Convert bubble size from pixels to cm
calibration_void	Calibrates differential pressure transducer and estimates and plot the bias, random and normalized errors on the void fraction measurements
figplotalP1_90.m	Plots rise time versus bubble velocity; and performs linear regression

Program: dataqvoidA.m

```

%
% Data acquisition for bubble tank
%
clear all
% CONSTANTS
FF=20000; % sampling frequency per channel
TT=5; % change to 3 or 4
TNS=FF*TT;
pointn= input(' Point # = ');
for ni=1:1
%for ni=pointn*10+1:pointn*10+5
    filename=sprintf('5%d',ni); % change to 3 or 4
    ai=analoginput('nidaq',1);
    addchannel(ai,[0:3]);
    ai.Channel.InputRange = [-10 10];
    set(ai,'SampleRate',FF);
    set(ai,'SamplesPerTrigger',TNS);
    start(ai);
    PT=getdata(ai,'native');
    save (filename,'PT');
    delete (ai)
    clear PT
end

```

Program: readvoid.m

```

%
% This program reads the data form the bubble
% tank and computes the mean
% void fraction
%
clear all
%Constants
HH=8+2.5/16;
a=5.004411;
b=-0.005336;
%
cc=0;
pointn= input(' Point # = ');
for ni=pointn*10+1:pointn*10+5
    VV=0;
    cc=cc+1;
    filename=sprintf('5%d',ni)
    load(filename);
    PT=double(PT);
    PH=PT(:,1);
    MM(cc,1)=((mean(PH)*20/2^16)*a-b)/HH;
    %
    P=PT(:,2);
    MM(cc,2)=voids(P);
    %
    P=PT(:,3);
    MM(cc,3)=voids(P);

```

```

%
P=PT(:,4);
MM(cc,4)=voids(P);
close all
clear PT
clear P
end
for i=1:4
    MM(cc+1,i)=mean(MM([1 5],i));
    MM(cc+2,i)=std(MM([1 5],i));
end
file2=sprintf('MM%d',pointn);
dlmwrite(file2,MM,'\t');

```

Program: voids.m

```

%
function vr = voids(V);
% histogram
hist(V)
a=min(V);
b=max(V);
c=b-a;
c;
thresh = 0.0;
%thresh=input('enter thresh value= ');
N=histc(V,a:thresh);
g=sum (N);
if thresh <=b
    M=histc(V,thresh:b);
    e=sum (M);
else
    e=0;
end
total=g+e;
if e > 0 & g > 0
    vr=(e/(g+e));
else
    vr = 0;
end
close all

```

Program: goodimageK500_3.m

```

% This program allows choosing the bubbles
% that can be individually identified for be used for
% calibration
% 1- Constants
clear all;
clc
close all
ups = 0;
%
ppm = input(' syn #');

```

```

fvelis = 0;
%
init = 4000;
%probe 1 UP1 90
syms = [1 1 1 1 2 2 3 3 3; % BG image
        1 1 1 3 1 1 3 1 1; % Initial point
        9 9 9 9 9 9 9 9 9; % Final point
        500 500 500 500 500 500 500 500 500; %
nfs
        37 0.100 262 400 590 782 840 902 902; %
Discharge (wd)
        1 1 0 1 1.64 -0.76 0 0 0; % probe calib dire
ups aa bb
        4 2 1 1 1 1 1 1 1]; % Lags
dirr=('I:\probe1-1U\');
dirrout=('I:\probe1-1U\');
dirrout2=('E:\Documents and Settings\German
Rojas\Desktop\figP1_90G\');
fr = [ 0.000 0.044 0.188 0.292 0.475 0.648
0.782 0.902 0.902; %1
        0.000 0.044 0.188 0.292 0.475 0.648 0.782
0.902 0.902; %2
        0.003 0.044 0.188 0.292 0.475 0.648 0.840
0.902 0.902; %3
        0.003 0.083 0.230 0.342 0.530 0.702 0.840
0.902 0.902; %4
        0.003 0.083 0.230 0.342 0.530 0.702 0.840
0.902 0.902; %5
        0.023 0.083 0.230 0.342 0.530 0.702 0.840
0.902 0.902; %6
        0.023 0.137 0.262 0.400 0.590 0.782 0.840
0.902 0.902; %7
        0.037 0.137 0.262 0.400 0.590 0.782 0.840
0.902 0.902; %8
        0.037 0.137 0.262 0.400 0.590 0.782 0.840
0.902 0.902; %9
];
fr = 1000*fr;
%
%probe 1 Up slow 1 90 (UP2)
syms = [1 1 1 1 1 1 1 1 1; % BG image
        1 1 1 1 1 1 1 1 1; % Initial point
        9 9 9 9 9 9 9 9 9; % Final point
        125 125 125 125 125 125 125 125;
        0 0 0 0 0 0 0 0;
        1 2 0 1 1.64 -0.76 0 0; % probe calib dire
ups aa b
        1 1 1 1 1 1 1 1 1];
dirr=('J:\probe1-slow\');
dirrout=('J:\probe1-slow\');
dirrout2=('E:\Documents and Settings\German
Rojas\Desktop\figP1_90H\');
%
%probe 1 UP3 90
%syms = [1 2 2 2 2 2 2 2 2; % BG image
%       1 1 1 1 1 1 1 1 1; % Initial point
%       9 9 9 9 9 9 9 9 9; % Final point
%       500 500 500 500 500 500 500 500 500; %
nfs
%       1604 1500 1401 1298 1201 1097 998 900
798; % Discharge (wd)
%       1 1 1 1 1.64 -0.76 0 0 0; % probe calib
dire ups aa bb
%       1 1 1 1 1 1 1 1 1];
%dirr=('D:\PROBE1-0-UP-1\');
%dirrout=('D:\PROBE1-0-UP-1\');
%       9 9 9 9 9 9 9 9 9; % Final point
%       500 500 500 500 500 500 500 500 500; %
nfs
%       1638 1527 1396 1308 1185 1098 1014 0
0; % Discharge (wd)
%       1 3 0 1 1.64 -0.76 0 0 0; % probe calib
dire ups aa bb
%       1 1 1 1 1 1 1 1 1]; % Lags
%dirr=('D:\P1_90_UP3\');
%dirrout=('D:\P1_90_UP3\');
%dirrout2=('E:\Documents and Settings\German
Rojas\Desktop\figP1_90G\');
%
%
%probe 1 Down1 90
%syms = [1 1 1 1 2 0; % BG image
%       1 1 1 1 3 0; % Initial point
%       9 9 6 9 9 0; % Final point
%       125 125 125 125 125 0;
%       199 199 296 296 399 0;
%       1 1 0 0 1.64 -0.76; % probe calib dire ups
aa b
%       1 1 1 1 1 1 1];
%dirr=('I:\PROBE 1\probe1-1D\');
%dirrout=('I:\PROBE 1\probe1-1D\');
%dirrout2=('E:\Documents and Settings\German
Rojas\Desktop\figP1_90B\');
%
%probe 1 Down2 90
%syms = [1 1 1 1 1 1 1 1 1; % BG image
%       1 1 1 1 1 1 1 1 1; % Initial point
%       9 9 9 9 9 9 9 9 9; % Final point
%       500 500 500 500 500 500 500 500;
%       1200 1200 1319 1313 1416 1414 1550
1550;
%       1 2 0 0 1.64 -0.76 0 0; % probe calib dire
ups aa b
%       1 1 1 1 1 1 1 1 1];
%dirr=('I:\PROBE 1\probe1-2 D\');
%dirrout=('I:\PROBE 1\probe1-2 D\');
%dirrout2=('E:\Documents and Settings\German
Rojas\Desktop\figP1_90\');
%
%probe 1 UP1 0
%syms = [1 1 1 1 1 1 2 2 2; % BG image
%       1 1 1 1 1 1 1 1 1; % Initial point
%       9 9 9 9 9 9 9 9 9; % Final point
%       500 500 500 500 500 500 500 500 500; %
nfs
%       1604 1500 1401 1298 1201 1097 998 900
798; % Discharge (wd)
%       1 1 1 1 1.64 -0.76 0 0 0; % probe calib
dire ups aa bb
%       1 1 1 1 1 1 1 1 1];
%dirr=('D:\PROBE1-0-UP-1\');
%dirrout=('D:\PROBE1-0-UP-1\');

```



```

%dirrout2=('E:\Documents and Settings\German
Rojas\Desktop\figP1_0F\');
%
%probe 1 UP2 0
%syns = [1 1 1 1 1 1 1 1 1; % BG image
% 1 1 1 1 1 1 1 1 1; % Initial point
% 9 9 9 9 9 9 9 9 9; % Final point
% 500 500 500 500 500 500 500 500 500; %
nfs
% 693 595 500 401 307 195 90 0 0; %
Discharge (wd)
% 1 2 1 1 1.64 -0.76 0 0 0; % probe calib
dire ups aa bb
% 1 1 1 1 2 2 3 4 0]; % Lags
%dirr=('C:\PROBE1-0-UP-2\');
%dirrout=('C:\PROBE1-0-UP-2\');
%dirrout2=('E:\Documents and Settings\German
Rojas\Desktop\figP1_0\');
%
%probe 1 UP3 0
%syns = [1 1 1 1 1 1 1 1 1; % BG image
% 1 1 1 1 1 1 1 1 1; % Initial point
% 9 9 9 9 9 9 9 9 9; % Final point
% 125 125 125 125 125 125 125 125 125; %
nfs
% 0 0 0 0 0 0 0 0 0; % Discharge (wd)
% 1 3 1 1 1.64 -0.76 0 0 0; % probe calib
dire ups aa bb
% 1 1 1 4 4 4 4 4 0]; % Lags
%dirr=('D:\P1_0_slow\');
%dirrout=('D:\P1_0_slow\');
%dirrout2=('E:\Documents and Settings\German
Rojas\Desktop\figP1_0\');
%
% probe 1 DOWN1 0
%syns = [1 1 1 1 0 0 0 0 0; % BG image
% 1 1 1 1 0 0 0 0 0; % Initial point
% 9 9 9 9 0 0 0 0 0; % Final point
% 125 125 125 125 0 0 0 0 0; % nfs
% 224 295 368 426 0 0 0 0 0; % Discharge
(wd)
% 1 1 1 0 1.64 -0.76 0 0 0; % probe calib
dire ups aa bb
% 2 2 2 2 2 2 2 2 2]; % Lags
%dirr=('I:\PROBE 1\probe1-ID\');
%dirrout=('I:\PROBE 1\probe1-ID\');
%dirrout2=('E:\Documents and Settings\German
Rojas\Desktop\figP1_0\');
%
% probe 2 UP1 90
%syns = [1 1 1 1 1 1 1 1 1; % BG image
% 1 1 1 1 1 1 1 1 1; % Initial point
% 9 9 9 9 9 9 9 9 9; % Final point
% 500 500 500 500 500 500 500 500 500; %
nfs

```

```

% 103 265 444 602 730 890 1035 1215
1410; % Discharge (wd)
% 2 1 0 1 1.68 -0.888 0 0 0; % probe calib
dire ups aa bb
% 3 1 1 1 1 1 1 1 1]; % Lags
%dirr=('K:\probe2-3U\'); % HD19 up
%dirrout=('K:\probe2-3U\');
%dirrout2=('E:\Documents and Settings\German
Rojas\Desktop\figP2_90E\');
%
% probe 2 UP2 90
%syns = [1 1 1 1 1 1 1 1 1; % BG image
% 1 1 1 5 1 1 1 1 1; % Initial point
% 9 9 6 9 9 9 9 9 9; % Final point
% 500 500 500 500 500 500 500 500 500; %
nfs
% 1013 1095 1200 1300 1404 1500 1620 0
0; % Discharge (wd)
% 2 2 0 1 1.68 -0.888 0 0 0; % probe calib
dire ups aa bb
% 1 1 1 1 1 1 1 1 1]; % Lags
%dirr=('K:\P2_90_2\');
%dirrout=('K:\P2_90_2\');
%dirrout2=('E:\Documents and Settings\German
Rojas\Desktop\figP2_90E\');
%
%probe 2 UP3 90 (slow)
%syns = [1 1 1 1 1 1 1 1 1; % BG image
% 1 1 1 1 1 1 1 1 1; % Initial point
% 9 9 4 9 9 9 9 9 9; % Final point
% 125 125 125 125 125 125 125 125 125; %
nfs
% 0 0 0 0 0 0 0 0 0; % Discharge (wd)
% 2 3 0 1 1.68 -0.888 0 0 0; % probe calib
dire ups aa bb::save = probe, ups,calib,ppm, filn
% 1 1 1 0 0 0 0 0 0]; % Lags
%dirr=('N:\probe2-slow\'); % HD19 up
%dirrout=('N:\probe2-slow\');
%dirrout2=('E:\Documents and Settings\German
Rojas\Desktop\figP2_90E\');
%
%probe 2 Down2 90
%syns = [1 1 1 1 2 2 2 2 2; % BG image
% 1 1 1 1 1 1 1 1 1; % Initial point
% 9 9 9 9 9 9 9 9 9; % Final point
% 125 125 125 125 125 125 125 125; % nfs
% 254 358 464 520 462 349 239 192; %
Discharge (wd)
% 2 2 0 0 1.68 -0.888 0 0 0; % probe calib dire
ups aa bb
% 2 2 2 1 1 1 1 1 1]; % Lags
%dirr=('K:\probe2-2D\'); % HD19 up
%dirrout=('K:\probe2-2D\');
%dirrout2=('E:\Documents and Settings\German
Rojas\Desktop\figP2_90E\');
%fr = [ 205 315 414 526 462 349 239 192 0; %I

```

```

% 205 315 414 526 462 349 239 192 0; %2
% 205 315 414 526 462 349 239 192 0; %3
% 205 315 414 526 462 349 239 192 0; %4
% 205 315 414 526 462 349 239 192 0; %5
% 254 358 464 520 406 294 192 178 0; %6
% 254 358 464 520 406 294 192 178 0; %7
% 254 358 464 520 406 294 192 178 0; %8
% 254 358 464 520 406 294 192 178 0; %9
%];

%
%
% probe 2-0 UP 1
%syns = [1 1 2 2 2 2 2 2 2; % BG image
% 1 1 1 1 1 1 1 1 1; % Initial point
% 9 9 9 9 9 9 9 9 9; % Final point
% 500 500 500 500 500 500 500 500 500; %
nfs
% 1603 1502 1400 1295 1200 1100 997 898
800; % Discharge (wd)
% 2 1 1 1 1.68 -0.888 0 0 0; % probe calib
dire ups aa bb
% 1 1 1 1 1 1 1 1]; % Lags
%dirr=('L:\PROBE2-0-UP-1\');
%dirrout=('L:\PROBE2-0-UP-1\');
%dirrout2=('E:\Documents and Settings\German
Rojas\Desktop\figP2_0\');
%
% probe 2-0 UP 2
%syns = [1 1 1 1 1 1 1 1 2; % BG image
% 1 1 1 1 1 1 1 1 1; % Initial point
% 9 9 9 9 9 9 9 9 9; % Final point
% 500 500 500 500 500 500 500 500 500; %
nfs
% 690 586 493 397 294 201 97 0 0; %
Discharge (wd)
% 2 2 1 1 1.68 -0.888 0 0 0; % probe calib
dire ups aa bb
% 1 1 1 1 1 2 2 3 4]; % Lags
%dirr=('L:\PROBE2-0-UP-2\');
%dirrout=('L:\PROBE2-0-UP-2\');
%dirrout2=('E:\Documents and Settings\German
Rojas\Desktop\figP2_0\');
%
% probe 2-0 UP 3
%syns = [1 1 1 0 0 0 0 0 0; % BG image
% 1 1 1 1 1 1 1 1 1; % Initial point
% 9 3 9 9 9 9 9 9 9; % Final point
% 125 125 125 125 125 125 125 125 125; %
nfs
% 0 0 0 0 0 0 0 0 0; % Discharge (wd)
% 2 3 1 1 1.68 -0.888 0 0 0; % probe calib
dire ups aa bb
% 2 2 2 2 2 2 2 2 2]; % Lags
%dirr=('N:\P2_0_slow\');
%dirrout=('N:\P2_0_slow\');

```

```

%dirrout2=('E:\Documents and Settings\German
Rojas\Desktop\figP2_0\');
%
% probe 2 down 1
%syns = [1 1 1 2 0 0 0 0 0; % BG image
% 1 1 1 1 1 1 1 1 1; % Initial point
% 9 9 9 9 9 9 9 9 9; % Final point
% 125 125 125 125 125 125 125 125 125; %
nfs
% 419 353 281 232 0 0 0 0 0; % Discharge
(wd)
% 2 1 1 0 1.68 -0.888 0 0 0; % probe calib
dire(0 degress) ups aa bb
% 3 2 2 2 2 2 2 2 2]; % Lags
%dirr=('L:\PROBE2-0-DOWN-1\');
%dirrout=('L:\PROBE2-0-DOWN-1\');
%dirrout2=('E:\Documents and Settings\German
Rojas\Desktop\figP2_0\');
%
%probe 3 UP1 90
%syns = [1 1 2 2 2 2 3 3 4; % BG image
% 1 1 1 3 1 1 3 1 1; % Initial point
% 9 9 9 9 9 9 9 9 9; % Final point
% 125 125 250 250 250 250 250 250 500; %
nfs
% 0 65 100 175 245 317 364 420 503; %
Discharge (wd)
% 3 1 0 1 1.54 -1.10 0 0 0; % probe calib
dire ups aa bb
% 1 1 1 1 1 1 1 1 1]; % Lags
%dirr=('D:\probe3-UP-1\');
%dirrout=('D:\probe3-UP-1\');
%dirrout2=('E:\Documents and Settings\German
Rojas\Desktop\figP3_90C\');
%
%probe 3 UP2 90
%syns = [1 1 2 3 3 4 0 0 0; % BG image
% 1 1 1 1 1 1 1 1 1; % Initial point
% 9 9 9 9 9 9 9 9 9; % Final point
% 500 500 500 500 500 500 500 500 500; %
nfs
% 600 672 732 835 835 910 0 0 0; %
Discharge (wd)
% 3 2 0 1 1.54 -1.10 0 0 0; % probe calib
dire ups aa bb
% 1 1 1 1 1 1 1 1 1]; % Lags
%dirr=('D:\probe 3-UP-2\');
%dirrout=('D:\probe 3-UP-2\');
%dirrout2=('E:\Documents and Settings\German
Rojas\Desktop\figP3_90C\');
%
%probe 3 UP3 90
%syns = [1 1 1 1 1 1 1 1 1; % BG image
% 1 1 1 1 1 1 1 1 1; % Initial point
% 9 9 9 9 9 9 9 9 9; % Final point

```

```

% 500 500 500 500 500 500 500 500 500; %
nfs
% 916 1006 1104 1200 1317 0 0 0 0; %
Discharge (wd)
% 3 3 0 1 1.54 -1.10 0 0 0; % probe calib
dire ups aa bb
% 1 1 1 1 1 1 1 1 1]; % Lags
%dirr=('K:\PROBE3-90-UP-3\');
%dirrout=('K:\PROBE3-90-UP-3\');
%dirrout2=('E:\Documents and Settings\German
Rojas\Desktop\figP3_90C\');
%
%
%probe 3 Up slow 90 (UP4)
%syms = [1 1 2 3 0 0 0 0; % BG image
% 1 1 1 1 1 1 1 1]; % Initial point
% 9 9 9 9 9 9 9 9; % Final point
% 125 125 125 125 125 125 125 125;
% 0 0 0 0 0 0 0 0;
% 3 4 0 1 1.64 -0.76 0 0; % probe calib dire
ups aa b
% 1 1 1 1 1 1 1 1]; %lags
%dirr=('D:\probe3-slow\');
%dirrout=('D:\probe3-slow\');
%dirrout2=('E:\Documents and Settings\German
Rojas\Desktop\figP1_90C\');
%
% probe 3-90-D -1
%syms = [1 1 2 2 3 2 4 4 4; % BG image
% 1 1 1 1 1 1 1 1 1]; % Initial point
% 9 9 9 9 9 9 9 9; % Final point
% 125 125 250 250 500 500 250 250 0; %
nfs
% 203 311 410 510 604 700 218 218 0; %
Discharge (wd)
% 3 1 0 0 1.54 -1.10 0 0 0; % probe calib
dire ups aa bb
% 1 1 1 1 1 1 1 1 1]; % Lags
%dirr=('D:\probe3-DOWN\');
%dirrout=('D:\probe3-DOWN\');
%dirrout2=('E:\Documents and Settings\German
Rojas\Desktop\figP3_90C\');
%
% probe 3-90-UP -1 B
%syms = [1 1 1 2 2 2 3 3 4; % BG image
% 1 1 1 1 1 1 2 1 1]; % Initial point
% 9 9 9 9 9 9 9 9 9]; % Final point
% probe 3-90-UP-2 B
%syms = [1 1 1 1 1]; % BG image
% 1 1 1 1 1]; % Initial point
% 9 9 9 9 9]; % Final point
%
% probe 3-0-UP -1
%syms = [1 1 1 1 2 2 2 2 2; % BG image
% 1 1 1 1 1 1 1 1 1]; % Initial point

```

```

% 9 9 9 9 9 9 9 9; % Final point
% 500 500 500 500 500 500 500 500 500; %
nfs
% 1604 1499 1398 1297 1204 1100 1000
903 800; % Discharge (wd)
% 3 1 1 1 1.55 -1.03 0 0 0; % probe calib
dire ups aa bb
% 1 1 1 1 1 1 1 1 1]; % Lags
%dirr=('M:\PROBE3-0-UP-1\');
%dirrout=('M:\PROBE3-0-UP-1\');
%dirrout2=('E:\Documents and Settings\German
Rojas\Desktop\figP3_0\');
%
% probe 3-0-UP -2
%syms = [1 2 2 2 2 2 2 2 2; % BG image
% 1 1 1 1 1 1 1 1 1]; % Initial point
% 9 9 9 9 9 9 9 9; % Final point
% 500 500 500 500 500 500 500 500 500; %
nfs
% 702 602 496 400 294 197 93 0 0; %
Discharge (wd)
% 3 2 1 1 1.55 -1.03 0 0 0; % probe calib
dire ups aa bb
% 1 1 1 1 1 2 2 3 4]; % Lags
%dirr=('M:\PROBE3-0-UP-2\');
%dirrout=('M:\PROBE3-0-UP-2\');
%dirrout2=('E:\Documents and Settings\German
Rojas\Desktop\figP3_0\');
%
% probe 3-0-DOWN -1
%syms = [1 1 1 1 1 1 1 1 1]; % BG image
% 1 1 1 1 1 1 1 1 1]; % Initial point
% 9 9 9 9 9 9 9 9 9; % Final point
% 125 125 125 125 125 125 125 125 125; %
nfs
% 401 347 302 238 193 174 0 0 0; %
Discharge (wd)
% 3 1 1 0 1.55 -1.03 0 0 0; % probe calib
dire(0 degress) ups aa bb::save = probe,
ups,calib,ppm, filn
% 3 2 2 2 2 2 2 2 2]; % Lags
%dirr=('M:\PROBE3-0-DOWN-1\');
%dirrout=('M:\PROBE3-0-DOWN-1\');
%dirrout2=('E:\Documents and Settings\German
Rojas\Desktop\figP3_0\');
%
% probe 3-0 UP 3
%syms = [0 0 1 0 0 0 0 0 0; % BG image
% 1 1 1 1 1 1 1 1 1]; % Initial point
% 9 3 9 9 9 9 9 9 9; % Final point
% 125 125 125 125 125 125 125 125 125; %
nfs
% 0 0 0 0 0 0 0 0 0; % Discharge (wd)
% 3 3 1 1 1.55 -1.03 0 0 0; % probe calib
dire ups aa bb
% 2 2 2 2 2 2 2 2 2]; % Lags

```

```

%dirr=('D:\P3_0_slow\');
%dirrout=('D:\P3_0_slow\');
%dirrout2=('E:\Documents and Settings\German
Rojas\Desktop\figP3_0\');
%for ppm = 1:9
%fvelis = 0;
%
nfs = syns(4,ppm);
wd= syns(5,ppm);
probe = syns(6,1);
calib = syns(6,2);
dire = syns(6,3);
ups = syns(6,4);
faa = syns(6,5);
fbb = syns(6,6);
lags = syns(7,ppm);
%
probess = [2.91 2.91 2.91];
format long
frq=100000;
nne = 1;
bbb =0;

ccbb =0;
%
%dirr = ('E:\Documents and Settings\German
Rojas\Desktop\PROBE 1\probe1-1D\');
%dirr=('E:\Documents and Settings\German
Rojas\Desktop\PROBE 2\probe2-3U\');
%dirrout
=('E:\MATLAB6p5\work\revision\P2\revision2\
);
ccf = 0;
clc
for filn = syns(2, ppm):syns(3, ppm) % Number
of Q's
%filn = input(' Run # (1..9) ');
if probe ==1 & dire == 0 & calib == 1
%%%%%%%%%%%%%for P1 UP1
DIR = 0
wd = fr(filn,ppm);
end
if probe ==2 & dire == 0
%%%%%%%%%%%%%
%%%%%%%%%%%%%for P2 DOWN2 DIR = 0
wd = fr(filn,ppm);
end

jk = syns(1, ppm);
if ups == 1
bname = sprintf('fsize%d%dU',probe,jk);
else
bname = sprintf('fsize%d%dD',probe,jk);
end
load (strcat(dirr,bname));

```

```

file0 =
sprintf('BG/BG%d_%d%d%d%d.tif',jk,0, 0,
0, 0, 0);
file0 = strcat(dirr,file0);
a0 = imread(file0);
a0 = double(a0)/255;
if dire == 1
scal = abs(xr(1)-xr(2));
else
scal = abs(yr(1)-yr(2));
end
if ups == 0
a0 =
imrotate(a0,180);%%%%%%%%%%
end
%
factor = probess(probe)/scal;% [mm]
filename =
sprintf('fop/syn%d/D%d.txt',ppm*100,filn);
V1 = load(strcat(dirr,filename));
filelim=min(2048/nfs*frq, length(V1)-1);
V = V1(2:filelim);
[SA xx0 VLS] = fbub6_2(dirr,V1, filn, ppm,
frq,nfs, filelim, init);
xxx1 = floor(xt)-10;
xxx2 = floor(xt)+10;
wv = wd/2.5/2.5;
if ups == 1
dist12 =
floor(1.2*(2*lags*(wv+30))/(nfs)*10*1/factor));
else
dist12 = floor(1.2*(2*lags*(wv-
30))/(nfs)*10*1/factor));
end
yyy2 = floor(yt)+dist12;
if yyy2 > 210
yyy2 = 210;
end
if SA~=0
A=zeros(1,5);
stt = (SA(:,1))*frq;
s = floor(stt/(frq/nfs));
mm = length(SA(:,4));
cvb = 0;
jhh = [1:size(SA,2)];
filtbox11=ones(210,240);
for tt = 1: mm
close all
% FILTBOX A
filtbox11 = ones(210,240);
%
% FILTBOX B
%%%%%%%%%%
for Probe2 UP 3
%filtbox11 = zeros(210,240);
%filtbox11(5:160, 10:ceil(xt)+50)=1;

```

```

%filtbox11(ceil(min(yr(1),yr(2))):floor(max(yr(1
),yr(2))),1:floor(min(xr(1),xr(2))))=0;
%ba = ceil(max(yr(1),yr(2)));
%mmx = (ba-yt)/(xt-min(xr(1),xr(2)));
%for xtr = min(xr(1),xr(2)):ceil(xt)
% yxu = ceil(ba-mmx*(xtr-
min(xr(1)))));
% filtbox11(floor(yt-(yxu-yt)):yxu,
ceil(xtr)=0;
%end
[ok11(tt) sst cords] =
ffastidAK(ups,nfs, dirr,s(tt),ppm,filn, a0,
xt,yt,wd,factor,xxx1,xxx2,yyy2, filtbox11);
if ok11(tt) == 1
IFT = ((SA(tt,1)*nfs));
IFT1 = sprintf('%0.5g',IFT);
nam = strcat(IFT1);
%
st1 = s(tt); % FOP
avisol = sprintf('Point #%%d #bub =
%%d/%%d',filn, tt,mm);
disp(avisol);
avisoz = sprintf('bubble # =
%%d',ccf+1);
disp(avisoz);

tA = (SA(tt,6));
tB = (SA(tt,7));
tC = (SA(tt,8));
tD = (SA(tt,9));
tE = (SA(tt,10));
VGS = (SA(tt,11));
LL1 = (SA(tt,12));
LL2 = (SA(tt,13));
numbins = (SA(tt,14));
nums1 = (SA(tt,15));
nums2 = (SA(tt,16));
fsignature2(V, tA, tB, tC, tD, tE, VGS,
VLS, LL1, LL2, tt, numbins, nums1, nums2);
%[b1 st bb11] = ffastid1K(nfs,dirr,st1,
xt, yt,ppm,filn, a0, filtbox11); % 1st image
[b1 st bb11] =
ffastid100K(ups,nfs,dirr,st1, xt, yt,ppm,filn, a0,
filtbox11); % 1st image
if st ~= 0 & bb11 ~=0
[b2 b3 b4 b5] =
ffastid2K(ups,dirr,st, xt, yt, lags, a0,ppm,filn);
%filtbox = ones(210,240);
fvelis = fvelis*10/factor/nfs*lags;
[MMBB, NNBB, expl, ok1, ok2] =
ffastid31k(ups,bb11,b1,b2, b3, b4, b5, xt, yt,
filtbox11, fvelis, yyy2);
%
% Velocity computations
%
if ok1 == 1 & ok2 ==1
[Vel] = velocities(ups,MMBB,
NNBB, factor, nfs,lags,SA(tt,3));
ccf = ccf +1;
% FOP + factor + velocities
AD(ccf,1) = SA(tt,1); % start
[sec]
AD(ccf,2) = SA(tt,2); % residence
[ms]
AD(ccf,3) = SA(tt,3); % rise [ms]
AD(ccf,4) = sst; % first image
AD(ccf,5) = factor;
AD(ccf,6) = 0; % explotes?
AD(ccf,7:10) = Vel(1,1:4); %
distancesX-1 - mm
AD(ccf,11:14) = Vel(2,1:4); %
distancesX-2
AD(ccf,15:18) = Vel(3,1:4); %
distancesX-3
AD(ccf,19:22) = Vel(1,5:8); %
distancesY-1
AD(ccf,23:26) = Vel(2,5:8); %
distancesY-2
AD(ccf,27:30) = Vel(3,5:8); %
distancesY-3
AD(ccf,31:34) = Vel(1,9:12); %
velocityX-1 - %[cm/s]
AD(ccf,35:38) = Vel(2,9:12); %
velocityX-2
AD(ccf,39:42) = Vel(3,9:12); %
velocityX-3
AD(ccf,43:46) = Vel(1,13:16); %
velocityY-1
AD(ccf,47:50) = Vel(2,13:16); %
velocityY-2
AD(ccf,51:54) = Vel(3,13:16); %
velocityY-3
AD(ccf,55:59) = SA(tt,6:10); %
tA, tB, tC, tD, tE
AD(ccf,60:64) = SA(tt,17:21); %
V(tA)...V(tE)
AD(ccf,65) = probe;
AD(ccf,66) = calib; % Calibration
AD(ccf,67) = ppm; % syn
AD(ccf,68) = filn; % run 1 to 9
AD(ccf,69) = nfs;
AD(ccf,70) = dire; % Probe
direction 0 degrees (y==1)
AD(ccf,71) = ups; % Flow up?
(y==1);
AD(ccf,72) = lags; % lagged
frames (5,6,7 or 8);
AD(ccf,73) = fvelis; % min vel
[cm/s] between frames
AD(ccf,74) = wd; % discharge

```

```

        AD(ccf,75) = jk; % background
image      AD(ccf,76) = tt; % bubble #
           AD(ccf,77) = SA(tt,17);
%V(timeA'); AD(ccf,78) = SA(tt,18);
%V(timeB'); AD(ccf,79) = SA(tt,19);
%V(timeC'); AD(ccf,80) = SA(tt,20);
%V(timeD'); AD(ccf,81) = SA(tt,21);
%V(ends'); %bb1
           AD(ccf,82) =
factor^2*MMBB(1,1); % Area mm2
           AD(ccf,83:86) =
factor*MMBB(1,2:5); % % CX mm CY mm Mj
1 - mm Mn 1 - mm
           AD(ccf,87:90) =
factor*NNBB(1,:); % bounding box
           %bb2
           AD(ccf,91) =
factor^2*MMBB(2,1); % Area mm2
           AD(ccf,92:95) =
factor*MMBB(2,2:5); % CX mm CY mm Mj 1 -
mm Mn 1 - mm
           AD(ccf,96:99) =
factor*NNBB(2,:); % bounding box
           %bb3
           AD(ccf,100) =
factor^2*MMBB(3,1); % Area mm2
           AD(ccf,101:104) =
factor*MMBB(3,2:5); % CX mm CY mm Mj 1 -
mm Mn 1 - mm
           AD(ccf,105:108) =
factor*NNBB(3,:); % bounding box
           %bb4
           AD(ccf,109) =
factor^2*MMBB(4,1); % Area mm2
           AD(ccf,110:113) =
factor*MMBB(4,2:5); % CX mm CY mm Mj 1 -
mm Mn 1 - mm
           AD(ccf,114:117) =
factor*NNBB(4,:); % bounding box
           %bb5
           AD(ccf,118) =
factor^2*MMBB(5,1); % Area mm2
           AD(ccf,119:122) =
factor*MMBB(5,2:5); % CX mm CY mm Mj 1 -
mm Mn 1 - mm
           AD(ccf,123:126) =
factor*NNBB(5,:); % bounding box
           AD(ccf,127) =
10^faa*AD(ccf,3)^fbb;
           AD(ccf,128) = faa;

        AD(ccf,129) = fbb;
        AD(ccf,131) = xt;
        AD(ccf,132) = yt;
        AD(ccf,133) = cords;
        end % ok1 and ok2
        end % st
        clear b1 b2 b3 b4 b5
        %else
        %AD(tt,1:129)=zeros(1,129);
        end % ok1

        end % tt
        clear SA SAA
        %else
        %AD = zeros(1,129);
        end % SA
    end % filn
%
if ups == 1
    filenameS = sprintf('goodimageU-%d-%d-
%d',probe,calib,ppm);
    else
        filenameS = sprintf('goodimageD-%d-%d-
%d',probe,calib,ppm);
    end
    %files = strcat(dirrout, filenameS);
    %save (files,'AD')
    files2 = strcat(dirrout2, filenameS);
    save (files2,'AD')
    if AD(1,1)~=0
        h = figure;
        V11= (AD(:,36).^2+AD(:,48).^2).^0.5;
        figure
        loglog(AD(:,3),V11,'r',AD(:,3),10^AD(1,128)*
AD(:,3).^AD(1,129),'b')
        axis([10^-2 10^1 1 1000])
    end

Program: fbub6_2.m

function [SA,xx0, thresh] = fbub6_2(dirr,V1,
filn, ppm, frq,nfs, filelim, init)
numsect=1;
SC=1.2;
thradj = 120/2^12*10;largev =
500/2^12*10;gdrop = -20/2^12*10;
gav = 800/2^12*10; gsigma = 100/2^12*10;
gslope = 10/2^12*10;
VL = -335/2^12*10;
V = V1(2:filelim);
VL=min(V);
thresh=VL+thradj ;
bbb=0;
bubnum = 0;

```

```

% 4- set the VL value and threshold Value
(threshold = VL+120) for best results
k=1;
i=init; % for t = 9; vector position = 10
VBhalf=thresh-VL;
VBC=SC*VBhalf;
lim=filelim-10;
while (i<=lim) % A1
    while ((i<=lim)&(V(i)>=thresh)) % A5
        i=i+1;
        if (V(i)>=(thresh+largev)) % A6
            ok=1;
            nn2=i;
            n2=i+5;
        end % A6
    end % A5
% 4- Look for the start of bubble
while ((i<=lim)&(V(i)<=thresh)) % A2
    i=i+10;
end % A2
for j=1:10 % A3
    jj=i-11+j;
    if (V(jj)<=thresh) % A4
        tA=jj+1;
    end % A4
end % A3
n1=i-11;
ok=0;
% 5- Look for the end of bubble
while ((i<=lim)&(V(i)>=thresh)) % A5
    i=i+1;
    nend = i;
    if (V(i)>=(thresh+largev)) % A6
        ok=1;
        nn2=i;
        n2=i+5;
    end % A6
end % A5
% 6- Doing Calculation for the bubble (if large
enough)
% Figure out bins for histogram, with resolution
not less than 2*VBC
if (ok==1) % A7
    hi=max(V(tA:nn2));
    lo=min(V(tA:nn2));
    avgbin = ((hi-lo)/(2*VBC));
    if (avgbin < 1)
        numbin=2;
    else
        numbin = (floor(avgbin)+1);
    end
    [numa,Xsa]=hist(V(tA:nend),numbin);
    [num,Xs]=hist(V(tA:nn2),numbin);
    [Y,I]=sort(num);
    ch1='y';
    ch2='n';
% 7- Bubble is too small
elseif (ok==0) % A7
    ch1='n';
    ch2='n';
end % A7
% 8- Value of VG (max Value) is chosen from
Histogram
loop=0;
while ((loop==0) & (i<lim) & (ok==1)) % A8
    VG=Xs(l(numbin));
    DV=VG-thresh;
    L1=thresh+0.1*DV;
    L2=thresh+0.9*DV;
% 9- Find the characteristic points C & D
j=tA;
tD=-1;
found=0;
while (tD<0) % A9
    if (V(j)>=L2) % A10
        diff1=V(j)-L2;
        diff2=L2-V(j-1);
        if (diff1<=diff2) % A11
            tD=j;
        elseif (diff1>diff2) % A11
            tD=j-1;
        end % A11
    elseif (V(j)>=L1 & found==0) % A10
        diff1=V(j)-L1;
        diff2=L1-V(j-1);
        if (diff1<=diff2) % A12
            tC=j;
        else % A12
            tC=j-1;
        end % A12
        found=1;
    end % A10
    j=j+1;
end % A9
% 10- Find the characteristic point B
tB=-1;
j=nn2;
while tB<0 % A13
    if V(j)>=L2 % A14
        tB=j+1;
        drop=V(tB)-V(tB-1);
        while (drop<gdrop) % A15
            tB=tB-1;
            drop=V(tB)-V(tB-1);
        end % A15
    end % A14
    j=j-1;
end % A13
loop=1;
% 11- Check that the bubble is with good
signature and then do its calculations
av=mean(V(tD:tB));

```

```

Sigma=std(V(tD:tB));
slope=(V(tA-1)-V(tD+1))/((tA-1)-(tD+1));
if ((av>=gav)& (Sigma<=gsigma)&
(slope>=gslope)) & max(V(tA:tB))<=9.6
    bbb = bbb+1;
    sig(k)=tA-1; % real time = position - 1
    sig(k+1)=tB-1;
    sig(k+2)=tC-1;
    sig(k+3)=tD-1;
    sig(k+4)=(V(tD)-V(tC))/(tD-tC);
    k=k+5;
    ends(bbb) = nend;
    xx0(((k-1)/5),:) = [tA-100 nend+100];
    VGS(bbb) = VG;
    LL1(bbb) = L1;
    LL2(bbb) = L2;
    numbins(bbb) = numbin;
    numsl(bbb) = numa(length(num));
    numsl2(bbb) = numa(1);
end
end % A8
end % A1
dt=1/frq;
bubnum=(k-1)/5;
if bubnum > 0
    for i=1:bubnum
        inc=5*(i-1);
        A=inc+1;
        B=inc+2;
        C=inc+3;
        D=inc+4;
        E=inc+5;
    % 2- read the times and calculate the Trgr and Ts
        start(i)=sig(A)*dt;
        gas(i)=(sig(B)-sig(A))*dt*1000;
        rise(i)=(sig(D)-sig(C))*dt*1000;
        velo(i) = sig(E);
        timeA(i) = sig(A);
        timeB(i) = sig(B);
        timeC(i) = sig(C);
        timeD(i) = sig(D);
        % slope(i)=sig(inc+5);
    end
    % 3- The format of writing and saving the times
    in an output file
        rang1=1;
        rang2=bubnum;
    %disp(sprintf('Number of bubbles %d',bubnum))
        rang=(rang1:rang2);
        st=start(rang);
        gs=gas(rang);
        rs=rise(rang);
        ve=velo(rang);
        %
        sz1=size(st);
        sz2=size(gs);

```

```

sz3=size(rs);
%
ttA(1:sz1(2),1)= st'; % in secs
ttA(1:sz2(2),2)=gs';
ttA(1:sz3(2),3)=rs';
ttA(1:sz3(2),4)=(ttA(1:sz1(2),1)*nfs/1000); %
if t = 0 then frame = 0.
    ttA(1:sz3(2),5)=ve';
    ttA(1:sz3(2),6)=timeA';
    ttA(1:sz3(2),7)=timeB';
    ttA(1:sz3(2),8)=timeC';
    ttA(1:sz3(2),9)=timeD';
    ttA(1:sz3(2),10)=ends';
    ttA(1:sz3(2),11)=VGS';
    ttA(1:sz3(2),12)=LL1';
    ttA(1:sz3(2),13)=LL2';
    ttA(1:sz3(2),14)=numbins';
    ttA(1:sz3(2),15)=numsl1';
    ttA(1:sz3(2),16)=numsl2';
    ttA(1:sz3(2),17)=V(timeA');
    ttA(1:sz3(2),18)=V(timeB');
    ttA(1:sz3(2),19)=V(timeC');
    ttA(1:sz3(2),20)=V(timeD');
    ttA(1:sz3(2),21)=V(ends');
    % FILE SAVE
    % (1) Time start
    % GAS RESIDENCE TIME (2) = B-A
    % RISE TIME (3) = D-C
    % IMAGE NUMBER (4)
    ni = filn;
    fname1=sprintf('Calhsc%d%d.xls',ppm, filn);
    fname = strcat(dirr,fname1);
    save(fname,'ttA','-ascii');
    SA = ttA;
else
    SA = 0;
    xx0 = 0;
end

```

Program: fastidAK.m

```

function [ok1, sst, cords] = ffastidAK(ups,nfs,
dirr,st1,ppm,filn, a0,
xt,yt,wd,factor,xxx1,xxx2,yyy2, filtbox);
%
ok1 = 0;
bb11 = 0;
cords = 0;
sst = 0;
wv = wd/2.5/2.5;
b1 =0; st =0;
if nfs == 125 | nfs == 250
    sst = [st1];
end
if nfs == 500

```



```

%subplot(2,3,1), subimage(b1);hold on;
%axis off;
%line(xt,1:210, 'Color', 'g');
%line(1:240,yt, 'Color', 'g');
%tit = sprintf('B1 = %d',bb11);
%title(tit)
%hold on;
%for ix=1:N
% fbubble=sprintf('%d',ix);
% if ix ~= bb11
%
text(centrex1(ix,1)+25,centrey1(ix,1),fbubble,'C
olor','b', 'FontSize',8);
% else
%
text(centrex1(ix,1)+25,centrey1(ix,1),fbubble,'C
olor','r', 'FontSize',10);
% end
%end
%hold on;
%line(1:240,yyy2, 'Color', 'b');
%hold on
%line(1:240,yt-10, 'Color', 'b');
%hold on
%ad = floor(NB(bb11,1,1)-10);
%if ad <= 0
% ad = 1;
%end
%line(ad,1:240,'Color', 'b')

%line(ceil(NB(bb11,1,1)+NB(bb11,3,1))+10,1:2
40,'Color', 'b')
%ok1
%subplot(2,3,2), subimage(b2);
%hold on;
%pause
end%
end % centery1
end % bb11

```

Program: fsignature2.m

```

function fsignature2(V, tA, tB, tC, tD, tE, VGS,
VLS, LL1, LL2, bbb, numbin, nums1,nums2);

%xx0(((k-1)/5),:) = [tA-100 tB+100];
if tA == tC
tC = tC + 1;
end
xx1 = [tA tC]; yy1 = [V(tA) V(tC)];
xx2 = [tC tD]; yy2 = [V(tC) V(tD)];
xx3 = [tD tB]; yy3 = [V(tD) V(tB)];
xx4 = [tB tE]; yy4 = [V(tB) V(tE)];
xx5 = [tA tE]; yy5 = [VGS VGS];
xx6 = [tA tE]; yy6 = [LL2 LL2];

```

```

xx7 = [tA tE]; yy7 = [LL1 LL1];
xx8 = [tA tE]; yy8 = [VLS VLS];
xx9 = [tA tE]; yy9 = [0.9*(V(tB)- V(tA))+V(tA)
0.9*(V(tB)-V(tA))+V(tA)];
xx10 = [tA tE]; yy10 = [0.1*(V(tB)-
V(tA))+V(tA) 0.1*(V(tB)-V (tA))+V(tA)];
%
%
hf = figure;
tty = tD-tC;
plot((tA-100:tE+100)/100000,V(tA-
100:tE+100),'k');
hold on
tit = sprintf('Bubble # %d', bbb );
%title(tit);hold on;
plot((tA-1)/100000,V(tA-1),'k*', (tC-
1)/100000,V(tC-1),'k*', (tD-1)/100000,V(tD-
1),'k*', (tB-1)/100000,V(tB-1),'k*'); hold on
text((tA+20)/100000,V(tA-1),'t_A'); hold on;
text((tC+20)/100000,V(tC-1),'t_C'); hold on;
text((tD+20)/100000,V(tD-1),'t_D'); hold on;
text((tB+20)/100000,V(tB-1),'t_B'); hold on;
%text(tE+20,V(tE-1),'tE'); hold on;
xlabel('Time(sec)')
ylabel('Voltage (V)')
set(gcf,'Color', [1 1 1])
%hold on
%subplot(1,2,2)
%hist(V(tA:tE),numbin)
%[num,Xsa]=hist(V(tA:tE),numbin);
%tit = sprintf('H1/H2 =
%0.5g',num(length(num))/num(1));
%title(tit)
pause
close (hf)

```

Program: ffastid100K.m

```

function [b1,st, bb11] =
ffastid100K(ups,nfs,dirr,st1, xt, yt,ppm,filn, a0,
filtbox11)
%
b1 =0; st =0; bb11=0;
if nfs == 125 | nfs == 250
sst = [st1 st1+1 st1+2];
end
if nfs == 500
sst = [st1+1 st1+2 st1+3];
end
if st1 >= 2043
sst = [2045 2046 2047];
end
if st1 <= 3
sst = [0 1 2];
end

```

```

for ppt = 1:size(sst,2)
    s1 = num2str(sst(ppt)); ss = size(s1);
    ss1 = ss(1,2); pos = ss1+1;
    for i = 5:-1:1
        pos = pos-1;
        if pos > 0
            s1(pos);
            A(ppt,i)=str2double(s1(pos));
        end
    end
end
file111
=sprintf('syn%d/%d/E%d_%d%d%d%d%d.tif',p
pm,filn,filn,A(1,1),A(1,2),A(1,3),A(1,4),A(1,5));
file1 = strcat(dirr,file111)
a1 = imread(file1);
if ups == 0
%
    a1 = imrotate(a1,180);
end
%
a1 = double(a1)/255;
b11 = 1-abs(a0-a1);
st = sst(1);
b1 = b11;
%
dist1 = 10000;
T1 = opthr(b1);
b111 = im2bw(b1,T1);
b111 = abs(double(b111)-1);
b111 = b111.*filtbox11;
b111 = imfill(b111,'holes');
SE = strel('octagon',3);
b111 = imerode(b111,SE);
b111 = imdilate(b111,SE);
[b1label, N] = bwlabel(b111,4);
geochar1 = imfeature(b1label,'Area',
'centroid','MajorAxisLength','MinorAxisLength',
'BoundingBox' );
for kk = 1:N
    MB(kk,1,1) = geochar1(kk).Area;
    MB(kk,2,1) = geochar1(kk,1).Centroid(1);
    centrex1(kk,1) = MB(kk,2,1);
    MB(kk,3,1) = geochar1(kk,1).Centroid(2);
    centrey1(kk,1) = MB(kk,3,1);
    MB(kk,4,1) =
    geochar1(kk).MajorAxisLength;
    MB(kk,5,1) =
    geochar1(kk).MinorAxisLength;
    NB(kk, :, 1) = geochar1(kk).BoundingBox;
    dist11 = ((centrex1(kk,1)-xt)^2 +
(centrey1(kk,1)-yt)^2)^0.5;
    if (dist11 <= dist1) & ( centrex1(kk,1)<xt*1.2)
    & ( centrey1(kk,1)>xt*0.8)
        dist1 = dist11;
        bb11 = kk;
    end
end

```

```

end
end

```

Program: ffastid2k.m

```

function [b2,b3,b4, b5] = ffastid2K(ups,dirr,st,
xt, yt, lags, a0,ppm,filn)
%
%if st >= 2015
% st = 2015;
%end
if st-4*lags < 0
    st = 4*lags;
end
sst = [st-lags st-2*lags st-3*lags st-4*lags];
for ppt = 1:size(sst,2)
    s1 = num2str(sst(ppt)); ss = size(s1);
    ss1 = ss(1,2); pos = ss1+1;
    for i = 5:-1:1
        pos = pos-1;
        if pos > 0
            s1(pos);
            A(ppt,i)=str2double(s1(pos));
        end
    end
end
file111
=sprintf('syn%d/%d/E%d_%d%d%d%d%d.tif',p
pm,filn,filn,A(1,1),A(1,2),A(1,3),A(1,4),A(1,5));
file1 = strcat(dirr,file111);
file112
=sprintf('syn%d/%d/E%d_%d%d%d%d%d.tif',p
pm,filn,filn,A(2,1),A(2,2),A(2,3),A(2,4),A(2,5));
file2 = strcat(dirr,file112);
file113
=sprintf('syn%d/%d/E%d_%d%d%d%d%d.tif',p
pm,filn,filn,A(3,1),A(3,2),A(3,3),A(3,4),A(3,5));
file3 = strcat(dirr,file113);
file114
=sprintf('syn%d/%d/E%d_%d%d%d%d%d.tif',p
pm,filn,filn,A(4,1),A(4,2),A(4,3),A(4,4),A(4,5));
file4 = strcat(dirr,file114);
a1 = imread(file1); a2 = imread(file2); a3 =
imread(file3); a4 = imread(file4);
if ups == 0
%
    a1 = imrotate(a1,180);
    a2 = imrotate(a2,180);
    a3 = imrotate(a3,180);
    a4 = imrotate(a4,180);
end
%
a1 = double(a1)/255; a2 = double(a2)/255; a3 =
double(a3)/255; a4 = double(a4)/255;

```

```
b2 = 1-abs(a0-a1); b3 = 1-abs(a0-a2); b4 = 1-
abs(a0-a3); b5 = 1-abs(a0-a4);
```

Program: ffastid31K.m

```
function [MMBB, NNBB, expl, ok1, ok2] =
ffastid31k(ups,bb11, b1,b2, b3, b4, b5, xt, yt,
filtbox,fveli, xxx2)
%
ok1 = 1; ok2 =1;
expl = 0;
M = 0;
MMBB = zeros(5,5);
NNBB = zeros(5,4);
bb = zeros(5);
bb12 =0; bb13 = 0; bb14 = 0; bb15 = 0;
%h2 = figure;
%aw = [100 100 600 400];
%set(h2,'Position',aw);
%hold on;
%
% Image 1
%
dist1 = 10000;
T1 = ophtr(b1);
b1 = im2bw(b1,T1);
b1 = abs(double(b1)-1);
b1 = double(b1).*filtbox;
b1 = imfill(b1,'holes');
SE = strel('octagon',3);
b1 = imerode(b1,SE);
b1 = imdilate(b1,SE);
[b1label, N] = bwlabel(b1,4);
NN(1) =N;
geochar1 = imfeature(b1label,'Area',
'centroid','MajorAxisLength','MinorAxisLength',
'BoundingBox' );
for kk = 1:N
    MB(kk,1,1) = geochar1(kk).Area;
    MB(kk,2,1) = geochar1(kk,1).Centroid(1);
    centrex1(kk,1) = MB(kk,2,1);
    MB(kk,3,1) = geochar1(kk,1).Centroid(2);
    centrey1(kk,1) = MB(kk,3,1);
    MB(kk,4,1) =
    geochar1(kk).MajorAxisLength;
    MB(kk,5,1) =
    geochar1(kk).MinorAxisLength;
    NB(kk,.,1) = geochar1(kk).BoundingBox;
end
%
% Image 2
%
dist1 = 10000;
T2 = ophtr(b2);
b2 = im2bw(b2,T2);
```

```
b2 = abs(double(b2)-1);
b2 = double(b2).*filtbox;
b2 = imfill(b2,'holes');
SE = strel('octagon',3);
b2 = imerode(b2,SE);
b2 = imdilate(b2,SE);
[b1label, N] = bwlabel(b2,4);
NN(2) =N;
geochar1 = imfeature(b1label,'Area',
'centroid','MajorAxisLength','MinorAxisLength',
'BoundingBox' );
for kk = 1:N
    MB(kk,1,2) = geochar1(kk).Area;
    MB(kk,2,2) = geochar1(kk,1).Centroid(1);
    centrex1(kk,2) = MB(kk,2,2);
    MB(kk,3,2) = geochar1(kk,1).Centroid(2);
    centrey1(kk,2) = MB(kk,3,2);
    MB(kk,4,2) =
    geochar1(kk).MajorAxisLength;
    MB(kk,5,2) =
    geochar1(kk).MinorAxisLength;
    NB(kk,.,2) = geochar1(kk).BoundingBox;
    dist11 = ((centrex1(kk,2)-MB(bb11,2,1))^2 +
    (centrey1(kk,2)-MB(bb11,3,1))^2)^0.5;
    %if ups ==1
        if (dist11 <= dist1) &
        (centrey1(kk,2)>centrey1(bb11,1)+fveli) %
        (centrex1(kk,2) >= NB(kk,1,1) & centrex1(kk,2)
        <= NB(kk,1,1) + NB(kk,3,1))% if up flow
            dist1 = dist11;
            bb12 = kk;
        end
    %else
        % if (dist11 <= dist1) &
        (centrey1(kk,2)<centrey1(bb11,1)+fveli)
        % dist1 = dist11;
        % bb12 = kk;
    %end
    %end
end
% Image 3
%
dist1 = 10000;
T3 = ophtr(b3);
b3 = im2bw(b3,T3);
b3 = abs(double(b3)-1);
b3 = double(b3).*filtbox;
b3 = imfill(b3,'holes');
SE = strel('octagon',3);
b3 = imerode(b3,SE);
b3 = imdilate(b3,SE);
[b1label, N] = bwlabel(b3,4);
NN(3) =N;
geochar1 = imfeature(b1label,'Area',
'centroid','MajorAxisLength','MinorAxisLength',
'BoundingBox' );
```

```

for kk = 1:N
    MB(kk,1,3) = geochar1(kk).Area;
    MB(kk,2,3) = geochar1(kk,1).Centroid(1);
    centrex1(kk,3) = MB(kk,2,3);
    MB(kk,3,3) = geochar1(kk,1).Centroid(2);
    centrey1(kk,3) = MB(kk,3,3);
    MB(kk,4,3) =
    geochar1(kk).MajorAxisLength;
    MB(kk,5,3) =
    geochar1(kk).MinorAxisLength;
    NB(kk,:,3) = geochar1(kk).BoundingBox;
    if bb12 ~=0
        dist11 = ((centrex1(kk,3)-MB(bb12,2,2))^2
+ (centrey1(kk,3)-MB(bb12,3,2))^2)^0.5;
        %if ups == 1
            if (dist11 <= dist1) &
(centrey1(kk,3)>centrey1(bb12,2)+fveli) %&
(centrex1(kk,3) >= NB(kk,1,2) & centrex1(kk,3)
<= NB(kk,1,2) + NB(kk,3,2))% if up flow
                dist1 = dist11;
                bb13 = kk;
            end
            %else
            %if (dist11 <= dist1) &
(centrey1(kk,3)<centrey1(bb12,2)+fveli)
                % dist1 = dist11;
                % bb13 = kk;
            %end
            %end
        else
            bb13 = 0;
        end
    end
    %
    dist1 = 10000;
    T4 = opthr(b4);
    b4 = im2bw(b4,T4);
    b4 = abs(double(b4)-1);
    b4 = double(b4).*filtbox;
    b4 = imfill(b4,'holes');
    SE = strel('octagon',3);
    b4 = imerode(b4,SE);
    b4 = imdilate(b4,SE);
    [b1label, N] = bwlabel(b4,4);
    NN(4) =N;
    geochar1 = imfeature(b1label,'Area',
'centroid','MajorAxisLength','MinorAxisLength',
BoundingBox');
    for kk = 1:N
        MB(kk,1,4) = geochar1(kk).Area;
        MB(kk,2,4) = geochar1(kk,1).Centroid(1);
        centrex1(kk,4) = MB(kk,2,4);
        MB(kk,3,4) = geochar1(kk,1).Centroid(2);
        centrey1(kk,4) = MB(kk,3,4);
        MB(kk,4,4) =
        geochar1(kk).MajorAxisLength;
        MB(kk,5,4) =
        geochar1(kk).MinorAxisLength;
        NB(kk,:,4) = geochar1(kk).BoundingBox;
        if bb13 ~= 0
            dist11 = ((centrex1(kk,4)-MB(bb13,2,3))^2
+ (centrey1(kk,4)-MB(bb13,3,3))^2)^0.5;
            %if ups == 1
                if (dist11 <= dist1) &
(centrey1(kk,4)>centrey1(bb13,3)+fveli) %&
(centrex1(kk,4) >= NB(kk,1,3) & centrex1(kk,4)
<= NB(kk,1,3) + NB(kk,3,3))% if up flow
                    dist1 = dist11;
                    bb14 = kk;
                end
                %else
                %if (dist11 <= dist1) &
(centrey1(kk,4)<centrey1(bb13,3)+fveli)
                    % dist1 = dist11;
                    % bb14 = kk;
                %end
                %end
            else
                bb14 = 0;
            end
        end
        %
        % Image 5
        %
        dist1 = 10000;
        T5 = opthr(b5);
        b5 = im2bw(b5,T1);
        b5 = abs(double(b5)-1);
        b5 = double(b5).*filtbox;
        b5 = imfill(b5,'holes');
        SE = strel('octagon',3);
        b5 = imerode(b5,SE);
        b5 = imdilate(b5,SE);
        [b1label, N] = bwlabel(b5,4);
        NN(5) =N;
        geochar1 = imfeature(b1label,'Area',
'centroid','MajorAxisLength','MinorAxisLength',
BoundingBox');
        for kk = 1:N
            MB(kk,1,5) = geochar1(kk).Area;
            MB(kk,2,5) = geochar1(kk,1).Centroid(1);
            centrex1(kk,5) = MB(kk,2,5);
            MB(kk,3,5) = geochar1(kk,1).Centroid(2);
            centrey1(kk,5) = MB(kk,3,5);
            MB(kk,4,5) =
            geochar1(kk).MajorAxisLength;
            MB(kk,5,5) =
            geochar1(kk).MinorAxisLength;
            NB(kk,:,5) = geochar1(kk).BoundingBox;
            if bb14 ~= 0
                dist11 = ((centrex1(kk,5)-MB(bb14,2,4))^2
+ (centrey1(kk,5)-MB(bb14,3,4))^2)^0.5;
            end
        end
    end
end

```

```

    %if ups == 1
        if (dist11 <= dist1) &
            (centrey1(kk,5)>centrey1(bb14,4)+fveli) %&
            (centrex1(kk,5) >= NB(kk,1,4) & centrex1(kk,5)
            <= NB(kk,1,4) + NB(kk,3,4))% if up flow
                dist1 = dist11;
                bb15 = kk;
            end
        %else
            %if (dist11 <= dist1) &
                (centrey1(kk,5)<centrey1(bb14,4)+fveli) %&
                (centrex1(kk,5) >= NB(kk,1,4) & centrex1(kk,5)
                <= NB(kk,1,4) + NB(kk,3,4))% if up flow
                    %dist1 = dist11;
                    %bb15 = kk;
                %end
            %end
        else
            bb15 = 0;
        end
    end
    %dist1 = 10000;
    %b5 = abs(b5-1);
    %subplot(2,3,5), subimage(b5);hold on;
    %axis off;
    %line(xt,1:210, 'Color', 'g');
    %line(1:240,yt, 'Color', 'g');
    %hold on;
    %tit = sprintf('B5 = %d',bb15);
    %title(tit)
    %for ix=1:N
        % fbubble=sprintf('%d',ix);
        % if ix ~= bb15
        %
        text(centrex1(ix,5)+25,centrey1(ix,5),fbubble,'C
        olor','b', 'FontSize',8);
        % else
        %
        text(centrex1(ix,5)+25,centrey1(ix,5),fbubble,'C
        olor','r', 'FontSize',10);
        % end
    %end
    %ok1 = input('Good image? (y ==1) ');
    %if ok1 == 1
        % gbi = sprintf(' [%d %d %d %d %d]',bb11,
        bb12, bb13, bb14, bb15);
        % disp(gbi)
        % ok2 = input('Good ID ? (y ==1, n == 0) ');
        % if ok2 == 1
            bb = [bb11 bb12 bb13 bb14 bb15];
            % else
            %bb(1) = bb11;
            %for ir = 2:5
            % tit = sprintf('Image %d, bubble # = ',ir);
            % bb(ir) = input(tit);
            %end

```

```

        %ok2 = 1;
        %end
    for i = 1: 5
        if bb(i) ~= 0
            MMBB(i,:) = MB(bb(i),:,i);
            NNBB(i,:) = NB(bb(i),:,i);
        end
    end
    %expl = input ('Explores? (y==1) ');
    %close (h2);
    %end
%clc

function T=opthr(I)
%*****
%*****
%*****
%FUNCTION T=OPTHR(I)
%AUTHOR: Felix Toran Marti.
%DATE: 8/5/00
%MATLAB VERSION: 5.x.
%To contact author use:
%E-MAIL: floran@aimme.es
%PHONE: +34 654082088
%
%This function finds the optimal threshold
corresponding to the intensity image I.
%The function is intended to be a enhancement
of the images toolbox for thresholding
%purposes. It can be a quick way to automate
the process of manually selecting a
%threshold after seeing the histogram of an
image. Also, the function helps user
%finding a reasonable good threshold value
when the selection is not evident.
%
%The following example code reads a TIFF
image, finds its optimal threshold, and converts
%it to a binary image:
%
%[x,map]=tiffread('c:\myimage.tiff');
%I=ind2gray(x,map);
%threshold=opthr(I);
%B=im2bw(I,threshold);
%imshow(B)
%
%If the histogram of image I is purely bimodal,
the threshold will take a value
%in the middle of the valley between the 2
modes (the logical election).
%In other difficult cases, when the modes are
overlapped, the threshold will minimize
%the error of interpreting background pixels as
objects pixels, and vice versa.
%

```

```

%This algorithm is a small version of a more
complex statistical method,
%offering good results and normally using a
reduced number of iterations.
%*****
%*****
%*****
%Image size
[rows,cols]=size(I);

%Initial consideration: each corner of the image
has background pixels.
%This provides an initial threshold (T),
calculated as the mean of the gray levels
contained
%in the corners. The width and height of each
corner is a tenth of the image's width
%and height, respectively.

col_c=floor(cols/10);
rows_c=floor(rows/10);

corners=[I(1:rows_c,1:col_c); I(1:rows_c,(end-
col_c+1):end);...
         I((end-rows_c+1):end,1:col_c);I((end-
rows_c+1):end,(end-col_c+1):end)];

T=mean(mean(corners));

%*****
%*****
% ITERATIVE PROCESS
%*****
%*****

while 1

    %1. The mean of gray levels corresponding to
objects in the image is calculated.
    %The actual threshold (T) is used to determine
the boundary between objects and
    %background.
    mean_obj=sum(sum( (I>T).*I
))/length(find(I>T));

    %2. The same is done for the background
pixels.
    mean_backnd=sum(sum( (I<=T).*I
))/length(find(I<=T));

    %3. A new threshold is calculated as the mean
of the last results:
    new_T=(mean_obj+mean_backnd)/2;

```

```

%4. A new iteration starts only if the threshold
has changed.
if(new_T==T)
    break;
else
    T=new_T;
end

end

%At this stage, the optimal threshold value is
contained in T.

```

Program: velocities.m

```

function [V] = velocities(ups,M,NN,factor, nfs,
lags, ress)
Mbox = zeros(5,4);
V = zeros(3,8);
distt = zeros(3,4);
VV = zeros(3,4);
sar = 0; scx = 0; scy = 0; smj = 0; smn = 0;
% Mean geometric properties
for ig = 1:5
    if M(ig,1) ~= 0
        sar = sar + M(ig,1); % area
        scx = scx + M(ig,2); % cx
        scy = scy + M(ig,3); % cy
        smj = smj + M(ig,4); % mj
        smn = smn + M(ig,5); % mn
    else
        sar = 0; % area
        scx = 0; % cx
        scy = 0; % cy
        smj = 0; % mj
        smn = 0; % mn
    end
end
P(1)= mean(sar); P(2) = mean(scx); P(3) =
mean(scy); P(4) = mean(smj); P(5) =
mean(smn);
for ig = 1:5
    if mean(sar)~=0
        if ups == 1
            Mbox(ig,1) = NN(ig,1) + 0.5*NN(ig,3);
            Mbox(ig,2) = NN(ig,2); % Front edge ID
        if going up
            Mbox(ig,3) = NN(ig,1) + 0.5*NN(ig,3);
            Mbox(ig,4) = NN(ig,2) + NN(ig,4); %
Back edge ID if going up
        else
            Mbox(ig,1) = NN(ig,1) + 0.5*NN(ig,3);
            Mbox(ig,2) = NN(ig,2)+ NN(ig,4); %
Front edge ID if going down
            Mbox(ig,3) = NN(ig,1) + 0.5*NN(ig,3);

```

```

        Mbox(ig,4) = NN(ig,2); % Back edge ID
if going down
    end
else
    Mbox(ig,1) = 0;
    Mbox(ig,2) = 0;
    Mbox(ig,3) = 0;
    Mbox(ig,4) = 0;
end
end
% Velocities
cc = 0;
for ig = 1:4
    for ik = ig+1:ig+1
        if (M(ig,1) & M(ik,1)) ~= 0
            %
            CX1 = M(ig,2); CX2 = M(ik,2); CY1 =
M(ig,3); CY2 = M(ik,3);
            disttx(1,ig) = factor*abs(CX1-
CX2);%[mm]
            distty(1,ig) = factor*abs(CY1-
CY2);%[mm]
            VVX(1,ig) = ( disttx(1,ig)/10/lags) /
(1/nfs); %[cm/s]
            VVY(1,ig) = ( distty(1,ig)/10/lags) /
(1/nfs); %[cm/s]
            %
            CX1 = Mbox(ig,1); CX2 = Mbox(ik,1);
CY1 = Mbox(ig,2); CY2 = Mbox(ik,2);
            disttx(2,ig) = factor*abs(CX1-
CX2);%[mm]
            distty(2,ig) = factor*abs(CY1-
CY2);%[mm]
            VVX(2,ig) = ( disttx(2,ig)/10/lags) /
(1/nfs); %[cm/s]
            VVY(2,ig) = ( distty(2,ig)/10/lags) /
(1/nfs); %[cm/s]
            CX1 = Mbox(ig,3); CX2 = Mbox(ik,3);
CY1 = Mbox(ig,4); CY2 = Mbox(ik,4);
            disttx(3,ig) = factor*abs(CX1-
CX2);%[mm]
            distty(3,ig) = factor*abs(CY1-
CY2);%[mm]
            VVX(3,ig) = ( disttx(3,ig)/10/lags) /
(1/nfs); %[cm/s]
            VVY(3,ig) = ( distty(3,ig)/10/lags) /
(1/nfs); %[cm/s]
        else
            disttx(1,ig) = 0;
            distty(1,ig) = 0;
            VVX(1,ig) = 0;
            VVY(1,ig) = 0;
            %
            disttx(2,ig) = 0;
            distty(2,ig) = 0;
            VVX(2,ig) = 0;

```

```

        VVY(2,ig) = 0;
        disttx(3,ig) = 0;
        distty(3,ig) = 0;
        VVX(3,ig) = 0;
        VVY(3,ig) = 0;
    end
end
end
%
V = [disttx distty VVX VVY];
% 1:4 5:8 9:12 13:16

```

Program: calibration_void.m

```

clear all
close all
clc
set(0,'DefaultTextinterpreter','default')
%
http://www.mathworks.com/access/helpdesk/help/techdoc/ref/text\_props.shtml#String
%
% Calibration 3
%
% figure 1
%
figure
V3 = [-4.5320e-5 0.1944 0.3995 0.5981 0.7980
1.0003];
H3 = [ 0 1 2 3 4 5]*2.5/100;
[Y1,Y95u,Y95b,Y95u1,Y95b1, mmxv3, bbv3,
rxy, simul, r23]= linearregression(V3,H3);
plot(V3, H3, 'ok', V3, bbv3 + mmxv3*V3,'k')
xlabel('Voltage, V (volt)','FontSize',10);
ylabel('\Delta\itH} (m)','FontSize',10);
ax=findobj(gcf,'Type','axes');
set(ax,'FontSize',8);
set(gca,'YTick',0:0.02:0.15)
set(gcf,'Color',[1,1,1])
set(0,'DefaultTextinterpreter','none')
h = ylabel('\Delta\itH} (m)','FontSize',10);
axpos = get(gca,'pos');
extent = get(h,'extent');
%set(gca,'pos',[axpos(1)*1 axpos(2)*1.1
axpos(3)*0.85 axpos(4)])
set(0,'DefaultTextinterpreter','default')
axis([0 1 0 14/100])
u = 3
mmxv3
bbv3
%
V4 = [0.6067e-5 0.2080 0.4055 0.6056 0.8010
0.9996];
H4 = [ 0 1 2 3 4 5]*2.5/100;

```



```

[Y1,Y95u,Y95b,Y95ul,Y95bl, mmxv4, bbv4,
 rxy, simul, r24]= linearregression(V4,H4);
u = 4
mmxv4
bbv4
%
V5 = [-5.6341e-5 0.1982 0.3396 0.5975 0.7992
1.0005];
H5 = [ 0 1 2 3 4 5]*2.5/100;
[Y1,Y95u,Y95b,Y95ul,Y95bl, mmxv5, bbv5,
 rxy, simul, r25]= linearregression(V5,H5);
u = 5
mmxv5
bbv5
r2mean = (r23+r24+r25)/3
load('E:\Program
Files\MATLAB71\work\calibration3\MMN33.m
at')
%load('E:\MATLAB6p5\work\calibration3\MM
N33.mat')
mn = 5;
cc = 0;
% mean values
for i = 4:10:mn*10-10+4
    cc = cc + 1;
    for j = 1:4
        MG(cc,j) = mean(MM(i:i+4,j));
    end
end
%
ccc = 0;
for i = 4:10:mn*10-10+4
    ccc = ccc + 1;
    cc = 0;
    for k = i:i+4
        cc = cc + 1;
        for j = 1:4
            MGA(cc,j) = MM(k,j);
        end
    end
    MMB(ccc,:) = mean(MGA);
    SMMB(ccc,:) = std(MGA);
    % bias 1, PH
    BB1 = mean(MGA(:,1));
    MGAA = MGA-BB1;
    B133(ccc,:) = sum(MGAA,1)/5;
    % bias 2, P average
    BB2 = mean(mean(MGA(:,2:4)));
    xx(ccc) = BB2;
    x21 = xx';
    MGAB = BB2-MGA;
    B233(ccc,:) = sum(MGAB,1)/5;
    % random error
    RE33(ccc,:) = std(MGA);
end
x1133 = MMB(:,1);% diff. pressure transducer

```

```

x2133 = x21;
ph133 = MMB(:,1);% diff. pressure transducer
p1133 = MMB(:,2);
p2133 = MMB(:,3);
p3133 = MMB(:,4);
%
sph133 = SMMB(:,1);
sp1133 = SMMB(:,2);
sp2133 = SMMB(:,3);
sp3133 = SMMB(:,4);
clear xx x21 MM MG MMB BB1 BB2 MGA
MGAB MMB SMMB
% void MM4.xls
load('E:\Program
Files\MATLAB71\work\calibration4\MMN4.m
at')
%load('E:\MATLAB6p5\work\calibration4\MM
N4.mat')
nn = 8;
cc = 0;
% mean values
for i = 4:10:nn*10-10+4
    cc = cc + 1;
    for j = 1:4
        MG(cc,j) = mean(MM(i:i+4,j));
    end
end
%
ccc = 0;
for i = 4:10:nn*10-10+4
    ccc = ccc + 1;
    cc = 0;
    for k = i:i+4
        cc = cc + 1;
        for j = 1:4
            MGA(cc,j) = MM(k,j);
        end
    end
    MMB(ccc,:) = mean(MGA);
    SMMB(ccc,:) = std(MGA);
    % bias 1, PH
    BB1 = mean(MGA(:,1));
    MGAA = MGA-BB1;
    B14(ccc,:) = sum(MGAA,1)/5;
    % bias 2, P average
    BB2 = mean(mean(MGA(:,2:4)));
    xx(ccc) = BB2;
    x21 = xx';
    MGAB = BB2-MGA;
    B24(ccc,:) = sum(MGAB,1)/5;
    % random error
    RE4(ccc,:) = std(MGA);
end
x114 = MMB(:,1);% diff. pressure transducer
x214 = x21;
ph14 = MMB(:,1);% diff. pressure transducer

```

```

p114 = MMB(:,2);
p214 = MMB(:,3);
p314 = MMB(:,4);
%
sx114 = SMMB(:,1);
x214 = x21;
sph14 = SMMB(:,1);
sp114 = SMMB(:,2);
sp214 = SMMB(:,3);
sp314 = SMMB(:,4);
clear xx x21 MM MG MMB BB1 BB2 MGA
MGAB SMMB
%
% void MM5.xls
load('E:\Program
Files\MATLAB71\work\calibration5\MMN5.ma
t')
%load('E:\MATLAB6p5\work\calibration5\MM
N5.mat')
nn = 7;
cc = 0;
% mean values
for i = 4:10:nn*10-10+4
    cc = cc + 1;
    for j = 1:4
        MG(cc,j) = mean(MM(i:i+4,j));
    end
end
%
ccc = 0;
for i = 4:10:nn*10-10+4
    ccc = ccc + 1;
    cc = 0;
    for k = i:i+4
        cc = cc + 1;
        for j = 1:4
            MGA(cc,j) = MM(k,j);
        end
    end
end
MMB(ccc,:) = mean(MGA);
SMMB(ccc,:) = std(MGA);
% bias 1, PH
BB1 = mean(MGA(:,1));
MGAA = MGA-BB1;
B15(ccc,:) = sum(MGAA,1)/5;
% bias 2, P average
BB2 = mean(mean(MGA(:,2:4)));
xx(ccc) = BB2;
x21 = xx';
MGAB = BB2-MGA;
B25(ccc,:) = sum(MGAB,1)/5;
% random error
RE5(ccc,:) = std(MGA);
end
x115 = MMB(:,1); % diff. pressure transducer
x215 = x21;

```

```

ph15 = MMB(:,1); % diff. pressure transducer
p115 = MMB(:,2);
p215 = MMB(:,3);
p315 = MMB(:,4);
%
sx115 = SMMB(:,1);
sx215 = x21;
sph15 = SMMB(:,1);
sp115 = SMMB(:,2);
sp215 = SMMB(:,3);
sp315 = SMMB(:,4);
clear xx x21 MM MG MMB BB1 BB2 MGA
MGAB SMMB
%
x11 = [ x1133; % diff. pressure transducer
        x114; % diff. pressure transducer
        x115]; % diff. pressure transducer
x21 = [ x2133;
        x214;
        x215];

ph1 = [ ph133; % diff. pressure transducer
        ph14; % diff. pressure transducer
        ph15]; % diff. pressure transducer
p11 = [ p1133;
        p114;
        p115];
p21 = [ p2133;
        p214;
        p215];
p31 = [ p3133;
        p314;
        p315];
PREE1 = [ p11 p21 p31];
PREE = mean(PREE1,2);
REE = [ RE33;
        RE4;
        RE5];
%
sph1 = [ sph133;
        sph14;
        sph15];
sp11 = [ sp1133;
        sp114;
        sp115];
sp21 = [ sp2133;
        sp214;
        sp215];
sp31 = [ sp3133;
        sp314;
        sp315];
%
% 95% confidence bands
%
xx1 = [ x11;
        x11;

```

```

    x11];
yy1 = [ p11;
    p21;
    p31];
x = xx1;
y = yy1;
[xx pos] = sort(x);
x = xx;
for i = 1: length(y)
    yy(i) = y(pos(i));
end
y = yy;
clear xx1 yy1
xx1 = x;
yy1 = y;
%result=rprcr(xx1,
yy1,'alpha',0.65,'k',5,'plots',0,'classic',1);
%r2robust = result.rsquared;
%
[Y1,Y95u,Y95b,Y95ul,Y95bl, mmxv, bbv, rxy,
simul, r2]= linearregression(xx1,yy1);
mmxv
bbv
r2
% figure 2
figure
%plot(x11, p11, 'k.', x11, p21, 'k*', x11, p31,
'k+',xx1, Y1,'k', xx1, Y95ul, 'k--', xx1, Y95bl,
'k--')
plot(x11, p11, 'k.', x11, p21, 'k*', x11, x11, 'k')
%% hold on
%% plot( x11, p31, 'ks', 'MarkerSize', 3.0)
x0 = '';
%x1 = '\wedge ';
x2 = '{< \alpha_ \Delta\it_H >}';
%xlabel({x0; x1; x2},'FontSize',10,
'VerticalAlignment','Middle')
xlabel({x2},'FontSize',13,
'VerticalAlignment','Middle')
y1 = ' \wedge ';
y2 = '{< \alpha_ P >}';
%ylabel({y1; y2},'FontSize',10,
'VerticalAlignment','Bottom')
ylabel({y2},'FontSize',13,
'VerticalAlignment','Bottom')
set(0,'DefaultTextinterpreter','none')
%h = ylabel({y1; y2},'FontSize',10,
'VerticalAlignment','Bottom');
h = ylabel({y2},'FontSize',13,
'VerticalAlignment','Bottom');
axpos = get(gca,'pos');
extent = get(h,'extent');
set(gca,'pos',[axpos(1) axpos(2) axpos(3)
axpos(4)])
set(0,'DefaultTextinterpreter','default')
axis([0 0.25 0 0.25])

```

```

axis square
set(gcf,'Color',[1,1,1])
ax=findobj(gcf,'Type','axes');
set(ax,'FontSize',8);
pause
%
B1 = [ B133;
    B14;
    B15];
B2 = [ B233;
    B24;
    B25];
B200 = [ x21 B2(:,2);
    x21 B2(:,3);
    x21 B2(:,4);
    ];
%
% figure 3
figure
%plot(p11, B1(:,2), 'k.', p21, B1(:,3), 'k*', p31,
B1(:,4), 'k+')
%plot( x11, p31, 'ks', 'MarkerSize', 3.0)
plot(ph133, B133(:,2), 'k.', ph133, B133(:,3),
'k*')
hold on
plot(ph133, B133(:,4), 'ks', 'MarkerSize', 3.0)
hold on
plot(ph14, B14(:,2), 'k.', ph14, B14(:,3), 'k*')
hold on
plot(ph14, B14(:,4), 'ks', 'MarkerSize', 3.0)
hold on
plot(ph15, B15(:,2), 'k.', ph15, B15(:,3), 'k*')
hold on
plot(ph15, B15(:,4), 'ks', 'MarkerSize', 3.0)
set(gcf,'Color',[1,1,1])
x0 = '';
x1 = '\wedge ';
x2 = '{< \alpha_ \Delta\it_H >}';
%xlabel({x0; x1; x2},'FontSize',10,
'VerticalAlignment','Middle')
xlabel({x2},'FontSize',10,
'VerticalAlignment','Middle')
y1 = ' \wedge ';
y2 = '{\rmb[\alpha\rmb_P]}';
%ylabel({y1; y2},'FontSize',10,
'VerticalAlignment','Bottom')
ylabel({y2},'FontSize',10,
'VerticalAlignment','Bottom')
ax=findobj(gcf,'Type','axes');
set(ax,'FontSize',8);
%h = ylabel({y1; y2},'FontSize',10,
'VerticalAlignment','Bottom');
h = ylabel({y2},'FontSize',10,
'VerticalAlignment','Bottom');
axpos = get(gca,'pos');
extent = get(h,'extent');

```

```

set(gca,'pos',[axpos(1)*1.1 axpos(2)*1.1
axpos(3)*0.8 axpos(4)])
line([0,0.25],[0,0],'Color','k')
set(0,'DefaultTextinterpreter','default')
axis([0 0.25 -0.030 0.030])
means= (mean(B1(:,2))+ mean(B1(:,3))+
mean(B1(:,4)))/3
pause
% Void average is exact
figure
plot(p11, B2(:,2), 'k.', p21, B2(:,3), 'k*', p31,
B2(:,4), 'k+')
set(gcf,'Color',[1,1,1])
x0 = '';
x1 = '\wedge ';
x2 = '< \alpha \it P_m_e_a_n >';
%xlabel({x0; x1; x2},'FontSize',10,
'VerticalAlignment','Middle')
xlabel({x2},'FontSize',10,
'VerticalAlignment','Middle')
y1 = '\wedge ';
y2 = '\rm [\alpha \rm P]';
%ylabel({y1; y2},'FontSize',10,
'VerticalAlignment','Bottom')
ylabel({y2},'FontSize',10,
'VerticalAlignment','Bottom')
ax=findobj(gcf,'Type','axes');
set(ax,'FontSize',8);
maxran1 = max((max(REE(:,2)./ph1),
(max(REE(:,3)./ph1))));
maxran11 = max(maxran1,max(REE(:,4)./ph1))
%legend('P1','P2','P3',0)
meanrandom = mean(mean(REE(:,2:4)))
maxrandom = max(max(REE(:,2:4)))
%
vv1 = [ ph1 REE(:,2);
        ph1 REE(:,3);
        ph1 REE(:,4)];
[Y1,Y95u,Y95b,Y95u1,Y95b1, mmxv, bbv, rxy,
simul, r2]= linearregression(vv1(:,1),vv1(:,2));
figure
plot(ph1, REE(:,2), 'k.', ph1, REE(:,3), 'k*', ph1,
REE(:,4), 'k+')
hold on
plot(ph1, bbv + mmxv*ph1)
axis([0 0.25 0 0.01])
set(gcf,'Color',[1,1,1])
pause
%
MSE1 = REE(:,2:4).^2 + B1(:,2:4).^2;
%%%%%%%%%%%% pay attention
%%%%%%%%%
%
RMSE100 = MSE1.^0.5;
MSE11 = mean(REE(:,2:4).^2);
RRMSE1 = [MSE1(:,1).^0.5./ph1
MSE1(:,2).^0.5./ph1 MSE1(:,3).^0.5./ph1];
RRMS1 = mean(RRMSE1);
xx1 = [ph1; ph1;ph1];
yy1 = [RRMSE1(:,1);
RRMSE1(:,2);RRMSE1(:,3)];
[Y1,Y95u,Y95b,Y95u1,Y95b1, mmxv, bbv, rxy,
simul, r2]= linearregression(xx1,yy1*100);
%
x = xx1;
y = yy1;

```

```

[xx pos] = sort(x);
x = xx;
for i = 1: length(y)
    yy(i) = y(pos(i));
end
y = yy;
clear xx1 yy1
xx1 = x;
yy1 = y;
%
figure
plot(ph1, RRMSE1(:,1)*100, 'k*', ph1,
RRMSE1(:,2)*100, 'k+')
%hold on
%plot(ph1, RRMSE1(:,3)*100, 'ks',
'MarkerSize', 3.0)
hold on
plot(xx1, xx1*mmxv+bbv,'k')
%
x1 = '\wedge ';
x2 = '{< \alpha_{\Delta}it_H >}';
%xlabel({x0; x1; x2}, 'FontSize', 10,
'VerticalAlignment', 'Middle')
xlabel({x2}, 'FontSize', 10,
'VerticalAlignment', 'Middle')
y1 = ' \wedge ';
y2 = '{< \epsilon_{\alpha}it_P >} > (%)';
ylabel({y2}, 'FontSize', 10,
'VerticalAlignment', 'Bottom')
set(gcf, 'Color', [1, 1, 1])
set(0, 'DefaultTextinterpreter', 'none')
h = ylabel({y2}, 'FontSize', 10,
'VerticalAlignment', 'Bottom');
axpos = get(gca, 'pos');
extent = get(h, 'extent');
set(gca, 'pos', [axpos(1)*1.1 axpos(2)*1.1
axpos(3)*0.8 axpos(4)])
axis([0 0.25 0 27])
set(0, 'DefaultTextinterpreter', 'default')
ax=findobj(gcf, 'Type', 'axes');
set(ax, 'FontSize', 8);
axis([0 0.2 0 30])
pause
%
NRMSE = mean(mean(RRMSE1))
pause
figure
V3 = [0.6067e-5 0.2080 0.4055 0.6056 0.8010
0.9996];
H3 = [ 0 1 2 3 4 5];
[Y1, Y95u, Y95b, Y95u1, Y95b1, mmxv3, bbv3,
rxy, simul, r2]= linearregression(V3, H3);
plot(V3, H3, 'k.', V3, bbv3 + mmxv3*V3, 'k')
axis([0 1 0 5 ])
xlabel('Voltage (V)')
ylabel('P (in)')

```

```

title('Calibration 2')
set(gcf, 'Color', [1, 1, 1])
eqn1 = sprintf('P = %0.5g + %0.5g * V', bbv3,
mmxv3);
text(0.1, 4, eqn1);
eqn2 = sprintf('R^2 = %d', r2);
text(0.1, 3.5, eqn2);
% void MM4.xls
x = [0.03077625 0.059935 0.0854665
0.11066475 0.131795 0.1517775 0.17745
0.208485];
ph = [0.030246 0.06025 0.087787 0.1152
0.13451 0.15573 0.17625 0.19486];
p1 = [0.026617 0.053192 0.073446 0.091459
0.11329 0.13452 0.15969 0.19714];
p2 = [0.030556 0.055587 0.085449 0.10802
0.13169 0.15502 0.17832 0.20913];
p3 = [0.035686 0.070711 0.095184 0.12798
0.14769 0.16184 0.19554 0.23281];
%
% Figure 4
figure
subplot(2, 1, 1)
plot(ph, p1, 'k.', ph, p2, 'k*', ph, p3, 'k+', [0
0.25], [0 0.25], 'k')
axis([0 0.25 0 0.25])
set(gcf, 'Color', [1, 1, 1])
title('Void fraction, calibration 2')
xlabel('{\alpha_{\Delta}it_H}')
ylabel('{\alpha_{Fiber_optic}'}
legend('P1', 'P2', 'P3', 2)
subplot(2, 1, 2)
plot(ph, p1, 'k.', ph, p2, 'k*', ph, p3, 'k+', [0 1], [0
1], 'k')
axis([0 1 0 1])
set(gcf, 'Color', [1, 1, 1])
%title('Void fraction, calibration 2')
xlabel('{\alpha_{\Delta}it_H}')
ylabel('{\alpha_{Fiber_optic}'}
legend('P1', 'P2', 'P3', 2)
std21 = std(ph-p1); std22 = std(ph-p2); std23 =
std(ph-p3);
%
% Figure 5
% Calibration 5
%
figure
V3 = [-0.56341e-5 0.1982 0.3996 0.5976 0.7992
1.0005];
H3 = [ 0 1 2 3 4 5];
[Y1, Y95u, Y95b, Y95u1, Y95b1, mmxv3, bbv3,
rxy, simul, r2]= linearregression(V3, H3);
plot(V3, H3, 'k.', V3, bbv3 + mmxv3*V3, 'k')
axis([0 1 0 5 ])
xlabel('Voltage (V)')
ylabel('P (in)')

```

```

title('Calibration 3')
set(gcf,'Color',[1,1,1])
eqn1 = sprintf('P = %0.5g + %0.5g * V', bbv3,
mmxv3);
text(0.1,4,eqn1);
eqn2 = sprintf('R^2 = %d', rxy);
text(0.1,3.5,eqn2);
%void MM5.xls
x = [0.02021475 0.054547 0.08411175
0.1119775 0.1408975 0.17413 0.184645];
ph = [0.018413 0.056426 0.089663 0.12147
0.15074 0.17107 0.18065];
p1 = [0.020996 0.054373 0.084827 0.1111
0.14418 0.17424 0.19055];
p2 = [0.020093 0.052484 0.075104 0.1081
0.1335 0.16245 0.18255];
p3 = [0.021357 0.054905 0.086853 0.10724
0.13517 0.18876 0.18483];
%
% figure 6
figure
subplot(2,1,1)
plot(ph, p1, 'k.', ph, p2, 'k*', ph, p3, 'k+', [0
0.25],[0 0.25],'k')
axis([0 0.25 0 0.25])
set(gcf,'Color',[1,1,1])
title('Void fraction, calibration 3')
xlabel('\alpha_{\Delta\it H}')
ylabel('\alpha_{F i b e r o p t i c}')
legend('P1','P2','P3',2)
subplot(2,1,2)
plot(ph, p1, 'k.', ph, p2, 'k*', ph, p3, 'k+', [0 1],[0
1],'k')
axis([0 1 0 1])
set(gcf,'Color',[1,1,1])
%title('Void fraction, calibration 3')
xlabel('\alpha_{\Delta\it H}')
ylabel('\alpha_{F i b e r o p t i c}')
legend('P1','P2','P3',2)
std31 = std(ph-p1); std32 = std(ph-p2); std33 =
std(ph-p3);

```

Program: figplotallP1_90.m.

```

close all
clc
%close all
clear all
MJMN = input('Max MJ/MN = ');
vmax = input('Velocity max = ');

% U1
load goodimageU-1-1-1;

```

```

A1 = AD;
load goodimageU-1-1-2;
A2 = AD;
load goodimageU-1-1-3;
A3 = AD;
load goodimageU-1-1-4;
A4 = AD;
load goodimageU-1-1-5;
A5 = AD;
load goodimageU-1-1-6;
A6 = AD;
load goodimageU-1-1-7;
A7 = AD;
load goodimageU-1-1-8;
A8 = AD;
load goodimageU-1-1-9;
A9 = AD;
% U2
load goodimageU-1-2-1;
A10 = AD;
load goodimageU-1-2-2;
A11 = AD;
load goodimageU-1-2-3;
A12 = AD;
load goodimageU-1-2-4;
A13 = AD;
load goodimageU-1-2-5;
A14 = AD;
load goodimageU-1-2-6;
A15 = AD;
load goodimageU-1-2-7;
A16 = AD;
load goodimageU-1-2-8;
A17 = AD;
load goodimageU-1-2-9;
A18 = AD;
%
%U3
load goodimageU-1-3-1;
A19 = AD;
load goodimageU-1-3-2;
A20 = AD;
load goodimageU-1-3-3;
A21 = AD;
load goodimageU-1-3-4;
A22 = AD;
load goodimageU-1-3-5;
A23 = AD;
load goodimageU-1-3-6;
A24 = AD;
load goodimageU-1-3-7;
A25 = AD;
load goodimageU-1-3-8;
A26 = AD;
load goodimageU-1-3-9;
A27 = AD;

```

```

%
%D1
load goodimageD-1-3-1;
A28 = AD;
load goodimageD-1-3-2;
A29 = AD;
load goodimageD-1-3-3;
A30 = AD;
load goodimageD-1-3-4;
A31 = AD;
load goodimageD-1-3-5;
A32 = AD;
load goodimageD-1-3-6;
A33 = AD;
load goodimageD-1-3-7;
A34 = AD;
load goodimageD-1-3-8;
A35 = AD;
load goodimageD-1-3-9;
A36 = AD;

A =[A1;
A2;
A3;
A4;
A5;
A6;
A7;
A8;
A9;
A10;
A11;
A12;
A13;
A14;
A15;
A16;
A17;
A18;
A19;
A20;
A21;
A22;
A23;
A24;
A25;
A26;
A27;
A28;
A29;
A30;
A31;
A32;
A33;
A34;
A35;
A36;
];

%
% Roundness
%A(:,17) = A(:,17)*cfac;
c = 0;
for i = 1: size(A,1)
    if A(i,15)/A(i,16) <= MJMN
        c = c + 1;
        j =[1:size(A,2)];
        AAB(c,j) = A(i,j);
    end
end
%
c = 0;
for i = 1: size(AAB,1)
    if AAB(i,17) <= vmax
        c = c + 1;
        j =[1:size(AAB,2)];
        AA(c,j) = AAB(i,j);
    end
end
%
% Curve fitting velocity
% First iteration
x = log(AA(:,3));
y = log( AA(:,17));
[B,stats] = robustfit(x,y);
c = 0;
for i = 1: length(x)
    if stats.w(i) >= 0.75
        c = c + 1;
        j =[1:size(A,2)];
        AAA(c,j) = AA(i,j);
    end
end
% second iteration
x = log10(AAA(:,2));
y1 = AAA(:,18);
y = log10(y1);
[B,stats] = robustfit(x,y);
c = 0;
for i = 1: length(x)
    if stats.w(i) >= 0.75
        c = c + 1;
        j =[1:size(A,2)];
        AB(c,j) = AAA(i,j);
    end
end
xr = log10(AB(:,3));
yr = log10(AB(:,17));
result=rprcr(xr,yr,'alpha',0.65,'k',5,'plots',0,'classic',1);
r2robust = result.rsquared;
%

```

```

% RISE VS VELOCITY
% fig 1
x = log10(AB(:,3));
y1 = AB(:,17);
y = log10(y1);
[Y1,Y95u,Y95b,Y95u1,Y95b1, mmx, bb, rxy]=
linearregression(x,y);
loglog(10.^x, 10.^y, 'l', 10.^x,
10.^Y1,'g',10.^x,10.^Y95u,'k',10.^x,10.^Y95b,'k'
)
hold on
loglog(10.^x,10.^Y95u1,'k-',10.^x,10.^Y95b1,'k-
')
hold on
XC = 10.^x;
YC = 10^1.64*XC.^(-0.760);
loglog(XC,YC,'r','LineWidth',2)
axis([10^-1 10^1 10^0 10^3])
xlabel('Rise Time [ms]')
ylabel('Velocity [cm/s]')
title ('PROBE 1')
%
eqn1 = sprintf(' %0.5g ',mmx);

```

```

eqn2 = sprintf('V = %0.5g*T_R',10^bb);
eqn3 = strcat(eqn2,'\^',eqn1);
eqn4 = sprintf(' R^2 = %0.5g',rxy);
eqn5 = strcat(eqn3,eqn4);
text(10^-0.25,700,eqn5, 'Color', 'g');
%
eqn1 = sprintf(' %0.5g ',result.slope);
eqn2 = sprintf('V_o_r_t_h_o =
%0.5g*T_R',10^result.int);
eqn3 = strcat(eqn2,'\^',eqn1);
eqn4 = sprintf(' R^2 = %0.5g',r2robust);
eqn5 = strcat(eqn3,eqn4);
text(10^-0.25,400,eqn5, 'Color', 'b');
%
eqn4 = strcat('V_c_l_a_i_r_e = 43.65*T_R','\^',
'-0.760');
text(10^0,200,eqn4,'Color', 'r');
eqn6 = sprintf('Number of bubbles
%d',length(AB));
text(10^0,100,eqn6);
%

```


Appendix B: Wave maker programs

This appendix contains the computer programs used in the wave maker experiments. All programs were written in MATLAB V 7.0. Table B.1 gives an overview of the programs treated in the appendix.

Table B.1 Computer programs used in the wave maker

Program name	description
thePacket_fast4.m	Generates the wave packet
PTW088160.m	Controls the wave maker and traverse
inout2.m	Subroutine that sets the digital and analog triggers
nwaves.m	Repeats the wave n times and acquires data from the wave tank paddle's transducer
tmaxvoid3.m	Sets traverse to a new position

Program: thePacket_fast4.m

```
%
% PROGRAM thePacket_fast4.m
%
% PROGRAM TO GENERATE A PACKET
OF WAVES COMPOSED
% OF 32 SINUSOIDAL COMPONENTS
%
% INPUT: fc: center frequency of packet (Hz)
%       bw: bandwidth of packet (Hz)
%       xb: breaking position (m)
%       tb: time to breaking (sec)
%       pd: period (sec) of entire signal
(pd<25), npt=pd/(1/fout)
%       case: slope (ak) is kept constant
%       tf: if yes => transfer function is applied
(amp. & phase)
%       if no => no transfer function is
applied
% DATA: nfc: number of frequency
components evenly spaced (32)
%       ak: constant (non dimensional)
%       aa: constant (cm)
%       npt: number of points forming the
packet (2000)
%       fout: output frequency of d/a board
(100 Hz)
%       h: depth of water (0.6m)
% OUTPUT: data: array containing packet
%
% 08-25-1990: FIRST WRITTEN BY ERIC
LAMMARE
% 07-10-2005: Change to UofA conditions by
GERMAN ROJAS
%
% D A T A
%
nfc=32; fout=5000; aa=1.0; ak= 0.01; g=9.81;
h=0.60;%gg=1.2;
%
a0=12.856; a1=-47.992; a2= 83.95; a3= -52.463;
a4= 10.843;
%
b0 = 21.813; b1 = -36.128;
%
% INPUT DATA
%
fc = input(' Enter fc (Hz): ');
%ddf = input(' df 0.73-1.00: ');
ddf = 0.73;
tb = 12.0;
pd = 20;
```

```
flags = 1.0; %flags=input(' keep ak constant?
(1/0)');
tf = 1.0;
gg = 1.0;
bw = fc*ddf;
xbkc = 18.5;
%
%
% COMPUTE WAVENUMBER CENTER
COMP. USING DISPERSION RELAT.
%
w2g = ((2*pi*fc)^2) / g;
ko = w2g;
kc = w2g / tanh(ko*h);
while (abs(kc-ko)> 0.0001)
    ko = kc;
    kc=w2g / tanh(ko*h);
end
xb = xbkc/kc;
kc
%xb
%ko
%
npt = pd / (1/fout);
%tf = input(' Apply transfer function [1 (for yes);
0 (for no): ');
if (tf == 0 )
    a0 = 5.0;
    a1 = 0.0;
    a2 = 0.0;
    a3 = 0.0;
    a4 = 0.0;
    alpha = 0.0;
else
end
%a0
%
% COMPUTE FREQUENCY COMPONENTS
[EVENLY SPACED IN FREQ. DOMAIN]
%
deltabw = bw / (nfc-1);
for i = 0:nfc - 1
    f(i+1) = (fc - bw/2.0) + deltabw * i;
end
%
% COMPUTE WAVENUMBER FOR EACH
FREQ. COMP. USING DISPERSION RELAT.
%
for i = 1:nfc
    w2g = ((2*pi*f(i))^2) / g;
    ko = w2g;
    k(i)=w2g / tanh(ko*h);
```

```

while (abs(k(i)-ko)> 0.0001)
    ko = k(i);
    k(i)=w2g / tanh(ko*h);
end
end
%
% COMPUTE PHASE OF EACH
COMPONENT WITH CORRECTION FOR
TRANS. FUNCT.
% a0pha (rad), a1pha (rad/Hz)
%
%for i = 1:nfc
% corrpha(i) = (b0 + b1*f(i));
%end
%
corrpha(i) = 0; % no transfer function applied
%
for i = 1: nfc
    if flags == 1
        a(i) = ak / (k(i)/100);
    else
        a(i)=aa;
    end
    a(i)= a(i) / (a0 + a1*f(i) + a2*f(i)^2 +
a3*f(i)^3 + a4*f(i)^4);
end
sumak = 0.0;
nakc = 0.0;
if flags == 1
    for i=1: nfc
        sumak = sumak + a(i) * (a0 + a1*f(i) +
a2*f(i)^2 + a3*f(i)^3 + a4*f(i)^4) * (k(i)/100);
    end
else
    for i=1: nfc
        nakc = nakc + a(i) * (a0 + a1*f(i) +
a2*f(i)^2 + a3*f(i)^3 + a4*f(i)^4);
    end
    nakc = nakc*(k(16)/100);
end
disp(sprintf('sumak = %d',sumak))
disp(sprintf('nakc = %d',nakc))
%
% COMPUTE SIGNAL BY SUPERPOSING
ALL NFC FREQUENCY COMPONENT
%
time = [1:1/fout:pd];
for i = 1: 32
    x(i,:) = a(i)*cos(-xb*k(i)-2*pi*f(i)*(time' - tb)
- corrpha(i));
end
data = sum(x);
%
% SET PARABOLIC INCREASE AND
DECAY USING 1.0 SEC
%

```

```

n = fout;
if data(n) > 0
    i = [1:1:n-1];
    data(i) = (data(n)^2*(i-1)/fout).^0.5;
else
    i = [1:n-1];
    data(i) = -(data(n)^2*(i-1)/fout).^0.5;
end
%
ii = [n+3:-1:4];
i = [npt-n+1:npt];
if data(npt-n) > 0
    data(i) = (data(npt-n)^2*(ii-1)/fout).^0.5;
else
    data(i) = -(data(npt-n)^2*(ii-1)/fout).^0.5;
end
data(1,fout*pd)= 0;
%
gg = input('Gain factor = ');
data1 = gg*data;
data14 = data1';
axx1 = [1/fout:1/fout:20]';
plot(axx1,data14)
set(gcf,'Color', [1 1 1])
xlabel('Time(s)')
ylabel('V')
%save('Packetpaper','axx1','data14')

```

Program: PTW088160.m

```

%
close all
clear all
clc
%
% WAVE PACKET LOADING
%
load('E:\Program
Files\MATLAB71\work\wavemaker\Wave
Packets\W088185')
finn = 100; % analog input
fout=5000; % analog output
td = 8;
pd = 20; % aao
pd2 = 20; % aai
gg = 1.59; % input('Gain factor = ');
tr = 80; % input('Time for Traverse
movement (30) = ');
%
npoints = input('# of points = ');
nrepeats = input('# repeats = ');
tbp = input('Time between packets (100) = ');
nrepeats = nrepeats + 2;
%
cwr = input('Controlwr...(1,2,3,4) = ');

```

```

filename1 = sprintf('c:\\Program
files\\matlab\\R2006a\\work\\Wave
Maker\\W088160\\controlwr%d',cwr);
data1 = gg*data;
clear data
data = [data1'];
clear data1
ii = [1:fout/finn:5000*pd]';
data1 = data(ii);
%
% test conection to traverse
%disp('Probe to initial position' )
%travgrid6
%pause
%
ppoint = 1;
disp(sprintf('Point %d',ppoint));
DSS1 = inout2(finn,pd2,fout,
nrepeats,data,td,ppoint,tbp,data1,filename1);
DSS(ppoint,1:nrepeats) = DSS1;
sums = sum(DSS1);
if sums == nrepeats; ok = 1; else ok = 0; end
disp(sprintf('ok = %d',ok));
%
% other points
%
for i = 2: npoints
    ppoint = i;
    disp(sprintf('Point %d',ppoint));
    tmaxvoid3(ppoint,ttr); DSS1 =
inout2(finn,pd2,fout,
nrepeats,data,td,ppoint,tbp,data1,filename1);
DSS(ppoint,1:nrepeats) = DSS1;
    sums = sum(DSS1);
    if sums == nrepeats; ok = 1; else ok = 0; end
    disp(sprintf('ok = %d',ok));
end
%
% return to zero
%serobjw = serial('COM1');% in DAQ AT MIO
16XE 50 it is COM2
%fopen(serobjw);
%fprintf(serobjw,'E,C,I2M-15000,R');% Vertical
movement
%fclose(serobjw)
%clear serobj

```

Program: inout2.m

```

function DSS = inout2(finn,pd2,fout,
nrepeats,data,td,ppoint,tbp,d1,filename1)
aai=analoginput('nidaq',1);
set(aai,'TransferMode','Interrupts');
addchannel(aai,0);
set(aai,'SampleRate',finn);

```

```

aai.Channel.InputRange= [-10 10];
set(aai,'SamplesperTrigger',finn*(pd2));
%
aao=analogoutput('nidaq',1);
addchannel(aao,0);
set(aao,'SampleRate',fout);
dio = digitalio('nidaq',1);
addline(dio,0,'out');
Tmax = 0; Tmin = 1000;
for i = 1:nrepeats
    DSS(i) = nwaves(dio,aao, aai, data,td,
ppoint,i,tbp,d1,filename1);
end
delete(aao); delete(aai); delete(dio);
clear aao aai dio
pause4(5)
pause4

```

Program: nwaves.m

```

function DS1 = nwaves(dio,aao, aai, data,td,
ppoint,i,tbp,d1,filename1);
putvalue(dio,1)
tic
putdata(aao,[data]);
start(aao)
start(aai);
aitim = clock;
aotim = aao.InitialTriggerTime;
dt = etime(aitim,aotim);
%
while toc <= td
    pause4(0.001)
end
putvalue(dio,0);
diotim = toc;
times = floor([aotim dt*1000 diotim*1000]);
clear tao taai tdio
while isrunning(aao)
    pause4(0.1)
end
%pause4(10)
[d11] = getdata(aai);
statc1 = repcontrol(d1, d11);
if statc1 == 0
    disp(sprintf('Error in point %d repeat
%d',ppoint,i));
end
%pause4
%beep
%disp(sprintf(' %d %d %d %d %d
%d %d %d',ppoint,i,...
% times(1,1), times(1,2), times(1,3),
times(1,4), times(1,5), statc1));

```

```

stop([aao aai dio])
flushdata(aai,'Triggers');
pause4(tbp)
pause4
p1 = int16(2^16*d11/20);
filename2 = sprintf('\P%d\cr_%d',ppoint,i);
filename = strcat(filename1,filename2);
save(filename,'times','statc1','p1')
DS1 = statc1;

```

Program: tmaxvoid3.m

```

function tmaxvoid3(ppoint,ttr)
serobjw = serial('COM1');% in DAQ AT MIO
16XE 50 it is COM2
fopen(serobjw);
if ppoint >= 2 & ppoint <= 5

```

```

fprintf(serobjw,'E,C,I2M5000,R');pause4(ttr);pause4;end;
%
if ppoint == 6
fprintf(serobjw,'E,C,I1M20000,R');pause4(ttr);pause4;end;
%
if ppoint >= 7 & ppoint <= 10
    fprintf(serobjw,'E,C,I2M-5000,R');pause4(ttr);pause4;end;
%
fclose(serobjw)
clear serobj

```

Appendix C Computer programs for the estimation of void fraction and bubble size distribution

This appendix contains the computer programs used in Chapter 3 and 4. All programs were written in MATLAB V 7.0. Table C.1 gives an overview of the programs treated in the appendix. There were different programs for each location. Only the programs for position A are displayed. All other positions were processed similarly.

Table C.1 Computer programs used in the estimation of void fraction and bubble size distribution

Program name	description
BPP1_maxvoid1.m	Computes the ensemble void fraction and the standard error on the mean void fraction
BPP1_maxvoid2A_D_E.m	Computes bubble size distribution for each beaking wave and also computes the standard error on the mean void fraction
fbub6_33BX.m	Subroutine to identify bubble signature points and performs bubble size distribution
htas_AA_30_std2.m	Displays the ensemble void fraction and the standard error on the mean void fraction
linearregression.m	Subroutine that performs linear regression
htas_AA_30_std3.m	Displays the ensemble void fraction and the standard error on the mean N value. Also performs histogram of the bubble time of arrival to the tip of the probe
meanpathA2.m	Estimates the mean path of the fiber-optic probes inside the bubble cloud
polycenter.m	Estimates the position of the bubble cloud centroid

Program: BPP1_maxvoid1.m

```

%
% Pannel # 1
% Void fraction 60 + 500 repeat runs

clear all
close all
clc
filename11 ='G:\WWP1088160_'; % HD #10
filename11 ='H:\WWP1088160_'; % HD #9
file51 = 'G:\void';
%file52 = 'E:\Program
Files\MATLAB71\work\voids_panel\void';
file52 = 'E:\Program
Files\MATLAB71\work\waves\P_ABCDE\void';
TT = ['A' 'B' 'C' 'D' 'E' 'W'];
frq = 100000;
filelim1 = 3; % Sampling time (sec)
thrs = 0.0; % Void constants
init = 10;
filelim = filelim1*frq - 100;
t1min = 100000;
t1max = filelim1*frq;

%
% WW088160 ppoint nrepeat1 nrepeats
WW088160 ppoint nrepeat1 nrepeats
WW088160 ppoint nrepeat1 nrepeats
WW088160 ppoint nrepeat1 nrepeats
%%%%%%%%%%
AA = [ 1 10 3 62 2 10 3
502 2 10 3 3 4 10 3
602; % Line A = 1161*2 = 2322
1 9 3 62 2 9 3
502 3 1 3 250 4 9 3
440; % Line B = 1250*2 = 2500
1 8 3 62 2 8 3
502 3 2 3 252 4 8 301
999; % Line C = 1410*2 = 2820
0 14 3 302 1 14 3
62 2 27 3 502 1 14 3
3; % Line D = 860*2 = 1720
0 11 3 302 1 11 3
62 2 30 3 502 4 30 3
1002; % Line E = 860*2 = 1720
5 1 3 1002 6 1 3
2002 5 1 3 3 5 1 3
3]; % comparison FOP vs HSC
%AA = [ 0 1 3 302 0 1 1
1 0 1 1 1 0 1 1
1; % Line C-1
% 0 2 3 302 0 2 1
1 0 2 1 1 0 2 1
1]; % Line C-2

```

```

% 1 8 3 62 2 8 3
502 3 2 3 252 4 8 3
1002; % Line C
% 0 14 3 302 2 27 3
502 4 10 1 1 4 10 1
1; % Line D
% 0 11 3 302 2 30 3
502 4 10 1 1 4 30 3
1002; % Line E
% 5 1 3 1002 6 1 3
2002 4 10 1 1 4 10 1
1]; % comparison FOP vs HSC

%AA = [ 1 16 3 62 1 16
1 1 1 16 1 1 1 16
1 1];
%%%%%%%%%%
cser = 0;
ncer = 100;
ccrn = 0;
for pts = 5:5 % Lines A-E + comparison FOP vs
HSC
    ppoint = pts;
    gnum = 0;
    wnum = 0;
    % Run #1
    filename =
strcat(filename11,sprintf('%d\ ',AA(pts,1)));
    npoint = AA(pts,2);
    nrepeat10 = AA(pts,3);
    nrepeats10 = AA(pts,4);
    VV100 = zeros(1,filelim1*frq); %
accumulates all void fraction measurements, P1
    VV200 = zeros(1,filelim1*frq); %
accumulates all void fraction measurements, P2
    VV300 = zeros(1,filelim1*frq); %
accumulates in grpoups of 100 void fraction
measurements, P1
    VV400 = zeros(1,filelim1*frq); %
accumulates in grpoups of 100 void fraction
measurements, P2
%
disp(sprintf('Point = %d',pts))
clear VSER
for i = nrepeat10 :nrepeats10
    %disp(sprintf('Repeat %d',i-2))
    filein =
strcat(filename,sprintf('P%d\d%d.mat',
npoint,i));%%%%%%%%%
    load (filein);
    V1 = datain;
%
    V10 =
double(V1(1:filelim1*frq,1))*20/2^16;

```

```

V20 =
double(V1(1:filelim1*frq,2))*20/2^16;
clear V1
xxt1 = find(V10 >0); VB1(xxt1) = 1.0;
xxt2 = find(V10 < 0); VB1(xxt2) = 0.0;
wnum = wnum + 1;
VV100 = VV100+VB1;
clear V10 xxt1 xxt2
xxt1 = find(V20 >0); VB2(xxt1) = 1.0;
xxt2 = find(V20 <0); VB2(xxt2) = 0.0;
wnum = wnum + 1;
VV200 = VV200+VB2;
clear V20 xxt1 xxt2
%
cser = cser + 1;
if cser < ncer
    VV300 = VV300+VB1;
    VV400 = VV400+VB2;
else
    VV300 = VV300+VB1;
    VV400 = VV400+VB2;
clear V10 V20 xxt1 xxt2 VB1 VB2
gnum = gnum + 1;
disp(sprintf('Group number = %d',gnum))
VSER1(gnum,:) = VV300/max(VV300);
VSER2(gnum,:) = VV400/max(VV400);
cser = 0;
VV300 = zeros(1,filelim1*frq);
VV400 = zeros(1,filelim1*frq);
end
end
%%%%%%%%%%%%%% Run #2
filename =
strcat(filename11,sprintf('%d\AA(pts,5));
npoint = AA(pts,6);
nrepeat20 = AA(pts,7);
nrepeats20 = AA(pts,8);
%disp(sprintf('Point # %d',npoint))
for i = nrepeat20 :nrepeats20
    %disp(sprintf('Repeat %d',i-2))
    filein =
strcat(filename,sprintf('P%d\d%d.mat',
npoint,i));%%%%%%%%%%
load (filein);
V1 = datain;
%
V10 =
double(V1(1:filelim1*frq,1))*20/2^16;
V20 =
double(V1(1:filelim1*frq,2))*20/2^16;
clear V1
xxt1 = find(V10 >0); VB1(xxt1) = 1.0;
xxt2 = find(V10 < 0); VB1(xxt2) = 0.0;
wnum = wnum + 1;
VV100 = VV100+VB1;
clear V10 xxt1 xxt2

```

```

xxt1 = find(V20 >0); VB2(xxt1) = 1.0;
xxt2 = find(V20 <0); VB2(xxt2) = 0.0;
wnum = wnum + 1;
VV200 = VV200+VB2;
clear V20 xxt1 xxt2
%
cser = cser + 1;
if cser < ncer
    VV300 = VV300+VB1;
    VV400 = VV400+VB2;
else
    VV300 = VV300+VB1;
    VV400 = VV400+VB2;
clear V10 V20 xxt1 xxt2 VB1 VB2
gnum = gnum + 1;
disp(sprintf('Group number = %d',gnum))
VSER1(gnum,:) = VV300/max(VV300);
VSER2(gnum,:) = VV400/max(VV400);
cser = 0;
VV300 = zeros(1,filelim1*frq);
VV400 = zeros(1,filelim1*frq);
end
end
%%%%%%%%%%%%%% Run #3
filename =
strcat(filename11,sprintf('%d\AA(pts,9));
npoint = AA(pts,10);
nrepeat30 = AA(pts,11);
nrepeats30 = AA(pts,12);
%disp(sprintf('Point # %d',npoint))
for i = nrepeat30 :nrepeats30
    %disp(sprintf('Repeat %d',i-2))
    filein =
strcat(filename,sprintf('P%d\d%d.mat',
npoint,i));%%%%%%%%%%
load (filein);
V1 = datain;
%
V10 =
double(V1(1:filelim1*frq,1))*20/2^16;
V20 =
double(V1(1:filelim1*frq,2))*20/2^16;
clear V1
xxt1 = find(V10 >0); VB1(xxt1) = 1.0;
xxt2 = find(V10 < 0); VB1(xxt2) = 0.0;
wnum = wnum + 1;
VV100 = VV100+VB1;
clear V10 xxt1 xxt2
xxt1 = find(V20 >0); VB2(xxt1) = 1.0;
xxt2 = find(V20 <0); VB2(xxt2) = 0.0;
wnum = wnum + 1;
VV200 = VV200+VB2;
clear V20 xxt1 xxt2
%
cser = cser + 1;
if cser < ncer

```



```

VV300 = VV300+VB1;
VV400 = VV400+VB2;
else
VV300 = VV300+VB1;
VV400 = VV400+VB2;
clear V10 V20 xxt1 xxt2 VB1 VB2
gnum = gnum + 1;
disp(sprintf('Group number = %d',gnum))
VSER1(gnum,:) = VV300/max(VV300);
VSER2(gnum,:) = VV400/max(VV400);
cser = 0;
VV300 = zeros(1,filelim1*frq);
VV400 = zeros(1,filelim1*frq);
end
end
%%%%%%%%%%%%%% Run #4
filename =
strcat(filename11,sprintf('%d\',AA(pts,13)));
npoint = AA(pts,14);
nrepeat40 = AA(pts,15);
nrepeats40 = AA(pts,16);
%disp(sprintf('Point # %d',npoint))
for i = nrepeat40 :nrepeats40
%disp(sprintf('Repeat %d',i-2))
filein =
strcat(filename,sprintf('P%d\d%d.mat',
npoint,i));%%%%%%%%%
load (filein);
V1 = datain;
%
V10 =
double(V1(1:filelim1*frq,1))*20/2^16;
V20 =
double(V1(1:filelim1*frq,2))*20/2^16;
clear V1
xxt1 = find(V10 >0); VB1(xxt1) = 1.0;
xxt2 = find(V10 <0); VB1(xxt2) = 0.0;
wnum = wnum + 1;
VV100 = VV100+VB1;
clear V10 xxt1 xxt2
xxt1 = find(V20 >0); VB2(xxt1) = 1.0;
xxt2 = find(V20 <0); VB2(xxt2) = 0.0;
wnum = wnum + 1;
VV200 = VV200+VB2;
clear V20 xxt1 xxt2
%
cser = cser + 1;
if cser < ncer
VV300 = VV300+VB1;
VV400 = VV400+VB2;
else
VV300 = VV300+VB1;
VV400 = VV400+VB2;
clear V10 V20 xxt1 xxt2 VB1 VB2
gnum = gnum + 1;
disp(sprintf('Group number = %d',gnum))

```

```

VSER1(gnum,:) = VV300/max(VV300);
VSER2(gnum,:) = VV400/max(VV400);
cser = 0;
VV300 = zeros(1,filelim1*frq);
VV400 = zeros(1,filelim1*frq);
end
end
gnum = gnum + 1;
disp(sprintf('Group number = %d',gnum))
VSER1(gnum,:) = (VV300 +
VV400)/(max(VV300) + max(VV400));
if pts == 6
file50 = strcat('E:\Program
Files\MATLAB71\work\waves\P_ABCDE\void
HSC');
save(file50, 'VSER1', 'VSER2', 'VV100',
'VV200', 'wnum');
clear VV100 VV200 VV100 VV200
VV300 VV400
else
file50 = strcat(file52,TT(pts));
save(file50, 'VSER1', 'VSER2','VV100',
'VV200', 'wnum');
clear VSER1 VSER2 VV100 VV200
VV300 VV400
end
end
end

```

Program: BPP1_maxvoid2A_D_E.m

```

clear all
close all
clc
thrs = 0;
frq = 100000;
TB = 8+40/30;
maxcs = 1000.0; % maximum cord size
delf = 10;
%
% Check signal repeatability
close all
clc
ssig = 0;
%%%%%%%%%%%%%%
% Pannel 1
%filename11 = 'G:\\WWP1088160_'; %HD10 in
office
%filename20 = 'G:\\void\'; %HD10 in office
filename11 = 'H:\\WWP1088160_'; %HD9 in
office
filename20 = 'H:\\void\'; %HD9 in office
filename12 = 'E:\Program
Files\MATLAB71\work\waves\P_ABCDE';
TT = ['A' 'B' 'C' 'D' 'E' 'W'];

```

```

% WW088160 ppoint nrepeat1 nrepeats
WW088160 ppoint nrepeat1 nrepeats
WW088160 ppoint nrepeat1 nrepeats
WW088160 ppoint nrepeat1 nrepeats
%%%%%%%%%%
AA = [ 1 10 3 62 2 10 3
502 2 10 3 3 4 10 3
602; % Line A
1 9 3 62 2 9 3
502 3 1 3 250 4 9 3
440; % Line B
1 8 3 62 2 8 3
502 3 2 3 252 4 8 301
999; % Line C
0 14 3 302 1 14 3
62 2 27 3 502 1 14 3
3; % Line D
0 11 3 302 1 11 3
62 2 30 3 502 4 30 3
1002; % Line E
5 1 3 1002 6 1 3
2002 5 1 3 3 5 1 3
3; % comparison FOP vs HSC
];
% A B C D E
% pts 1 2 3 4 5
xr1 = [ 0.2022 0 0 0.3569 0.4001];
xr2 = [ 0.3001 0 0 0.5355 0.5800];
% 1 2 3 4 5 6 7 8 9 10 11 12 13
vo = ['A' 'B' 'C' 'D' 'E' 'F' 'G' 'H' 'T' 'J' 'K' 'L' 'M'];
%
frq = 100000;
init = 10;
filelim1 = 2.5; % Sampling time (sec)
filelim = round(filelim1*frq) - 100;
%
% Velocity constants
b190 = -1.30; a190 = 1.49;
b100 = -0.87; a100 = 1.42;
b290 = -1.32; a290 = 1.41;
b200 = -0.94; a200 = 1.45;
%
maxcs1 = 20;
minbz = 0.7;
szbin0 = 0.10;
tbb = 1.33;
fcc = 0.88;
%
for pts = [1 4 5];
%
M1 = zeros(2000,13); M2 = zeros(2000,13);
szbin00 = szbin0*10.0;
minbsx = minbz + szbin00/2;
%rx12 = [minbsx:szbin00:maxcs1];
rx12 = [0.8:0.2:3.0 3.3:0.4:4.9 5.4:0.6:9.6
10.5:1.0:20.5 25:5:50];

```

```

for i = 1:12
rx13(i) = 0.2;
end
%
for i = 13:17
rx13(i) = 0.4;
end
%
for i = 18:25
rx13(i) = 0.6;
end
rx13(26)=0.9;
%
for i = 27:36
rx13(i) = 1.0;
end
rx13(37) = 4.5;
for i = 38:42
rx13(i) = 5.0;
end
%
%xr11 = [xr1(1) xr2(1)];
ppoint = pts;
cc1 = 0; cc2 = 0;
wnum = 0;
filename =
strcat(filename11,sprintf('%d\\',AA(pts,1)));
npoint = AA(pts,2);
nrepeat1 = AA(pts,3);
nrepeats = AA(pts,4);
npointr = npoint;
%
for i = nrepeat1 :nrepeats
wnum = wnum + 1;
disp(sprintf('Wave # %d',wnum));
clear MM11 MM12
TY1(1) = 0;
TY2(1) = 0;
filein =
strcat(filename,sprintf('\P%d\\d%d.mat',
npointr,i));%%%%%%%%%
fileout1 =
strcat(filename,sprintf('\P%d\\SD1%d.mat',npoi
ntr,i));%%%%%%%%%
fileout2 =
strcat(filename,sprintf('\P%d\\SD2%d.mat',npoi
ntr,i));%%%%%%%%%
load (filein);
V1 = datain;
V10 =
double(V1(1:filelim1*frq,1))*20/2^16;
V20 =
double(V1(1:filelim1*frq,2))*20/2^16;
clear V1 datain VV10 VV20
V10 = V10';
V20 = V20';

```

```

%
Prob = 1;
[FD1 FD2 MM11 cccb] =
fbub6_33BX(V10, frq, filelim, init, Prob,
ppoint,i,a190,a100,b190,b100,minbz,maxcs1,
rx12, xr1(pts), xr2(pts), fcc, tbb, rx13);
FF901(wnum,1:size(rx12,2))= FD1;
FF001(wnum,1:size(rx12,2))= FD2;
if cccb > 0
    for gt = 1 : cccb
        cc1 = cc1 + 1;
        M1(cc1,1:13) = MM11(gt,1:13);
    end
end
%
Prob = 2;
[FD1 FD2 MM12 cccb] =
fbub6_33BX(V20, frq, filelim, init, Prob,
ppoint,i,a290,a200,b290,b200,minbz,maxcs1,
rx12, xr1(pts), xr2(pts), fcc, tbb, rx13);
FF902(wnum,1:size(rx12,2))= FD1;
FF002(wnum,1:size(rx12,2))= FD2;
if cccb > 0
    for gt = 1 : cccb
        cc2 = cc2 + 1;
        M2(cc2,1:13) = MM12(gt,1:13);
    end
end
%
clc
end
%
filename =
strcat(filename11,sprintf('%d\\',AA(pts,5)));
npoint = AA(pts,6);
nrepeat1 = AA(pts,7);
nrepeats = AA(pts,8);
npointr = npoint;
for i = nrepeat1 :nrepeats
    wnum = wnum + 1;
    disp(sprintf('Wave # %d',wnum));
    clear MM11 MM12
    TY1(1) = 0;
    TY2(1) = 0;
    filein =
strcat(filename,sprintf('\P%d\\d%d.mat',
npointr,i));%%%%%%%%
    fileout1 =
strcat(filename,sprintf('\P%d\\SD1%d.mat',npoi
ntr,i));%%%%%%%%
    fileout2 =
strcat(filename,sprintf('\P%d\\SD2%d.mat',npoi
ntr,i));%%%%%%%%
    load (filein);
    V1 = datain;

```

```

V10 =
double(V1(1:filelim1*frq,1))*20/2^16;
V20 =
double(V1(1:filelim1*frq,2))*20/2^16;
clear V1 datain VV10 VV20
V10 = V10';
V20 = V20';
%
Prob = 1;
[FD1 FD2 MM11 cccb] =
fbub6_33BX(V10, frq, filelim, init, Prob,
ppoint,i,a190,a100,b190,b100,minbz,maxcs1,
rx12, xr1(pts), xr2(pts), fcc, tbb, rx13);
FF901(wnum,1:size(rx12,2))= FD1;
FF001(wnum,1:size(rx12,2))= FD2;
if cccb > 0
    for gt = 1 : cccb
        cc1 = cc1 + 1;
        M1(cc1,1:13) = MM11(gt,1:13);
    end
end
%
Prob = 2;
[FD1 FD2 MM12 cccb] =
fbub6_33BX(V20, frq, filelim, init, Prob,
ppoint,i,a290,a200,b290,b200,minbz,maxcs1,
rx12, xr1(pts), xr2(pts), fcc, tbb, rx13);
FF902(wnum,1:size(rx12,2))= FD1;
FF002(wnum,1:size(rx12,2))= FD2;
if cccb > 0
    for gt = 1 : cccb
        cc2 = cc2 + 1;
        M2(cc2,1:13) = MM12(gt,1:13);
    end
end
%
clc
end
%
filename =
strcat(filename11,sprintf('%d\\',AA(pts,9)));
npoint = AA(pts,10);
nrepeat1 = AA(pts,11);
nrepeats = AA(pts,12);
npointr = npoint;
for i = nrepeat1 :nrepeats
    wnum = wnum + 1;
    disp(sprintf('Wave # %d',wnum));
    clear MM11 MM12
    TY1(1) = 0;
    TY2(1) = 0;
    filein =
strcat(filename,sprintf('\P%d\\d%d.mat',
npointr,i));%%%%%%%%

```

```

fileout1 =
strcat(filename,sprintf('\P%d\SD1%d.mat',npoi
ntr,i));%%%%%%%%
fileout2 =
strcat(filename,sprintf('\P%d\SD2%d.mat',npoi
ntr,i));%%%%%%%%
load (filein);
V1 = datain;
V10 =
double(V1(1:filelim1*frq,1))*20/2^16;
V20 =
double(V1(1:filelim1*frq,2))*20/2^16;
clear V1 datain VV10 VV20
V10 = V10';
V20 = V20';
%
Prob = 1;
[FD1 FD2 MM11 ccbb] =
fbub6_33BX(V10, frq, filelim, init, Prob,
ppoint,i,a190,a100,b190,b100,minbz,maxcs1,
rx12, xrl(pts), xr2(pts), fcc, tbb, rx13);
FF901(wnum,1:size(rx12,2))= FD1;
FF001(wnum,1:size(rx12,2))= FD2;
if ccbb > 0
for gt = 1 : ccbb
cc1 = cc1 + 1;
M1(cc1,1:13) = MM11(gt,1:13);
end
end
%
Prob = 2;
[FD1 FD2 MM12 ccbb] =
fbub6_33BX(V20, frq, filelim, init, Prob,
ppoint,i,a290,a200,b290,b200,minbz,maxcs1,
rx12, xrl(pts), xr2(pts), fcc, tbb, rx13);
FF902(wnum,1:size(rx12,2))= FD1;
FF002(wnum,1:size(rx12,2))= FD2;
if ccbb > 0
for gt = 1 : ccbb
cc2 = cc2 + 1;
M2(cc2,1:13) = MM12(gt,1:13);
end
end
%
clc
end
%
filename =
strcat(filename11,sprintf('%d\AA(pts,13)));
npoint = AA(pts,14);
nrepeat1 = AA(pts,15);
nrepeats = AA(pts,16);
npointr = npoint;
for i = nrepeat1 :nrepeats
wnum = wnum + 1;
disp(sprintf('Wave # %d',wnum));

```

```

clear MM11 MM12
TY1(1) = 0;
TY2(1) = 0;
filein =
strcat(filename,sprintf('\P%d\d%d.mat',
npointr,i));%%%%%%%%
fileout1 =
strcat(filename,sprintf('\P%d\SD1%d.mat',npoi
ntr,i));%%%%%%%%
fileout2 =
strcat(filename,sprintf('\P%d\SD2%d.mat',npoi
ntr,i));%%%%%%%%
load (filein);
V1 = datain;
V10 =
double(V1(1:filelim1*frq,1))*20/2^16;
V20 =
double(V1(1:filelim1*frq,2))*20/2^16;
clear V1 datain VV10 VV20
V10 = V10';
V20 = V20';
%
Prob = 1;
[FD1 FD2 MM11 ccbb] =
fbub6_33BX(V10, frq, filelim, init, Prob,
ppoint,i,a190,a100,b190,b100,minbz,maxcs1,
rx12, xrl(pts), xr2(pts), fcc, tbb, rx13);
FF901(wnum,1:size(rx12,2))= FD1;
FF001(wnum,1:size(rx12,2))= FD2;
if ccbb > 0
for gt = 1 : ccbb
cc1 = cc1 + 1;
M1(cc1,1:13) = MM11(gt,1:13);
end
end
%
Prob = 2;
[FD1 FD2 MM12 ccbb] =
fbub6_33BX(V20, frq, filelim, init, Prob,
ppoint,i,a290,a200,b290,b200,minbz,maxcs1,
rx12, xrl(pts), xr2(pts), fcc, tbb, rx13);
FF902(wnum,1:size(rx12,2))= FD1;
FF002(wnum,1:size(rx12,2))= FD2;
if ccbb > 0
for gt = 1 : ccbb
cc2 = cc2 + 1;
M2(cc2,1:13) = MM12(gt,1:13);
end
end
%
clc
end
%
xx1 = find(rx12<=20);
A1 = sum(FF901,1); B1 = sum(FF902,1); C1
= A1 + B1;

```

```

nb90 = sum(C1(xx1));
A1 = sum(FF001,1); B1 = sum(FF002,1); C1
= A1 + B1;
nb00 = sum(C1(xx1));
clear A1 B1 C1
FF90m = mean([FF901;FF902]/1000);
FF90s = std([FF901;FF902]/1000);
SEom90 = (FF90s)/(2*wnum)^0.5;
MSEom90 = mean(SEom90/FF90m);
vv = 0;
h1 = figure;
plot(FF90m(xx1), SEom90(xx1),'.')
set(gcf,'Color', [1 1 1])
xlabel('N')
ylabel('SEOM')
disp(sprintf('Average Normalized Standard
error on mean 90 = %d',mean(MSEom90)))
vv = vv + 1;
filename12 = 'E:\Program
Files\MATLAB71\work\waves\P_ABCDE';
fileout114 =
strcat(filename12,'size_distribution',TT(pts),spri
ntf('%d',vv));
saveas(h1,fileout114,'fig')
%
FF00m = mean([FF001;FF002]/1000);
FF00s = std([FF001;FF002]/1000);
SEom00 = (FF00s)/(2*wnum)^0.5;
MSEom00 = mean(SEom00/FF00m);
h1 = figure;
plot(FF00m(xx1), SEom00(xx1),'.')
set(gcf,'Color', [1 1 1])
xlabel('N')
ylabel('SEOM')
disp(sprintf('Average Normalized Standard
error on mean 00 = %d',mean(MSEom00)))
vv = vv + 1;
fileout114 =
strcat(filename12,'size_distribution',TT(pts),spri
ntf('%d',vv));
saveas(h1,fileout114,'fig')
%
h1 = figure;
loglog(rx12,FF90m,'k*')
set(gcf,'Color', [1 1 1])
tk = strcat('Line ',TT(pts));
xlabel('s(mm)')
ylabel('N')
%
vv = vv + 1;
fileout114 =
strcat(filename12,'size_distribution',TT(pts),spri
ntf('%d',vv));
saveas(h1,fileout114,'fig')
%
h1 = figure;
loglog(rx12,FF00m,'ko')
set(gcf,'Color', [1 1 1])
xlabel('s(mm)')
ylabel('N')
vv = vv + 1;
fileout114 =
strcat(filename12,'size_distribution',TT(pts),spri
ntf('%d',vv));
saveas(h1,fileout114,'fig')
%
h1 = figure;
loglog(rx12,FF90m,'k*')
hold on
loglog(rx12,FF00m,'ko')
set(gcf,'Color', [1 1 1])
tk = strcat('Line ',TT(pts));
xlabel('s(mm)')
ylabel('N')
vv = vv + 1;
fileout114 =
strcat(filename12,'size_distribution',TT(pts),spri
ntf('%d',vv));
saveas(h1,fileout114,'fig')
%
aves = 3;
cc = 0;
clear A11 B11 C11 A1 B1 C1
for i = 1:aves:size(FF90m,2)
    cc = cc + 1;
    A11 = 0; B11 = 0; C11 = 0;
    for j = 1:aves
        A11 = A11 + FF90m(i+j-1);
        B11 = B11 + rx12(i+j-1);
        C11 = C11 + FF00m(i+j-1);
    end
    A1(cc) = A11/aves;
    B1(cc) = B11/aves;
    C1(cc) = C11/aves;
end
h1 = figure;
loglog(B1,A1,'k*')
hold on
loglog(B1,C1,'ko')
set(gcf,'Color', [1 1 1])
tk = strcat('Line ',TT(pts));
xlabel('s(mm)')
ylabel('N')
%axis([10^-0.1 50 10^-3 10^-0])
vv = vv + 1;
fileout114 =
strcat(filename12,'size_distribution',TT(pts),spri
ntf('%d',vv));
saveas(h1,fileout114,'fig')
%
h1 = figure;
loglog(B1,C1,'ko')

```

```

set(gcf,'Color',[1 1 1])
tk = strcat('Line ',TT(pts));
xlabel('s(mm)')
ylabel('N')
%axis([10^-0.1 50 10^-3 10^-0])
vv = vv + 1;
fileout114 =
strcat(filename12,'\size_distribution',TT(pts),sprin
ntf('%d',vv));
saveas(h1,fileout114,'fig')
clear A1 B1 C1 vv
%
% Bubble time histogram
%
rx = [1.2:0.0005*2:2.5];
MM = [M1; M2];
vv = find(MM(:,1) > 0);
NN = MM(vv,:);
NBS = size(NN,1);
disp(sprintf(' # bubbles = %d',NBS))
clear MM
MM = NN;
clear NN vv
%save(fileout112,'MM')
[yh12 xh12] = hist(MM(:,2)/frq,rx);
h = figure
plot((xh12-tbb)*fcc,yh12,'k','lineWidth',2)
yyx = [0:0.1:2.0];
%set(gca,'XTick',yyx)
%set(gca,'XTickLabel',yyx,'FontSize',12)
%yyy = [0:delf.maxf];
%set(gca,'YTick',yyy)
set(gcf,'Color',[1 1 1])
%axis([minx maxx 0 maxf])
x1 = ' \wedge';
x2 = ' t';
xlabel({x1; x2},'FontSize',14,
'VerticalAlignment','Middle')
ylabel('F_F','FontSize',14)
file1 = 'E:\Program
Files\MATLAB71\work\paper journal def _
2\ffreq';
fileout = strcat(file1,vo(pts),'.tif');
disp(fileout)
saveas(h,fileout)
fileout = strcat(file1,vo(pts),'.fig');
disp(fileout)
saveas(h,fileout)
MM = [M1; M2];
fileout114 =
strcat(filename12,'\size_distribution_data',TT(pts
));
save(fileout114,'nb90', 'nb00', 'FF90m',
'FF901', 'FF902', 'FF90s', 'SEom90', 'wnum',
'MSEom90', 'FF00m', 'FF001', 'FF002', 'FF00s',
'SEom00', 'MSEom00', 'MM')

```

```

clear fileout114 nb90 nb00 FF90m FF901
FF902 FF90s SEom90 wnum MSEom90 FF00m
FF001 FF002 FF00s SEom00 MSEom00 MM
M1 M2
clear FF002 FF00s SEom00 MSEom00
close all
pause(5)
clear MM M1 M2
end

```

Program: fbub6_33BX.m

```

function [FF1 FF2 MM ccbb] = fbub6_33BX(V,
frq, filelim, init, Prob,
ppoint,i,a1,a2,b1,b2,minbz,maxcs1, rx12, xxx1,
xxx2, fcc, tbb, rx13);

MM = zeros(1,13);
NN = zeros(1,13);
ccbb = 0;
ok10 = 0;
numsect=1;
SC=1.2;
thradj = 120/2^12*10;largev =
500/2^12*10;gdrop = -20/2^12*10;
gav = 800/2^12*10; gsigma = 100/2^12*10;
gslope = 10/2^12*10;
VL = -335/2^12*10;
thresh=VL+thradj ;
bbb=0;
bubnum = 0;
% 4- set the VL value and threshold Value
(thrshold = VL+120) for best results
k=1;
i=init; % for t = 9; vector position = 10
VBhalf=thresh-VL;
VBC=SC*VBhalf;
lim=filelim-10;
while (i<=lim) % A1
while ((i<=lim)&(V(i)>=thresh)) % A5
i=i+1;
if (V(i)>=(thresh+largev)) % A6
ok=1;
nn2=i;
n2=i+1;
end % A6
end % A5
% 4- Look for the start of bubble
while ((i<=lim)&(V(i)<=thresh)) % A2
i=i+10;
end % A2
for j=1:10 % A3
jj=i-11+j;
if (V(jj)<=thresh) % A4
tA=jj+1;

```

```

end % A4
end
% A3
n1=i-11;
ok=0;
% 5-Look for the end of bubble
while ((i<=lim)&(V(i)>=thresh)) % A5
    i=i+1;
    nend = i;
    if (V(i)>=(thresh+largev)) % A6
        ok=1;
        nn2=i;
        n2=i+1;
    end % A6
end
% A5

if (ok==1) % A7
    hi=max(V(tA:nn2));
    lo=min(V(tA:nn2));
    avgbin = ((hi-lo)/(2*VBC));
    if (avgbin <1)
        numbin=2;
    else
        numbin = (floor(avgbin)+1);
    end
    [numa,Xsa]=hist(V(tA:nend),numbin);
    [num,Xs]=hist(V(tA:nn2),numbin);
    [Y,I]=sort(num);
    ch1='y';
    ch2='n';
% 7- Bubble is too small
elseif (ok==0) % A7
    ch1='n';
    ch2='n';
end % A7
% 8- Value of VG (max Value) is chosen from
Histogram
loop=0;
while ((loop==0) & (i<lim) & (ok==1)) % A8
    VG=Xs(I(numbin));
    DV=VG-thresh;
    L1=thresh+0.1*DV;
    L2=thresh+0.9*DV;
% 9- Find the characteristic points C & D
j=tA;
tD=-1;
found=0;
while (tD<0) % A9
    if (V(j)>=L2) % A10
        diff1=V(j)-L2;
        diff2=L2-V(j-1);
        if (diff1<=diff2) % A11
            tD=j;
        elseif (diff1>diff2) % A11
            tD=j-1;
        end
    elseif (V(j)>=L1 & found==0) % A10
        diff1=V(j)-L1;
        diff2=L1-V(j-1);
        if (diff1<=diff2) % A12
            tC=j;
        else % A12
            tC=j-1;
        end % A12
        found=1;
    end % A10
    j=j+1;
end
% 10- Find the characteristic point B
tB=-1;
jj=nn2;
while tB<0 % A13
    if V(jj)>=L2 % A14
        tB=jj+1;
        drop=V(tB)-V(tB-1);
        while (drop<gdrop) % A15
            tB=tB-1;
            drop=V(tB)-V(tB-1);
        end % A15
    end % A14
    jj=jj-1;
end % A13
loop=1;
%% SIGNATURE POINTS
%
if tA == tC
    tC = tC + 1;
end

% 11- Check that the bubble is with good
signature and then do its calculations
if tB > tD
    av=mean(V(tD:tB));
    Sigma=std(V(tD:tB));
    slope=(V(tA-1)-V(tD+1))/((tA-1)-
(tD+1));
else
    av = 0;
    slope = 0;
    Sigma = 100;
end
%
if (av>=gav)& (slope >=gslope) & (Sigma
<= gsigma);
    bbb = bbb+1;
    sig(k)=tA-1; % real time = position - 1
    sig(k+1)=tB-1;
    sig(k+2)=tC-1;
    sig(k+3)=tD-1;
    sig(k+4)=(V(tD)-V(tC))/(tD-tC);
end

```



```

load(filename)
disp(sprintf('Number of waves %d',wnum))
VSER = [VSER1;VSER2];
aa = mean(VSER,1);
bb = std(VSER,1);
VVT = aa;
cc = bb./aa;
h = figure;
t1min = mint*frq; % seconds
t1max = maxt*frq; % seconds
h = figure;
plot((axx1-tbb)*fcc, VVT(axx2),'k',
'LineWidth',3);
sfont = 14;
yyx = [0:0.1:2.0];
set(gca,'XTick',yyx)
set(gca,'XTickLabel',yyx,'FontSize',12)
yyy = [0:0.2:1.2];
set(gca,'YTick',yyy)
set(gca,'YTickLabel',yyy,'FontSize',12)
axis([minx maxx -0.02 1.02])
set(gcf,'Color',[1 1 1])
x1 = '\wedge';
x2 = 't';
xlabel({x1; x2},'FontSize',14,
'VerticalAlignment','Middle')
y2 = '<\alpha\it>';
ylabel({y2},'FontSize',sfont)
hold on
[x y] = ginput(1);
tmax = x;
vmax = y;
plot(x,y,'ks','MarkerEdgeColor','k',
'MarkerFaceColor','w','MarkerSize',10)
hold on
[x y] = ginput(1);
xxx1 = x;
plot(x,y,'ko','MarkerEdgeColor','k',
'MarkerFaceColor','w','MarkerSize',10)
hold on
[x y] = ginput(1);
xxx2 =x;
plot(x,y,'ko','MarkerEdgeColor','k',
'MarkerFaceColor','w','MarkerSize',10)
%
disp(sprintf('Max void = %0.5g',vmax))
disp(sprintf('Tmax = %0.5g',tmax))
disp(sprintf('Frame # = %d',round((xxx1/fcc +
tbb)*30)))
disp(sprintf('-----'))
disp(sprintf('xxx1 = %0.5g',xxx1))
disp(sprintf('xxx2 = %0.5g',xxx2))
axx10 = [(xxx1/fcc + tbb):1/frq:(xxx2/fcc +
tbb)];
axx20 = round(axx10*frq);
vmean = mean(VVT(axx20));

```

```

disp(sprintf('Mean void = %0.5g',vmean))
file1 = 'E:\Program
Files\MATLAB71\work\paper journal def _
2\void';
fileout = strcat(file1,vo(i),'.tif');
disp(fileout)
fileout = strcat(file1,vo(i),'.fig');
disp(fileout)
pause(5)
figure
h = figure;
VV1 = aa + bb;
VV2 = aa - bb;
plot((axx1-tbb)*fcc, VV1(axx2),'k',
'LineWidth',2);
hold on
plot((axx1-tbb)*fcc, VVT(axx2),'k',
'LineWidth',3);
hold on
plot((axx1-tbb)*fcc, VV2(axx2),'k',
'LineWidth',2);
yyx = [0:0.1:2.0];
set(gca,'XTick',yyx)
set(gca,'XTickLabel',yyx,'FontSize',12)
yyy = [0:0.2:1.2];
set(gca,'YTick',yyy)
set(gca,'YTickLabel',yyy,'FontSize',12)
axis([minx maxx -0.02 1.02])
set(gcf,'Color',[1 1 1])
x1 = '\wedge';
x2 = 't';
xlabel({x1; x2},'FontSize',14,
'VerticalAlignment','Middle')
y2 = '<\alpha\it>';
ylabel({y2},'FontSize',sfont)
file1 = 'E:\Program
Files\MATLAB71\work\paper journal def _
2\fstd';
fileout = strcat(file1,vo(i),'.tif');
disp(fileout)
%
% Standard error on the mean
%
[x y] = ginput(2);
disp('Standard error on the mean void fraction
measured between points')
disp(sprintf('x1 = %0.5g',x(1)))
disp(sprintf('x2 = %0.5g',x(2)))
disp(sprintf('%d groups, each of 100 repeat
runs',size(VSER,1)))
cvvoid =
cc(round((x(1)/fcc+tbb)*frq):round((x(2)/fcc+tb
b)*frq))/size(VSER,1)^0.5;
meanstd = mean(cvvoid);
disp(sprintf('Standard error on the mean void
fraction = %0.5g',meanstd))

```

Program: linearregression.m

```

function [Y1,Y95u,Y95b,Y95u1,Y95b1, mmx,
bb, rxy, simul, r2, clb95,DB]=
linearregression(X,Y)
N = length(X);
M=mean(X);
MY = mean(Y);
x2=sum(X(:).*X(:));
y2=sum(Y(:).*Y(:));
xy=sum(X(:).*Y(:));
rxy1=(N*sum(X(:).*Y(:))-sum(X(:))*
sum(Y(:)));
rxy2=(N*x2-sum(X(:)^2)^0.5*(N*y2-
sum(Y(:)^2)^0.5;
% rxy = sample correlation coefficient
rxy=rxy1/rxy2;
%estimated regression coefficients
%
b=(N*sum(X(:).*Y(:))-sum(X(:))*
sum(Y(:)))/(N*x2-sum(X(:)^2));
mmx = b;
a=(sum(Y(:))-b*sum(X(:)))/N;
bb = a;
sx2=(N*x2-(sum(X(:))^2)/N^2;
sy2=(N*y2-(sum(Y(:))^2)/N^2;
sxy2=sy2*(1-rxy^2);
%t=b*sx2^0.5*(N-2)^0.5/sxy2^0.5;
P=tinv(0.975,N-2);
Estsxy=(N*sxy2/(N-2))^0.5;
DB= Estsxy*P/(sx2^0.5*N^0.5);
clb95 = DB;
simul = [P Estsxy N M sx2];
for j=1:length(X)
    XJ(j)=X(j);
    Y1(j)=a+b*XJ(j);
    DYP(j)=P*Estsxy*(1/N+(XJ(j)-
M)^2/(N*sx2))^0.5;
    DYP1(j)=P*Estsxy*(1+1/N+(XJ(j)-
M)^2/(N*sx2))^0.5;
    Y95b(j)=Y1(j) - DYP(j);
    Y95b1(j)=Y1(j) - DYP1(j);
    Y95u(j)=Y1(j) + DYP(j);
    Y95u1(j)=Y1(j) + DYP1(j);
end
r2 = sum((Y1-MY).^2)/sum((Y-MY).^2);

```

Program: htas_AA_30_std3.m

```

clear all
close all
clc
mmss = 8;

```

```

ffss = 16;
file1 = 'E:\Program
Files\MATLAB71\work\waves\P_ABCDE\size_
distribution_data';
TT = 'A';
filename = strcat(file1,TT);
load(filename)
%
rx12 = [0.8:0.2:3.0 3.3:0.4:4.9 5.4:0.6:9.6
10.5:1.0:20.5 25:5:50];
for i = 1:12
    rx13(i) = 0.2;
end
%
for i = 13:17
    rx13(i) = 0.4;
end
%
for i = 18:25
    rx13(i) = 0.6;
end
rx13(26)=0.9;
%
for i = 27:36
    rx13(i) = 1.0;
end
rx13(37) = 4.5;
for i = 38:42
    rx13(i) = 5.0;
end
%
nwt = 2*wnum;
%
disp(strcat('Position ',TT))
disp(strcat('Program: htas_',TT,TT,'_30_std2'))
disp(sprintf('# waves = %d',nwt))
FT = FF00m;
xcc = find(FT<=0);
FT(xcc) = 1;
disp(sprintf('Average mean standard error on the
mean (00) = %d', mean(FF00s/(nwt)^0.5./FT)))
aves = 3;
cc = 0;
clear A11 B11 C11 A1 B1 C1
for i = 1:aves:size(FF90m,2)
    cc = cc + 1;
    A11 = 0; B11 = 0; C11 = 0;
    for j = 1:aves
        A11 = A11 + FF90m(i+j-1);
        B11 = B11 + rx12(i+j-1);
        C11 = C11 + FF00m(i+j-1);
    end
    A1(cc) = A11/aves;
    B1(cc) = B11/aves;
    C1(cc) = C11/aves;
end

```

```

h1 = figure;
loglog(B1,A1,'k*','MarkerSize', mmss)
hold on
loglog(B1,C1,'ko','MarkerSize', mmss)
set(gcf,'Color', [1 1 1])
axis([0.7 20 10^-7 10^-4])
set(gca,'FontSize',ffss)
xlabel('s')
ylabel('N')
file1 = 'E:\Program
Files\MATLAB71\work\paper journal
def_3\figures\size_distribution';
file2 = strcat(TT,'1.fig');
file = strcat(file1, file2);
saveas(h1,file)
file2 = strcat(TT,'1.tif');
file = strcat(file1, file2);
saveas(h1,file)
%
h1 = figure;
xd = find(C1 > 0);
B10 = B1(xd);
C10 = C1(xd);
xz = [0.8
20];%%%%%%%%%%
%%%%%%%%%%
xd = find(B10 > xz(1) & B10 <= xz(2) & C10 >
0);
BB1 = B10(xd);
CC1 = C10(xd);
loglog(B10,C10,'ko--','LineWidth',3,
'MarkerSize', mmss)
x = log10(BB1);
y = log10(CC1);
set(gcf,'Color', [1 1 1])
xlabel('s','FontSize', ffss)
ylabel('N','FontSize', ffss)
axis([0.8 20 10^-7 10^-4])
set(gca,'FontSize',16)
hold on
[Y1,Y95u,Y95b,Y95u1,Y95b1, mmx11, bb11,
rxy, simul, r1, clb95,DB1]=
linearregression(x,y);
rxy2 = rxy;
xxx = [xz(1):0.1:xz(2)];
loglog(xxx,
10.^(log10(xxx)*mmx11+bb11),'k','LineWidth',2
)
a = mmx11; b = num2str(a); c1= b(1:5);
a = DB1; b = num2str(a); c2= b(1:4);
text(10^0.5, 10^-
4.8, strcat(c1, '\pm', c2), 'FontSize', ffss,
'FontWeight', 'Bold')
hold on
file2 = strcat(TT,'2.fig');
file = strcat(file1, file2);

```

```

saveas(h1,file)
file2 = strcat(TT,'2.tif');
file = strcat(file1, file2);
saveas(h1,file)
%
frq = 100000;
tbb = 1.33;
fcc = 0.88;
xs1 = find(MM(:,1) > 0);
NN = MM(xs1,:);
clear MM
MM = NN;
disp(sprintf('# bubbles = %d',size(MM,1)))
clear NN
%rx = [0.1:0.01:1.0];
clear NN vv
%save(fileout112,'MM')
%rx = [1.2:0.0005:2.5];
[yh12 xh12] = hist(MM(:,2)/frq);
h1 = figure;
plot((xh12-tbb)*fcc,yh12,'o-k','LineWidth',2)
yyx = [0.2:0.02:0.28];
set(gca,'XTick',yyx)
sfont = 14;
set(gca,'FontSize',sfont)
axis([0.2 0.28 0 15])
%set(gca,'XTickLabel',yyx,'FontSize',sfont)
%set(gca,'YTick',0:20:140, 'FontSize',16)
set(gcf,'Color', [1 1 1])
x1 = ' \wedge';
x2 = ' t';
xlabel({x1; x2},'FontSize',sfont,
'VerticalAlignment','Middle')
ylabel('F_a','FontSize',sfont)
file2 = strcat(TT,'3.fig');
file = strcat(file1, file2);
saveas(h1,file)
file2 = strcat(TT,'3.tif');
file = strcat(file1, file2);
saveas(h1,file)

```

Program: meanpathA2.m

```

clear
close all
clc
%
% 1 2 3 4 5 6 7 8 9 10 11 12 13
vo = ['A' 'B' 'C' 'D' 'E' 'F' 'G' 'H' 'I' 'J' 'K' 'L' 'M'];
lamb = 193.6;
hho = 60;
aaa = 17.81; % distance in cm tip of the probe at
point A to breaking point
bbb = 6.00; % distance in cm probe to water
surface

```

```

szsc = [0.0679 0.0738 0.0707 0.0679 0.0565
0.0893 0.0893 0.0346 0.0333 0.0339 0.0326
0.0565 0.0547 zeros(1,7) 0.0303 0 0.0303
zeros(1,14) 0.0314 zeros(1,11) 0.0200;
];
d1 = aaa;
%
cloudn = 1;
file1 = 'L:\AxisA\';
frames = [44:2:54];
x1 = [510]; % x tip
y1 = [523]; % y tip
file3 = 'L:\AxisA\f_047.tif';
%
cc = cloudn*10;
zzero1 = (y1(cloudn)*szsc(cloudn)+bbb)/lamb;
xt1 = (x1(cloudn)*szsc(cloudn));
yt1 = (y1(cloudn)*szsc(cloudn))/lamb-zzero1;
a1 = imread(file3);
h = figure;
subplot(1,1,1), subimage([(1*szsc(cloudn)-
d1)/lamb:1*szsc(cloudn)/lamb:(1000*szsc(cloud
n)-d1)/lamb],[1*szsc(cloudn)/lamb-
zzero1:1*szsc(cloudn)/lamb:(1000*szsc(cloudn))
/lamb-zzero1],a1(1:1000,1:1000));
hold on
plot(xt1-
d1)/lamb,(y1(cloudn)*szsc(cloudn))/lamb-
zzero1,'ok','MarkerFaceColor','w','MarkerSize',8)
yyx = [-0.2:0.05:0.2];
%set(gca,'YTick',yyx)
%set(gca,'YTickLabel',yyx*-1,'FontSize',14)
hold on
xy = [];
n = 0;
disp('Left mouse button picks points.')
disp('Right mouse button picks last point.')
but = 1;
while but == 1
    [xi,yi,but] = ginput(1);
    plot(xi,yi,'ro')
    n = n+1;
    xy(:,n) = [xi;yi];
end
[area,cx0,cy0] = polycenter(xy(1,:),xy(2,:));
close all
%axis([0.05 0.40 -0.15 0.10])
axs1 = -0.08; axs2 = 0.25; axs3 = -0.11; axs4 =
0.12;
cc = cloudn*10;
cvc = 0;
for ii = 1:length(frames)
    tt = frames(ii);
    st = tt;
    sst = [st];
    %

```

```

ppt = 1;
s1 = num2str(sst(ppt)); ss = size(s1);
ss1 = ss(1,2); pos = ss1+1;
for i = 3:-1:1
    pos = pos-1;
    if pos > 0
        s1(pos);
        A(ppt,i)=str2double(s1(pos));
    end
end
%
file2 =
sprintf('f_%d%d%d.tif',A(1,1),A(1,2),A(1,3));
%
file = strcat(file1,file2)
a1 = imread(file);
c1 = a1;
%zzero1 = (y1*szsc(cloudn)+bbb)/lamb;
%h = figure
%subplot(1,1,1), subimage(c1)
%pause
h = figure;
subplot(1,1,1), subimage([(1*szsc(cloudn)-
d1)/lamb:1*szsc(cloudn)/lamb:(1000*szsc(cloud
n)-d1)/lamb],[1*szsc(cloudn)/lamb-
zzero1:1*szsc(cloudn)/lamb:(1000*szsc(cloudn))
/lamb-zzero1],c1(1:1000,1:1000));
hold on
plot(xt1-
d1)/lamb,(y1(cloudn)*szsc(cloudn))/lamb-
zzero1,'ok','MarkerFaceColor','w','MarkerSize',8)
yyx = [-0.2:0.05:0.2];
%set(gca,'YTick',yyx)
%set(gca,'YTickLabel',yyx*-1,'FontSize',14)
hold on
xy = [];
n = 0;
disp('Left mouse button picks points.')
disp('Right mouse button picks last point.')
but = 1;
while but == 1
    [xi,yi,but] = ginput(1);
    plot(xi,yi,'ro')
    n = n+1;
    xy(:,n) = [xi;yi];
end
[area,cx(ii),cy(ii)] =
polycenter(xy(1,:),xy(2,:));
close all
h = figure;
subplot(1,1,1), subimage([(1*szsc(cloudn)-
d1)/lamb:1*szsc(cloudn)/lamb:(1000*szsc(cloud
n)-d1)/lamb],[1*szsc(cloudn)/lamb-
zzero1:1*szsc(cloudn)/lamb:(1000*szsc(cloudn))
/lamb-zzero1],c1(1:1000,1:1000));
hold on

```

```

plot((xt1-
d1)/lamb,(y1(cloudn)*szsc(cloudn))/lamb-
zzero1,'ok','MarkerFaceColor','w','MarkerSize',8)
hold on
plot(cx(ii),cy(ii),'*k','MarkerEdgeColor','w',
'MarkerFaceColor','k', 'MarkerSize',8)
%set(gca,'YTick',yyx)
%set(gca,'YTickLabel',yyx*-1,'FontSize',14)
x1 = '\wedge';
x2 = 'x';
xlabel({x1; x2},'FontSize',14,
'VerticalAlignment','Middle')
x1 = '\wedge';
x2 = 'y';
ylabel({x1; x2},'FontSize',14,
'VerticalAlignment','Middle')
set(gcf,'Color', [1 1 1])
%axis([axs1 axs2 axs3 axs4])
pause
close all
h = figure;
subplot(1,1,1), subimage([(1*szsc(cloudn)-
d1)/lamb:1*szsc(cloudn)/lamb:(1000*szsc(cloud
n)-d1)/lamb],[1*szsc(cloudn)/lamb-
zzero1:1*szsc(cloudn)/lamb:(1000*szsc(cloudn)
)/lamb-zzero1],c1(1:1000,1:1000));
hold on
plot((xt1-
d1)/lamb,y1(cloudn)*szsc(cloudn))/lamb-
zzero1,'ok','MarkerFaceColor','w','MarkerSize',8)
hold on
for ii = 1:length(frames)
plot(cx0 + ((xt1-d1)/lamb-cx(ii)), cy0 + (yt1-
cy(ii)),'ok','MarkerFaceColor','w','MarkerSize',8)
hold on
end
x1 = '\wedge';
x2 = 'x';
xlabel({x1; x2},'FontSize',14,
'VerticalAlignment','Middle')
x1 = '\wedge';
x2 = 'y';
ylabel({x1; x2},'FontSize',14,
'VerticalAlignment','Middle')
set(gcf,'Color', [1 1 1])
set(gca,'XTick',-1.0:0.05:1.0,'FontSize',14)
set(gca,'YTick',yyx)
set(gca,'YTickLabel',yyx*-1,'FontSize',14)
%axis([axs1 axs2 axs3 axs4])
hold on
ii = length(frames) + 1;
[cx(ii),cy(ii)] = ginput(1);
plot(cx(ii),cy(ii),'ok','MarkerFaceColor','w','Mark
erSize',8)
ii = length(frames) + 1;
[cx(ii),cy(ii)] = ginput(1);
plot(cx(ii),cy(ii),'ok','MarkerFaceColor','w','Mark
erSize',8)
cvc = cvc + 1;
file10 = 'E:\Program
Files\MATLAB71\work\paper journal def _
2\filepath';
fileout =
strcat(file10,vo(cloudn),sprintf('%d.tif',cvc));
disp(fileout)
saveas(h,fileout)
fileout =
strcat(file10,vo(i),sprintf('%d.fig',cvc));
saveas(h,fileout)
pause
c1 = imread(file3);
h = figure;

```

```

subplot(1,1,1), subimage([(1*szsc(cloudn)-
d1)/lamb:1*szsc(cloudn)/lamb:(1000*szsc(cloud
n)-d1)/lamb],[1*szsc(cloudn)/lamb-
zzero1:1*szsc(cloudn)/lamb:(1000*szsc(cloudn)
)/lamb-zzero1],c1(1:1000,1:1000));
hold on
plot((xt1-
d1)/lamb,yt1,'ok','MarkerFaceColor','w','MarkerS
ize',8)
hold on
ccx = [(xt1-d1)/lamb + ((xt1-d1)/lamb - cx(1,[1
length(cx)-1])) (xt1-d1)/lamb];
ccy = [(y1(cloudn)*szsc(cloudn))/lamb-zzero1 +
((y1(cloudn)*szsc(cloudn))/lamb-zzero1 -
cy(1,[1 length(cx)-1]))
(y1(cloudn)*szsc(cloudn))/lamb-zzero1];
ccx = [ccx cx(ii)];
ccy = [ccy cy(ii)];
[B IR] = sort(ccx);
ccxx = ccx(IR);
ccyy = ccy(IR);
xy = [ ccxx;
      ccyy];
%n = length(frames)+1;
n = 4;
t = 1:n;
ts = 1:0.1:n;
xys1 = spline(t,xy,ts);
% Plot the interpolated curve.
plot(xys1(1,:),xys1(2,:),'-w','Linewidth',2);
x1 = ' \wedge';
x2 = ' x';
xlabel({x1; x2},'FontSize',14,
'VerticalAlignment','Middle')
x1 = '\wedge';
x2 = 'y';
set(gcf,'Color', [1 1 1])
set(gca,'XTick',-1.0:0.05:1.0, 'FontSize',14)
set(gca,'YTick',yyx)
set(gca,'YTickLabel',yyx*-1,'FontSize',14)
axis([axs1 axs2 axs3 axs4])
cvc = cvc + 1;
file10 = 'E:\Program
Files\MATLAB71\work\paper journal def _
2\filepath';
fileout =
strcat(file10,vo(cloudn),sprintf('%d.tif',cvc));
disp(fileout)
saveas(h,fileout)
fileout = strcat(file10,vo(i),sprintf('%d.fig',cvc));
disp(fileout)
saveas(h,fileout)

```

Program: polycenter.m

```

function [area,cx,cy] = polycenter(x,y,dim)

%POLYCENTER Area and centroid of polygon.
% [AREA,CX,CY] = POLYCENTER(X,Y)
returns the area and the centroid
% coordinates of the polygon specified by the
vertices in the vectors X
% and Y. If X and Y are matrices of the same
size, then POLYCENTER
% returns the centroid and area of polygons
defined by the columns X and
% Y. If X and Y are arrays, POLYCENTER
returns the centroid and area of
% the polygons in the first non-singleton
dimension of X and Y.
%
% POLYCENTER is an extended version of
POLYAREA.
%
% The polygon edges must not intersect. If they
do, POLYCENTER returns
% the values of the difference between the
clockwise encircled parts and
% the counterclockwise ones. As in
POLYAREA, the absolute value is used
% for the area.
%
% [AREA,CX,CY] =
POLYCENTER(X,Y,DIM) returns the centroid
and area of the
% polygons specified by the vertices in the
dimension DIM.
%
% Example:
% -----
% L = linspace(0,2.*pi,6); xv = cos(L); yv =
sin(L);
% xv = [xv ; xv(1)]; yv = [yv ; yv(1)];
% [A,cx,cy] = polycenter(xv,yv);
% plot(xv,yv,cx,cy,'k+')
% title(['Area = ' num2str(A)]), axis equal
%
% Damien Garcia, 08/2007, directly adapted
from POLYAREA
%
% See also POLYAREA.

if nargin==1

error('MATLAB:polycenter:NotEnoughInputs',
Not enough inputs.);
end

if ~isequal(size(x),size(y))

```

```

error('MATLAB:polycenter:XYSizeMismatch',
X and Y must be the same size. ');
end

if nargin==2
    [x,nshifts] = shiftdim(x);
    y = shiftdim(y);
elseif nargin==3
    perm = [dim:max(length(size(x)),dim) 1:dim-1];
    x = permute(x,perm);
    y = permute(y,perm);
end

warn0 =
warning('query','MATLAB:divideByZero');
warning('off','MATLAB:divideByZero')

siz = size(x);
if ~isempty(x)
    tmp = x(:,:).*y([2:siz(1) 1],:) - x([2:siz(1) 1],:).*y(:,:);
    area = reshape(sum(tmp),[1 siz(2:end)])/2;
    cx = reshape(sum((x(:,:)+x([2:siz(1) 1],:)).*tmp/6),[1 siz(2:end)])./area;
    cy = reshape(sum((y(:,:)+y([2:siz(1) 1],:)).*tmp/6),[1 siz(2:end)])./area;
    area = abs(area);
else
    area = sum(x); % SUM produces the right
value for all empty cases
    cx = NaN(size(area));
    cy = cx;
end

warning(warn0.state,'MATLAB:divideByZero')

if nargin==2
    area = shiftdim(area,-nshifts);
    cx = shiftdim(cx,-nshifts);
    cy = shiftdim(cy,-nshifts);
elseif nargin==3
    area = ipermute(area,perm);
    cx = ipermute(cx,perm);
    cy = ipermute(cy,perm);
end

```